Ethoxylation Reactor Modelling and Design

by

Yen-ni Chiu

Bachelor of Engineering (Chemical) UNSW

A thesis submitted in fulfillment of the requirements for the degree of Doctor of Philosophy

Facaulty of Engineering and Industrial Sciences

Swinburne University of Technology

Melbourne, Australia

To Mum, Dad, Jess and Ted

Abstract

The manufacture of nonionic surfactants generally involves ethoxylation via ethylene oxide condensation onto a hydrophobe substrate, mostly in the presence of an alkaline catalyst. Nonionic surfactants are used widely in industrial applications, such as detergents, health and personal care, coatings, and polymers. In Australia, approximately one-third of the annual consumption of nonionic surfactants is imported from offshore manufacturers; the market is highly competitive with the local manufacturer facing increasing competition from imports. Optimisation is a pressing need for the current manufacturing plant of the industrial partner for this research project, Huntsman Corporation Australia Pty Limited, the sole domestic manufacturer of nonionic surfactants in Australia. Therefore, the objectives of this research project were

- to gain a better understanding of the various chemical and physical processes occurring simultaneously in an ethoxylation process;
- to identify the process limitation in an existing production plant operated by Huntsman Corporation Australia, and
- to explore measures for enhancing the asset productivity of the production plant.

An ethoxylation process working model, describing the chemical kinetics and the physical transport processes involved, was developed to aid the exploration of optimisation opportunities, which would otherwise be empirical. Accordingly, this research project was structured into a two-stage program. The first stage determined the ethoxylation kinetics experimentally. The second stage investigated the interactions of physical transport processes numerically using a computational fluid dynamics (CFD) technique. The manufacturing scheme discussed in this thesis gave particular emphasis to the ethoxylation process operated in semi-batch stirred reactors.

In the first stage, a series of kinetic experiments was performed in a well-stirred laboratory autoclave under base-catalysed conditions. The experimental outcomes were developed into a comprehensive kinetic model which took into account the non-ideal features in the reactor operation. Time-dependent physical changes of the reaction system, such as liquid volume, ethylene oxide solubility and density were also included. The ethoxylation behaviour predicted by the model was shown to be in good agreement with the experimental measurements. This indicated that the kinetic model was sufficiently robust to reproduce the reaction behaviour of a commercially operated ethoxylation operation.

In the second stage, numerical simulations of an existing ethoxylation reactor system were presented. In addition, two components were addressed: identification of the process limitation and increasing productivity of the industrial-scale ethoxylation plant. An important assumption was made for the ethylene

oxide injection system used in this research project which subsequently simplified the ethoxylation system into a single liquid with miscible chemical species.

In the identification of the process limitation, three possible rate-limiting factors were examined: mixing, heat removal and reactor pressure rating. Examination and analysis of the physical data available from plant batch reports found that the reactor pressure rating and the presence of nitrogen padding were the rate-limiting factors to the ethoxylation operations in the industrial reactors. It was recommended that the reactor pressure rating be increased to raise the asset productivity of the reactor.

In the numerical simulations of the ethoxylation reactor, time-dependent CFD models were developed for two systems: the ethylene oxide injection pipe and the stirred ethoxylation reactors.

The heat transfer of ethylene oxide liquid injection was calculated in a two-dimensional model of the dip-leg pipe used in an industrial-scale ethoxylation reactor. The computation gave the temperature of the injection outflow which was validated against the calculated value by empirical correlation. The effects of various surrounding reaction temperatures, injection rates and pipe sizes on the heat transfer rate were investigated. From these, a range of operating conditions yielding a liquid ethylene oxide outflow was selected. Furthermore, it was found that boiling of ethylene oxide was significantly reduced with increasing pipe diameters. It was recommended that the asset productivity of the reactor be improved by keeping more ethylene oxide injected as a liquid in the reaction mixture to raise the reaction rate and shorten the reaction time.

Three-dimensional simulations of a baffled reactor agitated by a single- or a dual-Rushton impeller were presented for both non-reactive and reactive flows. Multiple frames of reference and sliding grid methods were used in sequence to describe the relative motion between the rotating impeller and the stationary baffles. The turbulence parameters were modelled with the standard k-ε turbulence model.

The simulations of non-reactive flow were compared with the literature velocity data obtained from both the experiments and simulations. Good agreement was achieved. The model was then extended to incorporate ethoxylation flow with integration of the kinetics established in the first stage. Both the laboratory autoclave and the industrial-scale reactors were simulated. The former took into account the ethoxylation exotherm and the latter was carried out isothermally. Both simulations were validated against reaction data obtained from physical experiments, either the kinetic experiments or the plant batch productions. The validated model allowed us to determine the optimum operating condition and explore a new reactor system with enhanced asset productivity. A 50% increase in productivity could be accomplished if the ethoxylation was operated closer to the current design pressure limit. Furthermore, the

operating pressure of a new reactor system needed to be doubled if the asset productivity were to be increased to approximately three times the current performance.

Acknowledgements

I wish to thank my supervisors Professor Kerry Pratt, Dr. Kian Ngian and Dr. Jamal Naser for their guidance and continual encouragement for this fruitful fulfilment. Over the years, I really appreciated Kerry's invaluable comments and broad knowledge that stimulated and challenged my brain to extreme; Kian's unconventional engineering approach and deep expertise in the field that inspired me to think outside the square, and Jamal's witty approach that made the complex CFD problems a fascinating subject to tackle. I would also like to extend my appreciation to Associate Professor Alan Easton for his guidance in mathematical modelling.

I would like to acknowledge the Australian Research Council for provision of an Australian Postgraduate Award (Industry) as part of the Industry Linkage Program that allowed this research program to be undertaken. I also would like to acknowledge and thank Huntsman Corporation Australia for the financial support of this project. I am also very grateful to the technical staff at Huntsman Corporation Australia for providing the laboratory training, experimental advice and supervision during the lengthy hours of the laboratory work.

Special thanks go to Ms. Helen Camp and Ms. Helen Beaumont at the Office of Research for offering their warm-hearted help whenever I needed it. I also wish to express my gratitude to Ms. Anne Prince for providing me with helpful guidance and assistance in academic writing.

Nobody has been more important to me in the pursuit of this piece of research work than my family: my parents, Chia-Lin and Chien-Yi, my sister Jess and my brother Ted, to whom I would like to dedicate this work. Their love and support are always with me in whatever I pursue. To the rest of my family for doing all it takes to allure me towards the accomplishment of this research work: no word is expressive enough for my gratitude. Many friends over the years have given their support and endured with my constant whinging and incomprehensible descriptions: thank you very much and I love you all. Last, but by no mean the least, I am deeply thankful to Robert Dvorak for believing in me and encouraging me though all the ups and downs.

Declaration

This thesis contains no material which has been accepted for the award of any other degree or diploma, except where due reference is made in the text of the thesis. To the best of my knowledge, this thesis contains no material previously published or written by another person except where due reference is made in the text of the thesis.

……..

Yen-ni Chiu

Table of Contents

CONTENTS **PAGE NO.**

CONTENTS **PAGE NO.**

CONTENTS **PAGE NO.**

Chapter 7

List of Figures

FIGURE **PAGE NO.**

FIGURE **PAGE NO.**

FIGURE **PAGE NO.**

FIGURE **PAGE NO.**

List of Tables

TABLE **PAGE NO.**

Chapter 1

Introduction

Surface active agents, commonly known as surfactants, are materials that exhibit the characteristic of altering interfacial interactions via enhanced adsorption at interfaces. They have a diverse range of applications from household cleaners and laundry detergents to paints, coatings, food additives and specialised pharmaceutical formulations (Myers, 1988). Global demand for surfactants amounted to approximately 9.9 million tons in 1998 and is estimated to grow to 14.1 million tons in 2010 (Shell Chemicals, 2000). Nonionic surfactants are surfactants with electrical neutrality which imparts a significantly lower sensitivity to the presence of electrolytes in the system (Myers, 1988). This characteristic gives nonionic surfactants a chemical nature that outperforms other types of surfactants, making them very useful in chemical blends and mixtures.

The popularity of nonionic surfactants is increasing at the expense of traditional anionic surfactants. This is because of their excellent detergency properties and favourable environmental properties, such as rapid biodegradability and low toxicity. In addition, nonionic surfactants offer a high degree of flexibility for synthesis (van Os, 1998). The annual consumption of nonionic surfactants in Australia was estimated to be 50,000 tons in 2001, of which approximately 15,000 tons were imported into Australia from offshore manufacturers (Ngian, 2002). The market for nonionic surfactants in Australia is highly competitive with local manufacturers facing increasing competition from imports. Optimisation of the manufacturing plant is of great interest to our industrial partner of this research study, Huntsman Corporation Australia Pty Limited. If successful, Huntsman Corporation Australia would gain competitive advantages over other manufacturers, particularly imports.

A range of manufacturing processes is currently employed for nonionic surfactants production. Alkoxylation is the most common process for many classes of nonionic surfactants. Alkoxylation refers to the reaction between an alkoxide (ethylene oxide or propylene oxide) and a substrate containing one or more active hydrogen atoms in presence of a catalyst, either an alkaline homogenous catalyst or a "Narrow Range Ethoxylate" heterogeneous catalyst. A variety of substrates includes alkylphenols, fatty alcohols, fatty acids, fatty amines or mercaptans (Schick, 1967). Alkoxylation involves gas-liquid or gas-liquid-solid reactions, depending on the catalyst used.

1.1 Problem statement and aim

Huntsman Corporation Australia (HCA), part of the global Huntsman Performance Products Sciences Organisation, is the sole domestic manufacturer of nonionic surfactants in Australia. HCA operations comprise a nonionic surfactant manufacturing plant at Botany, New South Wales and a technical research and development centre at Ascot Vale, Victoria. The surfactants plant at Botany manufactures a wide range of basic nonionic surfactants (NIS) for sales to many essential industries including detergents, personal care, mining and textiles. The plant comprises three alkoxylation plants, NIS A, NIS B and NIS C, which are operated in a semi-batch manner either in stirred reactors or loop reactors. The total throughput of nonionic surfactants at the Botany site is about 35,000 to 40,000 tons/year. Products from the surfactants plant supply the domestic market and are also exported to surrounding Asia-Pacific countries.

HCA had been investigating technical opportunities for improving production efficiency and optimising their in-house operating process in order to be able to match, or potentially outperform, the efficiency achieved by competitors currently using patented technology. Overseas competitors are currently using state of the art proprietary equipment, such as BUSS and Pressindustria reactors with significantly higher productivity. Furthermore, HCA had established that the alkoxylation rates in the stirred laboratory autoclave at Ascot Vale were up to five times faster than the industrial NIS A reactors at Botany, even though the autoclave was perceived to be running under significant mass transfer control. This suggested that there was substantial scope for improving the full-scale alkoxylation reactors upon the establishment of a rational basis for the design of the reactors. In order to rationalise the reactor design, it was essential to understand the processes involved in the operation including chemical kinetics and physical transport processes such as heat, mass and momentum.

The aim of this research study was to gain a better understanding of the above-mentioned processes involved in an alkoxylation process, and to integrate them into a practical, but theoretically sound, process model for rationalising and debottlenecking the existing design of the HCA reactors. In addition, by using the validated model, measures for enhancing the productivity would be identified and recommended.

1.2 Research approach

One of the HCA's R&D objectives was to optimise their alkoxylation operations. Previous work performed by Khuu (2002) was focussed on the development of an appropriate control strategy in the loop NIS B reactor operations. This research project was specifically designed to focus on determining the optimum operating conditions for NIS A reactors in stirred tank configuration. Although all the alkoxylation reactors of HCA were designed in-house, understanding of the above-mentioned rate phenomena inside the reactors was still rudimentary. Optimisation of the reactor productivity without a predictive working model which could describe the various rate processes was extremely difficult and by necessity, empirical. It was for this reason that the overall research approach for this project was formulated into two stages.

The first stage of the project was to determine the kinetics of a base-catalysed alkoxylation in a well-stirred reactor operated by HCA. The approach taken to determine the alkoxylation kinetics was to conduct experiments in a HCA laboratory autoclave. In the experiments that were conducted, the rates of alkoxylation were measured in a temperature range where chemical kinetics was controlling. The existing kinetic models that were developed by Santacesaria *et al*. (1990) and Di Serio *et al*. (1995) provided a base for analysing our experimental alkoxylation rates but modification was required to incorporate the operating features in the HCA reactors. The kinetic information obtained was further integrated into a rigorous kinetic model, which was used to describe alkoxylation in the industrial-scale reactors.

The second stage of the project was to gain a better understanding of the physical transport processes that occurred in an industrial NIS A reactor operation including mass, heat, momentum and turbulence. This involved detailed analyses of these transport processes and the complex interactions among these mechanisms. Experimental investigation of such processes is expensive, time consuming and sometimes impossible. Computational Fluid Dynamics (CFD) techniques have been recognised as an alternative to detailed experimental investigation and traditional mathematical modelling. CFD has the ability to provide more accurate insights that might not be achievable from purely mathematical modelling. The advantage of a CFD model over other mathematical models allowed us to delineate complex flow behaviours that were involved in a mechanically agitated alkoxylation reactor. Therefore, by integration of the kinetic model established in the first stage of the project, a CFD model was developed which depicted the processes involved in a HCA stirred alkoxylation reactor. The CFD model was validated against the initial kinetic experiments conducted in the laboratory autoclave in the present study and the plant data collected from the industrial productions. From this, a level of confidence for the CFD model was established. In this stage of the research program, possible rate-limiting factors in the industrial-scale operation were also identified and systematically evaluated through a thorough and comprehensive analysis of the reaction data. Together with the CFD results analysis, the findings allowed us to determine an optimum operating condition.

1.3 Structure of this thesis

In this chapter, both kinetic modelling and numerical simulations of an alkoxylation reactor were briefly introduced. Accordingly, the thesis is structured in two parts. Part I deals with the kinetics of alkylphenol alkoxylation. Part II deals with the numerical simulations of an alkoxylation reactor. Each part details its related literature review, methodology and results achieved, followed by a comprehensive discussion.

Part I consists of three chapters. Chapter 2 gives an extensive review on the development of the kinetic theory for a gas-liquid alkoxylation system, in particular the based-catalysed ethoxylation process of alkylphenol in a well-stirred reactor and the corresponding reaction scheme. The existing kinetic models developed for simulating the ethoxylation behaviour are also described. Chapter 3 presents the experimental set-up of the laboratory autoclave used in the present study and the experimental procedures for generating reliable kinetic data. Chapter 4 presents the kinetic results obtained from the experiments performed. A modified kinetic model based on the existing models developed by Santacesaria and co-workers (1990; 1995) is also derived. The modified model incorporates the operation mode adopted in the reactors studied in this research project.

Part II consists of three chapters. Chapter 5 reviews the past studies on the flow characteristics induced by different impeller systems and numerical simulations on reactive flow. Chapter 6 gives a theoretical background to the numerical model of both the laboratory autoclave described in Chapter 3 and the industrial NIS A reactor. The governing equations are described, including momentum and heat transfer equations and descriptions for the turbulence model and reaction model. In Chapter 7, the process limitation in the current NIS A operations at Botany is identified. The system of ethylene oxide injection from a dip-leg pipe used in a NIS A reactor is studied. The fluid flow in the pipe with heat transfer is simulated to provide predictive findings for the state of ethylene oxide in the pipe. Chapter 7 also presents information concerning the model boundary conditions for subsequent comprehensive CFD simulations of ethoxylation flow in a full reactor vessel. The flows in both laboratory and industrial reactors are simulated. The simulation results are validated against the experimental data from Chapter 4 and the plant batch data. This validated reactive flow model is used to investigate opportunities that improve the asset productivity of the commercially operated NIS A reactor.

Chapter 8 details the findings of this research project and gives recommendations for future work.

Part I

Kinetic Modelling

Chapter 2

Kinetics Literature and Theory

2.1 Introduction

In the surfactants plant of Huntsman Corporation Australia (HCA) at Botany, New South Wales, nonionic surfactants are manufactured by alkoxylating hydrophobes in the presence of an alkaline catalyst. This highly exothermic reaction is conducted in a semi-batch reactor system normally at a temperature between 120 and 180°C and a pressure that sets the concentration of the alkoxide (ethylene oxide/propylene oxide) below the explosive limit with the aid of nitrogen padding. Due to its high volatility, the alkoxide, even though injected as a liquid from the storage tank, is partitioned between liquid and vapour, depending on the hydrophobe, temperature and pressure used. In HCA's NIS A alkoxylation reactors, the contact between the two phases is enhanced by agitation, which reduces the initial resistance to transport gas bubbles into the bulk liquid, where the alkoxylation takes place. Overall alkoxylation in the semi-batch NIS A reactors is a process that involves simultaneously, chemical reaction and catalysis as well as the phenomena of mass, heat and momentum transfer. As was mentioned in Chapter 1, the chemical kinetics of the alkoxylation in the existing NIS A reactors is the first rate process to be investigated. Understanding the chemical kinetics requires knowledge of the nature of the chemicals involved, leading to the mechanism of the reaction, and variables affecting the rates. This defined the scope of the literature review for the kinetics study in the first part of this research project.

This chapter begins by presenting a general introduction to nonionic surfactants, including their historical development, applications, most commercially important species and synthesis methods. The discussion then focuses on production of nonionic surfactants through alkoxylation as the most commonly used method in the industry, followed by the nature of the reactants involved, with particular reference to ethylene oxide as the alkoxide and alkylphenol as the hydrophobic substrate and their resulting products.

An outline is given of the reactor types employed in the industrial manufacture of nonionic surfactants. This chapter then presents important studies from a variety of authors leading to the postulation of the ethoxylation kinetic mechanism and the proposed reaction steps. This chapter also describes the most recent developments in kinetic modelling of a well-mixed ethoxylation stirred reactor.

2.2 Nonionic surfactants

Surface active agents or surfactants are materials that alter interfacial interactions through preferential adsorption at interfaces (Myers, 1988). The molecule of a surfactant consists of one or more groups with an affinity for markedly polar surfaces (hydrophilic group) and one or more groups with little affinity for water (hydrophobic group) (Davidsohn and Milwidsky, 1987). The basic chemical nature of surface active molecules is illustrated in Figure 2. 1. The hydrophobic tail is generally a long-chain hydrocarbon radical and it also can be a halogenated or an oxygenated hydrocarbon or a siloxane chain. The hydrophilic head group is an ionic or highly polar group that contributes some water solubility to the molecule. The nature of the hydrophile is the primary key for the classification of surfactants, with the subgroups being categorised by the nature of the hydrophobe (Myers, 1988). Based on the nature of the hydrophile, four general groups of surfactants are defined: anionic, cationic, nonionic and amphoteric surfactants. Nonionic surfactants are surfactants that carry no electrical charge. In other words, the hydrophilic group in a nonionic surfactant does not ionise to any great degree (Porter, 1994). In this case, the water solubility of nonionic surfactants is derived from highly polar groups, such as polyoxyethylene (-OCH_2CH_2O-) or polyol groups.

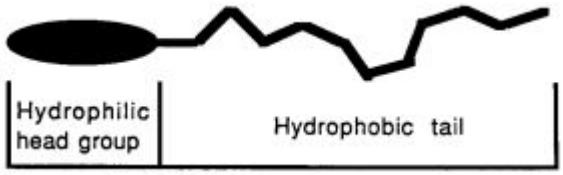

Figure 2. 1 The basic chemical nature of a surface active molecule (Myers, 1988).

2.2.1 A brief history on nonionic surfactants development

The development of nonionic surfactants first began during the 1920s at the I. G. Farbenindustrie in Germany, where research was aimed towards improvement in textile industries and later towards the replacement of animal fats and vegetable oils (Schick, 1967; Schonfeldt, 1969). Ethylene oxide adducts with surface activities had been mentioned in a report released by I. G. Farbenindustrie in mid-1930. However, the report did not reveal detailed knowledge of the solubilization principle of hydrophobic substances by a succession of ethylene oxide additions or the introduction of longer polyoxyethylene chains. It was the work of C. Scholler, published in later 1930, that provided the first detailed study on a new nonionic class of compounds with surface active properties (Schonfeldt, 1969). Continuing work by

Scholler and co-workers in this field led to the discovery of the new, nonionic class of compounds with surface active properties having promising detergent and wetting characteristics. This discovery led to a number of patent applications. Developments of other types of nonionic surfactants followed and progressed with improvements in surfactant science and technology, such as alkylphenol adducts, then with the trademark Igepal, which appeared on the market in 1937 (Schonfeldt, 1969). Nonionic surfactants started to spread around the world immediately after the end of the Second World War (Karsa, 1987). The share of nonionic surfactants in total use of surfactants has grown from 4% in 1970 (van Os, 1998) to approximately 40% of current worldwide surfactants usage (Schmitt, 2001).

The expansion of the nonionic surfactant industry can be attributed to a number of factors. These include their excellent detergency properties and favourable environmental characteristics, such as rapid biodegradability and low toxicity (van Os, 1998). Nonionic surfactants are generally less sensitive to water hardness than anionics, which makes the requirements for “builders” (builder ingredients) in laundry detergents less demanding. They are more effective than other surfactants in removing of oily soil from synthetic fabrics (Davidsohn and Milwidsky, 1987.) Most nonionic surfactants are considered low-foaming products, have good cold water solubility, and have a low critical micelle concentration, making them effective at low concentration. Their compatibility with cationic fabric softeners makes them preferable to anionics in certain formulations (Schmitt, 2001). In addition, the synthetic flexibility of nonionic surfactants facilitates the design for the required degree of solubility into the molecule simply by the careful control of the size of the hydrophilic group (Myers, 1988). This quality advantage of nonionic surfactants is preferred in the detergent industry because of their convenience in formulating concentrated powders and liquids (van Os, 1998).

2.2.2 Applications

Nonionic surfactants have been used extensively in the chemical industry in areas such as detergents, health and personal care, coatings and polymers (van Os, 1998). Other application areas include textiles, agrochemicals, minerals processing and coal-water fuels (Karsa, 1987). It is expected that the main use of nonionic surfactants will remain in the area of detergent, health and personal care formulations in combination with anionic surfactants (van Os, 1998). Nonionic surfactants are also used in novel applications in areas such as environmental protection systems, paper processing and thin films (Karsa, 1987; van Os, 1998).

2.2.3 Types of nonionic surfactants

Major species in the range of nonionic surfactants include fatty alcohol ethoxylates, alkylphenol ethoxylates, fatty acid glyceride ethoxylates (PEG esters), fatty acid ethoxylates, fatty amine ethoxylates, ethylene oxide-propylene oxide block copolymers, fatty acid sucrose esters, fatty acid sorbitan esters, and alkonolamides and ethoxylates. Among these, the ethylene oxide adducts of alkylphenols and fatty alcohols continue to dominate the nonionic market due to their superior cost-performance ratio (Karsa, 1987). However, the long-term future for the use of alkylphenol ethoxylates has fallen into slight disfavour because of their slower rate of biodegradation and concern regarding the toxicity of phenolic residues (Karsa, 1987). Nevertheless, the situation is not completely clear due to the conflicting claims as to the biodegradability of the alkylphenols, largely because an internationally accepted method for chemical determination of nonionics in micro quantities is not available (Davidsohn and Milwidsky, 1987). Although the concern over the biodegradability of alkylphenols has been around for twenty years, alkylphenol ethoxylates are still used primarily in commercial and industrial applications due to their lower cost than the similar alcohol ethoxylates (Porter, 1994). Recently, environmental monitoring studies have demonstrated that the rates of degradation of alkylphenol ethoxylates are sufficiently high to avoid accumulation in the environment. Moreover, studies have demonstrated high removal rates of polyoxyethylene alkylphenol from wastewater (van Os, 1998).

2.2.4 Synthesis methods

There are many manufacturing methods available in practice for synthesis of nonionic surfactants depending on the applications. For example, for food and animal feed industries, those based on sugars and sugar alcohols and glycerol are the most important and widely used synthetic routes, e.g., Foster D. Snell method (Karsa, 1987; Davidsohn and Milwidsky, 1987). For physicochemical investigations on the materials properties conducted in industrial and academic laboratories, the Williamson ether synthesis and esterification of tosylates for homogenous materials are used (Schick, 1967). For most industrial applications, ethylene oxide condensation is the most commonly used method for the vast majority of ethylene oxide based nonionic surfactants (Davidsohn and Milwidsky, 1987).

2.3 Ethylene oxide condensation

Ethylene oxide condensation is the synthesis method used in the NIS plants of HCA at the Botany site. This method is commercially the most popular route. The vast majority of the nonionic surfactants are synthesized via condensing ethylene oxide onto a hydrophobe. The hydrophobe is invariably a high-molecular weight material with an active hydrogen atom. The synthesis is simplified in Equation 2. 1 (Schick, 1967).

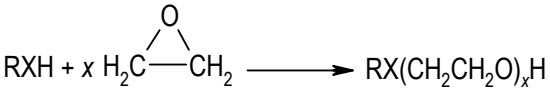

$$RXH + x\ H_2C\text{—}CH_2 \longrightarrow RX(CH_2CH_2O)_xH$$

2. 1

where

R= H (as for polyethylene glycols) or a hydrophobic group (usually C_1 to C_{20});

X= O, N, S or phenol;

x= number of moles of ethylene oxide reacted with per mole of the hydrophobe substance.

RXH is often referred to as the initiator. It can be an alcohol, alkylamine or alkylamide, mercaptan or alkylphenol when the heteroatom X is O, N, S and phenol, respectively. $RX(CH_2CH_2O)_xH$ is the general formula representing a polyoxyethylene surfactant. *x* is not necessarily an integer and represents the number-average degree of polymerisation of ethylene oxide in the product. In the absence of side reactions, the product is polydispersed. That is, it is a mixture consisting of molecules with a variety of chain lengths and in the form of $RX(CH_2CH_2O)_nH$ with *n* being an integer. Even when using less than one mole of ethylene oxide per mole of the initiator, this polydispersed characteristic is still found in most of the products from the reactions between active hydrogen-containing substrates with ethylene oxide. The exceptions are when the initiator is an alkylphenol, carboxylic acid or mercaptan (Schick, 1967; van Os, 1998) and will be discussed in a later section.

The reaction pattern for ethylene oxide condensation in a hydrophobic substrate can be generalised in two steps: (i) the insertion of an ethylene oxide unit to the fresh hydrophobe, followed by (ii) continuous insertions of ethylene oxide units to the initially formed adduct $RXCH_2CH_2OH$. Because $RXCH_2CH_2OH$ is also an active hydrogen containing species, it can compete with the initiator for the ethylene oxide units. The steps can be represented as the following equations:

First adduct

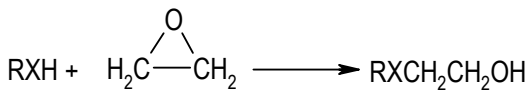

$$RXH + \ H_2C\text{—}CH_2 \longrightarrow RXCH_2CH_2OH$$

2. 2

Polymerisation

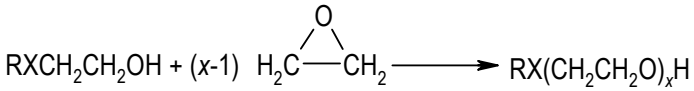

2. 3

The product distribution of $RX(CH_2CH_2O)_xH$ is dependent on the choice of initiator, the number of moles of ethylene oxide reacted per mole of the initiator (x), and the choice of the catalyst used (van Os, 1998). Based on the choice of the catalyst used, the polyoxyethylene distribution can be divided into two types: (i) conventional distributions and (ii) narrow-range distributions. The former is obtained by the use of homogeneous basic or acidic catalysts and the latter by the use of the new heterogeneous narrow-range ethoxylate (NRE) catalysts.

2.3.1 Conventional distributions

Conventional distributions can be further divided into two categories: (i) broader distribution obtained by the use of basic catalysts as shown in Figure 2. 2, and (ii) narrower distributions obtained by the use of acidic catalysts as shown in Figure 2. 3. The difference between conventional base-catalysed and acid-catalysed distribution is a result of catalyst association with different species, RXH or ethylene oxide, at onset. Under base-catalysed conditions, the catalyst is primarily associated with the initiator RXH, whereas under acid-catalysed conditions the catalyst is associated with ethylene oxide (van Os, 1998).

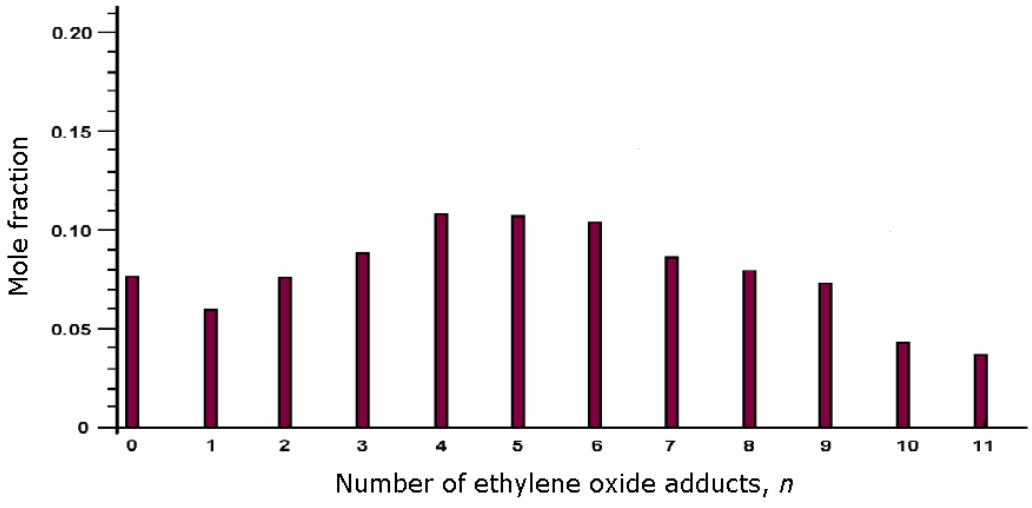

Figure 2. 2 Broad distribution obtained with the use of a basic catalyst. Products of the reaction of hexyl alcohol with 6.00 moles of ethylene oxide catalysed by 1 mole per cent NaOCH3 (Schick, 1967).

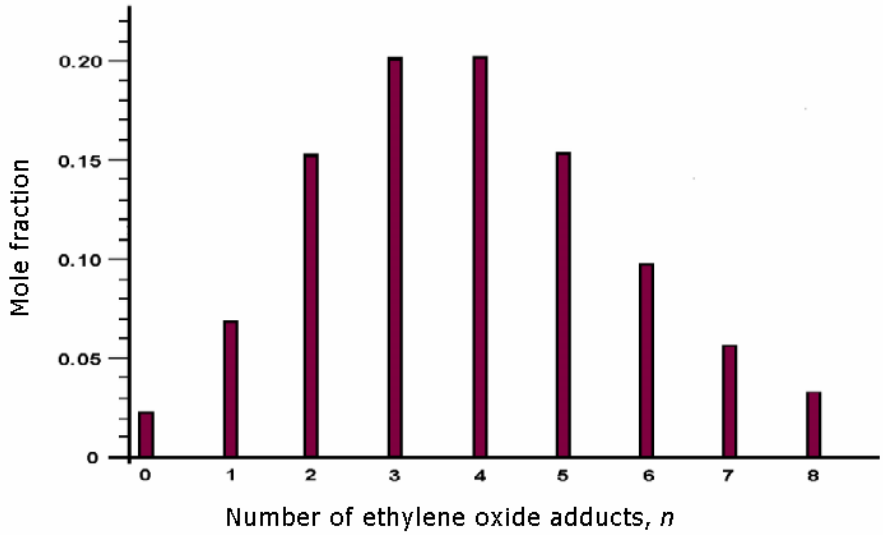

Figure 2. 3 Narrow distribution obtained with the use of an acidic catalyst. Products of the reaction of hexyl alcohol with 4.04 moles of ethylene oxide catalysed by 0.14 mole per cent SbCl5 (Schick, 1967).

The participation of a basic catalyst in industrial synthesis of nonionic surfactants emerged in the late 1940s (Nace, 1996). Examples of basic catalysts used to promote ethylene oxide condensation include those derived from alkali and alkaline earth metal hydroxides, oxides, or alkoxides and amines (van Os, 1998). Amongst these, potassium hydroxide (KOH) is the most commonly used catalyst in the commercial production of polyoxyethylene surfactants (van Os, 1998). It is, for convenience, introduced to the reactor as 50% aqueous potassium hydroxide solutions.

Acidic catalysts reported in literature include boron trifluoride (BF_3), stannic chloride ($SnCl_4$) and antimony pentachloride ($SbCl_5$) (Schonfeldt, 1969). However, the use of acidic catalysts has been phased out in commercial synthesis of polyoxyethylene surfactants due to undesirable side products that would have to be removed prior to use (van Os, 1998). Furthermore, in many cases the products from acid-catalysed reactions are either coloured or lead to coloured products in subsequent conversions (Schick, 1967). In comparison, the basic catalysts have advantages such as low cost, ease of handling, high activity, high selectivity for desired products, low levels of byproducts and ease of removal by neutralisation.

2.3.2 Narrow-range distributions

Yang *et al.* (1980) were the first to report on a sharper polyoxyethylene product distribution obtained when a non-acidic catalyst system was used. In their work, they used barium oxide as the catalyst in alcohol ethoxylation and found that the divalent metal cations were capable of producing different, and narrower, product distributions compared to those obtained using a group I base, such as KOH. This discovery soon

led to the recognition of other group II bases capable of producing narrower polyoxyethylene distributions as shown in Figure 2. 4 (van Os, 1998). Further explorations on the group II catalysts found that the polyoxyethylene distribution could be made even narrower if the group II metal alkoxide were activated through partial neutralisation (van Os, 1998). The activated basic group II alkoxides with phosphoric acid eventually led to the development of heterogeneous narrow-range catalyst systems which were capable of achieving extremely narrow product distribution. However, not all group II inorganic phosphate salts were able to produce the extremely narrow distribution, e.g., the simple calcium phosphate and magnesium phosphate were shown to be inactive. Until recently, systems using heterogenous mixed metal oxides which involve the activation of these inactive group II metal phosphates by solubilisation or partial solubilisation with carboxylic acids have claimed to produce narrow product distributions. (van Os, 1998). Hence, these recently developed heterogeneous narrow-range catalysts can be divided into the following categories according to their structures: (i) metal phosphates and (ii) mixed metal oxides.

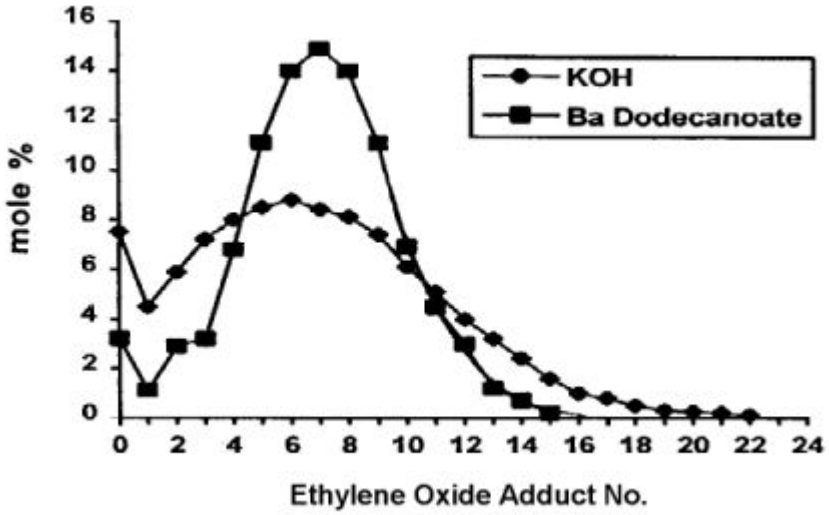

Figure 2. 4 Narrower distribution obtained with the use of a group II bases. Comparison of the product distributions obtained from the reaction of dodecanol with 7 moles of ethylene oxide using KOH and barium dodecanoate (van Os, 1998).

2.4 Base-catalysed ethylene oxide condensation

Ethylene oxide condensation in the presence of a basic catalyst is the reaction process studied in this research. Particular reference is given to the condensation of ethylene oxide onto an alkylphenol. Brief descriptions of the raw materials used in this research and their properties are given in this section. The following subsections describe the reactants, ethylene oxide and alkylphenols, followed by a description of their products, e.g., nonylphenol ethoxylates and the corresponding manufacturing processes. This section also reviews past studies leading to postulation of the reaction mechanism of ethylene oxide condensation.

2.4.1 Reactants

2.4.1.1 Ethylene oxide

Ethylene oxide, also called epoxyethane or oxirane, belongs to the lowest member of the cyclic ethers, the 1,2-epoxides. Ethylene oxide is the most reactive member of the family. The epoxide ring can be readily ruptured at the carbon-oxygen bond under acidic, basic or even essentially neutral conditions (Parker and Isaac, 1959). This behaviour is in contrast to that of larger cyclic ethers, which are neither readily hydrolysed by alkali nor susceptible to attack by anions (Schick, 1967). The significantly higher reactivity of ethylene oxide is attributed to its highly strained structure of the three-membered cyclic ethers (Parker and Isaac, 1959). The strained nature of these rings appears from the bond length and angles (Schick, 1967), which are illustrated in Figure 2. 5.

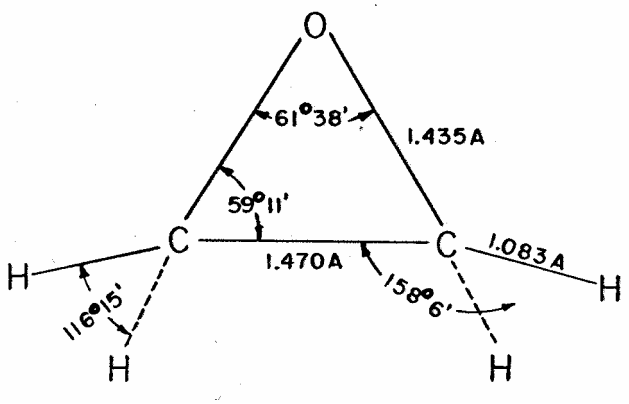

Figure 2. 5 The illustration of an ethylene oxide ring (Parker and Isaacs, 1959).

Each CH_2 group lies in a plane perpendicular to the plane of the ring (Parker and Isaacs, 1959). Figure 2. 5 shows that the C-C bond in the ethylene oxide ring structure has a length of 1.47 nm, which is intermediate between that of a normal single bond (1.54 nm) and that of a normal double bond (1.35 nm). Therefore, the C-C bond in the three-membered ethylene oxide ring has considerable double bond character (Schick, 1967). The strained ring prevents the C-O-C bond from rotating, leaving the oxygen atom to cope with a lone pair of electrons (van Os, 1998). This accounts for the increased nucleophilicity and basicity of ethylene oxide compared with the other ethers. The strain energy of ethylene oxide has an average value of approximately 54 kJ/mole, which is calculated as the difference between experimental and calculated heats of formation (Parker and Isaacs, 1959). In addition, opening of the three-membered ethylene oxide ring with an initiator results a high release of exothermic heat of 92 kJ/mole of ethylene oxide reacted (Schonfeldt, 1969; van Os, 1998; Santacesaria *et al.*, 1999).

Due to the extreme toxicity and potential for explosion, ethylene oxide is classified as a highly hazardous chemical and therefore, care must be taken to minimise personal exposure (Ethylene Oxide User's Guide, 1999). The International Agency for Research on Cancer (IARC) recently classified ethylene

oxide as class 1-carcinogen to humans (Ethylene Oxide User's Guide, 1999). Pure ethylene oxide is extremely flammable and explosive. Its flammability limits in air at 298K and 1 atmosphere are: lower: 2.6vol%; upper: 100vol%. The upper flammable limit at 100vol% means pure ethylene oxide can decompose in the absence of air or oxygen. Therefore, in many commercial operations a non-flammable inert gas, mostly nitrogen, is used in the vapour phase to dilute the vapour phase ethylene oxide concentration so that its flammability potential is reduced. Ethylene oxide can be stored in either carbon steel or stainless steel tanks, which must be pressurised with inert gas to keep the vapour space in a non-explosive region and prevent the potential for decomposition of the ethylene oxide vapour. The total pressure applied in the tank increases with ethylene oxide liquid temperature. Explosion limit tables must therefore be consulted prior to use (Kirk-Othmer Encyclopaedia of Chemical Technology, 1994).

Some of the physical properties of ethylene oxide are given in the following table:

Table 2. 1 Key physical properties of ethylene oxide (Schick, 1967).

Property	Ethylene oxide
Molecular weight, g/mol	44.05
Normal boiling point at 101.325 kPa, °C	10.7
Liquid specific gravity 20°C/20°C	0.875

2.4.1.2 Alkylphenols

Alkylphenols are compounds of phenol derivatives with one or more ring hydrogens being replaced by an alkyl group(s). The commercially important alkylphenols have alkyl groups ranging in size from one to twelve carbons (Kirk-Othmer Encyclopaedia of Chemical Technology, 1992). The type of alkyl substituent and its position on the ring strongly affect the physical properties of alkylphenols. For example, para isomers have the highest melting points within groups of substituted isomers; their boiling points are comparable to those of meta isomers but 10-20°C higher than the corresponding ortho-isomers (Ullmann's Encyclopaedia of Industrial Chemistry, 1991). Generally, the physical properties of alkylphenols are considered similar to those of phenols. The boiling points are typically over 200°C at atmospheric pressure and increase with the size of the molecule (Ullmann's Encyclopaedia of Industrial Chemistry, 1991).

The alkyl substituent group attached to the phenol is hydrophobic. Generally, alkylphenols are readily soluble in common organic solvents: lower alcohols, acetone, hydrocarbons and toluene. The solubility of alkylphenols in water decreases as the number and size of the alkyl substituents on the ring increases. Only lower alkylphenols show some solubility in water at increased temperature to a noticeable extent

(Ullmann's Encyclopaedia of Industrial Chemistry, 1991). As the alkyl substitutes increase in number and become larger, they eventually overcome the hydrophilic nature of the hydroxyl group.

The alkylphenol used in this research was 4-nonylphenol, a C_9 alkyl substituent, as shown in Figure 2. 6. 4-Nonylphenol is the most widely used alkylphenol in the synthesis of alkylphenol based ethoxylates (Schick, 1967). The two commercial purity grades of 4-nonylphenol are a technical grade and a higher purity grade. The technical grade contains 10-12% 2-nonylphenol, 85-90% 4-nonylphenol, and up to 5% 2,4-dinonylphenol. The higher purity grade is composed of 5% maximum 2-nonylphenol, 95% minimum 4-nonylphenol, and only a trace of 2,4-dinonylphenol (Kirk-Othmer Encyclopaedia of Chemical Technology, 1992).

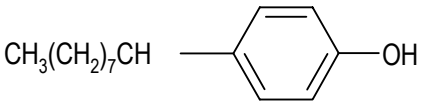

Figure 2. 6 Illustration of a nonylphenol molecule.

Some of the physical properties of nonylphenol are given below in Table 2. 2:

Table 2. 2 Key physical properties of nonylphenol (Schick, 1967; Kirk-Othmer Encyclopaedia of Chemical Technology, 1992).

Property	4-Nonylphenol
Typical assay (%)	90-95
Molecular weight, g/mol	220.3
Physical form at 25°C	Liquid
Normal boiling point at 101.325 kPa, °C	310
Freezing point, °C	20
Specific gravity	
25°C	0.950
90°C	0.909
Viscosity, cp	
25°C	1540
100°C	44

2.4.2 Products

2.4.2.1 Nonylphenol ethoxylates

Nonylphenol based nonionic surfactants are usually manufactured to consist of 1 to 40 ethylene oxide units on the basis of a mole ratio. Depending upon the exact properties required for an application, the size of the hydrophilic group is carefully controlled to achieve the required degree of solubility. With 4 units of ethylene oxide, nonylphenol is still insoluble in water; at 6-7 units it is completely soluble in water at room temperature; at 8-12 units it exhibits excellent detergency (Davidsohn and Milwidsky, 1987). Among these, the 9-unit ethoxylates are the most commonly manufactured nonylphenol based nonionic surfactants (Kirk-Othmer Encyclopaedia of Chemical Technology, 1992). Although the number of ethylene oxide units present is considered a basic property of the surfactant material, this number, defined as *x* in Section 2. 3, is only an average. That is, say, if there are 10 ethylene oxide units present, the actual molecular configuration can vary from 4 to 15 units (Davidsohn and Milwidsky, 1987). This refers to the polydispersed nature of a polyoxyethylene surfactant as previously described in Section 2.3. Base-catalysed ethoxylation gives a normal distribution of condensations, which can be approximated by a Poisson curve around the mean (Schick, 1967). The distribution has a peak at the desired ethylene oxide unit number. Figure 2. 7 gives an example showing the spread of ethylene oxide units in a typical product distribution for nonylphenol ethoxylates and the approximated curve by the Poisson distribution.

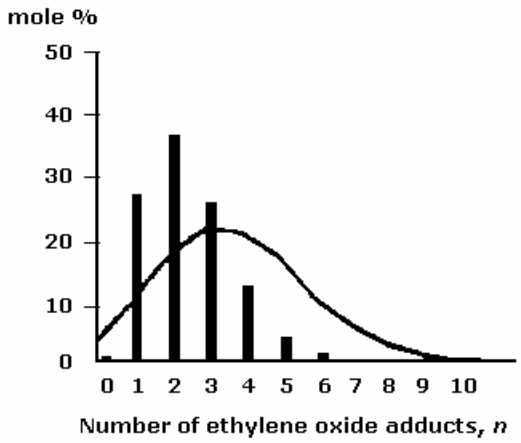

Figure 2. 7 Products of the reaction of 1 mole of nonylphenol with 2.5 moles of ethylene oxide catalysed by KOH. The solid line is the Poisson distribution. The solid bars are the experimental molar percentage for each polyoxyethylene product (Santacesaria et al., 1990).

2.4.2.2 Manufacturing processes

Most industrial synthesis of polyoxyethylene alkylphenols operates in one of the following gas-liquid contact schemes: (i) the gas phase dispersion into the liquid phase or (ii) the liquid phase dispersion into the gas phase (Schonfeldt, 1969; Hall and Agrawal, 1990; Dimiccoli *et al*., 2000). The first scheme involves dispersing ethylene oxide in the alkylphenol to be ethoxylated as bubbles by agitation. The ethylene oxide may be introduced via a sparger in the bottom of the reactor or directly added to the vapour space of the reactor when the synthesis takes place in a semi-batch stirred reactor (Santacesaria *et al.*, 1990; van Os, 1998; Dimiccoli *et al.*, 2000). It may also be mixed with the bulk liquid in an external pumped circulating loop when the ethoxylates are made in a Venturi loop reactor (van Os, 1998; Dimiccoli *et al.*, 2000). The second scheme involves spraying the alkylphenol mixture containing the catalyst into an atmosphere of gaseous ethylene oxide (Schonfeldt, 1969; Hall and Agrawal, 1990; Santacesaria *et al*., 1995; Santacesaria *et al*., 1999). The sprayed liquid forms droplets, which are promptly saturated by the gaseous reagent. This approach also involves a process in which recirculation of the liquid mixture is used. The reactor employed in this scheme is a spray tower loop reactor, which behaves like a plug-flow reactor (Dimiccoli *et al.*, 2000). Figures 2. 8 to 2. 10 represent the three reactor types used in the two schemes for the industrial synthesis of polyoxyethylene alkylphenols, discussed above.

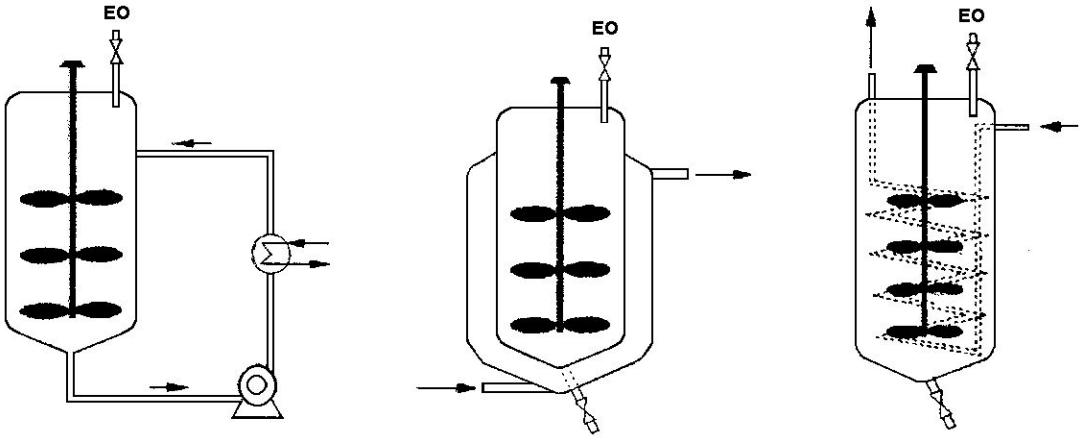

Figure 2. 8 Schemes of the semi-batch stirred reactors, differing only in the heat exchange system equipped (Dimiccoli *et al.*, 2000).

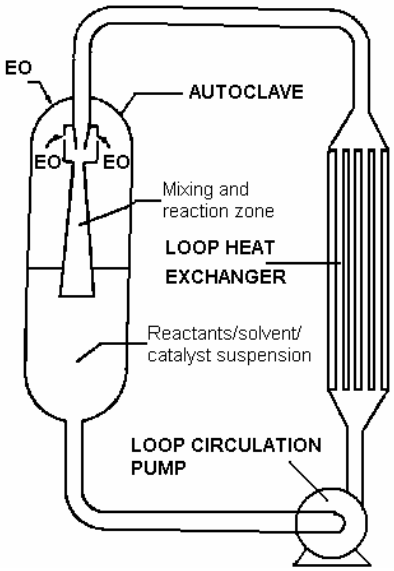

Figure 2. 9 Scheme of the Venturi loop reactor (Dierendonck et al., 1998).

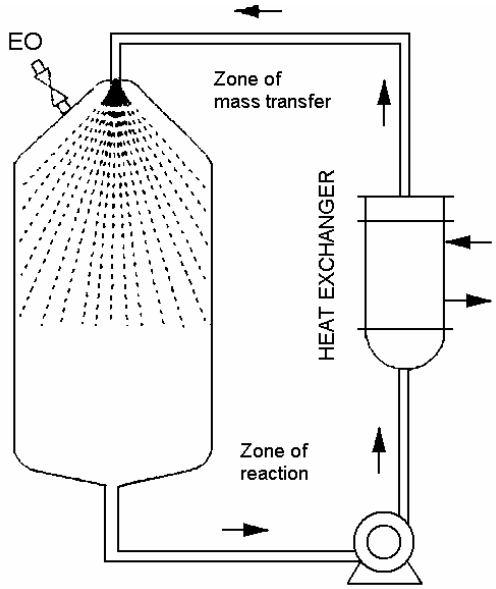

Figure 2. 10 Scheme of the spray tower loop reactor (Santacesaria *et al.*, 1995; Dimiccoli *et al.*, 2000).

In both schemes, ethylene oxide is present in the reactors as the gas phase. As the main reaction occurs in the bulk liquid, the gaseous ethylene oxide must be transferred to the liquid phase prior to the occurrence of the reaction. Therefore, the overall ethoxylation process can be seen as an occurrence of the interfacial mass-transfer and liquid-phase reaction kinetics in series (Hall and Agrawal, 1990). As can be seen in these figures, mass transfer and reactions occur in the different parts of a reactor according to the scheme by which it is operated. In the first two reactors (Figures 2. 8 and 2. 9), mass transfer and reactions occur in the same zone of the reactor. In the last reactor (Figure 2. 10), mass transfer and reactions occur in two different zones of the reactor: mass transfer takes place in the upper zone of the

reactor and reactions in the lower zone of the reactor. The NIS A reactors used by HCA operate in the semi-batch process with features similar to the reactor shown in Figure 2. 8(c).

The semi-batch process of alkylphenol ethoxylation is operated in an autoclave at a fixed temperature and pressure with the use of sodium hydroxide or potassium hydroxide as the catalysts. The reaction takes place at a temperature ranging from 100°C to 180°C and a pressure between 5 and 6 bars gauge, with a catalyst concentration of 0.1% to 0.3% by weight (van Os, 1998). More detailed manufacturing procedures will be introduced in the next chapter. The following sections focus on the understanding of the reaction mechanism for base-catalysed ethylene oxide condensation in a reactor operated in semi-batch process under ideal conditions, e.g., well mixed stirred tank.

2.4.3 Reaction mechanism

Past studies on reaction mechanism were initially focused on reactions of ethylene oxide with phenols. It was not until 1990 when further studies were performed to determine the reaction mechanism of ethylene oxide with alkylphenols and other hydrophobes with major commercial uses. In order to have a more complete picture of the mechanism, the following review covers the mechanism of reactions between ethylene oxide and phenols including alkylphenols and is also extended to fatty alcohols. The content reviewed here, however, need not lead to substances with surface active properties.

2.4.3.1 Ethylene oxide ring opening

According to Ingold (1953) and Parker and Isaacs (1959), the reaction between ethylene oxide and a compound containing an active hydrogen atom is a nucleophilic substitution (S_N). This reaction scheme can be explained, using an example, such as the reaction between one molecule of water and one molecule of ethylene oxide as follows:

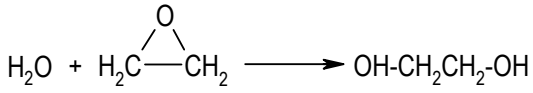

2. 4

The carbon atom undergoes a nucleophilic attack and the ether oxygen atom of the three-membered ring is substituted by the oxygen atom of the water. Since bases and acids are often used as catalysts to facilitate this type of reaction, the mechanism depends on the type of catalyst used. In the case of base-catalysed conditions, the process of reacting water with ethylene oxide is a bimolecular reaction (S_N2) (Ingold, 1953), which is shown as follows:

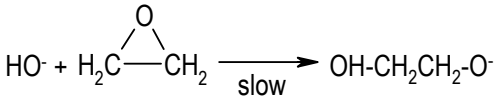

2. 5

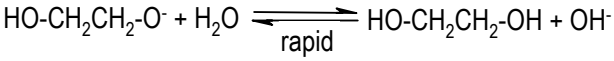

2. 6

Equation 2. 5 shows the reaction between ethylene oxide and the hydroxyl ion, which gives rise to a glycol ion. This step is slow and therefore is the rate determining step. Spontaneously a rapid equilibrium reaction takes place between a glycol ion and water molecule to form ethylene glycol, the product, and reform a hydroxyl ion. The rate-determining reaction and the formation of the reaction product take place in a single stage, which exhibits an S_N2 mechanism.

2.4.3.2 Ethylene oxide addition to phenols

Boyd and Marle (1914) were the first to investigate the kinetic aspects of the reaction between derivatives of phenols and ethylene oxide, which was noted in a review by Schonfeldt (1969). The kinetic variable investigated in the work by Boyd and Marle (1914) and the following work by Boyd and Thomas (1919) was based on the structure of phenols. In their work, sodium derivatives of a variety of phenols were reacted with ethylene oxide at an equimolar quantity at 70.4°C. The experimental results indicated that the speed of reaction decreased with increase in the acidity of the phenol. Boyd and Marle (1914) also measured the reaction velocities by varying the concentration of sodium derivatives of phenols. Based on the effect of varying the phenol concentration on the reaction velocities, Boyd and Marle (1914) proposed this type of reaction to be an S_N2 mechanism in nature and suggested that the reaction between phenol with one molar equivalent of ethylene oxide probably took place via the phenoxy-ion in the first instance as follows:

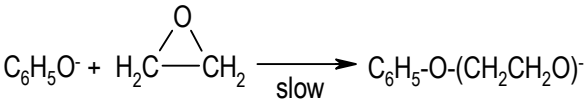

2. 7

The initial additive product afterwards reacted with the excess of phenol to give an undissociated glycol ether and a new phenoxy-ion:

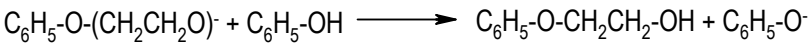

2. 8

The mechanism above described by Boyd and Marle (1914) was later supported by the experimental observations of Miller *et al*. (1950). In addition, Miller *et al.* (1950) found the reaction between phenol and

the first equivalent mole of ethylene oxide proceeded initially as far as phenoxyethanol, the first member in the product ether series. The formation of higher members in the ether series proceeded at a kinetically identical rate only after the phenol was fully converted into the first member.

The study by Miller *et al*. (1950) was primarily focused on describing the distribution of the products from the reaction between ethylene oxide and phenol. The reaction was carried out under the catalysis of sodium or sodium hydroxide in the absence of a solvent at 190-210°C. The composition of the product was determined by distillation. Examining the product obtained from the reaction with phenol with one equivalent or less of ethylene oxide, Miller *et al.* (1950) observed that continued distillation of the product gave no material with a higher boiling point than phenoxyethanol. In a further experiment where phenoxyethanol was condensed with just less than its equivalent of ethylene oxide, it was found the product consisted of a mixture of ethers. Based on these experimental findings, the first stage in the reaction of ethylene oxide with phenol in the presence of an alkaline catalyst was found to be in agreement with the reaction mechanism postulated by Boyd and Marle (1914) (as in Equation 2. 7). That is, the first stage was to form the ion of phenoxyethanol. So long as there was free phenol present, the next step must be proton exchange between this ion and the phenol molecule (Miller *et al*., 1950):

$$C_6H_5\text{-}O\text{-}(CH_2CH_2O)^- + C_6H_5\text{-}OH \rightleftharpoons C_6H_5\text{-}O\text{-}CH_2CH_2\text{-}OH + C_6H_5\text{-}O^- \quad \textbf{2. 9}$$

Combining Equation 2. 7 and the above equilibrium equation, the course of the reaction showed an S_N2 mechanism. Since the acidity of phenol (C_6H_5OH) was higher than the phenoxyethanol ($C_6H_5OCH_2CH_2OH$), the above equilibrium shifted to the right, reforming the phenoxy-ion ($C_6H_5O^-$). This explained the observation that the subsequent formation of polymer homologues would only appear when the free phenol had been completely reacted. The same observation was noted by Patat *et al.*(1952; 1954) and Patat and Wojtech (1960) (cited Schonfeldt, 1969).

In the same work by Miller *et al.* (1950), the preferential formation of the first member of the ether series was also noted with reference to alkylphenol ethoxylation. This was obtained when Miller *et al.* (1950) reacted alkylphenols with just less than the equivalent amount of ethylene oxide.

Although no detailed kinetic study was made by Miller *et al.* (1950), they assumed that the ionic formation of the next few members in the ether series following the formation of polyoxyethanol was built up by a sequence of kinetically identical steps. This assumption was based on an earlier demonstration that all these reactions proceeded with equal ease as cited by Miller *et al.* (1950). The ionic formation was to be accompanied by its interaction with an un-ionised molecule of hydroxy-ether, not necessarily of the same chain length. That is,

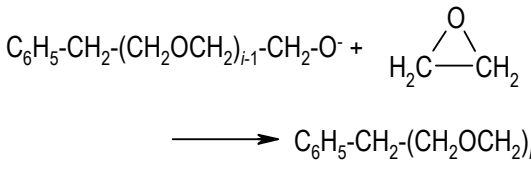

2. 10

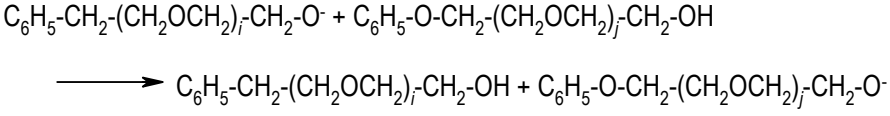

2. 11

where *i* and *j* are integers with $i \neq j$.

Work by Patat *et al.* (1952; 1954) was focused on the kinetics of the first two reaction stages of addition of ethylene oxide to phenol catalysed by sodium phenoxide, in which ethylene oxide was in excess. The reactions were performed at temperatures between 60 and 90°C with varying initial molar concentrations of phenol to ethylene oxide. The overall amount of phenol reacted during the reaction was taken for the kinetic analysis. The results did not completely agree with the earlier mechanism postulated by Boyd and Marle (1914) and Miller *et al.* (1950), nor did Patat *et al.* (1954) in their own treatment provide a satisfactory explanation for the experimental facts, as noted in a review by Schonfeldt (1969). Lowe and Weibull (1954) later made a recalculation of these kinetic results presented by Patat *et al.* (1952; 1954) and indicated that the reaction exhibited a first order dependence on sodium, free phenol and ethylene oxide, overall a termolecular reaction. That is, a third-order kinetic law was derived.

The third order kinetics for the rate of reaction between ethylene oxide and phenols under a base-catalysed condition was also assumed by Patat and Wojtech (1960), Sakai and Ishii (1959) and Ishii *et al*. (1962) and also cited in Schonfeldt (1969). Patat and Wojtech (1960) repeated the experiments by Patat *et al.* (1954) at 60, 70 and 80°C with different initial catalyst concentrations. Sakai and Ishii (1959) studied the effects of substituents of phenol on the rate of ethylene oxide addition to phenol with caustic potash (KOH) as the catalyst. Ishii *et al*. (1962) determined the rate constants for ethylene oxide addition to both phenol and phenoxyethanol in the presence of an alkaline catalyst in the temperature range between 45 and 75°C. In all cases studied by Ishii *et al*. (1962), a fixed 5:1 molar ratio of hydrophobe substance to ethylene oxide was maintained. All these authors derived a third-order kinetic law based on a similar explanation, a mechanism of complex formation. Described in the review by Schonfeldt (1969), Patat and Wojtech (1960) assumed an etherate was first produced by formation of hydrogen bonds between phenol and ethylene oxide. The etherate then reacted with sodium phenolate to form a ternary complex. Sakai and Ishii (1959) and Ishii *et al*. (1962), however, explained their results by assuming the formation of an intermediate complex between phenol and the catalyst first, followed by a reaction between the complex and ethylene oxide.

On the basis of the above experimental results, no definite conclusion could be drawn for ethylene oxide addition to phenol as to which of the suggested mechanisms was closest to the truth, as was noted by Schonfeldt (1969). The derivation of the third order kinetic law might be due to the low temperatures (below 100°C) used in those studies. On the other hand, the work by Satkowski and Hsu (1957) and Gee *et al.* (1959a; 1959b) both suggested an S_N2 mechanism for ethylene oxide addition to alcohols.

2.4.3.3 Ethylene oxide addition to alcohols

Satkowski and Hsu (1957) postulated a mechanism for the ethoxylation of alcohols after their investigation into the effects of kinetic variables on the rate of ethoxylation. The kinetic variables investigated were catalysts, temperature, alcohol structure and pressure. In their study, gaseous ethylene oxide was reacted with pure normal alcohols (C_5, C_{10} and C_{17}) and oxo alcohols (C_8, C_{10} and C_{13}). In particular, tridecyl alcohol (C_{13}) was extensively used to study the effects of catalysts, temperature and pressure. The reactions were performed at temperatures between 105 and 200°C with catalysts of varying alkalinity. The catalysts included potassium hydroxide (KOH), sodium hydroxide (NaOH), metallic sodium (Na), sodium methoxide ($NaOCH_3$), sodium ethoxide ($NaOC_2H_5$), potassium carbonate (K_2CO_3) and sodium carbonate (Na_2CO_3).

In studying the effect of catalytic activity on the rate of ethoxylation, Satkowski and Hsu (1957) found that K_2CO_3 and Na_2CO_3 showed little to no activity in alcohols within the temperature range studied. This is shown in Figure 2. 11. The rest of the catalysts showed comparable activities at a moderate temperature (135-140°C) with the exception of NaOH, which was relatively less active at this temperature as shown in Figure 2. 11(a), while at higher temperature (195-200°C), the activities were practically the same as shown in Figure 2. 11(b). The same catalysts were studied by Ishii and Ozeki (1960) at a lower temperature, 100°C. At this low temperature, the activity of these catalysts was significantly dependent on their basic strength. Accordingly, the order of catalytic activity was:

$$KOH > NaOC_2H_5 > NaOCH_3 > NaOH$$

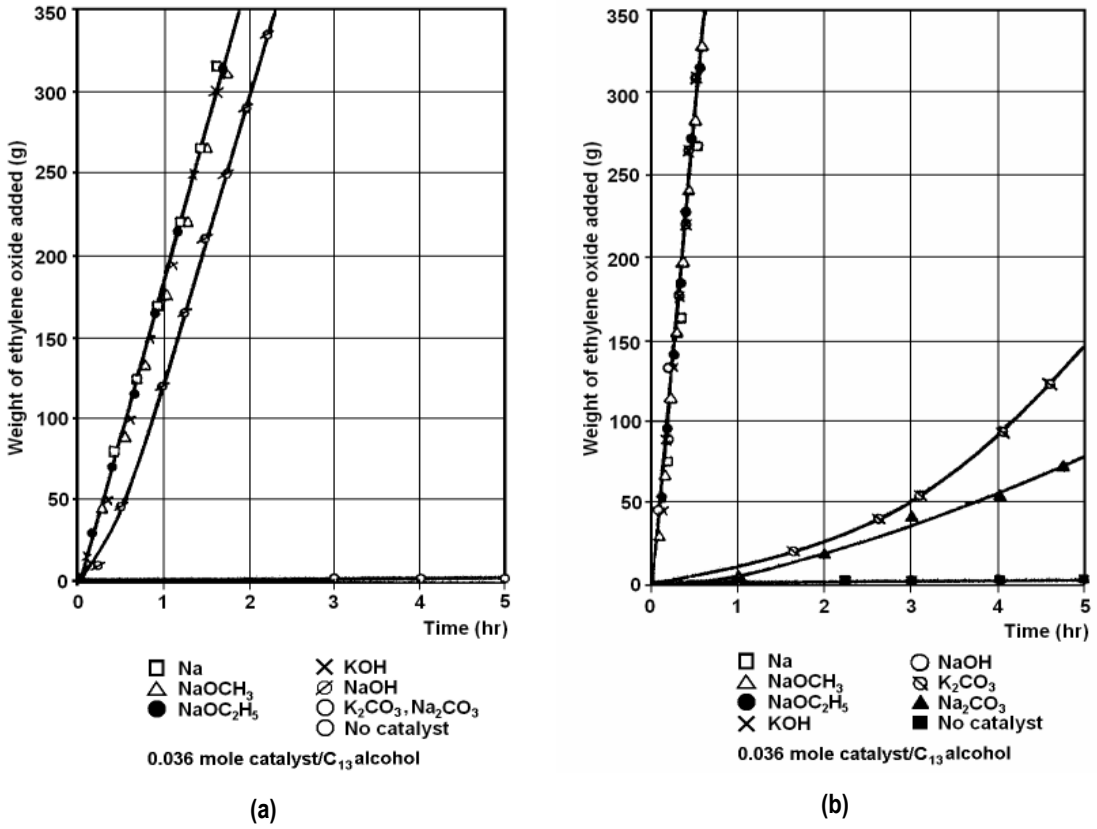

Figure 2. 11 Effect of catalyst on the rate of ethoxylation: (a) at 135-140°C (b) at 195-200°C (Satkowski and Hsu,1957).

In studying the effect of catalyst concentration on the rate of ethoxylation, Satkowski and Hsu (1957) found the rate of reactions increased with the catalyst concentration. However, the rate was more sensitive at low catalyst concentration than at high concentration. As can be seen in Figure 2. 12, the rate was found to be less than first order in catalyst concentration, noted by Schick (1967). This indicated that ethylene oxide reacted principally with free alkoxide ion rather than with the non-ionised metallic alkoxide. An explanation for this was that the degree of ionisation of metallic alkoxide decreased with the increase in catalyst concentration. Satkowski and Hsu's (1957) observation was in agreement with the mechanism proposed by Boyd and Marle (1914) and Miller *et al.* (1950) for phenol ethoxylation. On the other hand, it was in slight disagreement with the findings concluded by Gee *et al.* (1959a; 1959b) for methanol ethoxylation in dioxan solution between 30 and 50°C catalysed by the corresponding sodium alkoxide solution. Based on their detailed kinetic study, Gee *et al.* (1959a; 1959b) observed that the reaction proceeded with the alkoxide ion and the ion pair, metallic alkoxide, due to the small degree of dissociation of metallic alkoxide at low concentrations of the conjugate alcohol. In a later study, Ishii and Ozeki (1960) found that in the absence of solvents, alcohol ethoxylation at low temperatures between 85 and 130°C took place with ion pairs, while at higher temperatures, an ionic mechanism controlled of the reactions. Their findings were also cited in Schick (1967), Schonfeldt (1969) and Santacesaria *et al*. (1992a).

Nevertheless, Ishii and Ozeki (1960) noted that the degree of dissociation of a metallic alkoxide was largely dependent on temperatures and the nature of the medium. In a recent investigation on the kinetics and mechanisms of fatty alcohol ethoxylations in presence of potassium hydroxide, Santacesaria *et al*. (1992a) reported that the alkaline catalysts acted as an ionic couple rather than simple anions. This was deduced from the observed strong influences of the cations on the kinetic behaviours. The observation became more evident with narrow-range ethoxylation in the presence of the alkaline earth catalysts, which was a consequence of the ionic pair intervention (Santacesaria *et al*., 1992b).

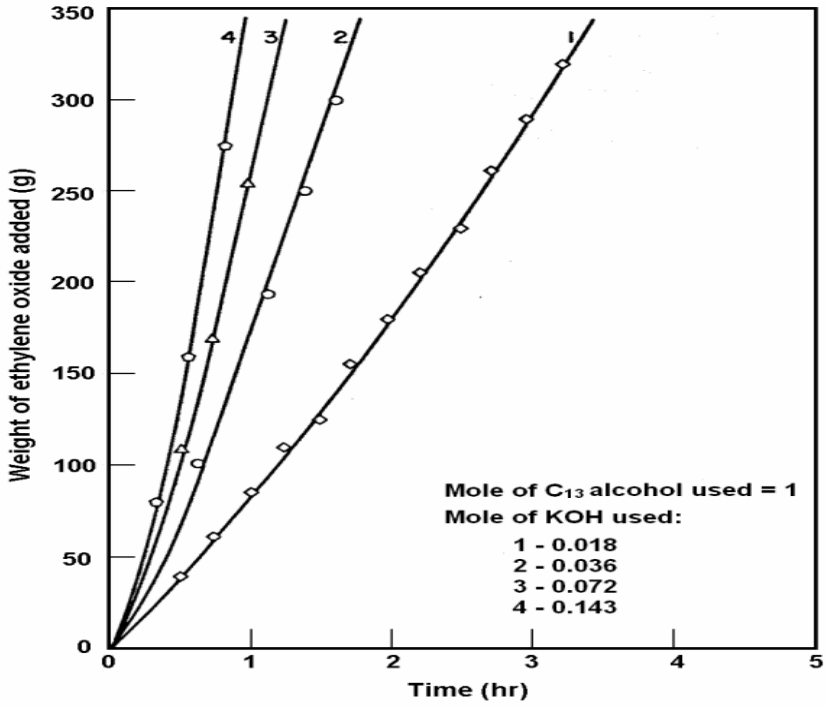

Figure 2. 12 Effect of catalyst concentration on the rate of ethoxylation at 135-140°C with KOH as catalyst (Satkowski and Hsu, 1957).

To study the effect of temperature on the rate of ethoxylation, Satkowski and Hsu (1957) performed ethoxylation experiments at various temperatures. Starting at 105°C, they increased the reaction temperature in increments of 30°C to 200°C. They observed that the rate of ethoxylation increased with reaction temperature as shown in Figure 2. 13. However, the increase in these two parameters did not correspond to a linear relationship. The rate of ethylene oxide addition at the same temperature increment was more apparent at the lower temperatures than the higher temperatures as can be seen in Figure 2. 13.

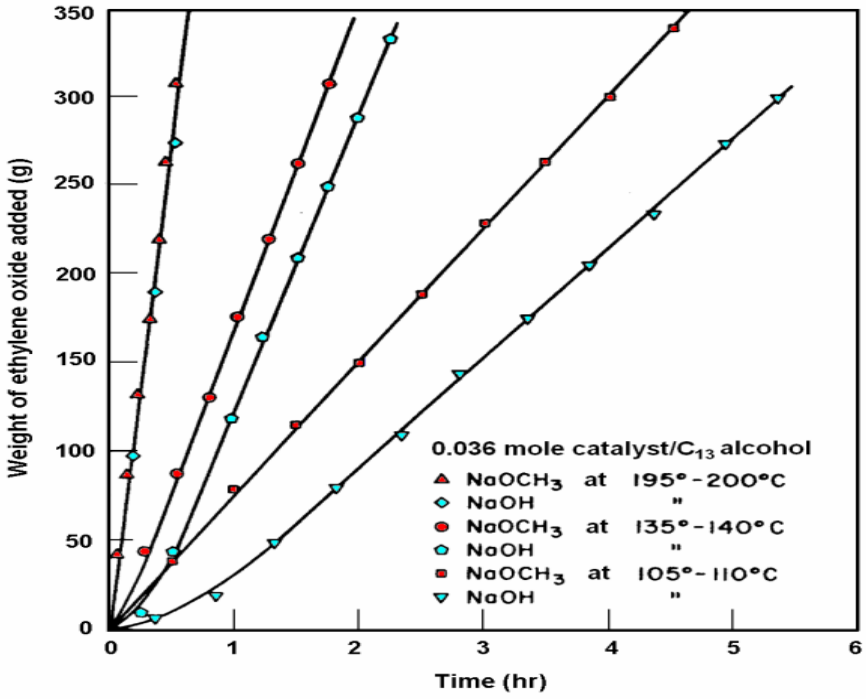

Figure 2. 13 Effect of temperature on the rate of ethoxylation with NaOCH3 or NaOH as the catalyst (Satkowski and Hsu, 1957).

In terms of the effect of pressure on the rate of ethoxylation, Satkowski and Hsu (1957) found it was insignificant due to the low pressure systems used in their study. However, Satkowski and Hsu (1957) noted that in higher pressure systems the rate of ethoxylation was found to increase considerably with the increase in ethylene oxide pressure. This was because ethylene oxide pressure was directly related to the concentration of ethylene oxide present in the system.

In terms of the effect of structure of the alcohol on the rate of ethoxylation, Satkowski and Hsu (1957) observed that the rate decreased with an increase in the carbon chain length in an alcohol. The same observation was also made by Ishii and Ozeki (1960). Their explanation was based on the belief that ethylene oxide associated primarily with the alkoxide ion. Therefore, the structure of the initial alkoxide ion was expected to have some effects on the rate of ethoxylation.

On the basis of their experimental findings, Satkowski and Hsu (1957) postulated the mechanism of base-catalysed ethoxylation of alcohols to consist of a series of consecutive S_N2 reactions. The reaction steps followed the ethylene oxide addition to phenols, which were described earlier by Boyd and Marle (1914) and Miller *et al.* (1950). These steps were described in Equations 2. 9 to 2. 11 with the phenol species being replaced by alcohol and alcohol ethoxylates.

As was mentioned earlier, Gee *et al.* (1959a; 1959b) noted that the reaction mechanism of alcohol ethoxylation occurred with undissociated ion-pairs of a metallic alkoxide from the catalysts. In their kinetic study, Gee *et al.* (1959a; 1959b) reacted ethylene oxide with various low molecular weight alcohols under the catalysis of the corresponding sodium alkoxide. At least a fivefold excess of the alcohol (in moles) was used. Kinetic experiments were performed at temperatures between 24.8 and 40.3°C. Gee *et al.* (1959a; 1959b) took measurements of the reaction velocities by varying the concentrations of ethylene oxide, the catalyst and the alcohol. For the base-catalysed alcohol ethoxylation, the reaction velocities were measured to be first order in ethylene oxide and apparent orders of less than unity in the catalyst concentration. The latter was a consequence of the incomplete dissociation of a catalyst. The incomplete dissociation reduced the reaction rate because the catalytic power of the undissociated metallic alkoxide was lower than that of a free alkoxide ion. In most cases, the rate was also found to be dependant upon the alcohol concentration. However, the dependency was attributed to the effect of alcohol concentration on the degree of catalyst dissociation. Hence, the reaction was a bimolecular event between ethylene oxide and the dissociated alkoxide anion. This work by Gee *et al.* (1959a; 1959b) gave no support to the termolecular reaction proposed earlier by Lowe and Weibull (1954) that an alcohol molecule was involved in the transition complex.

2.4.3.4 Proposed reaction steps

From the literature reviewed above, it was found that the S_N2 mechanism was generally the more accepted reaction pattern where an ethylene oxide ring was opened by a nucleophilic attack of an anion at a carbon atom. The reaction pattern of ethylene oxide ring opening under basic conditions in its addition to hydrophobic substrate was thoroughly elaborated in the review by Schick (1967) and more recently by van Os (1998) and Santacesaria *et al.* (1999). As was mentioned earlier, the overall reaction of ethylene oxide addition to phenol takes place in two steps: the formation of the monoadduct of ethylene oxide to the fresh phenol, followed by a series of ethylene oxide additions to form subsequent adducts. For the convenience of presentation, the notations defined in Section 2. 3 are used hereafter. In addition, the ethylene oxide unit is denoted as EO in the equations. Because phenol has an acidic character, the effect for the ionic couple observed by Santacesaria *et al*. (1992a; 1992b) for the mechanism of fatty alcohol ethoxylation is less important (Santacesaria *et al*., 1999). The reaction steps which involve potassium hydroxide as the catalyst are therefore expressed as follows (Schick, 1967; Santacesaria *et al*., 1990; van Os, 1998):

Activation (fast)

$$RXH + KOH \longrightarrow RX^-K^+ + H_2O \qquad \textbf{2. 12}$$

Initiation step

$$RX^- + EO \longrightarrow RX(EO)_1^- \qquad \textbf{2. 13}$$

Proton transfer (fast)

$$RXH + RX(EO)_i^- \rightleftharpoons RX^- + RX(EO)_iH \qquad i = 1..\ n \qquad \textbf{2. 14}$$

Propagation steps

$$RX(EO)_1^- + EO \longrightarrow RX(EO)_2^- \qquad \textbf{2. 15}$$

$$RX(EO)_2^- + EO \longrightarrow RX(EO)_3^- \qquad \textbf{2. 16}$$

$$RX(EO)_i^- + EO \longrightarrow RX(EO)_{i+1}^- \qquad \textbf{2. 17}$$

Proton transfer (fast)

$$RX(EO)_iH + RX(EO)_j^- \rightleftharpoons RX(EO)_i^- + RX(EO)_jH \qquad \text{where } i \neq j \qquad \textbf{2. 18}$$

Termination

$$RX(EO)_x^- + HA \longrightarrow RX(EO)_xH + A^- \qquad \text{where HA = acid} \qquad \textbf{2. 19}$$

The activation step (Equation 2. 12) refers to activation of the initiator by the basic catalyst, resulting in the metallic salt of the deprotonated initiator RX^- and water. Water reacts with ethylene oxide to form polyoxyethylene glycol. Although the polyoxyethylene glycols are not usually considered an undesirable impurity (Schick, 1967), their content is to be minimised in investigating the ethoxylation rate. This is because the formation of polyoxyethylene glycols is a result of water competition with the deprotonated initiator for ethylene oxide molecule. Therefore, water is to be removed prior to the initiation step which introduces ethylene oxide to the deprotonated initiator. The resulting mixture from the activation step is to undergo a dehydration process in order to lower the water content to a level generally to less than 0.1% by weight (van Os, 1998).

The initiation step (Equation 2. 13) involves the ethylene oxide addition to the deprotonated initiator RX^-. The step is categorised as a nucleophilic substitution. The reaction rates are shown to be dependant on both the concentration of deprotonated initiator RX^- and ethylene oxide EO as $[RX^-][EO]$ and hence an S_N2 mechanism. The initiation step is accompanied by the chain transfer equilibrium reaction as given in

Equation 2. 14. The chain transfer reaction is the fastest step of the overall reaction because of the involvement of an acid-base proton transfer. This effect is thermodynamic rather than kinetic (Hall and Agrawal, 1990). In the case of phenol, the acidity of phenol is greater than that of the subsequent polyoxyethylene adducts, the thermodynamic equilibrium is heavily favoured towards the right of Equation 2. 14. Hence, the equilibrium constant Ke_{NP} is much greater than one as follows:

$$Ke_{NP} = \frac{[RX^-][RX(EO)_i H]}{[RXH][RX(EO)_i^-]} >> 1 \qquad \textbf{2. 20}$$

As a result of the acidic nature of phenol, the subsequent propagation steps are prohibited as long as free phenol is present.

The propagation steps (Equations 2. 15 to 2. 17) refer to the formation of higher members of polyoxyethylene products. Each step is considered as proceeding at a kinetically identical rate because the polyoxyethylene products with different numbers of ethylene oxide adducts are similar in structures and acidities. A unique equilibrium constant for the accompanying proton transfer equilibria (Equation 2. 18) is assumed, that is, $Ke = Ke_1 = Ke_2 = \ldots = Ke_i$, and has a value of unity. These polyoxyethylene products are also compounds containing an active hydrogen atom and their corresponding anions are more nucleophilic than the phenoxide ion when phenol is the initiator. Therefore, the propagation steps evidently occur at a higher reaction rate than the initiation step as shown in Figure 2. 14 (Patat *et al*., 1954).

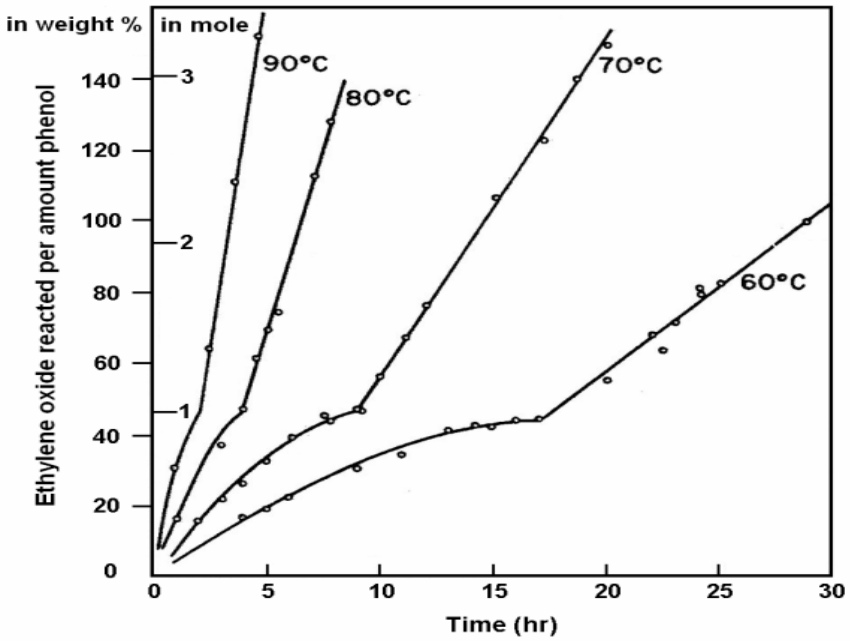

Figure 2. 14 Rate of ethylene oxide addition to phenol in excess ethylene oxide using sodium phenoxide catalyst (Patat *et al.*, 1954).

It should be mentioned here that two distinct rate regions are observed for the ethoxylation of phenols as illustrated in Figure 2. 14 but only one rate region is observed for the alcohol ethoxylation as shown in Figures 2. 11 to 2. 13. This suggests that the reactivity of an alcohol towards ethylene oxide is the same as the reactively of an alcohol ethoxylated to varying extents (Hall and Agrawal, 1990). This is because the nature of the polar group, containing the active hydrogen atom in the hydrophobe, remains unaffected by the ethoxylation process.

Chain growth of a polyoxyethylene product normally continues until all of the ethylene oxide has been consumed and the basic chains are neutralised with an acid (van Os, 1998). Therefore, ethoxylation is depicted as an example of a living polymerisation. To terminate the chain growth when all the desirable amount of ethylene oxide has been reacted in, the reaction mixture is to be neutralised with an acid, as shown in Equation 2. 19.

2.4.3.5 Recent developments

Up until 1990, most of the published kinetics was derived based on the consumption of ethylene oxide. Santacesaria *et al.* (1990) noted that the derivation of the third order kinetics might have been caused by the complicated and unreliable analytical procedure employed in the earlier work. Santacesaria *et al.* (1990) incorporated high-performance liquid chromatography (HPLC) with a UV detector to determine the concentrations of all the oligomers formed in the ethoxylations of a hydrophobic substrate, so that the reaction kinetics could be followed more exactly. With the use of the HPLC technique along with a UV

detector, Santacesaria and co-workers revised the kinetics of base-catalysed ethoxylation of alkylphenols (Santacesaria *et al.*, 1990; Di Serio *et al*., 1995) and fatty alcohols with both conventional (Santacesaria *et al*., 1992a) and narrow-range distribution (Santacesaria *et al*., 1992a; Santacesaria *et al*., 1992b; Di Serio *et al*., 1995). Their work also covered fatty acids ethoxylation (Di Serio *et al*., 1994) and extended to propoxylation of fatty alcohols (Di Serio *et al*., 1996).

Alkylphenol based ethoxylates have emerged as a substantial proportion of the total world production of nonionic surfactants since the mid-1940s (Schick, 1967). However, the first thorough quantitative investigation on the reaction kinetics of alkylphenol ethoxylations was not carried out until 1990 by Santacesaria and his co-workers. In the same year, Hall and Agrawal (1990) published their work on the quantitative aspects of the role of interfacial mass-transfer and reaction kinetics in ethoxylation of lauryl alcohol in a batch recirculation reactor. Since then, studies on the kinetic aspects have become focused on commercially important nonionic surfactants.

2.5 Kinetic modelling of nonylphenol ethoxylation catalysed by potassium hydroxide

A comprehensive kinetic model for ethoxylation of nonylphenol under a base-catalysed condition in a well-mixed stirred reactor was developed by Santacesaria *et al.* (1990). The model was capable of representing both the rates of ethylene oxide consumption and the evolution of product homologues under various kinetic conditions. The model also took into account the changes with time of physical parameters of the system, including ethylene oxide solubility and the liquid volume.

In this work, Santacesaria *et al.* (1990) added gaseous ethylene oxide to nonylphenol using a potassium hydroxide catalyst in an isothermal semi-batch reactor. The reactor had a capacity of 1.5 litres and was equipped with a magnetically driven stirrer. In order to collect reliable kinetic data, Santacesaria *et al.* (1990) had ensured the mass transfer effect to be a minimum and the kinetic data was collected at lower temperatures. The minimisation of the mass transfer effect was achieved by setting the stirrer at its maximum stirring speed so that the greatest possible interfacial contact between the ethylene oxide and the liquid mixture was created. Running low temperature kinetic experiments between 73 and 113°C ensured that the chemical regime was operative in this temperature range. That is, the reaction rates were virtually unaffected by stirring rates. Other kinetic variables also included in the investigation were catalyst concentrations and ethylene oxide pressures. Santacesaria *et al.* (1990) conducted the measurement on ethylene oxide consumption and homologue distribution in the product mixture at different times that were analysed by the previously mentioned HPLC technique. By applying a second-order kinetic model derived from the classical S_N2 mechanism, Santacesaria *et al.* (1990) found the experimental data was satisfactorily reproduced, while a third-order kinetic law failed to reproduce the data. Kinetic and equilibrium parameters were hence determined on the basis of the best fit from fitting the model prediction

to the experimental runs. Independent experiments for ethylene oxide solubility and density of the liquid mixtures were also performed by Santacesaria *et al.* (1990) and later by Di Serio *et al*. (1995) so that the correct physical parameters could be accounted for in the model. The following sections elaborate the kinetic model developed by Santacesaria *et al.* (1990) and their further improved work (Di Serio *et al*., 1995).

2.5.1 Mass transfer

As was mentioned in Section 2.4.2.2, the industrial manufacture of alkylphenol based nonionic surfactants employs one of the two gas-liquid contact schemes, which involves ethylene oxide as the gas reactant. Prior to the reaction, gaseous ethylene oxide must be absorbed into bulk liquid phase. The reaction is therefore a series of mass transfer and kinetic processes. For high temperature operation (175-200°C) in a semi-batch stirred reactor, the reaction rates were observed to have been strongly influenced by the stirring speed, which resulted from the control by mass transfer (Santacesaria *et al*., 1990). That is, the ethylene oxide consumption could be limited by diffusion according to the operative conditions (Santacesaria *et al*., 1995). Moreover, Hall and Agrawal (1990) reported that no enhancement due to chemical reaction was found in mass transfer during an ethoxylation reaction. The enhancement factor was thus taken as unity and the ethoxylation was noted to have a negligible proportion of the reaction that took place in the diffusion film. In this respect, ethoxylation of alkylphenol was classified as a typical moderately slow, gas-liquid reaction (Hall and Agrawal, 1990; Santacesaria *et al*., 1990). This classification was in agreement with the one reported by Charpentier (1981). Because of the absence of the enhancement due to chemical reaction in the diffusion film, the process of alkylphenol ethoxylation was essentially one of physical absorption followed by the reaction in the bulk liquid (Santacesaria *et al*., 1990). The mass transfer of ethylene oxide between phases is described as

$$J = k_L a\left([EO]_{if} - [EO]_b\right) \qquad \textbf{2. 21}$$

where J is the mass transfer rate, $k_L a$ is the volumetric mass transfer coefficient with the assumption that there is no gas-side mass transfer resistance and the liquid phase resistance is controlling, $[EO]_{if}$ is the concentration of ethylene oxide in the gas-liquid interface, that is, the ethylene oxide solubility, and $[EO]_b$ is the concentration of ethylene oxide in the bulk liquid.

2.5.2 Reaction kinetics

The derivation of the rates of alkylphenol ethoxylation is based on the Equations 2. 13 to 2. 18. The activation reaction, Equation 2. 12, is not included because it is easily accomplished and not generally of interest. The reaction steps included are ethoxylations and proton exchange reactions. Since the proton exchange reactions are generally very fast relative to ethoxylations, they are assumed to always be in

equilibrium in this kinetic model. The rates of each ethoxylation step according to the described mechanism can be written as follows:

$$\frac{dm_0}{dt} = -k_i[EO]_b[RX^-] \qquad \textbf{2. 22}$$

$$\frac{dm_1}{dt} = [EO]_b\,(k_i[RX^-] - k_p[RX(EO)_1^-]) \qquad \textbf{2. 23}$$

$$\vdots$$

$$\frac{dm_i}{dt} = k_p[EO]_b([RX(EO)_{i-1}^-] - [RX(EO)_i^-]) \qquad \textbf{2. 24}$$

where k_i = the second-order rate constant for the initiation reaction, Equation 2. 13, where the subscript i stands for initiation;

k_p = the second-order rate constant for the further propagation reactions, Equations 2. 15 to 2. 17, where the subscript p stands for propagation;

m_0 = [RXH]+[RX$^-$], that is, the total concentration of the alkylphenol, and

m_i = [RX(EO)$_i$H]+[RX(EO)$_i^-$] with i=1 to n.

In each ethoxylation step, there is one ethylene oxide molecule that is consumed. Thus, the overall consumption of ethylene oxide is written as:

$$\frac{d[EO]_b}{dt} = [EO]_b\,(k_i[RX^-] + k_p\sum_{i=1}[RX(EO)_i^-])\,. \qquad \textbf{2. 25}$$

In the case of a stirred ethoxylation reactor, where gaseous ethylene oxide was dispersed in the well-mixed liquid phase, the performance of the reactor can be described with the Equations 2. 21 to 2. 25. As can be seen in Equations 2. 21 and 2. 25, the driving force for the mass transfer was ($[EO]_{if}$–$[EO]_b$), whereas the driving force for the chemical kinetics was $[EO]_b$ (Hall and Agrawal, 1990).

Since ethoxylation is typical of moderately slow gas-liquid reactions, with an enhancement factor or a Hatta number (the ratio of reaction to diffusion) near 1 (Charpentier, 1981), a pseudo-steady-state condition for ethylene oxide retention could be assumed when reaction rates were under the influence of mass transfer resistance (Di Serio *et al.*, 1995). That is,

$$J = k_L a([EO]_{if} - [EO]_b)$$

$$= [EO]_b (k_i [RX^-] + k_p \sum_{i=1} [RX(EO)_i^-]) = \frac{d[EO]_b}{dt}$$

2. 26

Consequently, an expression for ethylene oxide concentration in the bulk liquid can be determined from:

$$[EO]_b = \frac{k_L a [EO]_{if}}{k_i [RX^-] + k_p \sum_{i=1} [RX(EO)_i^-] + k_L a}$$

2. 27

It was apparent from Equation 2. 27, when there was negligible diffusion limitation, $[EO]_b \approx [EO]_{if}$, ethylene oxide bulk concentration simply corresponded to the ethylene oxide solubility.

The acidity of nonylphenol had a strong influence on both the rate of the initiation step and the equilibrium of proton transfer (Santacesaria *et al*., 1992a). Therefore, the equilibrium conditions must also be considered in the kinetic model. This was accomplished by incorporating the equilibrium relationship in Equation 2. 20 into the above rate equations. By defining a constant, γ, as

$$\gamma = \frac{[RX(EO)_i H]}{[RX(EO)_i^-]} = Ke_{NP} \frac{[RXH]}{[RX^-]},$$

2. 28

as the ratio between the concentration of an un-dissociated ethoxylate and its dissociated ion, the above rate equations (Equations 2. 22 to 2. 24) can be transformed into a form expressed in total molarity of an ethoxylate as follows:

$$\frac{dm_0}{dt} = -k_i [EO]_b \frac{Ke_{NP} m_0}{\gamma + Ke_{NP}}$$

2. 29

$$\frac{dm_1}{dt} = [EO]_b \left(k_i \frac{Ke_{NP} m_0}{\gamma + Ke_{NP}} - k_p \frac{m_1}{1+\gamma}\right)$$

2. 30

$$\frac{dm_i}{dt} = k_p \frac{[EO]_b}{1+\gamma} (m_{i-1} - m_i)$$

2. 31

The expression for bulk ethylene oxide concentration becomes

$$[EO]_b = \frac{k_L a[EO]_{if}}{k_i \frac{Ke_{NP}}{\gamma + Ke_{NP}} + k_p \sum_{i=1} \frac{m_i}{1+\gamma} + k_L a}$$

2. 32

Prior to solving the above mathematical model for the kinetics, the value for γ needed to be solved from the following equation (Santacesaria *et al*., 1990):

$$\gamma^2 - \gamma\left[Ke_{NP}\left(\frac{R^0}{B^0} - 1\right) - \frac{\sum m_i}{B^0}\left(Ke_{NP} - 1\right) - 1\right] - Ke_{NP}\left(\frac{R^0}{B^0} - 1\right) = 0$$

2. 33

where R^0 is the total concentration of the initial alkylphenol and B^0 is the initial concentration of the catalyst. The detailed derivation for Equation 2. 33 is given in Appendix A. Another parameter needed to be determined prior to solving the kinetic model was the value for $[EO]_b$, which was related to the solubility of ethylene oxide $[EO]_{if}$. Values for the rate constants, k_i and k_p, and the equilibrium constant, Ke_{NP}, were obtained from the Arrhenius and van't Hoff expressions, respectively. An Arrhenius type of equation for a rate constant k is defined by the following form:

$$k = Ae^{-E/RT}$$

2. 34

where A is the pre-exponential factor, E is the activation energy, R is the universal gas constant and T is temperature in Kelvin. The Van't Hoff equation for an equilibrium constant Ke is expressed as

$$Ke = Ke^0 e^{He/RT}$$

2. 35

where Ke^0 and H_e are the entropic and enthalpic contributions to the equilibrium constant Ke, respectively. The parameters involved in these expressions for the ethoxylation of nonylphenol are given in Table 2. 3. As is shown in Table 2. 3, the values derived in the studies in the literature differed from one another. This was due to the methods used to evaluate the solubility of ethylene oxide, which is to be explained in the following section.

Table 2. 3 Kinetic and equilibrium constants for the ethoxylation of nonylphenol.

	k_i		k_p		Ke_{NP}	
	Ln*A*	*E* (kcal/mol)	Ln*A*	*E* (kcal/mol)	Ke^0_{NP}	H_e (kcal/mol)
Santacesaria *et al*. (1990)	35.31 ± 0.03	24.59 ± 0.56	37.82 ± 0.09	25.79 ± 0.54	$(3.10 \pm 0.12) \times 10^{-12}$	-21.75±0.43
Di Serio *et al*. (1995)	26.0 ± 0.3	18.2 ± 0.5	28.7 ± 0.2	19.4 ± 0.4	$(2.4 \pm 0.3) \times 10^{-11}$	-21.5±0.3

The pre-exponential factor *A* has a unit of $cm^3/mol.s$.

The equilibrium constant calculated from van't Hoff equation was only valid for T < 130°C. For T ≥ 130°C, $Ke_{NP} = 0.5 \pm 0.1$ (Di Serio *et al*., 1995).

2.5.3 Changes of physical properties

The semi-batch operation resulted in a significant increase in liquid phase volume as more ethylene oxide molecules were added. The volume of the reaction mixture usually doubled or tripled that of the original liquid. For example, in the ethoxylation of lauryl alcohol where the average ethylene oxide molecules added per molecule of lauryl alcohol was 5, the final liquid-phase volume was three times the original volume (Hall and Agrawal, 1990). This increase in liquid phase volume evidently changed the physical properties of the system. Therefore, it was of great importance to take into account the changes of physical properties in the kinetic model.

2.5.3.1 Density

The density of the polyoxyethylene mixtures was measured by a picnometer at different molecular weight averages and temperatures (Santacesaria *et al*., 1990; Di Serio *et al*., 1995). Based on the measurement, Di Serio *et al.* (1995) established an empirical correlation that expressed the density as a function of both temperature and mean number of ethylene oxide adducts per mole of hydrophobe substrate, N_{EO}. For nonylphenol-based polyoxyethylenes with up to 10 units of ethylene oxide molecules, the density function is given by the following empirical relation (Di Serio *et al*., 1995):

$$\rho = 950 + 23.3N_{EO} - 0.533N_{EO}^{\ 2} - 0.0638N_{EO}^{\ 3} - 0.65 \times (T - 273.15) \qquad \textbf{2. 36}$$

where ρ is the density in kg/m^3 and *T* is as previously defined.

2.5.3.2 Ethylene oxide solubility

Ethylene oxide solubility plays an important role in the kinetic model for the ethoxylation. This is because the reaction kinetics directly depends on the ethylene oxide concentration in the liquid phase $[EO]_b$ (Santacesaria *et al*., 1990; Hall and Agrawal, 1990; Santacesaria *et al*., 1992a; Di Serio *et al*., 1995), which is directly related to the solubility $[EO]_{if}$, as was shown in Equation 2. 27. Furthermore, the ethoxylation is a highly exothermic reaction which gives out about 90 kJ/mole of ethylene oxide reacted.

An accumulation of ethylene oxide in the liquid phase could be the origin of reactor instability (Di Serio *et al*., 1995; Dimiccoli *et al.*, 2000). Therefore, it is important to know the ethylene oxide solubility in the reaction mixture at any time.

As was mentioned earlier, the liquid volume in a semi-batch operation increased with the progression of the ethoxylation. In addition, the reaction environment gradually transformed from hydrophobic to hydrophilic as more ethylene oxide molecules were added. As a consequence, ethylene oxide solubility in the reaction mixture changed with the extent of the ethoxylation. Santacesaria *et al.* (1990), Patel and Young (1993) and Di Serio *et al*. (1995) all reported data on the vapour-liquid equilibria of ethylene oxide in admixture with nonylphenol and elaborated them with models applicable to the description of vapour liquid equilibria, such as UNIFAC, NRTL and Wilson.

Santacesaria *et al.* (1990) reported some data on ethylene oxide solubility in solvents of nonylphenol and the corresponding ethoxylates at two temperatures of 100 and 125°C. The partition coefficient K was defined as

$$K = P_{EO}/X_{EO},$$

2. 37

where P_{EO} is the vapour pressure of ethylene oxide and X_{EO} is the ethylene oxide mole fraction in the liquid. Santacesaria *et al.* (1990) found that ethylene oxide exhibited a near constant solubility at a fixed temperature in the experimental field examined and that it followed the very simple Henry's Law $H=X_{EO}/P_{EO}$, with H simply the reciprocal of the partition coefficient K. For solubilities at a temperature outside those reported, Santacesaria *et al.* (1990) suggested an approximation by the following equation:

$$K_i = K_1\left(\frac{K_2}{K_1}\right)^{\left(\frac{T_2}{T_1-T_2}\right)\left(\frac{T_1}{T_i}-1\right)}$$

2. 38

where K_1 and K_2 are partition coefficients at valid temperatures of T_1 and T_2, respectively and K_i is the partition coefficient to be determined at temperature T_i. Despite the approximation, Santacesaria *et al.* (1990) successfully used these extrapolated solubility data in the kinetic model to simulate the performance in the industrial reactors. They noted it was probably because kinetic parameters and solubilities were strongly correlated and the errors in the calculation of the exact solubility were compensated by the corresponding errors in the kinetic constants (see also Santacesaria *et al.*, 1995). As a consequence, Santacesaria *et al.* (1995) and Di Serio *et al.* (1995) noted that changing the method for evaluating solubilities could require the adjustment of the kinetic parameters if there were differences in the evaluated solubility values.

More phase equilibrium data in the form of ethylene oxide gas solubility and vapour-liquid equilibria were reported for a binary system of ethylene oxide and nonylphenol and three different nonylphenol ethoxylates by Patel and Young (1993). The vapour-liquid equilibrium data were collected at four temperatures in the range of 90-190°C. These phase equilibria provided the needed connection among pressure, temperature and composition.

In the work of Di Serio *et al.* (1995), all the existing solubility data reported in the earlier works by Santacesaria *et al*. (1990) and Patel and Young (1993) were combined with new data generated in the further measurements by Di Serio *et al.* (1995). Di Serio *et al.* (1995) correlated these data with the following three different methods: (i) UNIFAC, (ii) Wilson and (iii) two parameters NRTL. In all cases, the vapour phase was considered ideal with negligible effect of non-ideality. Furthermore, the system was considered to consist of pseudo-binary components with the polyoxyethylene mixture characterised as a unique component with an averaged molecular weight. By subjecting all collected vapour-liquid equilibrium data to statistical regression analysis, the two interaction parameters in the NRTL and Wilson equations, Λ_{12} and Λ_{21}, were derived to give their optimum forms to be used in the modelling. As a result, the Wilson method gave the best results with a mean error less than 17% while UNIFAC had the largest error of more than 30%. Table 2. 4 shows an example of ethylene oxide solubility equilibrium data at different temperatures and the comparison of the performances obtained with UNIFAC, NRTL and Wilson models.

Table 2. 4 Examples of ethylene oxide equilibrium data at different temperatures and the comparison of the performances obtained with UNIFAC, NRTL and Wilson models to describe ethylene oxide solubility in ethoxylated nonylphenol with 9 units of ethylene oxide molecules (Santacesaria *et al.*, 1995).

X_{EO}	P_{EO} (atm)			Mean error %		
	90°C	110°C	130°C	UNIFAC	NRTL	Wilson
0.240	0.99	1.41	1.97			
0.514	2.82	3.95	5.55	33	5	6
0.700	4.93	7.05	9.87			
0.774	6.06	9.16	12.69			

Di Serio *et al*. (1995) and Santacesaria *et al*. (1995) explained that the difficulty in achieving precision in the determination of ethylene oxide solubility in such systems might be largely related to the non-ideality of ethylene oxide behaviour in vapour-liquid equilibria. They also suggested that the error was related to the large differences in molecular size between ethylene oxide and the hydrophobic compounds. In addition, the representation of a single compound with an averaged molecular weight for polyoxyethylene mixtures of various oligomers might also contribute to the difficulty in interpreting the data. Despite these drawbacks, Di Serio *et al*. (1995) still observed that, by using the Wilson method, ethylene oxide solubility

was successfully related, respectively, to pressure, temperature and average number of ethylene oxide adducts. This validation allowed the possibility of interpolation or extrapolation of ethylene oxide solubility data for operations in practice under a broader range of conditions, in particular the industrial plant conditions.

The Wilson method comprises two interaction parameters, Λ_{12} and Λ_{21}, which were correlated with the mean number of the ethylene oxide adducts N_{EO} in quadratic polynomial relations by Di Serio *et al.* (1995). Equations 2. 39 and 2. 40 represent the expressions for the parameters used in the Wilson equations.

$$\Lambda_{12} = 4.01 + 1.797\times10^{-1} N_{EO} + 1.351\times10^{-2} N_{EO}^{\ 2}$$

2. 39

$$\Lambda_{21} = 8.987\times10^{-1} + (-4.423\times10^{-2}) N_{EO} + 5.329\times10^{-4} N_{EO}^{\ 2}$$

2. 40

The above parameters have negligible dependency on the temperature. The coefficients in the polynomials were determined through regression analysis on the experimental data by finding the minimum misfit to the objective function (Di Serio *et al.,* 1995):

$$F = \frac{1}{N}\sum_{i=1}^{N}\left(\frac{P_{si} - P_{ci}}{P_{si}}\right)^2$$

2. 41

where P_{si} is the ethylene oxide pressure obtained from the measurement and P_{ci} is the corresponding modelled pressure. With the assumption of an ideal vapour phase, P_{ci} was determined by the following equation

$$P_{ci} = x_{EO}\gamma_{EO}P^{\circ}_{EO}\,.$$

2. 42

P°_{EO} is the saturation vapour pressure of ethylene oxide in atm and its value can be given by the following Antoine equation (Prausnitz, 1980):

$$P^{\circ}_{EO} = \exp[16.74 - \frac{2568}{(T - 29.01)}]/760$$

2. 43

where T is the temperature in Kelvin. The Wilson equations for calculating the activity coefficients are formulated as follows:

$$\ln\gamma_1 = -\ln(x_1 + x_2 \cdot \Lambda_{12}) + x_2 \cdot \left[\frac{\Lambda_{12}}{(x_1 + x_2 \cdot \Lambda_{12})} - \frac{\Lambda_{21}}{(x_1 \cdot \Lambda_{21} + x_2)} \right]$$

2. 44

$$\ln\gamma_2 = -\ln(x_1 \cdot \Lambda_{21} + x_2) - x_1 \cdot \left[\frac{\Lambda_{12}}{(x_1 + x_2 \cdot \Lambda_{12})} - \frac{\Lambda_{21}}{(x_1 \cdot \Lambda_{21} + x_2)} \right]$$

2. 45

The performance of the above Wilson method in predicting the equilibrium pressures is shown in Figure 2. 15. The comparison of the calculated and experimental ethylene oxide equilibrium pressures was obtained from the respective binary systems of ethylene oxide-nonylphenol and ethylene oxide-ethoxylated nonylphenol at different numbers of ethylene oxide adducts and different temperatures. As can be seen in Figure 2. 15, the predictive Wilson method gave satisfactory results for nonylphenol with different ethylene oxide to substrate ratios.

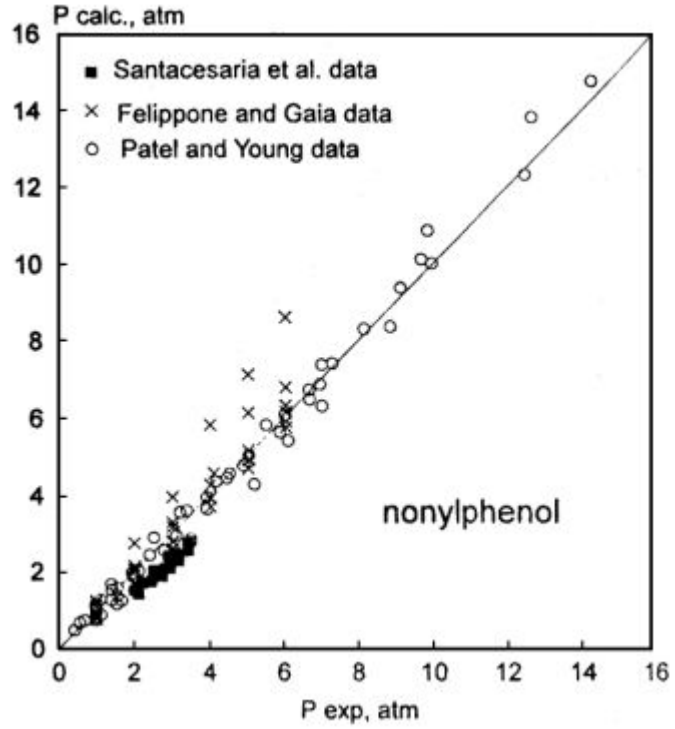

Figure 2. 15 Performance of the Wilson method in predicting the equilibrium pressures for the respective binary systems ethylene oxide-nonylphenol and ethylene oxide-ethoxylated nonylphenol with different numbers of ethylene oxide adducts and different temperatures (Di Serio *et al.*, 1995).

2.6 Conclusions

The literature review has extensively discussed the kinetics of the base-catalysed ethoxylation, in the current context - the manufacture of nonionic surfactants. Ethoxylation was classified as a gas-liquid reaction. Gaseous ethylene oxide must be absorbed into the bulk hydrophobic mixture prior to the reaction. The reaction was characterised by the mass transfer resistance in series with the chemical reactions. The reaction pattern followed an S_N2 mechanism. Based on these findings, a comprehensive kinetic model was developed by Santacesaria *et al*. (1990) and Di Serio *et al*. (1995) which was able to predict the reaction behaviour, such as ethylene oxide consumption rate and the evolution rate of product oligomers, during the ethoxylation of an alkylphenol under a base-catalysed condition. The kinetic model also took into account the changes of density and ethylene oxide solubility as a result of reaction liquid volume increase from the semi-batch operation. Ethylene oxide solubility was also applied as an important measure for reactor stability.

From the literature review, it had become clear that despite the industrial importance of alkylphenol based ethoxylates, studies that shed quantitative information on the kinetic rates with direct relevance to a manufacturing process of this type of nonionic surfactants remained scarce. Moreover, these studies were not performed until about a decade ago when the analytical techniques for surface active agents were available in terms of their ability to provide accurate analytical results at a reasonable cost (Schmitt, 2001). It was also apparent that these studies with the application of the advanced analytical techniques, such as HPLC, which aided the investigation of the ethoxylation kinetics were all conducted by the same group of researchers led by Professor Santacesaria. Therefore, it would be valuable to perform further validation on the kinetic data that were published in the literature through the use of an ethoxylation reactor in operation in the industry, which had a slightly different operating arrangement to the ideal reactors assumed in the literature.

Consequently, the aims of the first stage of this project were as follows:

“Further development of the existing kinetic model to fully incorporate “non-ideal” features in a real industrial reactor, in order to describe the reaction rates which occurred in the in-house system and for integration into the future CFD model that allowed the CFD validation to be realised.”

Chapter 3

Ethoxylation Kinetics Experiments

3.1 Introduction

In Chapter 2 the mechanisms proposed in the literature for the base-catalysed ethoxylation of an alkylphenol were thoroughly reviewed. A classic S_N2 mechanism was considered to best describe the base-catalysed ring-opening reaction of ethylene oxide and which was assumed to be the rate-determining step. Following this derivation, Santacesaria *et al*. (1990) and Di Serio *et al*. (1995) had developed a mathematical model that described the kinetics of base-catalysed nonylphenol ethoxylation in a semi-batch stirred reactor. Their experimental approach for measuring the ethoxylation kinetics was also discussed in Chapter 2. In order to validate further the kinetic data published by Santacesaria *et al.* (1990) and Di Serio *et al*. (1995), a new set of kinetic experiments was conducted in this research project. The experiments were conducted by using the existing alkoxylation facilities in the Huntsman Corporation Australia Technical Centre, located at Ascot Vale, Victoria. This chapter describes the reagents, apparatus and experimental procedures used in the laboratory ethoxylation operation owned by Huntsman Corporation Australia (HCA). An overview of the experimental approach undertaken in the present study is also given in this chapter.

Because the experimental process involved handling of a hazardous, explosive chemical, laboratory safety measures were enforced through an autoclave operation training program and full time supervision from experienced HCA laboratory staff during the entire course of the experiments.

3.2 Materials

The following is a list of reagents used in this experimental study.

For ethoxylation experiments

- Neodol 91: synthetic alcohol 91, consisted of C9 to C11 primary alcohol: 13 – 23% C9, 37 – 47% C10, 33 – 43% C11, was supplied by Shell Chemical (Aust.) Pty Ltd
- Nonylphenol: 4-nonylphenol (mixture of alkyl chain isomers), consisted of 2% maximum w/w di-nonylphenol, 10% maximum w/w o-nonylphenol and 90% minimum w/w p-nonylphenol, was supplied by Schenectady
- Ethylene oxide (highest purity), HCA's own manufacture
- Nitrogen (high purity), supplied by BOC
- Potassium hydroxide (caustic potash, liquid), 48.0-50.0% w/w KOH, supplied by Orica Chemnet
- Acetic acid (industrial grade), 89-91 % acetic acid, supplied by Orica Chemnet

The kinetics of nonylphenol ethoxylation with the use of a basic catalyst was the main focus in this experimental study. Thus, nonylphenol was the sole hydrophobic substrate used in the kinetic experiments. The use of neodol 91 will be explained in the later section.

For gas chromatography analysis

- Dichloromethane (AR grade), supplied by Merck Australia
- Bis(trimethylsilyl)trifluoroacetamide catalysed with 1% trimethylchorosilane, known as BSTFA+1% TMCS, supplied by Alltech Associates, Inc.

3.3 Apparatus

3.3.1 Two-litre autoclave

All laboratory experiments were conducted in a two-litre autoclave in the autoclave building at the Ascot Vale technical centre. The autoclave building was specifically designed to minimise the hazards associated with the use of toxic and highly flammable materials under conditions of high pressure and temperature. The building has two areas: a control room and six external reactor bays. The control room is always maintained above atmospheric pressure to prevent ingress of gases. Each autoclave is equipped with its own control unit and panel within the building so that an operator spends a minimal amount of time outside in the actual bay.

The control unit, shown in Figure 3. 1, has a main power switch and switches for the stirrer control and heater. It also has a heater dial to set the temperature for the heater and a graph for recording temperature changes within the vessel.

Figure 3. 1 The control unit (Courtesy of HCA).

The inside panel contains various control valves as shown in Figure 3. 2. The nitrogen pad valve feeds nitrogen to the top of the reactor only. The ethylene oxide/input valve feeds ethylene oxide or nitrogen from a storage cylinder through a dip-leg pipe into the bottom of the reactor. The cooling water valve controls the cooling water flow into the internal coil of the reactor when cooling is applied. The vacuum water tap supplies vacuum to the reactor from a water-driven vacuum pump. The reactor is placed under vacuum when both the vacuum valve and the cooling water valve are opened.

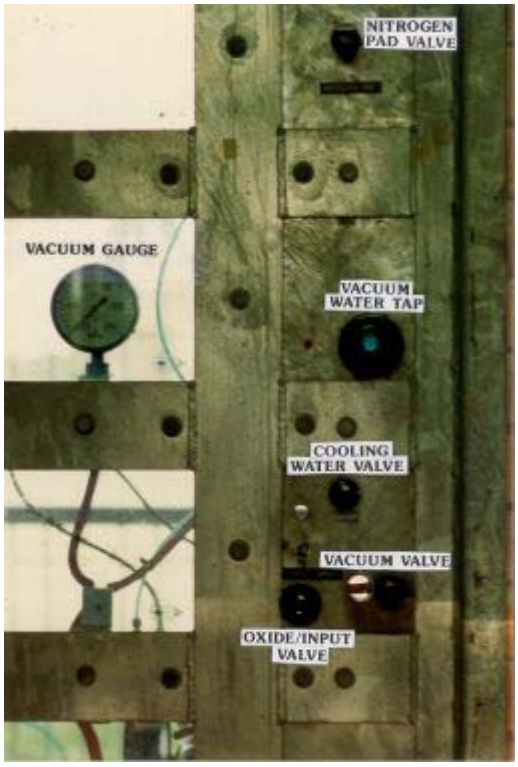

Figure 3. 2 The inside panel (Courtesy of HCA).

The outside bay where the autoclave is housed is shown in Figure 3. 3. The main features of the autoclave system are shown in the schematic illustrated in Figure 3. 4. The vessel is of 316 stainless steel construction and capable of sustaining pressures up to 38MPa, however the maximum working pressure is set at 600kPa and the normal operating pressure is 400kPa. The vessel also has several bursting discs which are designed to release pressure when the disc's pressure rating is exceeded. Internally, the reactor is equipped with an agitation system, which is a packless magnetic driven stirrer motor with variable speed control. The agitator has a working speed between 540 and 1800rpm. The impeller is a six-blade disc turbine mounted on the shaft. The shaft has an aspiration hole near the bottom end. The aspiration hole allows the gas to be drawn through the hollowed shaft then sparged into the bulk liquid. In combination with the effect of agitation, the interfacial contact between dispersed gas and bulk liquid is enhanced. Internally, the reactor is also fitted with a helical coil for cooling water flow. Other internal components in

the reactor include a thermowell, which holds a thermocouple, and a dip-leg pipe, which extends through to the bottom of the vessel. The dip-leg pipe provides the path that delivers ethylene oxide or nitrogen in direct contact with liquid mixture upon entry. The top end of the dip-leg pipe is connected to a flexible hose and an ethylene oxide/input line, linking the vessel to a storage cylinder of ethylene oxide. The cylinder is made of 304 stainless steel and fitted with manifolds to facilitate ethylene oxide transfer as shown in Figure 3. 5. The cylinder is normally pressurised by nitrogen to 700kPa but not beyond 900kPa and placed onto a digital balance. The nitrogen bypass valve on the feed cylinder manifold, when opened, allows nitrogen to be passed through the flexible ethylene oxide addition line.

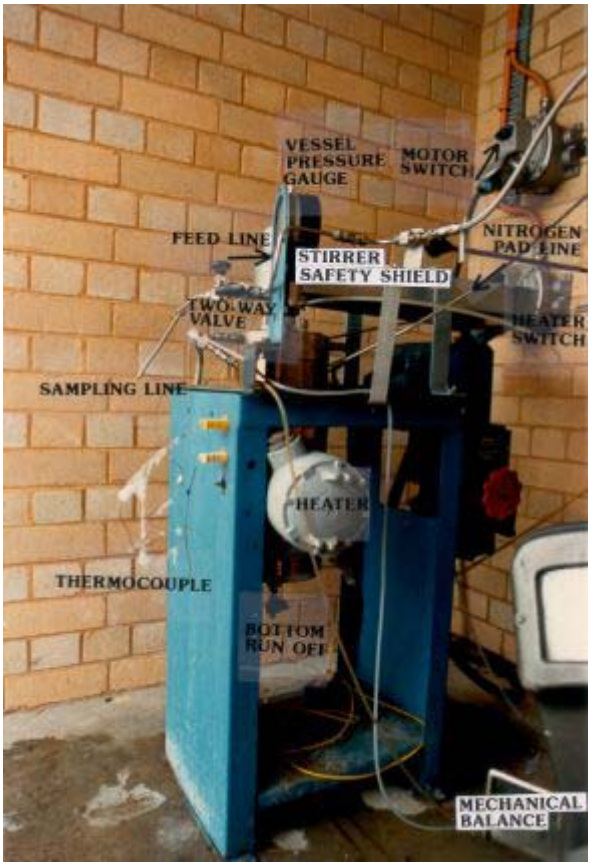

Figure 3. 3 Two-litre autoclave (Courtesy of HCA).

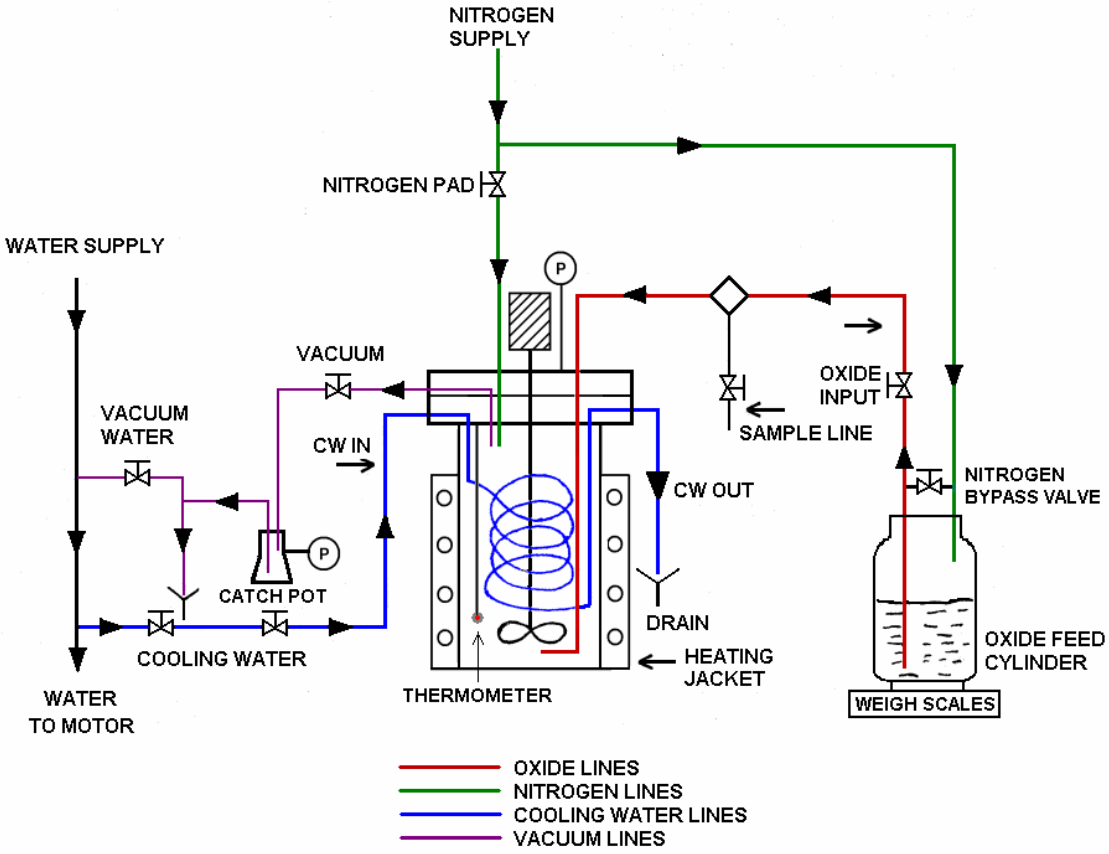

Figure 3. 4 Autoclave schematic.

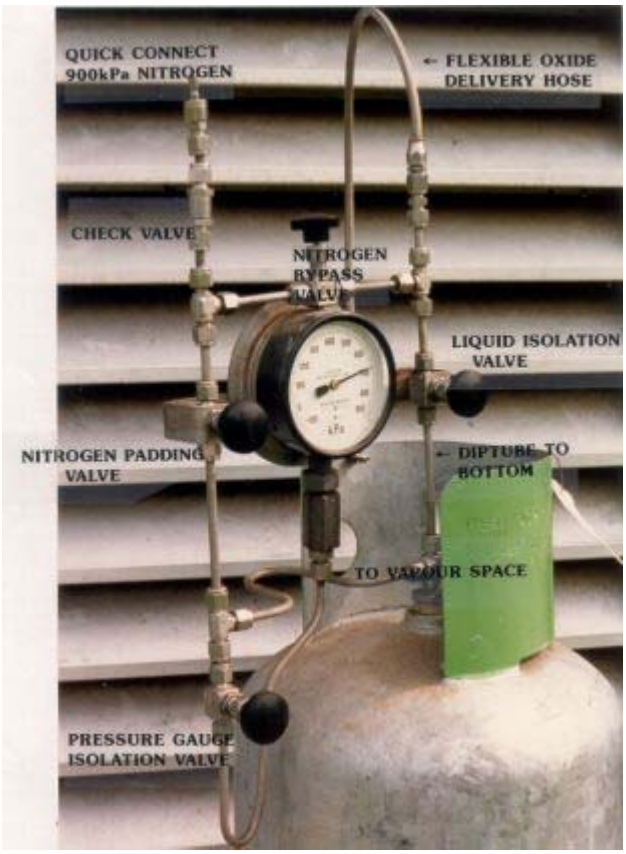

Figure 3. 5 Feed cylinder manifold (Courtesy of HCA).

The reactor body is wrapped with an electrical heating jacket that provides the heating to the reactor contents. The vessel is also equipped with a pressure gauge that measures the pressure of the vessel itself. The minimum and the maximum working volume for the vessel are 80ml and 1.6 litres respectively. Table 3. 1 summarises the specifications of the vessel used in the present study.

Table 3. 1 Summary of the specifications of the vessel used in this study.

Vessel Specifications	2-litre Autoclave
Materials of construction	316SS
Minimum volume to stir, ml	80
Maximum operating volume, ml	1600
Maximum working pressure, kPa	600
Normal operating pressure, kPa	400
Bursting disc settings at 22°C, kPa	1000; 37,900
Stirring speed working range, RPM	540-1800
Heating	External
Cooling	Internal coil
Minimum volume to coil, ml	130
Minimum volume to thermowell, ml	130

3.3.2 Gas chromatograph

The homologue distribution of low molecular weight ethoxylates of an alcohol or an alkylphenol was quantified by a Hewlett Packard 5890 Series II gas chromatograph (GC), equipped with single flame ionisation detector (FID). The GC column used was a DB-1 capillary column with 0.250mm internal diameter, 15m in length and 0.1μm film thickness (J&W Scientific Inc.). The column oven temperature was programmed from 35 to 65°C at a rate of 15°C/min (no hold), then ramped to 340°C at 4°C/min and held for 30 min. Injector and detector temperatures were set at 38 and 350°C, respectively. Helium was used as both carrier and make-up gases with the flow rates of 1.5 ml/min and 19.3ml/min, respectively. The detector hydrogen flow was 33ml/min and air flow was 300ml/min. GC signals were processed using a Hewlett Packard ChemStation Series II software.

The GC method was applicable to alcohol ethoxylates or alkylphenol ethoxylates between molecular weights of approximately 100 to 900.

3.4 Ethoxylation experiment procedures

A typical ethoxylation run consists of a sequence of operational procedures. They are vessel pressure test, raw materials charge, dehydration, ethylene oxide addition and product neutralisation. Each of these procedures requires absolute precautions to ensure safety.

3.4.1 Vessel pressure test and raw material charging

It is important to take precautions against ethylene oxide explosion hazard before ethylene oxide is admitted into the vessel for a reaction. For this purpose, safety precautions including an initial pressure test and elimination of oxygen were conducted.

First, it was important to ensure that the vessel was cool, dry and clean. This was tested by the introduction of nitrogen, approximately to 200kPa, to the sealed vessel. The nitrogen was introduced via the nitrogen pad valve. The sampling tube was then cautiously opened to expel nitrogen. As the nitrogen was expelled, any physical sign of moisture was visually and manually inspected. As discussed in Section 2.4.3.4, water also reacts with ethylene oxide, resulting in a competitive side-reaction. If no sign of moisture was evident, the vessel was confirmed dry and clean, otherwise, further drying was necessary. Next, the vessel was tested for pressure leaks. It was essential that the vessel was cool and isolated. Then the vessel was pressurised with nitrogen to approximately 400kPa and allowed to stand for a period of 15 minutes. Any pressure drop during this period of time was observed. If a pressure drop was less than 10kPa, the vessel was confirmed pressure tight and safe to use. If the vessel failed the pressure test, it was unsafe to operate and any leaks, however small, had to be rectified prior to raw material charging. Leaks at joints or valves could be detected with a spray of a soap solution.

Once the vessel was confirmed pressure tight, the charging of the raw materials began. The liquid raw materials, including the initiator and aqueous potassium hydroxide (50% w/w), were drawn into the vessel via the sampling line under the vessel evacuation through a fully opened vacuum valve. Once charged with raw materials, the vessel was evacuated and nitrogen purged three times to eliminate any air that may have entered the vessel with the raw materials. Exposure of ethylene oxide to oxygen creates an explosion danger. The purged nitrogen was delivered via the feed cylinder manifold with the nitrogen bypass valve opened. The heating of the raw materials commenced after the oxygen elimination.

3.4.2 Dehydration and sampling procedures

In order to prevent competitive polyoxyethylation of water during the polyoxyethylation of an alkylphenol, significant effort must be made to remove residual water, which produces polyethylene glycol with ethylene oxide. The water was initially introduced to the reactor system from the addition of aqueous potassium hydroxide. More water was formed during the activation step (see Equation 2. 12). As

previously mentioned in Section 2.4.3.4 in Chapter 2, the activation step was an equilibrium reaction. The removal of the water would facilitate the high conversion to the potassium salt.

The water was removed by sparging nitrogen under vacuum during heating of the raw materials mixture. The nitrogen was introduced via the nitrogen bypass valve on the feed cylinder. The heating normally started at ambient temperature after the vessel, filled with the raw materials, was purged to eliminate oxygen. The heating continued and the temperature rose. When the temperature approached 120°C, the heating was adjusted so that it maintained at the intensity that stabilised the temperature at this value. The mixture of the raw materials was then left to dehydrate with the vessel placed under vacuum. Nitrogen bleed was applied to facilitate dehydration process, but was kept at a very low flow (the vacuum gauge registered <10kPa). This minimised any raw material to be carried over into the catch pot (see Figure 3. 4). Stirring could also be applied occasionally. The dehydration continued for approximately one hour under constant monitoring to prevent reactor contents carryover. At the end of the one-hour drying step, the reactor vessel was cooled to approximately 80°C for a sampling routine. One waste beaker and a sample jar were prepared and both pre-weighed. The vessel, with the stirrer off, was pressurised to approximately 150kPa of nitrogen. First, the pre-weighed beaker was placed under the sampling tube and approximately 20ml of waste was collected. Then, a further approximately 10ml of reactor contents was collected into the sampling jar for water analysis. Both waste beaker and sampling jar were weighed again and the weights recorded. The contents of the sampling jar was tested for its free water by the Karl Fisher titration method (ASTM E203). The Karl Fisher method determines the free water and water of hydration in most solid or liquid organic and inorganic compounds with the use of the Karl Fischer reagent and electrometric end-point detection.

Hall and Agrawal (1990) investigated the effect of water content on the ethoxylation rate and found that a 32-fold increase of water content in fatty alcohol resulted in a 22% increase in the reaction rate. They also suggested that the effect of residual water on the reaction rates became insignificant when the water content in a hydrophobic substrate was kept sufficiently low, for example, at 0.04% by weight. Van Os (1998) suggested the water content to be lowered to a level less than 0.1% by weight (Section 2.4.3.4). In our experimental work, it was decided that the water content in the raw materials was removed to a level below 0.05% by weight. When the Karl Fisher analysis showed a water content below this set point in the sample taken at the end of one hour dehydration, it indicated that the dehydration was satisfactorily achieved. Otherwise, further dehydration was necessary until the water content in a sample met the requirement. Once a testing sample showed a satisfactory water level, the vacuum valve was closed and the remaining contents allowed to heat or cool to reaction temperature.

3.4.3 Ethylene oxide addition

Once the temperature stabilised at the desired set temperature for an initiation reaction, ethoxylation was set to commence. For the kinetic study, ethoxylation was to take place at a fixed temperature and pressure so that a reaction rate could be determined.

When the temperature was stabilised at the set value for the initiation in ethoxylating the remaining hydrophobic substrate, the heating or cooling was discontinued. The nitrogen bypass valve was shut and the liquid isolation valve was opened to allow ethylene oxide into the ethylene oxide/input line. The digital balance was switched on and manipulated to obtain zero tare so that any weight loss from the cylinder could be monitored. Ethylene oxide was added into the autoclave by cracking open the ethylene oxide/input valve on the inside panel as shown in Figure 3. 2. Initial additions of ethylene oxide were stepwise, by bringing the reactor pressure from vacuum to the experimental set point. At each of the initial additions, the pressure increase was kept below 50kPa; the temperature was maintained by controlling the exotherm via the internal cooling coil. The stepwise additions prevented the accumulation of a large amount of unreacted ethylene oxide in the system, which could cause possible hazards if the reaction got out of control. When the reactor pressure reached the experimental operational level, the ethylene oxide/input valve was closed. The pressure was allowed to drop and the temperature was maintained constant via cooling. When a pressure drop was observed to be 15-25kPa, further ethylene oxide was added in those amounts that sufficiently compensated for the pressure drop. Time of each injection was recorded, as well as the weight of ethylene oxide added, which was read from the digital balance panel as the loss of weight from the ethylene oxide storage cylinder. Temperature, pressure and ethylene oxide injections were all manually manipulated via the inside panel and the control unit. Temperature variations were controlled to within $\pm$ 2 °C from the preset value.

When the desired amount of ethylene oxide had been added, the liquid isolation valve on the feed cylinder was shut and the nitrogen bypass valve was opened. However, it was estimated that up to 10g of ethylene oxide remained in the flexible hose and the lines leading to the vessel. This remaining amount of ethylene oxide in the line had to be purged by nitrogen via the ethylene oxide/input valve. Repeats of nitrogen purge were necessary to ensure all possible ethylene oxide in the lines was flushed. The ethylene oxide was then allowed to react fully under the additional nitrogen pressure (to 400kPa) from the purging procedure whilst the reaction temperature was maintained. Constant pressure and temperature signalled the end of reaction and the product was ready to be neutralised (see below).

3.4.4 Nitrogen solubility in ethylene oxide

On selected kinetic runs, a study of nitrogen solubility in ethylene oxide was performed prior to the nitrogen purge procedure described above. This nitrogen solubility study was initiated because a positive reactor pressure, stabilised, was observed when all ethylene oxide was allowed to react in completely before the vessel was re-pressurised by nitrogen (the nitrogen purge procedure). Since all ethoxylation runs began at the vacuum, the positive pressure reading indicated that there was an accumulation of an inert gas, most likely nitrogen, in the reactor system. This presence of nitrogen reduced the partial pressure of ethylene oxide when the overall reactor pressure was maintained constant at the reaction set value. Consequently, the rate of ethoxylation was reduced with the decrease of ethylene oxide pressure. In order to accurately evaluate the reaction kinetics, the amount of nitrogen that accumulated with the extent of an ethoxylation process had to be accounted for, and hence the study of the nitrogen solubility in ethylene oxide.

The nitrogen accumulation in the reactor vessel was believed to originate from the ethylene oxide storage cylinder. As described in Section 3.3.1, the storage cylinder of ethylene oxide was normally pressurised by nitrogen to a pressure between 700 and 900kPa. The pressurised cylinder was considered as a system consisting of the binary components of nitrogen and ethylene oxide. Therefore, it was expected that this co-existence of nitrogen and ethylene oxide would establish a vapour-liquid equilibrium within the cylinder. As a result, the nitrogen should dissolve in the bulk liquid of ethylene oxide in the storage cylinder in accordance with its solubility depending on the temperature and pressure. The dissolved nitrogen was then entrained with the additions of ethylene oxide into the autoclave reactor. This nitrogen, inert to the ethoxylation, ended up accumulating in the vapour space of the reactor and exerted increasing pressure with the progress of the reaction as a result of the liquid volume rise.

To obtain the amount of nitrogen accumulated in the reactor, ethylene oxide, after its last addition via the ethylene oxide input/valve, was left to react away prior to repeats of the nitrogen purge. This was needed because repeats of the nitrogen purge of the lines inevitably added further nitrogen pressure into the autoclave reactor, which would be very difficult to be account for. When the reactor pressure reading finally dropped no further and maintained a constant value, it signalled the complete exhaustion of ethylene oxide. This pressure reading simply represented the amount of nitrogen accumulation that originated from its dissolution in the ethylene oxide storage cylinder. This pressure value will be used to derive nitrogen solubility later in Chapter 4. After the pressure was noted, the nitrogen purge procedure was resumed to flush the residual ethylene oxide in the lines and the contents were allowed to complete the reaction, followed by the neutralisation step.

3.4.5 Neutralisation

Before neutralisation, the reactor contents were cooled to 80°C under continuous agitation. The reactor was then evacuated and nitrogen purged three times in the absence of the stirring. This vacuum and nitrogen purge procedure was essential to eliminate any unreacted ethylene oxide in the product prior to opening the sampling line. To neutralise the product, liquid neutralising agents were used which also fully terminated the reaction as described in Equation 2. 19. In this experimental work, acetic acid was used at a molar amount equivalent to the potassium hydroxide. The injection of the equi-molar amount of acetic acid was via the sampling line under the evacuation of the reactor, followed by three vacuum and nitrogen purge cycles to expel oxygen, which might have entered with the acetic acid. Agitation was re-applied and the reactor contents stirred for 15-20 minutes before the product was collected. The product was expelled from the vessel into a pre-weighed container via the sampling line with the vessel pressurised to approximately 200kPa of nitrogen. The product was then weighed and a sample was analysed for its polyethoxylates distribution in a GC column.

3.4.6 Product analysis

The surfactant product obtained from the ethoxylation process was analysed by the GC column that had been set up in the Ascot Vale technical centre, provided that the surfactant product was first derivatised. In a sample vial, a small amount (~2 μl) of the surfactant product was added to dichloromethane, then derivatised by BSTFA+1% TMCS (see Section 3. 2) to replace the active hydrogen atom of the hydroxyl group with a trialkylsilyl group. The derivatised sample was then analysed using the on-column injection capillary gas chromatography under the operating conditions described in Section 3.3.2. Peak areas were identified and inputted into a spreadsheet. The amount of each homologue was calculated as a percentage of the total area. Figure 3. 6 is an example of the GC analysis of nonylphenol ethoxylates, with the specific peaks identified. Various peaks were identified via retention time comparison with standards run under similar conditions.

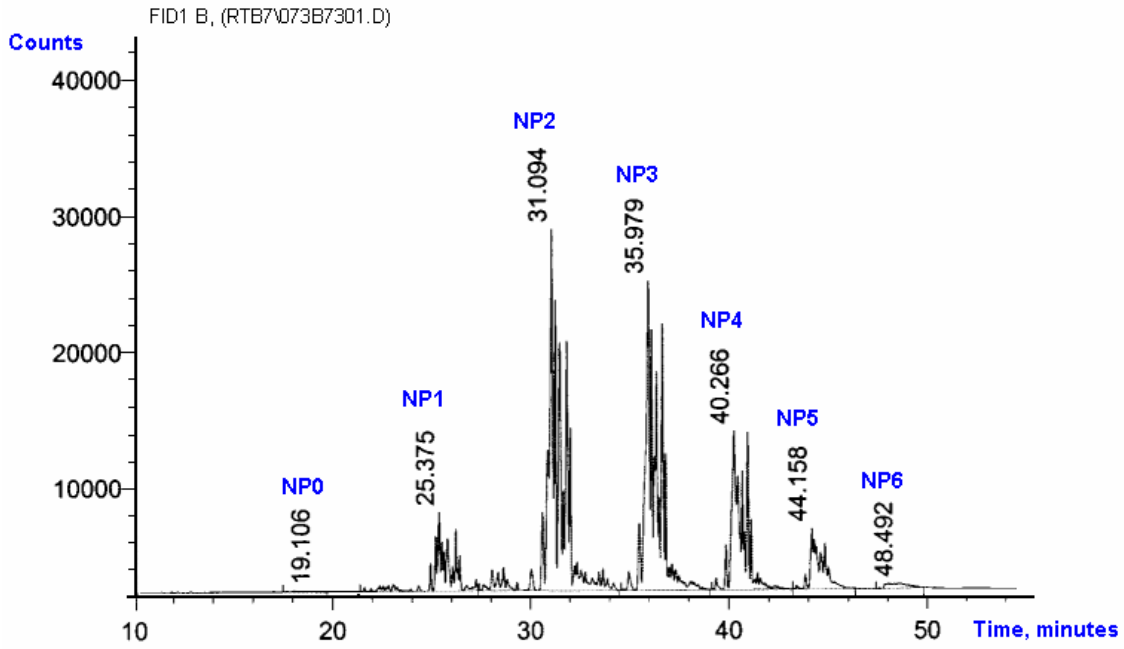

Figure 3. 6 GC analysis of nonylphenol ethoxylates. Peaks assignments: NP0, free nonylphenol; NP1, nonylphenol+1EO; NP2, nonylphenol+2EO; NP3, nonylphenol+3EO and so on with EO denoted to an ethylene oxide molecule.

3.5 Overview of the experimental approach

The intrinsic reaction rate parameters will be represented in the form of the Arrhenius Law. Therefore, the ethoxylation rates are to be measured at various temperatures. In order to obtain reliable reaction rates for the kinetic analysis, ethoxylation is to take place in the regime where chemical kinetics controls. This will be achieved under two conditions: (i) absence of the mass transfer resistance and (ii) low reactor temperature operation (below the lower commercially operating limit of 130°C). A typical ethoxylation run consists of a series of operational procedures described above; each of these procedures needs to be carried out under closely controlled conditions. Thus, a low temperature operation may mean the entire ethoxylation course could stretch into many hours. One way to facilitate ethoxylation rates in the kinetics-control regime so that the experimental measurements could be conducted in a more manageable way was to use a catalyst level that maximised the ethoxylation rate. For this reason, the effect of catalyst concentrations on ethoxylation rates was first investigated.

After the working catalyst concentration above was established, the effect of mass transfer limitation associated with agitation speeds on ethoxylation rates was investigated. A comparison of the ethoxylation rates at the different agitator speeds should point towards an agitation setting with the least resistance to the reaction rate. Neodol 91, a type of fatty alcohol and a common substrate used in the commercial production of nonionic surfactants by HCA, was used in the study of the agitation effect on ethoxylation

rate due to its linear ethoxylation behaviour. The agitation speed determined above was used throughout the kinetic experiments conducted in this present study, along with the working catalyst level previously established.

A detailed experimental plan for the kinetic experiments conducted at low temperatures will be presented in Chapter 4.

3.6 Conclusions

As mentioned in Chapter 1, the first stage of this research project was to experimentally determine the kinetics of an alkaline catalysed ethoxylation in a well-stirred reactor operated by HCA that also served as a validation for the existing kinetic data presented in Chapter 2. Accordingly, the overall experimental approach for the first stage of the project was divided into three parts, such that the rate measurements and acquisition of reliable kinetic data were facilitated. The first determined an optimum working catalyst concentration which best facilitated the ethoxylation rate. The second investigated the influence of several agitation speeds on ethoxylation rate. The third performed kinetic runs at various low temperatures. Chapter 4 presents the results obtained from the above-mentioned program. In particular a full analysis of kinetic data obtained from the experimental approach will be discussed.

Chapter 4

Ethoxylation Results and Kinetic Modelling

4.1 Introduction

The results obtained from the experimental approach described in Chapter 3 are presented and discussed in this chapter. This chapter also aims to develop a useful kinetic model for a well-agitated in-house ethoxylation reactor system used in this research project. To achieve this aim, there were two requirements. These were (i) reliable kinetic data that was obtained experimentally, and (ii) a sound mathematical working model that was developed based on the existing model by Santacesaria *et al*. (1990) and Di Serio *et al*. (1995). This chapter also presents the validation of the experimentally derived intrinsic kinetic rates against the literature published data.

4.2 Ethoxylation experiments results

The details of all experimental measurements for the runs to be discussed in this section are presented in Appendix B. An experimental overview of these runs is given in Appendix B. 1.

4.2.1 Effects of catalyst concentrations

A trial run was first conducted that repeated the operating condition reported by Santacesaria *et al*. (1990) for nonylphenol ethoxylation catalysed by potassium hydroxide at 73°C, except for the reactor pressure. The run used the same catalyst concentration of 0.48% w/w of potassium hydroxide in nonylphenol and the same reactor temperature but a higher reactor pressure. The reactor pressure in this trial run was 1 atm higher than that used by Santacesaria *et al*. (1990) due to the confusion between gauge and absolute pressure value reported in the literature. The experimental measurements obtained from this trial run are reported in Appendix B. 2. At this combination of catalyst level, reactor temperature and pressure, there

was no sign of reaction in the autoclave reactor system of HCA. The experiment was abandoned after 285 minutes because the overall pressure drop observed was only 35kPa as reported in Appendix B. 2. In order to initialise the ethoxylation at low temperature operations and conduct the experiment in a more manageable way in the autoclave reactor used throughout this work, a higher catalyst level was needed. Thus, a series of ethoxylation runs were performed at various catalyst concentrations. Table 4. 1 summarises the operating conditions used for each run in this investigation.

Table 4. 1 Overview of experimental conditions for studying the effect of catalyst concentrations at T= 130°C, P_T = 250kPa and RXH= nonylphenol. The catalyst concentration was based on the weight percentage of the starting RXH.

Run No.	KOH concentration (weight%)	Initial RXH (grams)
cat.1	0.5	513.2
cat.2	0.75	500.0
cat.3	0.825	531.5
cat.4	0.875	540.0
cat.5	0.918	512.0
cat.6	0.983	508.6

All these six experiments were conducted at a constant reactor temperature and pressure of 130°C and 250kPa, respectively; only the catalyst concentration was varied between 0.5 and 0.983% w/w of potassium hydroxide based on the starting nonylphenol. Appendix B. 3 contains details of every addition of ethylene oxide that took place in the ethoxylation runs reported in Table 4. 1. These ethoxylation runs were carried out as far as the initiation step lasted. From the measurements of ethylene oxide addition, an ethoxylation rate of the initiation step was determined which was expressed as the production rate of the mean ethylene oxide adducts per mole of nonylphenol (N_{EO}). The rates obtained with various catalyst concentrations studied are shown in Figure 4. 1.

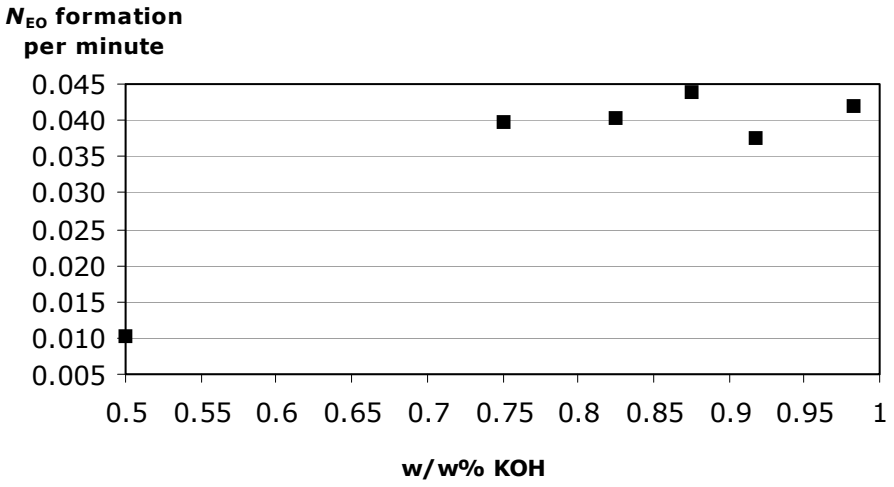

Figure 4. 1 Effect of catalyst concentration on the ethoxylation rate of nonylphenol during the initiation step at T =130°C and P_T=250kPa.

As shown in Figure 4. 1, when the catalyst concentration rose from 0.5 to 0.75% w/w, the rate of N_{EO} formation increased from approximately 0.01 to 0.04 per minute. This increase was nearly four fold. Further increase in the catalyst concentrations from 0.75% w/w to a higher level did not have a significant effect on the measured reaction rates. The reaction rate, in the range between 0.75 and 0.983% w/w, lingered at around N_{EO}=0.04 per minute. This suggested that the ethoxylation rate became less sensitive at a high catalyst concentration than a low concentration. This finding was in agreement with the data of Satkowski and Hsu (1957), who studied the effect of catalyst concentration on ethoxylation rate of C_{13} alcohol, as discussed in Section 2.4.3.3. Consequently, we chose a catalyst concentration at 1% w/w for ethoxylation experiments that were subsequently carried out.

4.2.2 Effect of agitation speeds

As mentioned in Chapter 3, the agitator in the ethoxylation reactor system of the laboratory scale had a working speed between 540 and 1800rpm. To examine the effect of agitation speeds on the reaction rates, a set of ethoxylation runs were conducted, each at different stirring speed that was randomly selected within the working range. Details of the experimental condition for each run are given in Table 4. 2. Appendix B. 4 reports every measurement taken from the runs listed in Table 4. 2.

Table 4. 2 Overview of experimental conditions for studying the effect of agitation speeds on the ethoxylation rate at T = 100°C, P_T = 250kPa, KOH = 1% w/w and RXH = neodol91.

Run No.	Agitator speed (rpm)	Initial RXH (moles)
stir.1	970	3.16
stir.2	1270	3.24
stir.3	1700	3.11

Neodol91 was used as the initiator in this investigation. As discussed in Section 2.4.3.4, the polar nature of an alcohol group remained unaffected during the ethylene oxide attacks on the hydrogen atom. A unique ethoxylation rate was obtained as can be seen in Figure 4. 2. In these experiments, the reactor temperature and pressure were kept constant at 100°C and 250kPa respectively. The ethoxylation rates measured were expressed in mean ethylene oxide adducts per mole of the neodol91 as a function of time. Figure 4. 2 also gives a comparison of the ethoxylation rates of neodol91 at different stirring speeds.

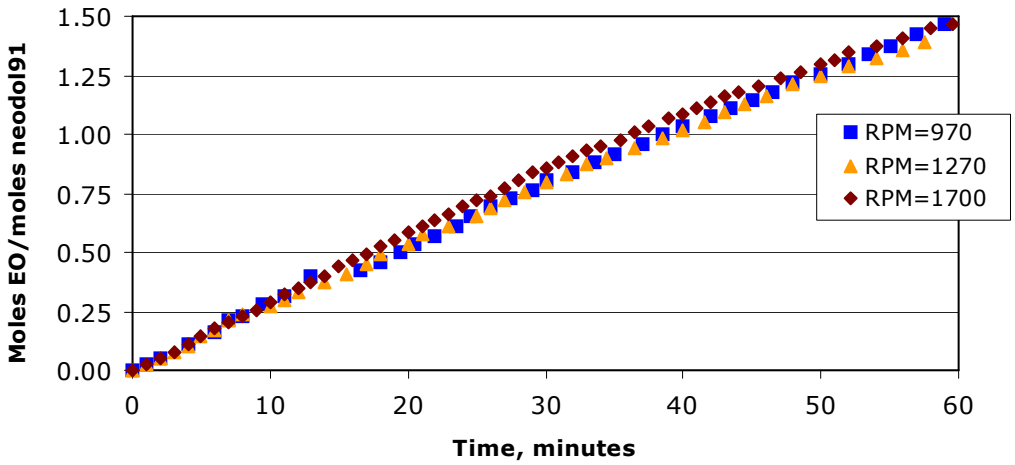

Figure 4. 2 Effect of stirring rates on the ethoxylation behaviour of neodol 91 in the runs performed at T = 100°C, P_T = 250kPa and 1% w/w KOH.

Increasing the stirring speed from 970 to 1700rpm might be expected to lead to a corresponding increase in the interfacial area between the gas and liquid; an increase in the interfacial area should lead to an improvement in the ethoxylation rates. However, this was not observed in this investigation. As shown in Figure 4. 2, the resulting ethoxylation rates did not exhibit a marked improvement with an increase in the stirring speed from 970 to 1270rpm. Further increase of the stirring speed to 1700rpm increased the reaction rate only insignificantly. These results suggested that the rate of ethylene oxide additions was invariant with the stirring speeds above, indicating that the mass transfer resistance was not

influencing the ethoxylation rates. For the subsequent ethoxylation experiments for the kinetic study, the agitation speed was set at 1700rpm.

4.2.3 Kinetic experiments

Kinetic experiments were conducted at a fixed catalyst concentration and stirring speed of 1.0% w/w and 1700rpm, respectively, as determined above. The experiments also needed to be conducted at relatively low temperatures so that the chemical kinetics was the rate-limiting process. Table 4. 3 gives an overview of the operating conditions used for each kinetic run.

Table 4. 3 Overview of experimental conditions for studying the kinetics of nonylphenol ethoxylation. The KOH concentration was 1.0% w/w and the agitator speed was set at 1700rpm.

Run No.	Temperature (ºC)	Total Pressure (kPa)	Initial RXH (moles)
kin.1a	88	251.3	3.16
kin.2a	99.5	251.3	3.24
kin.3a	115	251.3	3.11
kin.4a	125	251.3	2.89
kin.5a	130	251.3	3.07

Repeat runs were also conducted at each temperature. The repetition of each temperature is presented in Appendix B. 1 as runs kin.1b to kin.5b. In Section 4.4.3, analysis of the rate constants derived from both sets of the kinetic experiments will show that the experimental repeatability was consistent. Detailed experimental measurements of all kinetic runs mentioned here are given in Appendices B. 5 and B. 6.

Owing to the non-linear nature of the kinetics (Equations 2. 29 to 2. 32), the determination of the kinetics required the application of a non-linear regression analysis, which will be discussed in detail in the Section 4. 4.

4.3 Results for the Santacesaria base model

As mentioned in the introductory section to this chapter, a sound working mathematical model was required for a full development of the kinetics of base-catalysed nonylphenol ethoxylation. For this reason, the first kinetic modelling was performed to reproduce the literature published results. This exercise allowed us to assess the accuracy of our numerical solutions as well as to gain a level of confidence when it came to modify the existing model to suit our application. These replications of the literature results on the kinetic modelling of nonylphenol ethoxylation are presented and discussed in this section.

As previously discussed in Section 2.5.3.2, the earlier work by Santacesaria *et al*. (1990) used constant ethylene oxide solubility in the computation of the kinetic model. The latter work by Di Serio *et al*. (1995), which improved on the model by Santacesaria *et al*. (1990), took into account the variations in ethylene oxide solubility with the extent of the ethoxylation. Both of the models are examined in this section, nevertheless, the working model developed by Santacesaria *et al.* (1990) serves as a starting point for all kinetic modelling presented in this chapter. For simplicity of the presentation, we present the comparison of the replicated results obtained in this work with two of the literature kinetic experiments, one from each study cited above. In both cases, the mean kinetic parameters reported in the literature (given in Table 2. 3) were used.

4.3.1 Numerical procedures

The rate expressions to be solved for the kinetics of a base-catalysed nonylphenol ethoxylation were given as Equations 2. 29 to 2. 32 in Section 2.5.2. Solutions to these rate expressions gave the concentrations of each polyoxyethylene product and ethylene oxide consumption with time. To solve these kinetic expressions, numerical computation was performed in *Mathematica* 4.2. Figure 4. 3 describes the flowchart of the solution procedures implemented in the numerical model.

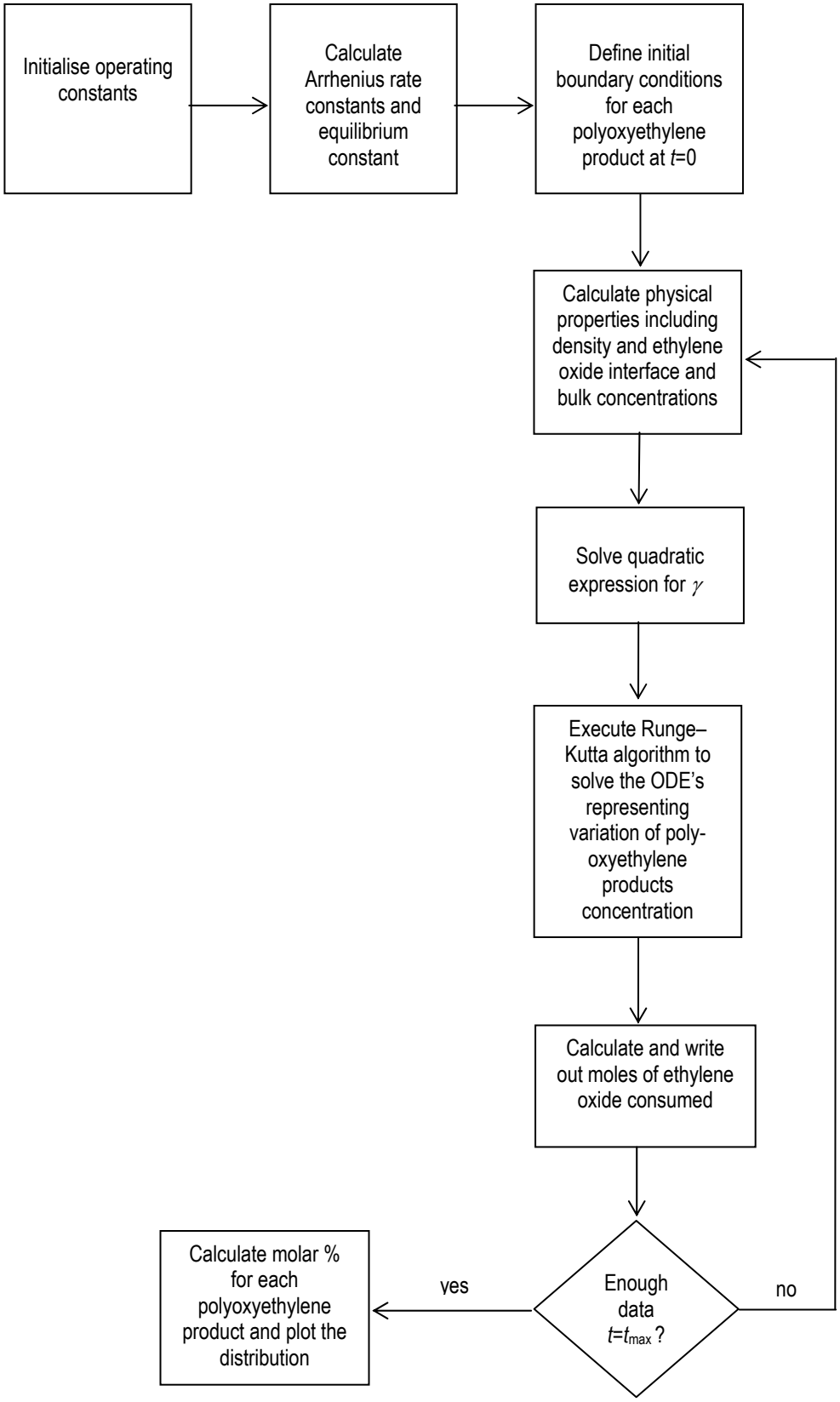

Figure 4. 3 Flowchart depicting the procedures used in the numerical program.

The solution procedures commenced with a program initialisation which input the values of initial reactor operating constants, followed by the calculation of the Arrhenius rate constants, k_i and k_p, and the equilibrium constant Ke_{NP} by the parameters given in Santacesaria *et al*. (1990) (see Table 2. 3). The operating variables included the values for the reactor temperature T, pressure P_T, initial concentration of nonylphenol and potassium hydroxide, R^0 and B^0 respectively, the numbers of polyoxyethylene products n, size of time step Δt, length of reaction time t_{max} and volumetric interfacial mass transfer constant k_La. As Equation 2. 27 for the expression of the bulk ethylene oxide concentration suggested, when the mass transfer resistance was negligible compared to the chemical kinetics, as in the kinetic experiments, ethylene oxide bulk concentration simply corresponded to the ethylene oxide solubility. In this case, the values assigned for the volumetric mass transfer coefficient, k_La, were not crucial in the kinetic computations, however they were chosen to be large enough so that the mass transfer would not become a limiting process.

Following the initiation of the operating constants, the program assigned the initial boundary conditions for each polyoxyethylene product. Then, the program entered a computational loop, within which the variables were updated at the end of each time step. These variables in the loop included the values for (i) density of the polyoxyethylene mixture, (ii) the solubility of ethylene oxide, followed by (iii) the ethylene oxide bulk concentration and (iv) γ, defined in Equation 2. 28 as the concentration ratio of an un-dissociated polyethoxylate to the dissociated ion. These values needed to be defined before the fourth-order Runge-Kutta algorithm was executed to solve the rate expressions (Equations 2. 29 to 2. 32) for each polyethoxylate, which were governed as a set of ordinary differential equations. The program then wrote out the solutions for each polyethoxylate concentration and the amount of ethylene oxide consumed before proceeding to the next time step. The looping routine continued until the total reaction time set in the program initiation was reached. The results were represented graphically: bar charts for a polyoxyethylene distribution or a time-dependant plot for ethylene oxide consumption.

4.3.2 Comparison of results

The simulation performed in the present study for the literature kinetic runs mentioned above is summarised in Table 4. 4.

Table 4. 4 Summary of the literature ethoxylation conditions simulated in the present study.

Experimental data	Temperature (°C)	Total pressure (atm)	KOH* concentration	EO solubility
Santacesaria *et al*. (1990)	73	3	0.48% w/w	constant
Di Serio *et al*. (1995)	130	3	1 mole%	variable

*The catalyst concentration was based on the weight or molar percentage of the starting nonylphenol as indicated.

The computed results obtained from the use of constant ethylene oxide solubility (estimated by the interpolation in Equation 2. 38) are given in Figures 4. 4 and 4. 5. Figure 4. 4 presents the oligomer distribution in the polyoxyethylene mixture as the ethoxylation progressed. Figure 4. 5 plots the average ethylene oxide consumption versus time. Comparison of the results obtained from the simulation in this work with the experimental measurements by Santacesaria *et al*. (1990) is also presented in both figures. The computed results in this work corresponded very well with the experimental data published in the mentioned literature; the difference between the two for the ethylene oxide consumption as a function of time was only marginal (by 2.5% at most). The discrepancy was attributed to the use of the mean kinetic parameters, which had an error range of 10-15% (Di Serio, 1998).

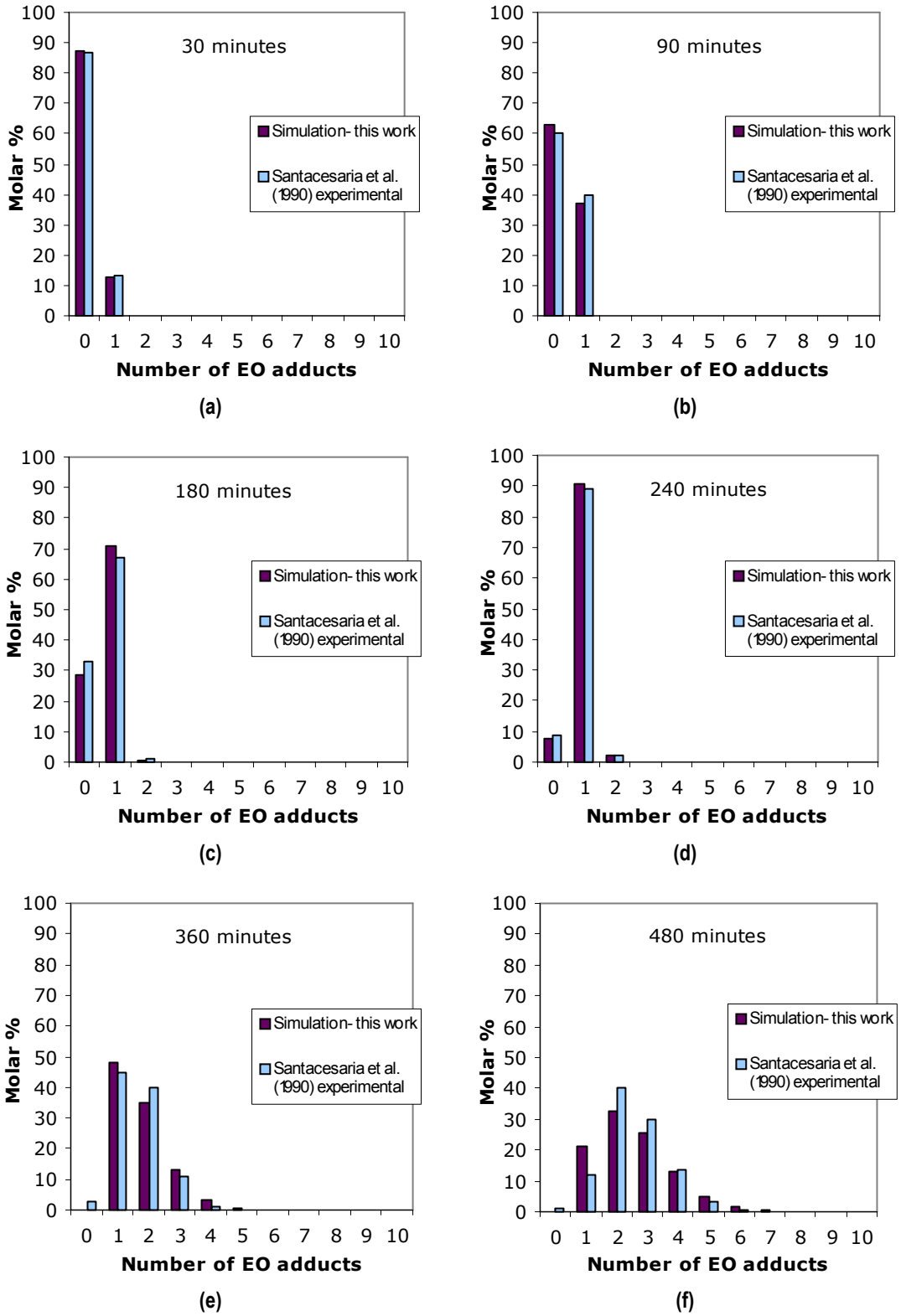

Figure 4. 4 Predicted and experimental polyoxyethylene distributions at different times for products from the reaction of nonylphenol with 2.5 moles of ethylene oxide catalysed by 0.48% w/w KOH at 73°C. The predicted results were computed by *Mathematica* 4.2 in this work. The experimental data was reported by Santacesaria *et al.* (1990).

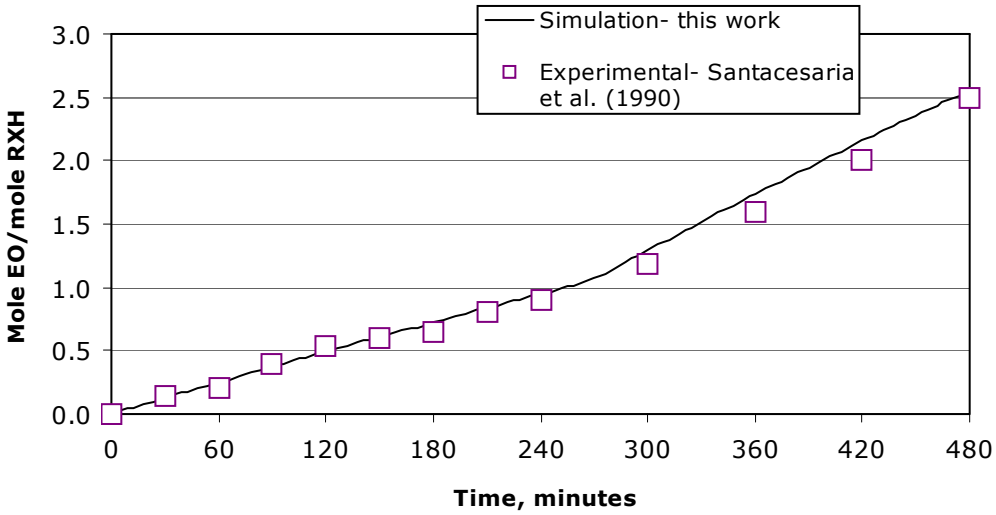

Figure 4. 5 Predicted and experimental ethylene oxide consumption rate for the reaction of nonylphenol with 2.5 moles of ethylene oxide catalysed by 0.48% w/w KOH at 73°C. Solid line is the predicted data computed by *Mathematica* 4.2 in this work. Symbols are published experimental data by Santacesaria *et al.* (1990).

As can be seen in Figure 4. 4(a) to (d), the diminution of the initial nonylphenol substrate contributed significantly to the concentration of the first member in the polyoxyethylene product series only. This indicated the ethoxylation was at the initiation step. Once the initiation reaction was completed at the equi-molar amount of ethylene oxide to the starting nonylphenol, the propagation steps began. The propagation steps gave rise to the production of higher members in the polyoxyethylene product series, each competitively reacted with an ethylene oxide molecule at an equal rate to form the subsequent member. This can be seen in the concentration profile in Figures 4. 4(e) and (f) where the distributions spread into a skewed, bell-shape curve with peaks reflecting the averaged ethylene oxide adduct formed. The propagation steps also had a marked increase in the reaction rate compared to that of the initiation step as shown in Figure 4. 5.

The computation run which updated the ethylene oxide solubility according to the extent of ethoxylation (the case of Di Serio *et al*. (1995)) is presented in Figure 4. 6. The values of ethylene oxide solubility in the reaction mixture at different reaction times were estimated by the Wilson method. Details of the Wilson method were discussed in Section 2.5.3.2. As can be seen in Figure 4. 6, the simulation results obtained by *Mathematica* 4.2 in this work agreed very well with the calculated data in the cited literature for both the ethylene oxide consumption with time and the oligomer distribution in the final polyoxyethylene product. The discrepancy might be explained by the attribution of the mean kinetic parameters used, which had a range of validity of 10-15%.

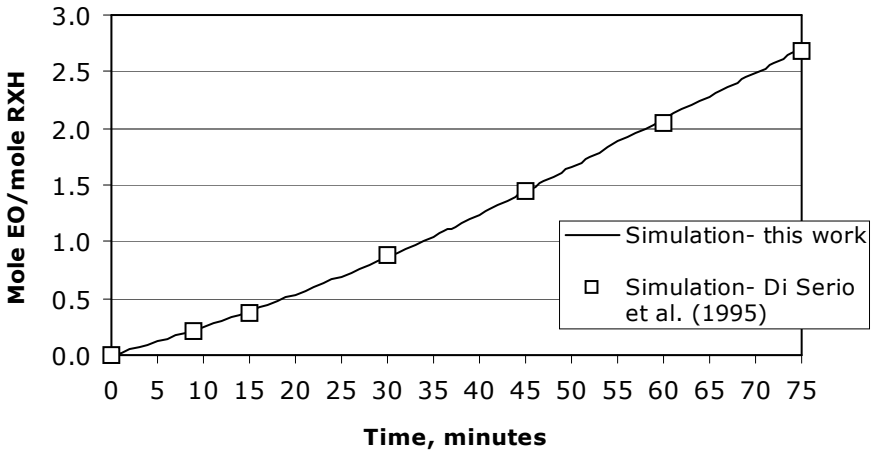

(a)

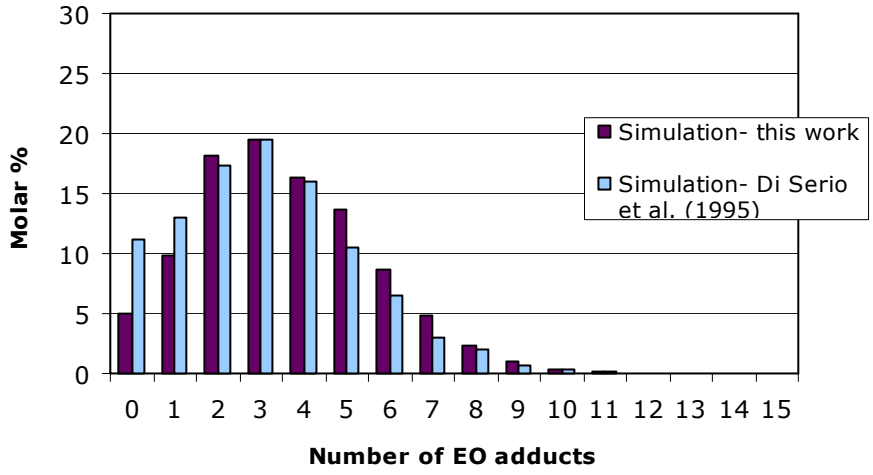

(b)

Figure 4. 6 The predicted results obtained from the simulation in this work and Di Serio *et al*. (1995) for (a) ethylene oxide consumption rate and (b) the final polyoxyethylene product distribution for the reaction of nonylphenol with 2.7 moles of ethylene oxide catalysed 1 mole% KOH at 130°C.

It may be noted in Figure 4. 6(a) that the transition of the reaction rate from the initiation step to the propagation steps at 130°C was not as marked as that at 73°C, observed in Figure 4. 5. The plot of the time-variant consumption of ethylene oxide did not have a prominent change at the equi-molar amount of ethylene oxide to nonylphenol in Figure 4. 6(a). A possible explanation for this was that the polar nature of nonylphenol at higher temperatures was no longer of a much higher acidity than the subsequent polyoxyethylene adducts. Hence, its influence on both the rate of the initiation step and the equilibrium of proton transfer, given in Equation 2. 14, was not as strong as that at low temperatures. Di Serio *et al*. (1995) reported that, at a temperature above 130°C, the equilibrium constant for the proton exchange reaction between nonylphenol and a de-protonated polyoxyethylene adduct had a value of 0.5, as

opposed to >>1 at temperatures below 130°C (Equation 2. 20). The two-stage reaction behaviour was expected to be masked at high temperature ethoxylations.

Based on the existing kinetics from the literature, we have thus far developed a working model in *Mathematica* 4.2 for the kinetic modelling of base-catalysed nonylphenol ethoxylation. The model proved to be a reliable working tool for predicting the time-variant ethoxylation behaviour. The model with the incorporation of the Wilson method for the ethylene oxide solubility as proposed by Di Serio *et al*. (1995) served as a basis for the simulation of the ethoxylation experiments reported in Table 4. 3.

4.4 Analysis of two-litre laboratory autoclave experiments

The analysis of the ethoxylation kinetic data collected from the laboratory autoclave needs to take into account key factors influencing the analysis. In the present study, this refers to the presence of nitrogen.

4.4.1 Nitrogen solubility in ethylene oxide

As described in Section 3.4.4, while all ethoxylation runs performed in the laboratory autoclave began at the vacuum, a positive pressure was observed after all the ethylene oxide added had reacted completely with the reaction mixture. This pressure was ascribed to nitrogen presence due to the thermodynamic equilibrium established between nitrogen and ethylene oxide in the storage cylinder described in Section 3.3.1. Inert to the reaction, the nitrogen continuously accumulated with the additions of ethylene oxide and progressively exerted higher partial pressure as a result of the liquid volume expansion. This increasing nitrogen pressure consequently lowered the partial pressure of ethylene oxide with the extent of the ethoxylation, which in turn, reduced the ethoxylation rate. This aspect of nitrogen presence, though not discussed in any reported literature, was important to the development of an accurate kinetic model for the ethoxylation performed in the laboratory autoclave system used in this research project.

The derivation of nitrogen solubility in ethylene oxide should be confined to the nitrogen amount that was accumulated with the ethylene oxide additions but before any additional amount was used to purge the remaining ethylene oxide in the lines (the nitrogen purge procedure described in Section 3.4.4). This allowed us to establish that the nitrogen present in the reactor vessel before the nitrogen purge procedure originated purely from its dissolution in the bulk ethylene oxide liquid in the storage cylinder. Unless otherwise mentioned, all variables used in the nitrogen solubility derivation referred to the point when, prior to the nitrogen purge, all ethylene oxide was reacted completely and the reactor pressure reading became constant. The positive pressure, described above, thus corresponded to the partial pressure of the dissolved nitrogen. The overall amount of nitrogen (in moles) entering the vessel was deduced from the ideal gas law as follows:

$$n_{N_2} = \frac{P_{N_2} V_G}{RT}$$

4. 1

where P_{N_2} is the partial pressure of nitrogen, which is obtained experimentally, V_G is the volume of the gas occupying the head space of the laboratory autoclave and T is the reactor temperature, which is maintained at the reaction value. The value for V_G was calculated as the difference between the reactor volume, i.e., 2 litres, and the volume of the polyoxyethylene product V_L, where V_L was determined as follows:

$$V_L = \frac{W_L}{\rho_L}$$

4. 2

In this expression, W_L and ρ_L represent, respectively, the total weight and density of the polyoxyethylene product. W_L could be estimated as the summation of total ethylene oxide mass added W_{SUM_EO} and the actual nonylphenol mass that took part in the reaction W_{NP}. That is,

$$W_L = W_{SUM\_EO} + W_{NP}.$$

4. 3

The density of the polyoxyethylene product ρ_L was estimated according to Equation 2. 36 as a function of the average number of ethylene oxide adducts N_{EO} and temperature T. The value for N_{EO}, defined as a molar ratio, was given by the following expression:

$$N_{EO} = \frac{W_{SUM\_EO} / MW_{EO}}{W_{NP} / MW_{NP}}$$

4. 4

where *MW* stands for molecular weight of the substance in the subscript. In the experiments, we recorded the amount of ethylene oxide as the weight withdrawn from the storage cylinder. Although the overall weight withdrawn from the cylinder W_{SUM_CYL} consisted of both nitrogen and ethylene oxide, it was expected that only a fraction of mass was contributed by nitrogen. That is, $W_{SUM\_EO} >> W_{SUM\_N_2}$, the weight of ethylene oxide W_{SUM_EO} was much greater than that of the nitrogen $W_{SUM\_N_2}$. Accordingly, it was assumed that $W_{SUM\_EO} \approx W_{SUM\_CYL}$ and Equations 4. 3 and 4. 4 were transformed into:

$$W_L = W_{SUM\_EO} + W_{NP} \approx W_{SUM\_CYL} + W_{NP}$$

4. 5

and

$$N_{EO} = \frac{W_{SUM\_EO}/MW_{EO}}{W_{NP}/MW_{NP}} \approx \frac{W_{SUM\_CYL}/MW_{EO}}{W_{NP}/MW_{NP}}$$

4. 6

These approximations enabled the evaluation of the liquid volume in Equation 4. 2 and the subsequent calculation of the amount of nitrogen dissolved in ethylene oxide in Equation 4. 1. The amount of ethylene oxide was then deduced by a subtraction of the nitrogen weight $W_{SUM\_N_2}$ from the total weight loss from the cylinder W_{SUM_CYL}. The nitrogen solubility in ethylene oxide $S_{N_2,EO}$, expressed in mass of nitrogen per mass of ethylene oxide, was calculated as:

$$S_{N_2,EO} = \frac{W_{SUM\_N_2}}{W_{SUM\_EO}} = \frac{W_{SUM\_N_2}}{W_{SUM\_CYL} - W_{SUM\_N_2}}$$

4. 7

where $W_{SUM\_N_2} = n_{N_2} * MW_{N_2}$.

Two of the kinetic runs reported in Table 4. 3, kin.4a and kin.5a, were chosen for the nitrogen solubility study. From the steady pressure readings reported in Appendix B. 5, we obtained $S_{N_2,EO}$=0.0025kg N_2/kg EO. This figure was converted to the form of Henry's Law constant. The Henry's Law constant for nitrogen in ethylene oxide at ambient temperature was averaged as 2295 atm/mole fraction from the laboratory autoclave experiments in this work. This value compared very well with the Henry's Law constant (mole fraction) reported by Olson (1977), which, at 25ºC, was 2180 atm. The difference might be attributed to the assumptions made in the analysis above as well as the approximation of the weight quantities involved in the calculations, such as that for W_{NP}. The value for W_{NP} was an approximate estimate because some nonylphenol initially charged was carried over into the catch pot when the reactor was evacuated during the dehydration process (see Section 3.4.2). The majority of this amount was accounted for, but some remained in the catch pot. Collecting the amount of nonylphenol from the catch pot was particularly difficult because the viscosity of nonylphenol at the ambient temperature was relatively high at 1540cp (Table 2. 2).

4.4.2 Base model modification

In order to accurately obtain the kinetic parameters from the experiments performed in this research project, the features observed from the operations in the laboratory autoclave used need to be taken into account. This particularly referred to the presence of nitrogen as it inevitably reduced the partial pressure of ethylene oxide and consequently, the reaction rate. The base model previously developed in Section 4.3.1 was thus modified accordingly. This section presents details of solution routine which transforms the base model to suit HCA's applications, including the commercially operated industrial reactors where additional nitrogen is present due to the initial padding used for safety concerns.

Previously, in the base model developed by Di Serio *et al*. (1995), the vapour phase was considered to be composed of gaseous ethylene oxide only. The partial pressure of the ethylene oxide was simply represented by the total reactor pressure. That is,

$$P_{EO} = P_T$$

4. 8

In the modification of the base model, a reduction of ethylene oxide partial pressure due to the nitrogen accumulation in the vapour space was used:

$$P_{EO} = P_T - P_{N_2}$$

4. 9

It was assumed that the solubility of nitrogen in polyoxyethylene mixture was negligible. P_T is the reactor pressure set point used in the experiments and P_{N_2} is the partial pressure of nitrogen resulted from its dissolution in ethylene oxide $W_{SUM\_N_2}$ and is calculated from the ideal gas law:

$$P_{N_2} = \frac{(W_{SUM\_N_2}/MW_{N_2})RT}{V_G}$$

4. 10

It should be noted that $W_{SUM\_N_2}/MW_{N2}$ represents the number of moles of nitrogen n_{N_2}. However, from Equation 4. 7, we can write

$$W_{SUM\_N_2} = S_{N_2,EO} W_{SUM\_EO}$$

4. 11

which is further deduced in terms of the nitrogen solubility and the cylinder weight recorded from the experiments:

$$W_{SUM\_N_2} = \frac{S_{N_2,EO}}{1 + S_{N_2,EO}} W_{SUM\_CYL},$$

4. 12

since

$$W_{SUM\_EO} + W_{SUM\_N_2} = W_{SUM\_CYL}.$$

4. 13

As Equation 4. 12 shows, the amount of nitrogen accumulated in the vapour space $W_{SUM\_N_2}$ was readily assessable, given that the solubility $S_{N_2,EO}$ had been determined independently (see Section 4.4.1) and the weight withdrawn from the storage cylinder W_{SUM_CYL} was obtained from experimental measurements.

To implement the nitrogen participation derived above, the numerical scheme presented in Section 4.3.1 for the solution of the base model of Di Serio *et al*. (1995) was modified to include the following steps:

- Inclusion of value definition for $S_{N_2,EO}$ in the program initiation.

In the computational loop:

- Transformation of the accumulated weights from the cylinder W_{SUM_CYL} to be a time-dependent function so that an interpolation of weight added could be obtained for quantities between two consecutive additions.
- Evaluation of the cumulative amount of $W_{SUM\_N_2}$ by Equation 4. 11 with the use of interpolated results from the preceding step.
- Calculation of partial pressure of ethylene oxide P_{EO} as described in Equation 4. 9, followed by the Wilson method to calculate the solubility of ethylene oxide in the polyoxyethylene mixture.

4.4.3 Kinetic parameters determination

The rate constants for an isothermal run were determined through non-linear regression analysis on the experimentally measured consumption rate of ethylene oxide, represented in Equation 2. 25. This approach required the information concerning polyoxyethylene distribution at various reaction times during both the initiation step and the propagation steps. The distributions of each polyoxyethylene product would necessarily be obtained by collecting samples of the reaction contents during an ethoxylation run, which were then analysed by gas chromatography for their compositions. This scheme, with the use of non-linear regression analysis, was adopted in the work by Santacesaria *et al*. (1990) and all their related work on ethoxylation. In the above-mentioned literature, the sampling method was not detailed but a sampling device was shown in the schematic illustration of the reactor unit used. It was the understanding of the author of this thesis that a small portion of the reactor contents could be extracted during an ethoxylation run through the sampling device without posing a hazard of ethylene oxide exposure. Contrary to the this method of sampling, extraction of the reactor contents during an ethoxylation run at the laboratory autoclave facility in HCA required a complete (confirmed) clearance of ethylene oxide in the system as the priority concern for health hazards. Therefore, the information on the polyoxyethylene distribution in a surfactant product was only available from the sample collected after ethylene oxide was confirmed exhausted in the system, with the aid of multiple applications of the vacuum and nitrogen purge cycle. Confirmed, complete reaction of ethylene oxide often needed a long reaction time, especially for low temperature operations as can be seen in Appendices B. 5 and B. 6. This would lead to even longer reaction times when samples at several more degrees of substitution were needed to profile the course of the reaction. Sampling in this way was clearly impractical under the current set-up of the laboratory autoclave. With the lack of polyoxyethylene distribution at various reaction times, a graphical fitting method was proposed as our approach for the analysis of the kinetic runs based on the experimental

measurements available to us. Therefore, the rate constants were obtained from the line that best fitted the profile of experimental ethoxylation behaviour, in particular the ethylene oxide consumption with time.

The graphical fitting of the experimental ethylene oxide consumption rates was performed in the extended model developed in Section 4.4.2 with the use of Mathematica 4.2. In this approach, the rate constants k_i and k_p were adjusted from their respective initial guess values until the resulting ethylene oxide consumption rates were fully optimised against the experimental measurements. The initial guess values for k_i and k_p came from the published literature of Di Serio *et al*. (1995); the optimum values established the line of best fit of the averaged ethylene oxide consumption rate that yielded the least residual sum of squares. The residual sum of squares was a measure for the deviations between each data point and its corresponding value on the fitted line.

The ethylene oxide consumption rates collected from runs kin.1a to kin.4a in Table 4. 3 were chosen for the determinations of first, the rate constants at each reaction temperature, then the Arrhenius rate parameters (Equation 2. 34). Run kin.5a was used for validation of the rate constant values so obtained. Figure 4. 7 shows the lines of the best fit obtained from the graphical fitting of the experimental measurements in terms of the averaged ethylene oxide consumption versus time.

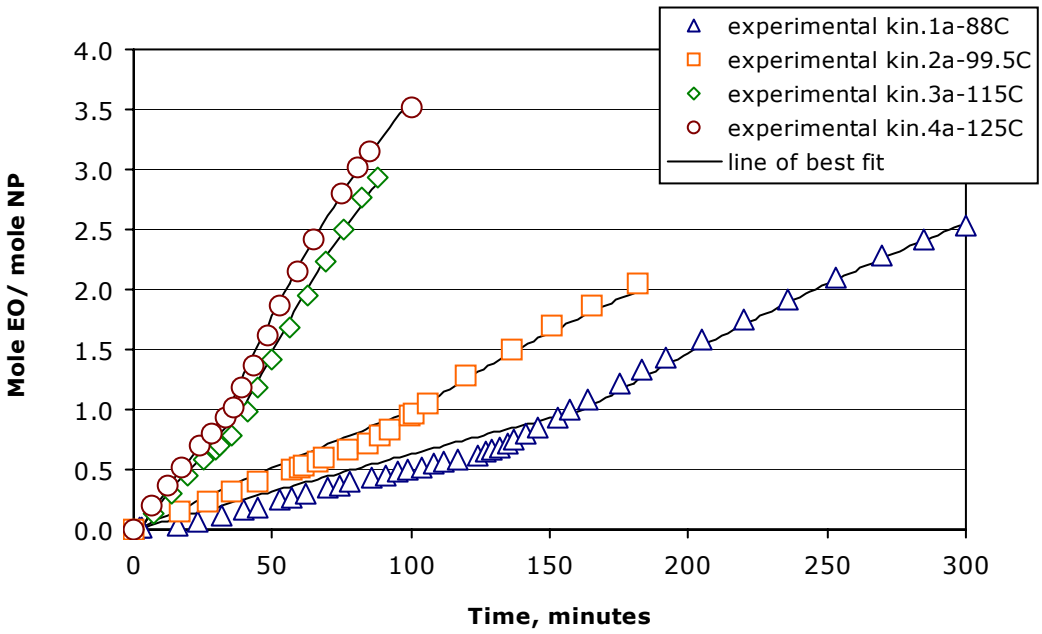

Figure 4. 7 Plot of the experimental measurements and the lines of best fit of ethylene oxide consumption versus time from runs kin.1a to kin.4a reported in Table 4. 3.

As can be seen from the experimental data of the lower temperature runs at 88 and 99.5°C in Figure 4. 7, the onset of the propagation steps occurred at less than the equi-molar amount of ethylene oxide to nonylphenol. This differed from the chemistry suggested (see Section 2.4.3.4). Although the cause of the discrepancy has not yet been identified, it should not deter the graphical fitting approach outlined above for the kinetic analysis, in particular for the higher temperature operations. It is noted in Figure 4. 7 that the discrepancy is not found at the higher temperature runs at 115 and 125°C which are more typical of commercial operation. Thus, the graphical fitting routine for the low temperature runs was conducted with an added constraint which fixed the onset of the propagation steps at the equi-molar amount of ethylene oxide to nonylphenol. In this case, the residual sum of squares was based on the line fitted at the propagation steps only, while at the initiation step, it was allowed to co-exist with large errors as shown in the figure.

Figure 4. 8 plots the polyoxyethylene distribution in the final product obtained from the kinetic modelling with the use of the k_i and k_p values determined from the line of the best fit described above. A comparison of the computed results with the gas chromatography data is also shown in Figure 4. 8. The agreement between the simulated and experimental results was very satisfactory. This suggested that the kinetic model developed was capable of predicting the distribution of a polyoxyethylene product despite the less than satisfactory fits at the low temperatures.

We also noted that a reduction of reaction rate due to the presence of nitrogen was evident in Figure 4. 7. As can been in Figure 4. 7, the experimentally measured ethylene oxide consumption departed from a constant rate behaviour of which it initially displayed at the beginning of either the initiation step or the propagation steps. The data towards the later stage of the reaction step(s) gradually dropped away from a straight line. This was clearly due to the decrease in the partial pressure of ethylene oxide as a result from the accumulation of nitrogen. The effect of this nitrogen pressure on the reaction rates was also accurately reflected in the fitted lines generated from the kinetic model developed in Section 4.4.1. As was discussed in Section 4.4.1, nitrogen that dissolved in ethylene oxide in the pressurised storage cylinder was brought into the vessel with the ethylene oxide feed. Since it was inert to the reactions and its solubility in the reaction mixture was negligible, it continued to accumulate in the vapour space with time. Thus, a decrease in the reaction rates resulted.

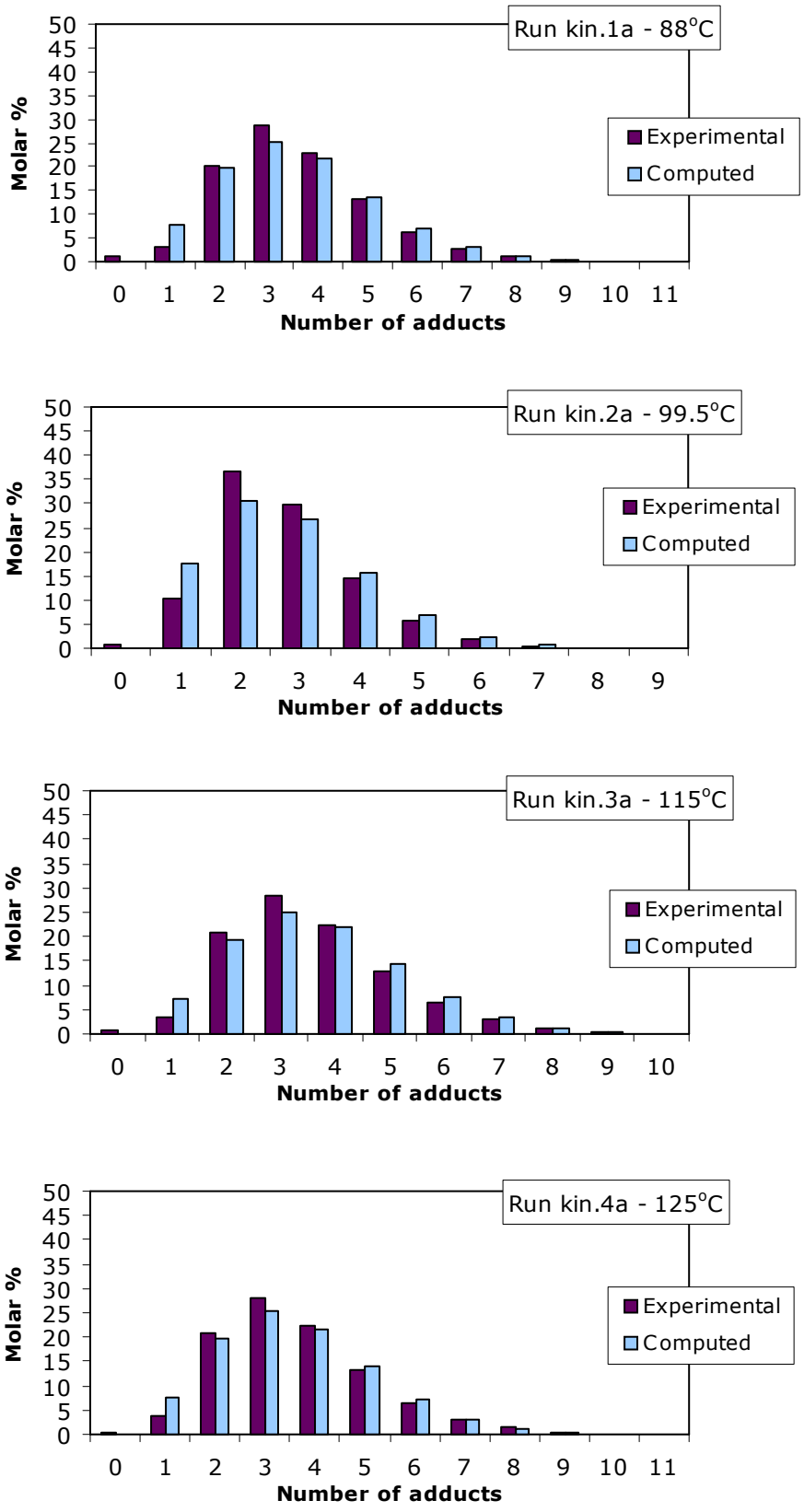

Figure 4. 8 Comparison of computed and experimental molecular distribution of each oligomer in the final product obtained from the reactions reported in Table 4. 3.

Kinetic data obtained by the graphical fitting approach for various isothermal runs was arranged in an Arrhenius-type plot, as shown in Figure 4. 9. From the plot, the mean activation energy and pre-exponential factor were determined from the slope and the y-axis intercept by a linear regression analysis of the data. Table 4. 5 summarises the results of the Arrhenius parameters from the linear regression analysis and compares them to the data of Di Serio *et al*. (1995). The accuracy of these mean parameters for the initiation step and the propagation steps were 10-28% and 5-24% respectively, assessed as the minimum and maximum deviations from the real data. Both the pre-exponential parameter and activation energy for the propagation steps were in good agreement with the published data, while those for initiation displayed some discrepancy. The discrepancy was mainly caused by the poor fits at the lower temperature runs, due to the earlier onset of the propagation reactions.

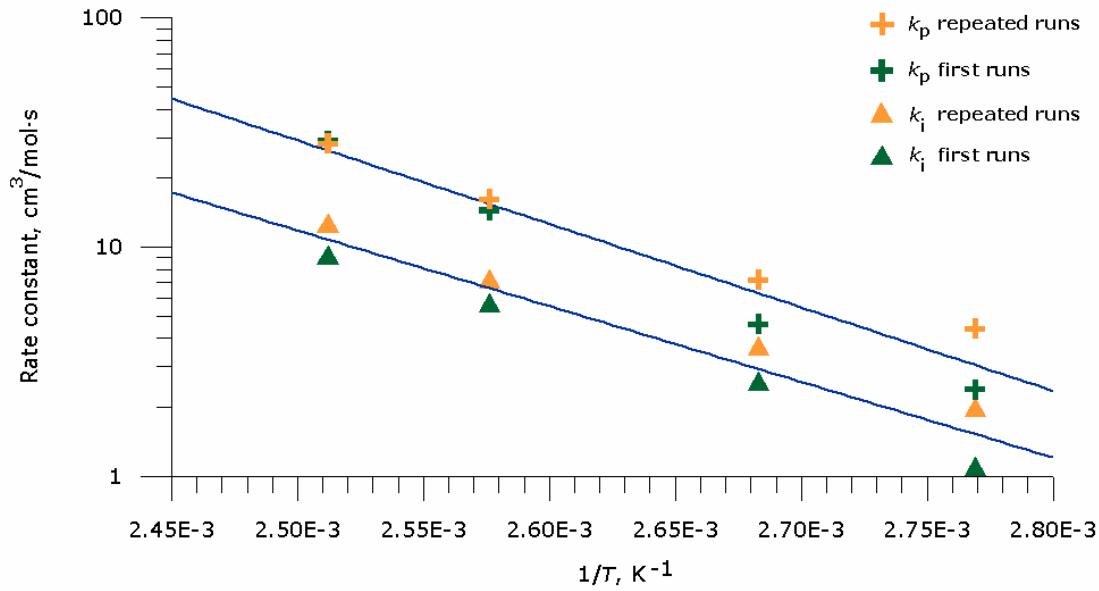

Figure 4. 9 Arrhenius-type plot for the kinetic constants k_i and k_p. Symbols: empirical rate constants. (Δ) for k_i ;(+) for k_p. Colours: green for runs kin.1a to kin.4a reported in Table 4. 3; orange for repeated runs kin.1b to kin.4b reported in Appendix B. 1. Lines: linear regression analysis.

Table 4. 5 Comparison of the experimentally obtained and the literature published kinetic constants. Literature source: Di Serio *et al*. (1995).

	k_i (cm^3/mol.s)		k_p (cm^3/mol.s)	
	LN *A*	*E* (J/mol)	LN *A*	*E* (J/mol)
Experimental	22.7 ± 0.7	(6.8 ± 0.4)×10^4	28.0 ± 0.3	(8.2±0.4)×10^4
Di Serio *et al*. (1995)	26.0 ± 0.3	(7.6 ± 0.2)×10^4	28.7 ± 0.2	(8.1 ± 0.2)×10^4

4.5 Validation

Validation of the kinetic constants obtained from the experiments was performed in two ways. These were the molecular distribution of various ethylene oxide adducts in the final polyoxyethylene product and the ethylene oxide consumption rate. The experimental conditions of the run kin.5a in Table 4. 3 were the inputs of the kinetic model in this validation exercise. At 130°C, as the reaction temperature set in run kin.5a, the rate constants were evaluated according to the mean Arrhenius parameters reported in Table 4. 5 and were 11.1 and 34.0 mol/cm^{3}s for the initiation step and propagation steps respectively. These values were initialised in the working model along with the experimental conditions to compute the ethylene oxide consumption rate and polyoxyethylene distribution. Figure 4. 10 presents the comparison of the computed results with the experimental data. For both the ethylene oxide consumption rate and the polyoxyethylene distribution, the agreement between the computed and experimental data was very good.

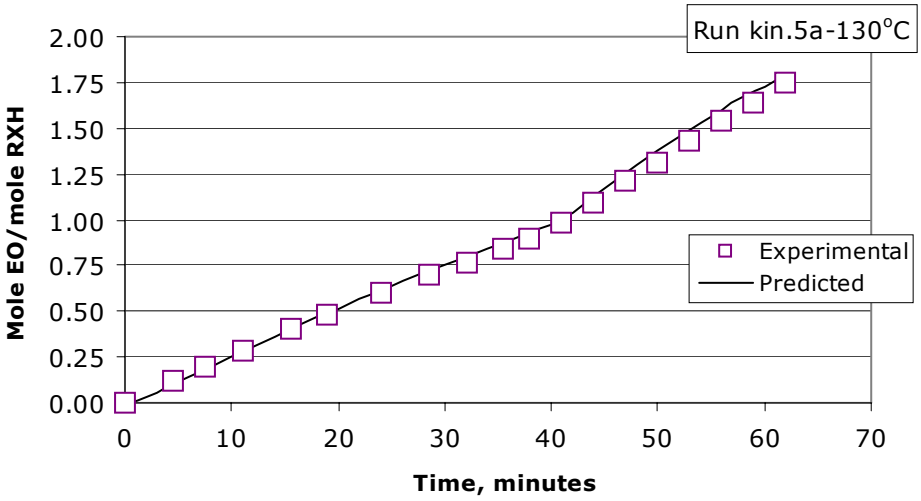

(a)

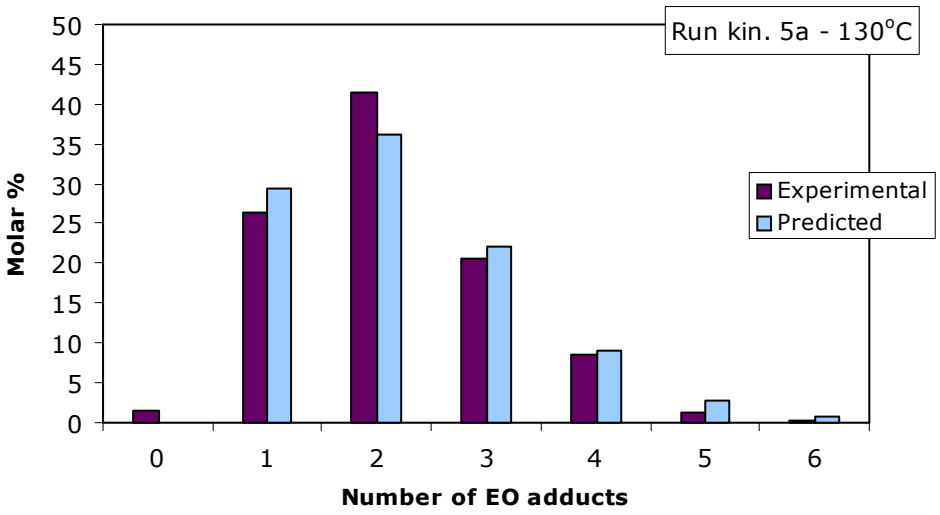

(b)

Figure 4. 10 Comparison of the predicted and the experimental (a) ethylene oxide consumption with time and (b) molecular distribution in the produced polyoxyethylene surfactant. Products of the reaction of nonylphenol with 2.15 moles of ethylene oxide catalysed by 1.0 w/w% KOH at T = 130°C and P_T = 251.3kPa (Run kin.5a in Table 4. 3).

4.6 Conclusions

Further validation of the published kinetic data for a gas-liquid nonylphenol ethoxylation in the presence of a basic catalyst was performed in a laboratory-scale autoclave employed by Huntsman Corporation Australia. Intrinsic reaction rates at four different temperatures between 88 and 125ºC were analysed from the ethoxylation runs conducted in this research project at a catalyst level of 1% w/w to nonylphenol and with the confirmed absence of mass transfer limitation. The intrinsic reaction rates were further expressed in the form of the Arrhenius equation. These experimentally derived Arrhenius parameters compared very well with the literature data. The validity of the experimentally derived kinetics was further established at another temperature (130ºC) for both the ethylene oxide consumption rate and the polyoxyethylene product distribution. This indicated that the modification of the existing kinetic model from the literature was capable of closely describing the reaction behaviour observed from an industrial ethoxylation operation.

The modification referred to the inclusion of nitrogen accumulation in the vapour space of the laboratory autoclave. This was the most important feature differentiating the operation of HCA with the literature described. A positive pressure was observed at the end of the complete reaction of ethylene oxide in an operation, commenced at vacuum, using the laboratory autoclave of HCA. This positive pressure was deduced to arise from nitrogen, which originated from its dissolution in ethylene oxide in the storage cylinder. The observation of nitrogen pressure prompted the further development of the existing kinetic model to incorporate the solubility of nitrogen in ethylene oxide such that the kinetics was correctly evaluated as presented above.

The experimentally obtained kinetics and the existing kinetic model with modification to include the nitrogen solubility have now been integrated into a rigorous kinetic model, established to suit HCA operations. This model allows the intrinsic kinetic rates to be realised in the industrial-scale reactors and will be incorporated to describe the chemical reactions in a computational fluid dynamic model to be developed as the next stage of this research project.

Part II

Process Optimisation and CFD Simulations

Chapter 5

Mixing Vessel Flow Dynamics and CFD Literature Review

5.1 Introduction

As outlined in Chapter 1, this research project on modelling the ethoxylation in the batch NIS A reactors of Huntsman Corporation Australia (HCA) involving catalysed chemical reaction and the phenomena of mass, heat and momentum transfer was carried out in two stages. Chapters 2 to 4 presented the first stage, namely the kinetic modelling of base-catalysed alkylphenol ethoxylation. In the first stage, the chemical kinetics of the ethoxylation, determined using an in-house laboratory reactor of HCA, was further developed into a comprehensive and rigorous kinetic model. In the second stage, the interaction of the chemical kinetics, particularly the full-scale operations, and the physical processes is to be explored. Understanding the interaction between chemical and physical processes will allow us to rationalise the design of a commercial stirred ethoxylation reactor and provide a perspective for any improvement of the productivity. The physical processes to be investigated in the second stage will include transfer of mass and heat. The former involves aspects of mixing of the reaction contents; the latter relates to heat removal by means of cooling water coils.

Mixing accelerates the rates of transport processes and reactions occurring in the vessel (Ranade and Joshi, 1989a). Mixing of the reaction contents in NIS A reactors is achieved by means of mechanical agitators. HCA had established that, under the same operating conditions, the ethoxylation rates displayed noticeable differences between two NIS A reactors of identical vessel size and design, however equipped with different types of impellers. In addition, as described in Chapter 1, HCA had also established that the ethoxylation rates in a laboratory-scaled autoclave were higher than those of the industrial-scaled NIS A

reactors, though the autoclave was perceived to be running under significant mass transfer control. However, it was not known if mixing was the factor causing the observed differences. The classic method to determine if mixing was an important process variable was to change the impeller rotation speed and record the change in the process result. Other methods to determine the importance of mixing were to change the feed rate and location, any sparging or recycle rates, and power distribution in the process (Tatterson, 1994). Experimental investigation of such changes in commercial reactors is expensive, time consuming and sometimes impossible. Recent advances in numerical simulation, such as computational fluid dynamics (CFD) techniques, provide an alternative to detailed experimental investigation with a proven ability to delineate complex flow behaviours in a mechanically agitated vessel.

This chapter begins with basic concepts for fluid mixing that will help to understand the nature of hydrodynamics of different impeller types, in particular the interactions between dual impellers used in most of the NIS A reactors. It then presents an assumption concerning the major phases involved in the ethoxylation process in both the autoclave and NIS A stirred reactors with reference to the current mode of operation employed by HCA. This will help to classify the mixing operations to be examined in the present reactors of HCA. Accordingly, literature data available for examining impeller performance is summarised and compared. The chapter also presents various CFD techniques available for simulations of a stirred vessel with turbulence and chemical reactions.

5.2 Basic concepts for mixing

Mixing is the contacting mechanics by which materials are brought together to obtain or achieve a process objective, for example, to obtain a mixture, cause mass transfer, effect a chemical reaction, obtain an emulsion, or transfer oxygen to micro organisms. As such, mixing is an integral part of the infrastructure of the chemical, petrochemical, and biochemical industries (Tatterson, 1994).

5.2.1 Applications

Table 5. 1 lists some of the major modern applications of mixing.

Table 5. 1 Mixing processes (Oldshue and Herbst, 1990).

Physical Processing	Application Class	Chemical Processing
Suspension	Liquid-Solid	Dissolving
Dispersion	Liquid-Gas	Absorption
Emulsification	Immiscible liquids	Extraction
Blending	Miscible liquids	Reactions
Pumping	Fluid motion	Heat Transfer

A number of distinctive types of mixers have been developed over the years to accomplish such a range of duties efficiently. These include mechanically agitated vessels, jet mixers, in-line static mixers, in-line dynamic mixers, dispersion mills, valve homogenisers, ultrasonic homogenizers and extruders (Harnby *et al*., 1985). This research project is concerned with the manufacture of nonionic surfactants in a mechanically agitated vessel. This type of mixing situation is discussed in further detail in the next section.

5.2.2 Typical arrangement of a stirred vessel

Stirred tanks are extensively used by chemical, pharmaceutical, food and water treatment industries during the manufacture of paints, polymers, detergents, drugs, food-stuffs and during the purification of industrial and household waste (Ciofalo *et al*., 1996). The processes range from simple fluid mixing to complex multiphase interactions of gas-liquid or gas-liquid-solid. A typical configuration of a mechanically agitated vessel is illustrated in Figure 5. 1. Basic components of a mechanically agitated vessel include a vessel, baffles and impeller(s). The following briefly covers the main features of the component items and variables associated with fluid mixing.

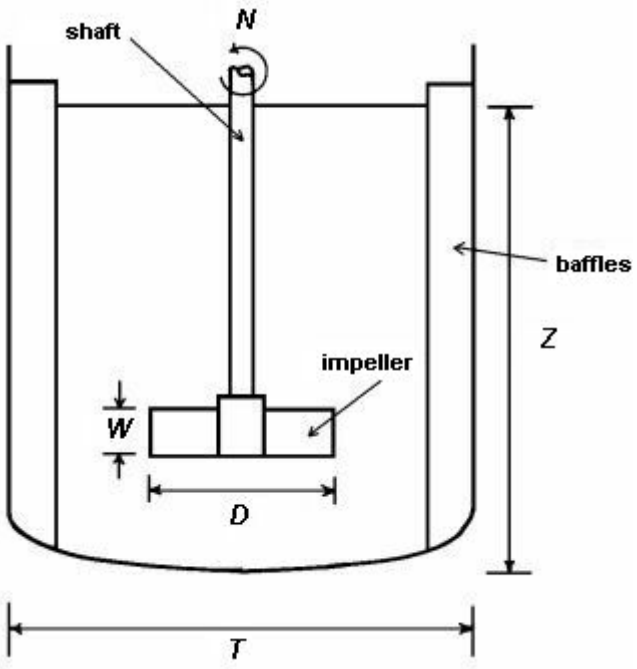

Figure 5. 1 Typical arrangement for a mechanical agitated vessel (Harnby *et al.*, 1985).

The vessel is typically a vertical cylindrical tank with tank bottom flat, dished, conical or spherical. In general, the best tank design has the ratio *Z*/*T* of the static liquid depth *Z* to the tank diameter *T* in the range of 1.0 to 1.2 (Oldshue and Herbst, 1990). Multiple mixing impellers are used when the ratio *Z*/*T* was greater than 1.2.

Baffles are flat metal plates, typically four in number, located 90° apart and mounted or suspended with a small clearance to the vessel wall. The width of a baffle is normally equivalent to one-tenth or one-twelfth of the tank diameter; the length extends vertically down the straight side of the tank. Without baffles, the entire liquid body may swirl with a rotary pattern in which very little real mixing takes place. Furthermore, the vortex formed in the absence of baffles might incorporate air bubbles leading to an undesirable chemical effect (e.g. oxidation) or undesirable physical effects (e.g., frothing, foaming) (Oldshue and Herbst, 1990). Installation of baffles effectively changes the flow from a rotary, which is essentially static, to a mixing pattern and inhibits excess swirling, vortex formation and air induction. Baffles also assure that the entire batch passes through the zone of the impeller where the steepest velocity gradients occur (Oldshue, 1983). Moreover, baffles promote stronger axial flows, leading to an improved mixing rate (Ciofalo *et al.*, 1996).

Impellers of a mixing vessel are usually mounted on a central vertical shaft inside the vertical cylindrical tank. Defined as widely used notations, *D* denotes the impeller diameter, *w* impeller width and *C* the impeller distance from the tank bottom to the horizontal centreline of the impeller blades. The most fundamental function of a mixing impeller is to dispense all the power *P* supplied to create a quantity of

flow and an impeller head or shear rate (Oldshue, 1983). The flow rate, Q_p, refers to the primary pumping capacity of the mixing impeller, which controls the circulation rate throughout the vessel. The terms "head" and "shear", referred to as *H'*, are used interchangeably in fluid mixing technology. *H'* is proportional to the velocity head of the fluid, which is dissipated on circulation through the vessel. For low-viscosity liquids the head can be considered in terms of turbulence generated (Harnby *et al*., 1985). Turbulence is found to be most intense in the region of the impeller and decays in the regions away from the impeller. The regions with high intensity of turbulence are well suited for dispersive mixing processes, such as liquid-liquid, gas-liquid contacting as well as for generation of good conditions for mass transfer, so called shear-controlled operations. While shear-controlled operations require the generation of large turbulent shear stresses for dispersion, flow-controlled operations require a strong circulation throughout the vessel with a minimum amount of fluid shear. Examples of flow-controlled operations include blending, solid suspension and heat transfer (Oldshue and Herbst, 1990). Thus, all mixing operations require some degree of both turbulence (head) and circulation (flow). Good impeller selection, as Harnby *et al*. (1985) described, ensures that the power input to the agitator provides the correct balance between flow and fluid shear.

A brief description of the commonly used impellers and their resulting flow patterns is given in the following section.

5.2.3 Types of mixing impellers and the flow patterns

Mixing impellers in common use include propellers, turbines, paddles, anchors, helical ribbons and helical screws (Harnby *et al*., 1985). In general, mixing impellers can be divided into two broad categories - axial flow impellers and radial flow impellers (Oldshue, 1983). Their typical primary flow patterns are illustrated in Figures 5. 2 and 5. 3 respectively.

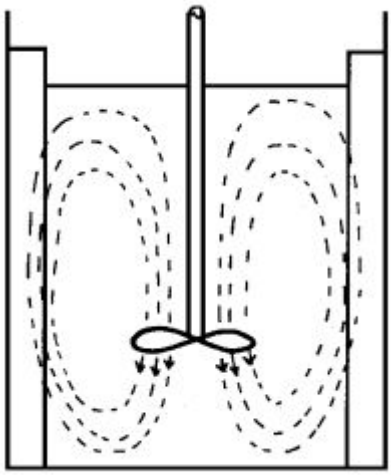

Figure 5. 2 Flow pattern for a downward pumping axial flow impeller (Harnby *et al*., 1985).

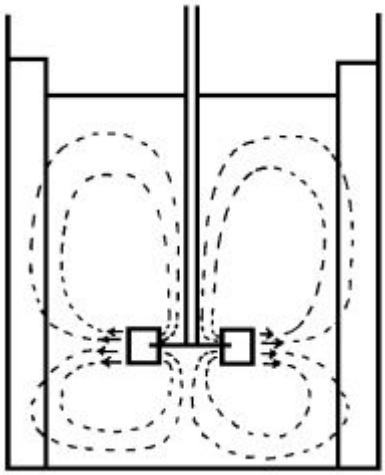

Figure 5. 3 Flow pattern for a radial flow impeller (Harnby *et al*., 1985).

The flow profiles shown in the above figures are the conventional representations given in classic fluid mixing texts (e.g. Oldshue, 1983; Harnby *et al*., 1985; Uhl and Gray, 1986). In a recent review on the experimental techniques for flow visualisation in stirred vessels, Mavros (2001) suggested that with the use of more sophisticated techniques for the study of the flow patterns induced by various types of agitators, the visualisation of the flows at various parts of the vessel led to the re-definition of the "standard" flow patterns presented above. For example, the use of novel flow mapping techniques, such as laser Doppler velocimetry (LDV), showed that axial impellers left a substantial part of the fluid in the upper part of the vessel poorly agitated, where the velocities were often lower than 10% of the agitator tip speed (Mavros *et al*., 1996). Ensemble measurements by the LDV technique also showed that with a radial impeller, the upper circulation loop was narrower than expected and the jet emerging from the turbine was not symmetrical but slightly skewed upwards (Mavros *et al*., 1996). In addition, Marvos *et al*. (1996) observed that the fluid in the region near the upper vessel walls was agitated in a secondary flow loop as shown in Figure 5. 4. Nevertheless, circulation patterns such as those in Figures 5. 2 and 5. 3 are useful in establishing the dead and active zones and serve as a first indication of the suitability of an impeller for a particular given duty (Harnby *et al*., 1985; Mavros, 2001).

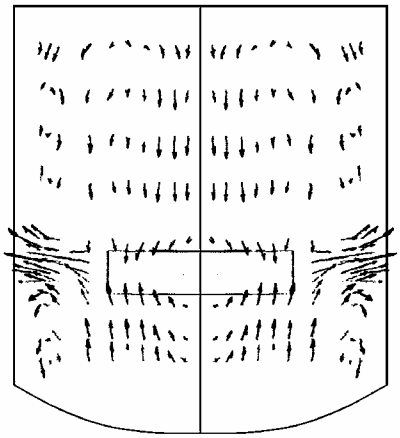

Figure 5. 4 Illustration of the departure of "standard" from actual flow pattern: flow pattern determined by LDV (Mavros *et al*., 1996; Mavros, 2001).

The flow pattern in a stirred vessel is a function of the internal vessel configuration, such as baffles, coils, vessel bottom shape and fluid properties including viscosity, number of phases and density. It also depends on the impeller-to-the-tank geometry configurations and flow regime (Ibrahim and Nienow, 1995; Mavros, 2001). It should be mentioned that the velocities at any point are three-dimensional and unsteady.

5.2.3.1 Axial flow impellers

Axial flow impellers produce a principal direction of discharge which coincides with the axis of impeller rotation. As shown in Figure 5. 2, a single circulation loop emerges from lower surface of the impeller, toward the bottom of the tank, up the side walls to the upper part of the tank, and back to the impeller through the core of the tank. This axial flow can be upwards or downwards depending on the direction of rotation. These axial flow impellers produce a large circulation with more flow per horsepower than radial flow impellers and are generally suited to flow-controlled operations, such as solid suspension and mixing of miscible liquids. Examples of axial flow impellers include the pitched-blade turbine (PBT), marine-type propeller (A100), the high-efficiency axial flow impeller (A310, A315) and helical impellers. Figures 5. 5 and 5. 6 show some of the axial flow impellers used in the NIS A reactors employed by HCA; a six-bladed, 60° pitched blade turbine (Figure 5. 5), and dual Lightnin A315 impellers (Figure 5. 6).

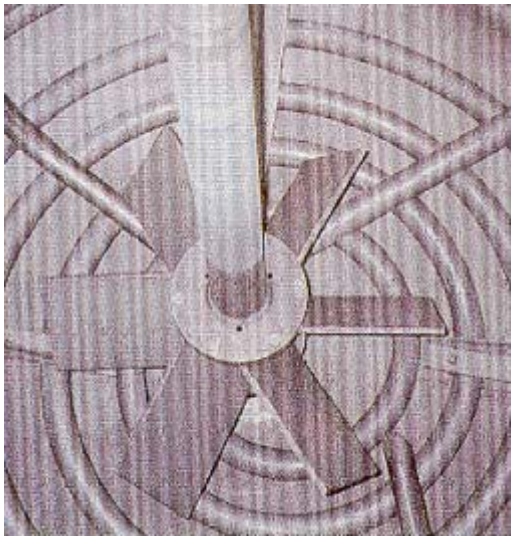

Figure 5. 5 A 60° pitched blade turbine.

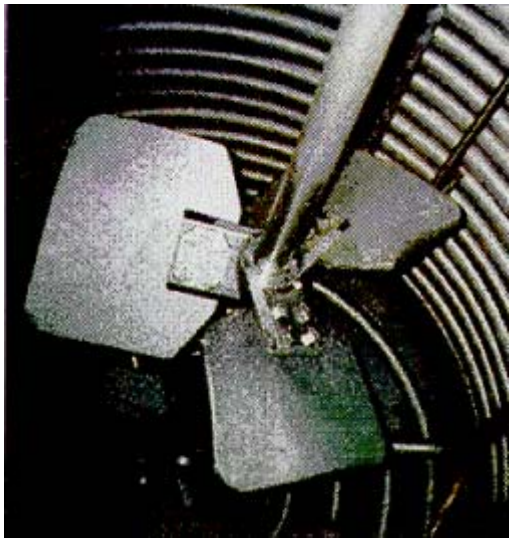

Figure 5. 6 A dual-Lightnin A315 impeller.

The A315 axial flow impeller was developed to solve the problem of flooding, the main obstacle which traditionally prevented the use of axial flow impellers for high gas rate application, as noted by Oldshue (1989). Experimental data with an A315 impeller to this date are scarce as they are seldom reported in the open literature. Therefore, the following review on axial flow impellers mainly focuses on the standard pitched blade turbines for which experimental measurements on the flow field have been more extensively reported. However data on the A315 will also be discussed where available.

Studies have shown the flow pattern induced by PBTs was strongly affected by the impeller Reynolds number or impeller speed, e.g. Nouri and Whitelaw (1990), Hockey and Nouri (1996), Shafer *et al*. (1998), and the impeller clearance, e.g. Jaworski *et al*. (1991), Kresta and Wood (1993), Mao *et al.* (1998). The Reynolds number for Newtonian fluids in mechanically agitated vessels is defined as

$$Re = \rho N D^2 / \mu \,, \qquad \textbf{5. 1}$$

where ρ and μ are density and dynamic viscosity of the fluid, N is the impeller rotational speed in revolutions per second (rps) and D is the impeller diameter. Flow in the tank is turbulent when Reynolds number is greater than 10,000; laminar when Reynolds number is below 10. Between Reynolds numbers of approximately 10 and 10,000 is a transition regime in which flow is turbulent at the impeller and laminar in remote parts of the vessel (Perry and Green, 1984).

Nouri and Whitelaw (1990) and Hockey (1990) observed that with 45° and 60° PBTs, the impeller stream changed direction with decreasing *Re*, from primarily axial to primarily radial flow at Reynolds numbers of 490 and 650 respectively. At these lower Reynolds numbers, Nouri and Whitelaw (1990) and later Schafer *et al*. (1998) also observed a second recirculation along the vessel bottom toward the axis.

The strength and size of the secondary loop was found to decrease with increasing *Re*. Using double the impeller size of the earlier investigations while the impeller tip velocity ($U_{tip} = \pi ND$) was kept the same, Hockey and Nouri (1996) observed the abrupt transition in the flow pattern from a radial to an axial flow with 60° PBTs at the Reynolds number of 1200. This observation indicated that the dependency of the flow transition on Reynolds number had a direct proportionality to the impeller size. A further note by Schafer *et al*. (1998) added that at the *Re* around the transition from radial to axial flow, the impeller discharge flow direction was unstable, varying from radial to axial; at *Re*>2,300, the flow pattern was primarily axial.

Impeller clearance from the bottom of the vessel was also an important factor affecting the flow patterns in the stirred vessels with PBTs, as was observed by Jaworski *et al*. (1991); Kresta and Wood (1993), and Mao *et al*. (1998). Jaworski *et al*. (1991) examined the flow pattern with a single PBT of diameter *D*=*T*/3 with four blades at two clearances (*C*=*T*/2 and *C*=*T*/4) and concluded that the off-bottom clearance strongly influenced the circulation patterns in the region below the impeller. Kresta and Wood (1993) characterised the impeller discharge stream and bulk circulation flow produced by a 45° PBT with two impeller diameters, *D*=*T*/2 and *D*=*T*/3, and with the impeller clearance systematically varied from *C*=*T*/20 to *C*=*T*/2. They found that with the large impeller *D*=*T*/2, the formation of a strong secondary circulation loop at higher clearance displaced the impeller discharge stream, changing the axial velocity profile, and increasing the radial velocity (Since the graphical representation of this flow pattern transformation in Kresta and Wood (1993) was given, other than the mean velocity vectors in a vertical plane, the graphical representation in Mao *et al*. (1998) was used instead. See Figures 5. 7 (a) and (b)). In addition, Kresta and Wood (1993) also found that the distinct transition of the PBT flow field occurred at a *C*/*D* ratio of 0.6. The angle of the flow discharge changing from the axial toward the radial direction, however, was not observed in the small impeller *D*=*T*/3: the secondary circulation loop was not as strong, and did not affect the angle of the impeller discharge (see Figure 5. 7 (c)). Mao *et al*. (1998) also observed that the occurrence of the secondary circulation loop deflected the discharge angle toward horizontal of the flow generated by both four- and six-bladed 45° PBTs of *D*=*T*/2 and *C*=*T*/2.

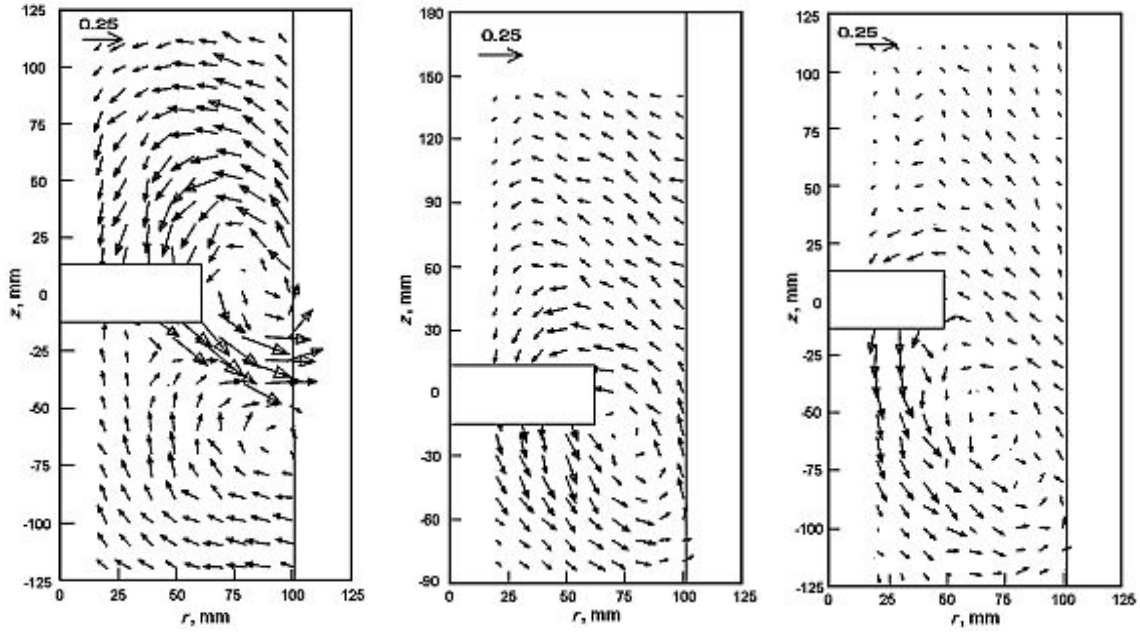

Figure 5. 7 Mean velocity V_{rz} vectors in *r-z* plane generated by a 45° PBT impeller: (a) *D*=*T*/2, *C*=*T*/2; (b) *D*=*T*/2, *C*=*T*/3; (c) *D*=*T*/3, *C*=*T*/2 (Mao *et al*., 1998).

The turbulent flow generated in a vessel stirred by two PBTs was characterised using laser Doppler anemometer (LDA) measurements by Mishra *et al*. (1994). The two impellers were both mounted on the same shaft, each with a diameter of *D*=*T*/3, and operated in the down-pumping mode. Two flow patterns were observed with respect to the impeller clearance between the two PBTs. At closer impeller clearances where the impeller clearance was less than the impeller diameter, only one circulation loop was formed around both the PBTs. The down-flowing liquid from the upper impeller entered the suction part of the lower impeller; the overall flow pattern remained similar to that of a single PBT. When the clearance between the two impellers was increased to above 1.5*D*, the impellers behaved independently from each other. That is, each PBT formed its characteristic single loop flow pattern, resulting in two circulation zones for overall flow pattern in the vessel.

The dual-Lightnin A315 impeller used in the surfactant plants of HCA at Botany have a diameter of *D*=0.44*T*. The clearance between the two impellers is *C*=1.1*D*. According to Mishra *et al*. (1994), this was likely to form a single-loop circulation since the separation was much below 1.5*D* but close to the impeller diameter.

5.2.3.2 Radial flow impellers

Radial flow impellers create a strong flow outwards from the impeller that is normal to the axis of impeller rotation as shown in Figure 5. 3. This flow characteristic creates two circulation zones, above and below the impeller. The strong discharge flow from radial impellers generates high shear stresses and turbulence

in that region. Hence, radial flow impellers are suited to shear-controlled operations, e.g., dispersive mixing processes. Examples of radial flow impellers include disc turbine (Rushton) and anchor. A standard Rushton turbine consists of six flat blades and is widely used in industrial applications, particularly in the chemical industry (Harnby *et al*., 1985). The disc turbine employed by HCA is shown in Figure 5. 8. It is a set of dual Rushton impellers, each with 18 flat blades. Disc turbines with 12 or 18 blades were recommended particularly for gas-liquid stirred vessel (Harnby *et al*., 1985).

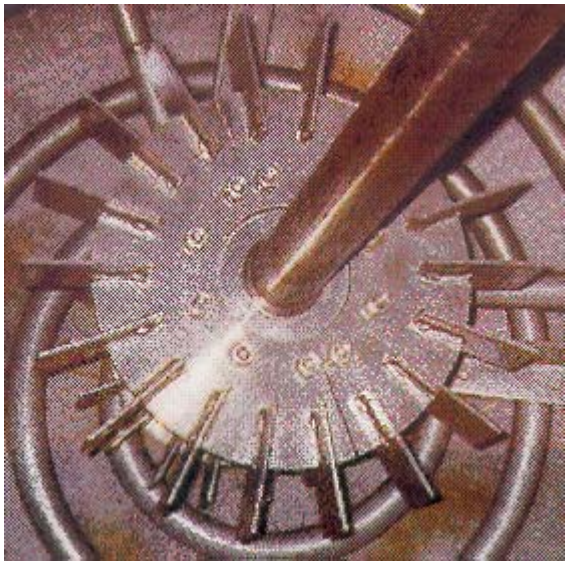

Figure 5. 8 The Rushton impeller employed by HCA.

The type of flow pattern generated by a radial-flow impeller can be altered by changing the impeller geometry, for example, reducing the impeller clearance. By decreasing the standard clearance of $C=T/3$ to $0.2T$ or less, the Rushton characteristic double-loop flow pattern was observed to undergo a transition to a single-loop one (Ibrahim and Nienow, 1995; Armenante *et al*., 1998; Montante *et al*., 1999); the impeller stream direction became partly axial and inclined at around 25 to 30° to the horizontal (Montante *et al*., 1999). This phenomenon was first reported by Nienow (1968) (as cited by Montante *et al*. (1999)), who observed that reducing the impeller clearance to $T/6$ caused the stream emerging from the impeller to dip towards the tank corner.

The flow induced in vessels stirred by two standard Rushton impellers was strongly dependent on the clearance of the lower impeller above the base of the vessel ($C1$), the separation between the impellers ($C2$), and the submergence ($C3$) of the upper impeller below the top of the liquid column height (Z) as reported by Mahmoudi and Yianneskis (1992) and Rutherford *et al*. (1996a). Three distinct stable flow patterns were observed with the variations of these distances. They were: parallel, merging and

diverging flow patterns as shown in Figure 5. 9 (Hudcova *et al*., 1989; Mahmoudi and Yianneskis, 1992; Rutherford *et al*., 1996a).

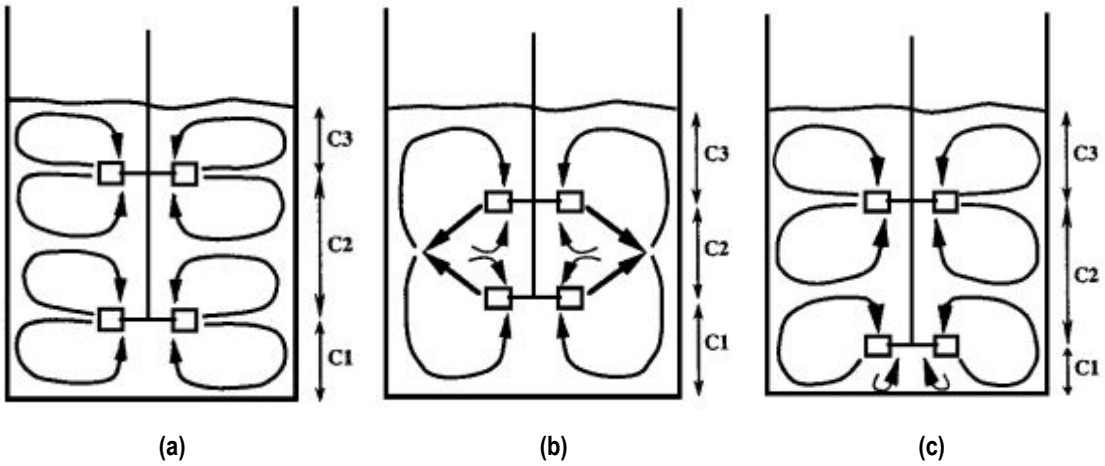

Figure 5. 9 Stable flow patterns obtained in a dual-Rushton turbine stirred vessel: (a) parallel flow; (b) merging flow; (c) diverging flow (Rutherford *et al*., 1996a).

The parallel flow pattern in Figure 5. 9(a) was generated with the impeller clearance $C1=0.25T$, the impeller separation $C2=0.50T$, and the upper impeller submergence $C3$ of $0.025T$. With this configuration, the Rushton impellers operated essentially independently of one another. As can be seen in the illustration, each Rushton impeller produced its own characteristic upper and lower ring vortex, leading to the formation of four well-defined ring vortices. Rutherford *et al*. (1996a) noted that this parallel flow pattern was maintained with $C1$ greater than $0.20T$, $C2$ greater than $0.385T$, leaving $C3$ having a value less than $0.415T$.

The merging flow pattern shown in Figure 5. 9(b) was produced when the impeller clearance and separation was each equal to $T/3$. Within the zone between the two impellers, the impeller streams followed a near straight-line at 45° toward one another and merged at mid-way of the zone. As a result, two large ring vortices were formed around each impeller. To maintain this merging flow pattern, $C1$ value needed to be kept above $0.17T$ and $C2$ less than $0.385T$, as observed by Rutherford *et al*. (1996a).

The diverging flow pattern shown in Figure 5. 9(c) has two stable ring vortices above and below the upper Rushton impeller and only one large ring vortex in the lower impeller. This flow pattern was observed with $C1$ equal to $0.15T$, $C2$ equal to $0.5T$ and $C3$ equal to $0.35T$. This low clearance between the lower Rushton impeller and the base of the tank caused the flow stream emerging from the lower impeller to be directed towards the base of the tank, evidently changing the characteristic double-loop to single-loop flow pattern. The diverging flow pattern could be maintained, given that the separation $C2$ was

greater than 0.385*T* and the lower impeller clearance *C*1 was less than 0.15*T*, as noted by Rutherford *et al*. (1996a) or 0.17-0.19*T* as reported by Mahmoudi and Yianneskis (1992). So long as *C*1 had a value between 0.15*T* and 0.2*T*, the lower Rushton impeller underwent the transition as noted by both Armenante *et al*. (1998) and Montante *et al*. (1999) discussed above.

Table 5. 2 summarises the available experimental data that examine the effect of impeller clearance on the transition from one flow regime to the other for systems with single and dual Rushton impellers. Mahmoudi and Yianneskis (1992) and Rutherford *et al*. (1996a) further commented that combinations of *C*1 and *C*2 values other than those mentioned above resulted in unstable flow patterns alternating between any two or all three of the parallel, merging, and diverging regimes over periods of seconds or minutes.

Table 5. 2 Summary of the range of the impeller clearance corresponding to the stable flow patterns from the literature.

Stable flow patterns	Impeller clearance range	Experimental data/Author
Parallel flow	$C1>0.19T$, $C2>0.4T$	Mahmoudi and Yianneskis (1992)
	$C1>0.20T$, $C2>0.385T$, $C3>0.415T$	Rutherford *et al*. (1996a)
Merging flow	$C1>0.17T$, $C2<0.34T$	Mahmoudi and Yianneskis (1992)
	$C1>0.17T$, $C2<0.385T$	Rutherford *et al*. (1996a)
Diverging flow	$C1<0.17\text{-}0.19T$	Mahmoudi and Yianneskis (1992)
	$C1<0.15T$, $C2>0.385T$	Rutherford *et al*. (1996a)
Single loop flow pattern	$C1<0.167T$	Nienow (1968) and Ibrahim and Nienow (1995)
	$C1<0.15\text{-}0.2T$	Armenante *et al*. (1998) and Montante *et al*. (1999)

The dual-Rushton impeller used by HCA has the clearance of the lower impeller above the base of the vessel *C*1 equal 0.172*T* and the separation between the impellers *C*2 equal to 0.273*T*. According to the findings by Rutherford *et al*. (1996a) summarised in Table 5. 2, this arrangement was potentially a "merging" flow pattern since $C1>0.17T$ and $C2<0.385T$ if the two impellers were of the same size. However, the HCA dual Rushton impellers are different in sizes: the bottom one is half the size of the upper one.

5.2.4 Scope of the problem

The previous section discussed the mixing applications in general and the mixing equipment of interest to this research project. This section will identify the major phases involved in a base-catalysed ethoxylation process taking place in the stirred ethoxylation reactors operated by HCA. This will help to classify the mixing operations to be examined by the computational fluid dynamics techniques performed in this stage of the research program.

The first stage of the research program examined the base-catalysed ethoxylation process as a typical gas-liquid reaction system (see Section 2.4.2.2). Injected either via a sparger in the bottom of the reactor or directly to the vapour space, ethylene oxide was introduced, in the literature reviewed, as a gaseous bubble dispersion into the substrate to be ethoxylated through the effect of agitation. Since the process involved contact between gas and liquid, the ethoxylation was considered a gas-liquid mixing process. However, the use of a dip-leg pipe which provides the path of ethylene oxide injection in the ethoxylation reactors employed by HCA raises the possibility that the ethoxylation process in the current operation may be essentially a single-phase liquid mixing. This assumes that ethylene oxide enters as a miscible liquid component into the bulk substrate.

A thorough revision on the operations employed in the kinetic experiments conducted in Chapter 3 allowed us to establish that the assumption of single-phase liquid mixing of two miscible liquids of ethylene oxide and substrate (hydrophobe) was considered valid in the laboratory autoclave. An explanation for this was that, in the operating procedures performed for the kinetic experiments, the injections of ethylene oxide were controlled to a rate corresponding to the set system pressure, which was maintained constant during the ethoxylation as described in Section 3.4.3. This rate simply represented the maximum allowable injection of ethylene oxide at that system pressure, above which ethylene oxide would begin to boil as its saturation vapour pressure exceeded the system pressure. Therefore, the amount in each ethylene oxide injection should follow the ethylene oxide solubility in the bulk liquid phase corresponding to that system pressure.

This mode of operation is also employed in the industrial-scale NIS A reactor operations of HCA. Ethylene oxide feed rates are adjusted in a way that the ethylene oxide vapour pressure is kept below the explosive limit, set according to the presence of nitrogen blanket. Figure 5. 10 plots the ratio of ethylene oxide partial pressure to the total reactor pressure versus the extent of the reaction, represented in terms of the liquid contents height to the vessel diameter ratio (z/T), for an ethoxylation run reported from one of the NIS A reactors. As can be seen in Figure 5. 10, the ethylene oxide pressure peaked at nearly 50% of the total reactor pressure at the early stage of the ethoxylation (z/T=0.6-0.7) then fell down to about 30% and then continued to keep falling. Moreover, an examination of the percentage of gaseous ethylene oxide content in the overall ethylene oxide feed revealed that majority of the ethylene oxide remained in the bulk

liquid (also see Figure 5. 10 below). A maximum of about 6% of ethylene oxide liquid was converted to ethylene oxide gas. The liquid ethylene oxide was either consumed or dissolved; the unreacted amount then vaporised to the headspace of the reactor.

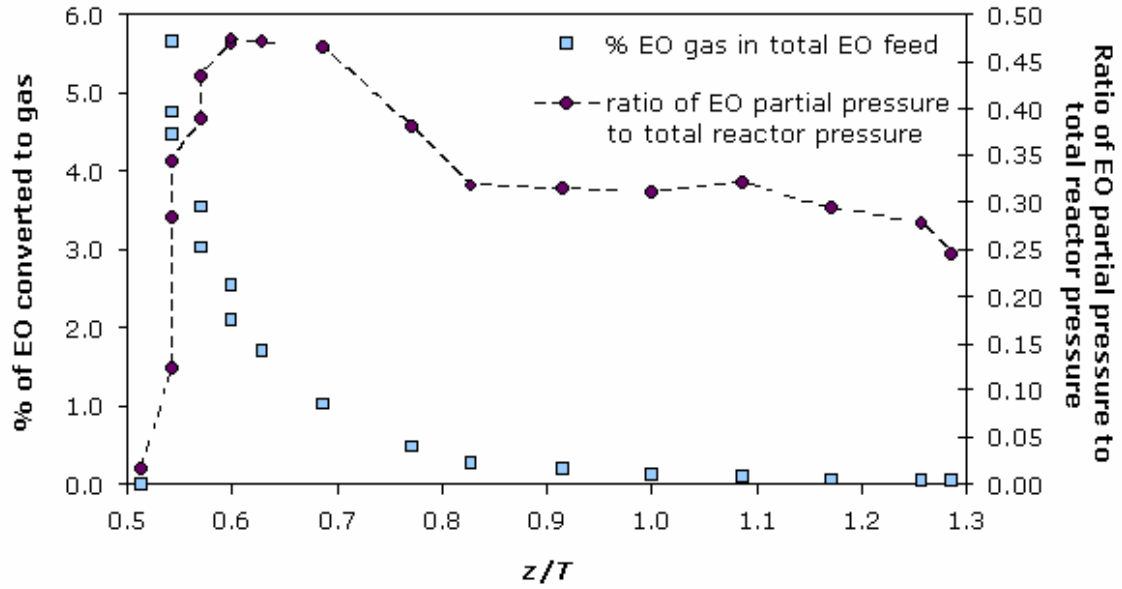

Figure 5. 10 Plot of the percentage of conversion of total ethylene oxide to gaseous ethylene oxide vs the reaction content height (*z*) to tank diameter (*T*) ratio for the reaction of nonylphenol with 11 moles of ethylene oxide at 160°C.

Therefore, in this research work, ethoxylation in semi-batch mode operated in the NIS A stirred reactors of HCA was assumed to be treatable as miscible liquids mixing followed by chemical reaction. This is different from the above-mentioned literature that classified ethoxylation as a gas-liquid reaction. The heat transfer of the ethylene oxide injection pipe system will be further studied by a predictive CFD simulation in Chapter 7. Hence, particular emphasis is given to single-phase liquid mixing systems in the following review.

5.2.5 Comparison of impeller performance

Mixer performance is typically expressed in terms of liquid velocity generated, total pumping capacity of the impeller, and total flow in the tank, or in terms of mixing time or a readily evaluated solids-suspension criterion (Oldshue, 1983). These terms are defined as the characteristics of the impeller performance or measures of process performance. With the improved understanding of the fluid mechanics in stirred vessels over the years, many new impellers had been developed to achieve higher flow per horsepower. However, with these new impellers the use of terms such as high efficiency, high performance, super performance, or low energy often misled readers and ignored the facts that different processes had different requirements for flow, fluid shear and other fluid mechanics properties (Oldshue, 1989). Harnby *et*

al. (1985) also commented that care had to be taken in interpreting the information in the literature on the flow generated by different impellers. For instance, the circulation rate through the vessel was not necessarily the same as the discharge flow from the impeller. The discharge flow leaving the impeller, referred to as primary flow or agitator pumping capacity, entrains liquids elsewhere in the vessel, which contributes the circulation pattern of the impeller. The total flow in the tank was often found to be in the order of twice the discharge rate since it comprised both primary flow and entrained flow. Harnby *et al*. (1985) further emphasised that the value of the discharge rate Q_p was of itself not a useful value unless it was related to the measures of process performance, such as mixing time.

Mixing time refers to the length of time from the instant of addition of all the components with the mixer running until the point when the vessel contents have reached a specified degree of uniformity required by the process (Harnby *et al*., 1985; Oldshue and Herbst, 1990). Knowledge of power input to the system is also a very important measure of the performance of impellers and is expressed as the non-dimensional power number, N_P:

$$N_p = P / \rho N^3 D^5 ,$$

5. 2

where ρ is the fluid density and P is the power input which was calculated from the induced torque measurement as $P = \omega T_r$, where ω is the shaft rotational speed in rad/s, T_r was measured by supporting the vessel on an air bearing connected to a calibrated local cell (Hockey and Nouri, 1996). It is noted that for all agitators, the dimensionless power number linearly decreases with Reynolds number in the laminar flow regime, while in a fully turbulent system power number is relatively constant through a wide range of Reynolds number (Jaramir *et al*., 1985; Oldshue and Herbst, 1990).

Power numbers were shown to be sensitive to impeller clearance by Nienow and Miles (1971) (cited Jaworski *et al*., 1991). Ibrahim and Nienow (1995) reported a reduction of approximately 25% in power numbers for a Rushton impeller of $D=T/3$ when the impeller clearance was lowered from $C=T/4$ to $T/6$. A similar magnitude of power number reduction was also reported for a PBT of $D=0.52T$ when C was lowered from $T/3$ to $T/4$. Montante *et al*. (1999) also observed a reduction of approximately 30% with the change of the Rushton characteristic double- to single-loop pattern as the impeller clearance was lowered to 0.15-0.2T (see Table 5. 2). Power numbers were also shown to be affected by the thickness of impeller blade t_b and disk t_d (Rutherford *et al*., 1996b). Rutherford *et al*. (1996b) found that a thinner blade and disk thickness led to a higher N_P than a thicker impeller. Rutherford *et al*. (1996b) also showed that the variations in D/T had almost no effect on the power numbers.

The total circulation rate, Q_C, in the tank is the total volumetric turnover rate in the tank. Pumping capacity Q_P is the volumetric flow rate of impellers passing through the impeller-swept volume (Tatterson,

1991). The difference between the total circulation rate and pumping capacity is the entrained circulation. Pumping capacity is usually expressed as a dimensionless parameter, impeller flow number, N_{QP}:

$$N_{QP} = \frac{Q_P}{ND^3}.$$

5. 3

Similarly, a dimensionless circulation flow rate number, N_C, is expressed as

$$N_C = \frac{Q_C}{ND^3}.$$

5. 4

The values of N_P, N_{QP} and N_C enable the characterisation of several agitator performance indices, such as the pumping effectiveness (Mavros *et al*., 1996; Hockey and Nouri, 1996) and the circulation efficiency number (Jaworski *et al*., 1996). The pumping effectiveness η_p is a measure of effectiveness of an impeller in generating pumping flow rate per unit of power input, which is given by the following equation:

$$\eta_P = \frac{N_{QP}}{N_P}.$$

5. 5

In an investigation on the effect of impeller type on the liquid flow patterns, Mavros *et al.* (1996) performed LDV measurements of instantaneous radial, axial and tangential velocities in a dished-bottom stirred vessel with a Rushton turbine and two axial agitators, the Mixel TT and the Lightnin A310, of $D=T/2$ at $C=T/3$ for turbulent flow regime with water. The Rushton turbine was found to provide the most thorough liquid circulation due to the formation of the two primary circulation loops in the upper and lower parts of the vessel while axial impellers established a main circulation loop around the agitator. Mavros *et al.* (1996) also showed that the flow induced by the Rushton turbine was considerably higher than the axial agitators as can be seen in the spatial distribution illustrated in Figure 5. 11(a). The highest velocities emerging from the Rushton impeller were found at off the side of the rotating blades (Figure 5. 11(a)), while flow in most of the vessel was generally slow with velocity magnitudes approximately 20% of U_{tip}. In comparison to the spatial distribution of the flow induced by the axial impellers, these magnitudes were considerably higher as can be seen in Figures 5. 11(b) and (c). Jaworski *et al*. (1991) also noted that the Rushton turbine induced a higher discharge velocity of $0.8U_{tip}$ (Yianneskis *et al*., 1987) than the $0.45U_{tip}$ for a 45° PBT. The axial impellers however consumed less power than radial flow impellers, resulting in considerably higher values of the pumping effectiveness η_p. Similar conclusions were found by Hockey and Nouri (1996) where a PBT (η_P=0.4) was 2.5 times more efficient in circulating flow per power input than a Rushton impeller (η_P=0.16) (Hockey, 1990; Nouri and Whitelaw, 1994).

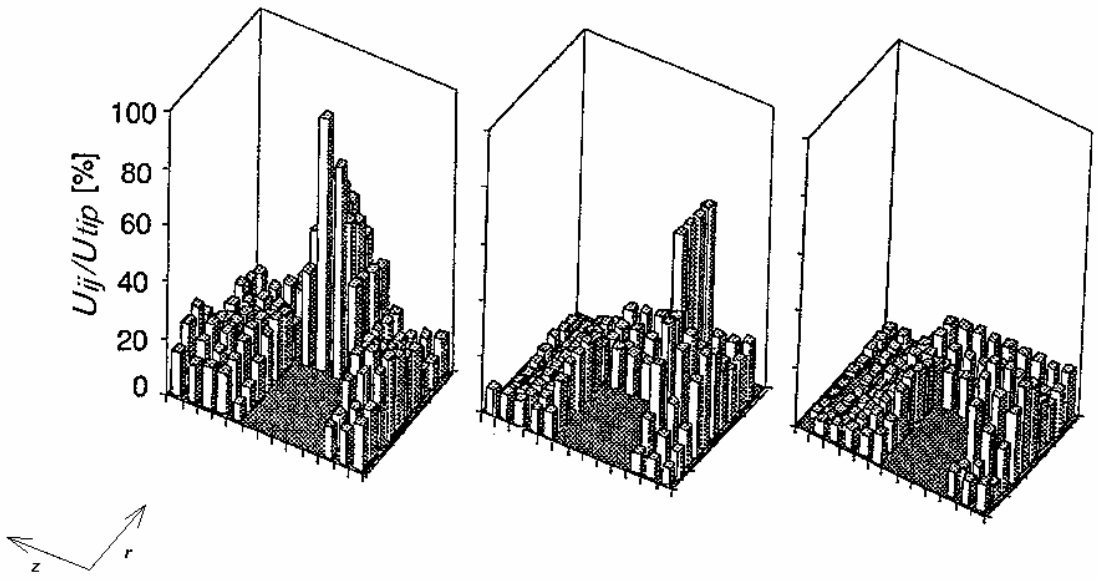

(a) Rushton **(b) Mixel TT** **(c) Lightnin A310**

Figure 5. 11 Spatial distribution of total velocity- geometric sum of the three velocity components- as a percentage of U_{tip}. Measurements of velocities were taken in the plain water for turbulent flow (Mavros *et al.*, 1996).

Jaworski *et al*. (1996) proposed that the total circulation produced by the impeller (Q_C) was more important than its pumping capacity (Q_P) and hence defined a circulation efficiency number η_C using the global stirred vessel characteristics such as the power number N_P and the circulation flow number N_C. The circulation efficiency number η_C describes the impeller capacity to circulate the liquid in relation with its power consumption. This relation enables agitators of different sizes to be compared in a turbulent flow regime:

$$\eta_C = \frac{N_C}{N_P}\left(\frac{D}{T}\right)^4 . \qquad \textbf{5. 6}$$

The value of η_C is independent of impeller speed. Equation 5. 6 also serves as a compact criterion for comparing impellers of different types in the turbulent flow regime. The higher the circulation efficiency number η_C, the more efficient is the impeller in generating a circulating flow for a given power input. Jaworski *et al*. (1996) calculated an η_C of 0.019 for a PBT and 0.023 for a Rushton turbine, both of $D=T/3$.

Mavros and Baudou (1997) proposed an agitation index, I_g, as a measure of the effectiveness of an agitator in inducing flow in a tank:

$$I_g = 100\frac{\hat{U}}{U_{tip}}[\%],$$

5. 7

where $\hat{U}$ is volume-weighted average velocity:

$$\hat{U} = \frac{\sum_i \sum_j V_{ij} U_{ij}}{\sum_i \sum_j V_{ij}},$$

5. 8

where U_{ij} is the resultant mean velocity of the time-averaged velocity components (U_x, U_y, U_z or U_z, U_r, U_θ) at a LDV measuring point (i, j) and V_{ij} is the cell volume surrounding that measuring point.

The higher the value of I_g, the better is the agitator since the velocities inside the vessel are higher. As shown earlier by Mavros *et al*. (1996), the flow induced by the two axial flow impellers, the Mixel TT and the Lightnin A310, was considerably slower than the turbine-induced flow. This was well reflected by the values of the agitation indices: in the same medium of water in a dished-bottom, cylindrical agitated vessel of standard configuration (Z=T), I_g varied from 17.8% for the Rushton turbine to 12% for the Mixel TT and to 8.5% for the Lightnin A310 (Mavros and Baudou, 1997). These values of I_g supported the findings of Mavros *et al*. (1996). That is, the Rushton turbine was the most efficient agitator, however it was significantly more energy intensive.

The efficiency of an agitator can also be measured as a function of the spatial distribution of kinetic energy (Mavros *et al*., 1998). The turbulent kinetic energy, k, is calculated from the average of the fluctuating terms in the velocity measurements, the root-mean-square (rms) velocities:

$$k = \frac{1}{2}\left(u_x'^2 + u_y'^2 + u_z'^2\right).$$

5. 9

The quantity is made dimensionless by normalising with the square of impeller-blade-tip velocity U_{tip}^2. The dimensionless turbulent kinetic energy (k/U_{tip}^2) is usually found highest in the impeller discharge region. For a Rushton turbine, the highest turbulence is next to the impeller, where the flow is ejected jet-wise radially (Mavros *et al*., 1998). For a 45° PBT in down-pumping mode, the highest turbulence is at the impeller tip and just below (Aubin *et al*., 2001).

The contours of the dimensionless k/U_{tip}^2 for the three stable flow patterns induced by the dual-Rushton agitator described in Section 5.2.3.2 were compared by Rutherford *et al*. (1996a). Their remarks were as follows:

- parallel flow for achieving higher turbulence levels and more uniform blending in the bulk of the vessel away from the impeller streams since the parallel flow produced the most uniform distribution of *k* throughout the vessel;
- merging flow for locally intensive mixing in the middle of the vessel since steep gradients of turbulent kinetic energy were found over the entire region between the impellers, and
- diverging flow for suspension of solids deposited on the bottom of the vessel since the highest turbulence level was produced beneath the lower impeller.

However, a merging flow pattern was preferable for overall blending performance, due to the 20% lower mixing time recorded for this configuration (Mahmoudi and Yianneskis, 1992). It should also be noted that the unstable flow impeller spacings corresponded to the longest mixing times.

As Oldshue (1989) pointed out, it was seldom possible, either economically or time-wise to investigate every potential mixing variable or compare the performance of many impeller types. The above review allowed us to gain a level of fundamental understanding of the flow pattern induced by various impeller arrangements and the resulting applications. The literature review also sourced experimental data that allowed assessment of the performance of the impellers with relevance to the NIS A reactors. Table 5.3 summarises a number of studies that experimentally quantify the mixing characteristics and efficiency indices described in this section. Table 5. 4 presents the values reported in these studies. Comparisons of the measured power numbers among different references for a particular impeller is difficult since most investigations did not provide the information on the impeller disk thickness that is known to affect the power numbers as discussed previously.

Table 5. 3 References with experimental data for standard six-bladed disc turbines or pitched blade impellers of the mixing characteristics summarised in Table 5. 4.

Reference	Impeller type	Geometrical and operating parameters
Yianneskis *et al*. (1987)	Rushton	T=0.294m, Z/T=1, D=1/3T, C =1/4T, 1/3T, 1/2T
Ranade and Joshi (1989a)	45°, 60° PBT	T=0.3, 0.5m, Z/T=1, D=1/3T, C=1/2T Re>10,000
Ranade and Joshi (1990)	Rushton	T=0.3m, Z/T=1, D=1/3T, C=1/2T t_b=2.0mm, t_d=2.7mm Re=50,000
Jaworski *et al*. (1991)	45° PBT	T=0.146m, Z/T=1, D=1/3T, C=1/2T Re>10,000
Dyster *et al*. (1993)	Rushton	T=0.150m, Z/T=1, D=1/3T, C=1/4T, 1/2T t_b=1.5mm, t_d=1.5mm Re=24,000
Nouri and Whitelaw (1994)	Rushton 60° PBT	T=0.144m, Z/T=1, D=1/3T, C=1/3T t_b=1.5mm, t_d=1.5mm Re=24,000
Bakker and Van den Akker (1994)	Rushton PBT A315	T=0.444m, Z/T=1, D=0.4T, C=0.3T Re=95,000 (Rushton) Re=189,000 (PBT, A315)
Hockey and Nouri (1996)	60° PBT	T=0.294m, Z/T=1, D=1/3T, C=1/3T t_b=3.0mm Re=48,000
Mavros *et al*. (1996)	Rushton	T=0.19m, Z/T=1, D=1/2T, C=1/3T Re=27,100
Aubin *et al*. (2001)	45° PBT	T=0.19m, Z/T=1, D=1/2T, C=1/3T Re=45,000

Table 5. 4 Summary of the power and flow characteristics of the impellers with relevance to this research project.

Impeller	N_P	N_{QP}	η_P	η_C
Rushton	4.8[a], 4.3[b], 5.0[c], 5.10[k], 5.6[m]	0.785[a], 0.89[b], 0.74[c,g], 0.72[d], 0.76[l], 0.78[m]	0.2[b], 0.16[h]	0.023[c]
PBT	2.21[f], 2.1[j], 1.70[c], 1.55[l], 1.93[k]	0.73[c,e], 0.85[f], 0.91[j], 0.81[l], 0.75[k]	0.4[i], 0.43[j], 0.39[k]	0.019[c]
A315	0.76[l]	0.74[l]		

[a]Yianneskis et al. (1987); [b]Mavros et al. (1996); [c]Jaworski et al. (1996); [d]Weetman and Oldshu (1988) (cited [e]Jaworski et al., 1991); [f]Ranade and Joshi (1989a); [g]Ranade and Joshi (1990); [h]Nouri and Whitelaw (1994); [i]Hockey and Nouri (1996); [j]Mishra (1993) (cited [k]Aubin et al., 2001); [l]Bakker and Van den Akker (1994); [m]Dyster et al. (1993)

As can be seen in Table 5. 4, the dimensionless power number and flow number published by Bakker and Van den Akker (1994) for an A315 impeller with D=0.4T at C=0.3T leads to the pumping effectiveness η_p of the order of 0.97 by Equation 5. 5. This suggests an A315 impeller is approximately 2.4 times and 6 times more efficient in generating pumping flow rate per power input than a PBT and a Rushton turbine respectively.

5.3 Stirred tank flow simulation

Computational fluid dynamics (CFD) programs were first developed in the 1960s; they were however severely restricted due to the limited computing power in those days (Bakker *et al*., 2001). It was not until the early 1980s that commercial codes became available, mainly because of the spectacular progress in digital computing in the past two decades.

The application of CFD to stirred tank reactors dates back to the late 1970s (Harris *et al*., 1996). The particular challenge of this type of numerical simulation lies in the relative motion between stationary baffles and the rotating impeller, resulting in the flow domain changing with time. With the advances in computing power together with modern methods, CFD has reached a level that gives reliable and accurate results for applications involving stirred tank reactors (Bartels *et al*., 2002). Several methods had been successfully developed to simulate the flow in a stirred vessel, where good agreement of the mean flow field with experimental data was achieved. Recent reviews of these methods can be found in Harris *et al*. (1996) and Brucato *et al.* (1998). Earlier numerical simulations employed a two-dimensional (2D) treatment, i.e. based on assumption of axial symmetry, and later steady-state three-dimensional (3D) treatment where the impeller region was treated as a black box. That is, the impeller swept-region was excluded from the computational domain and replaced with either a boundary condition at its surface or source terms distributed throughout its volume (Brucato *et al*., 1998). This approach, referred to as impeller boundary conditions, required prescription of empirical values of mean velocities and turbulence

quantities. Three-dimensional steady-state predictions based on this approach were presented by Middleton *et al*. (1986), Ranade and Joshi(1990), Kresta and Wood (1991), Fokema *et al*. (1994), Jenne and Reus (1999) and Brucato *et al*., (1989, 1990), Weetman (1991) (cited Micale *et al*., 1999). Gosman *et al*. (1992) extended this approach to simulate two-phase flow in a Rushton stirred vessel. Advantages of this approach included the reliable description of the outflow region of the impeller and the reduced computational expenses of steady simulations compared to transient simulations (Jenne and Reus, 1999). Disadvantages were its inability to capture any significant details of flow within the impeller swept volume, e.g. trailing vortices behind turbine blades (see Van't Riet and Smith, 1973; Yianneskis *et al*., 1987; Stoots and Calabrese, 1995). Furthermore, the usefulness of this approach was inherently limited because of its lack of generality since time-consuming experimentation in advance was usually available only for a few vessel-impeller geometrical configurations (Micale *et al*., 1999). Table 5. 5 shows a summary of publications concerning simulations of the liquid flow in baffled stirred-tank reactors using experimental data as impeller boundary condition (Jenne and Reus, 1999).

Table 5. 5 Publications concerning simulations of the liquid flow in stirred-tank reactors using experimental data as impeller boundary conditions (Jenne and Reus, 1999).

Reference	Dimensionality	Impeller modelled	Turbulence model
Platzer (1981)	2D		Standard k-ε
Harvey and Greaves (1982)	2D		Standard k-ε
Placek *et al*. (1986)	2D	Rushton	Three equation k_P-k_T-ε
Middleton *et al*. (1986)	3D	Rushton	Standard k-ε
Ju (1987)	3D	Rushton	Modified k-ε
Ranade and Joshi (1989a, 1990)	3D	Rushton	Standard k-ε
Kresta and Wood (1991)	3D	Rushton	Standard k-ε
Bakker and Van den Akker (1994)	3D	Rushton, PBT, A315	Algebraic stress
Fokema *et al*. (1994)	3D	PBT	Standard k-ε
Togatorop *et al*. (1994)	2D	Rushton	Standard k-ε
Jenne and Reus (1999)	3D	Rushton	Modified k-ε

In the last decade, a number of approaches have been developed that required no prescribed experimental data as boundary or initial conditions. The methods can be divided into two categories: fixed coordinate system and rotating coordinate system (Deen, 2001).

5.3.1 Fixed coordinates system

An improved computational procedure over the impeller boundary conditions (IBC) approach is the snapshot method implemented by Ranade and Van den Akker (1994) and Ranade (1997) for single-phase turbulent flow agitated by a Rushton turbine. The method simulated the flow characteristics between the impeller blades without solving the full time-dependent flow equations by taking snapshots of the flow in the vessel with the impeller in some particular positions with respect to the baffles. It captured most of the significant details of the flow both within and outside the impeller without using any empirical input, by specifying a mass source and mass sink at the back and front of the impeller blade respectively to represent the corresponding ejection and suction of fluid from the impeller blades. When modelled correctly, this led to realistic rotational flow. In addition, appropriate source and sink terms were defined for all the other variables as well. The standard k-ε model of turbulence was used for solution along with the momentum transport equations. The predicted values of global parameters such as power number (Equation 5. 2) and pumping number (Equation 5. 3) of the impeller showed a good agreement with published data.

5.3.2 Rotating coordinates system

Numerical approaches for simulating baffled tanks employing a rotating coordinates system applied two frames of reference: one associated with the impeller and one with the baffles. The approaches were further divided into (i) time-dependent computation, e.g., the sliding grid method, and (ii) steady-state computation, e.g., the inner-outer method and multiple frames of reference.

The transient computation by sliding grid (SG) calculation was first reported by Luo *et al.* (1993) and later used by Harvey and Rogers (1996), Lee *et al*. (1996), Jaworski *et al*. (1997) and Ng *et al*. (1998) for the simulation of turbulent flow in a baffled stirred tank, equipped with a Rushton turbine. The flow field was divided into two sub-domains; one with rotational motion, enclosing the impeller, and the other at rest, containing the remainder of the computational domain. At the interface between the two domains, the mesh attached to the rotating block was allowed to slide/and or shear relative to the stationary block. The computation proceeded simultaneously over the entire flow field and the solutions in both rotating and stationary domains were coupled at all times. The procedure repeated the calculation for the entire computational domain at each step of the relative motion. The method required no input of the velocity field and other empirical parameters within the impeller sweep volume. The sliding mesh treatment correctly captured the inherent unsteadiness of the flow in the vicinity of the impeller as well as the

periodic unsteadiness due to the relative motion between the rotating impeller blades and the stationary baffles (Tabor *et al*., 1996). However, this time-dependent method is computationally very intensive and the requirement of excessive computational resources makes it impractical to use for the design of fluid flow equipment on a regular basis (Bartels *et al*., 2002). Two alternative methods using steady-state computation were then proposed: the inner-outer (IO) method introduced by Brucato *et al.* (1994) and multiple frames of reference applied by Luo *et al.* (1994).

With the IO method the whole vessel volume was subdivided into two partially overlapping zones: the inner zone, containing the impeller, and the outer zone, containing baffles. The choice for the interface between the inner and outer regions did not have a significant effect on the results as long as none of the boundaries was very close to the impeller (Montante *et al*., 2001). Brucato *et al*. (1994) began this iterative procedure with simulation of the flow field in the inner zone in a reference frame rotating with the impeller, imposed with the boundary condition of the still fluid on the outer surface. Information including velocity, turbulence energy and dissipation on the boundary surfaces obtained from the inner zone simulation was then translated into the stationary frame, averaged in the azimuthal direction, and used as the boundary conditions for the simulation of the flow field in outer zone, taking the reference frame of the laboratory. The simulation of the outer zone generated the results which were azimuthally averaged and corrected for the relative motion, translating a new set of boundary condition for the next inner zone simulation. The procedure was iterative and repeated in this fashion until no difference between subsequent impeller boundary conditions was observed.

In contrast to the inner-outer method where cells partly overlapped, the multiple frames of reference method (MFR) of Luo *et al*. (1994) implicitly matched the inner and outer steady-state solutions along a single boundary surface and no external iterations were required. The MFR method was developed to cut the costly computer memory and time resulting from time-dependent calculations. It was based on the assumption that at one particular radial location in the flow established by full unsteady computations, steady flow conditions existed (Luo *et al*., 1994). This was particularly apparent for those geometries where the clearance between the impeller and the baffles was comparable with or greater than the impeller diameter, as noted by Tabor *et al*. (1996). This particular radial location where flow variables were unchanged either with θ or with time was where the two different frames of reference were set. The inner frame enclosing the impeller rotated at the impeller speed and was used to compute the flow within the impeller in steady state manner. The outer frame remained stationary and was used to compute the flow away from the impeller. Unlike the SG method, the mesh that lay at the interface between the two domains always remained static. The interface between the two computational regions where the different frames of reference met had the two solutions matched locally via appropriate velocity transformations from one frame to the other. The MFR computation by Luo *et al*. (1994) showed a saving of over ten times in

computer time compared to the full unsteady calculation while a degree of accuracy similar to the SG method, e.g., Luo *et al*. (1993) was also achieved.

5.3.3 Comparison of the methods

Tabor *et al*. (1996) compared the treatment of the impeller motion, in particular the behaviour of impeller stream, using both the MFR and the SG techniques with the experimental data. Both techniques were able to depict the trailing vortices behind the impeller blades which matched well with experimental observation by, e.g., Van't Riet and Smith (1973) and Yianneskis *et al.* (1987). With the use of the k-ε model of turbulence, the MFR method was found to give better predictive results. Tabor *et al*. (1996) explained that it was probably because the turbulence model was better tuned for a time-independent flow. Another explanation involved the numerical errors associated with the complexity of the SG procedure. Because the grids at the interface between the two computational domains continuously changed with time in a SG computation, additional errors related to temporal discretisation were likely to be introduced. Brucato *et al*. (1998) compared the IBC, IO and SG methods. The IBC approach only yielded satisfactory results if reliable empirical data were available for the flow near the impeller, otherwise the method led to large errors. The other two methods were fully predictive, which required no empirical information, and generated satisfactory results, however, the SG calculation gave the best predictive results. Montante *et al*. (2001) applied both the SG and IO methods to evaluate the capability of the CFD code in predicting the transition from the double- to single-loop. The simulations were performed for the flow pattern and the turbulence fields in a fully baffled vessel stirred by a Rushton turbine at various impeller clearances. Both methods were found to correctly predict the flow pattern transition as well as the C/T values at which the transition occurred, indicating that the IO approach was a useful alternative to the SG calculation on savings of the computational requirements. The simulations also predicted well the sharp drop of the power number accompanying the transition to the single-loop pattern. Apart from the usually reported under-estimation of turbulence energy by the k-ε based simulations (Daskopoulos and Harris, 1996), the major discrepancy of the simulation results by Montante *et al*. (2001) was the over-estimation of the discharge angle of the impeller stream at a lower impeller clearance of the single-loop flow characteristics, e.g. C/T=0.15.

Micale *et al*. (1999) extended the comparison of the three alternative modelling techniques, the IBC, IO and SG methods, to the reproduction of the turbulent flow fields in a dual-impeller stirred vessel with the experimental LDV measurements by Rutherford *et al*. (1996a), discussed in Section 5.2.3.2. Both the SG and IO techniques satisfactorily reproduced the characteristics of the mean flow field and the distribution of turbulence energy for all three stable-flow configurations. The usual under-prediction of turbulence energy was also common in these simulations. Major discrepancies were reported in the merging and diverging flow cases on the over-prediction of the angle formed by the flow emerging from the impeller with

horizontal. The cause of the discrepancies was explained by the inherent limitations of the *k-ε* model for flow with strong streamline curvature. The IBC method, on the other hand, gave satisfactory results only in the simplest case of parallel flow and failed to predict the effect of the relative location of the two impellers on the overall flow patterns. This confirmed that there were no universal impeller outflow profiles existing. Thus, the IBC technique was only reliable if experimental data for the flow at the impeller's periphery were available for the overall configuration of both the impeller and vessel under study.

5.3.4 Turbulence modelling

So far as the overall flow fields were concerned, the predictive mean velocity data obtained by CFD simulations for conventional geometrical configurations showed quantitatively good agreement with experimental data. On the other hand, the under-prediction of the turbulence level with the use of the standard *k-ε* model was also extensively reported (Ranade and Joshi, 1990; Tabor *et al*., 1996; Daskopoulos and Harris, 1996; Brucato *et al*., 1998; Ng *et al*., 1998). A possible cause for the discrepancy was explained by the underlying assumption of the *k-ε* model that the turbulence in the impeller vicinity was local isotropic (Abbott and Basco, 1989), while in fact the turbulence was mostly anisotropic ($u_x' \neq u_y' \neq u_z'$) close to the blades (Ng. *et al*., 1998; Lee and Yianneskis, 1998). The anisotropy of turbulence was also reported for the flows in the vessel stirred by dual impellers (Rutherford *et al*., 1996a). Tatterson (1991) suggested the use of three-dimensional non-isotropic version of the *k-ε* model provided the most realistic simulation of the flow fields. Bakker *et al*. (1996) compared three different turbulence models, the *k-ε* model, the *k-ε* RNG model and the Reynolds stress model (RSM), for the turbulent operation of a PBT. Little difference was found between the predictions using the three turbulence models. Since Bakker *et al*. (1996) did not carry out grid sensitivity studies, nor did they take into account the trailing vortices in this work, the usefulness of their data was questioned by Wechsler *et al*. (1999). On the other hand, the comparison made by El-Wazzen (1997), also cited in Lee and Yianneskis (1998) and Ng *et al*. (1998), of the flow using the *k-ε* model and the RSM with experimental data showed that the latter yielded turbulence values closer to the measurement. Recently, the application of Large Eddy Simulation (LES) for modelling the flow field in a standard configuration stirred tank has achieved good agreement between predicted and measured turbulence levels (Derksen and Van den Akker, 1999). However, this approach is computationally very demanding. Other work performed to improve the predictions of turbulence quantities included grid refinements, particularly for the region enclosing the impeller, by Ng *et al*. (1998) and Wechsler *et al*. (1999). Apart from the use of coarse grids which led to severe under-prediction of the turbulence level, results obtained using finer grids were encouraging, though unlikely to approach the experimental values.

The use of the *k-ε* model might not be considered entirely applicable for all regions of the flow since the turbulence in the impeller stream deviated from isotropy. The deviation, however, became smaller in

locations further way from the impeller, in which the turbulence might be regarded as isotropic. The use of the k-ε model was considered sufficient in such locations where good agreement between the predictions and the experimental data was obtained (Lee and Yianneskis, 1998; Ng *et al*., 1998).

5.3.5 Reactive mixing

While much attention was focused on exploring ways to improve the accuracy for the flow field predictions, a number of studies incorporating mixing-sensitive reactive flow in the CFD simulations of a stirred vessel were reported, e.g., Middleton *et al*. (1986), Bakker and Fasano (1993) and Brucato *et al*. (2000). These simulations took into account the "macro-mixing" phenomenon in the vessel, while "micro-mixing" phenomena were neglected. The term "macro-mixing" refers to the bulk circulation and larger-scale turbulent motion; "micro-mixing" concerns variations at the scale of Kolmogoroff eddies down to molecular scale (Brucato *et al*., 2000).

The work of Middleton *et al*. (1986) not only was the first three-dimensional simulation of a stirred vessel to be reported in the open literature, but also simulated a consecutive-competitive reaction sequence, with localised injection of one of the reactants so that the final outcome was dependent on the mixing generated by the flow circulation in the vessel. The simulation computed the final yield as a function of impeller speeds for a 30L vessel and gave a reasonably accurate prediction to the experimental outcome. Bakker and Fasano (1993) studied the same pair of consecutive-competitive reactions used by Middleton *et al*. (1986) with the assumption that small scale mixing only limited the conversion rate of the fastest reaction of the pair. After fitting coefficients in the turbulent micro-mixing models using the data of Middleton *et al*. (1986), the results of Bakker and Fasano (1993) correctly predicted the effects of scale, impeller speed and feed locations. Brucato *et al*. (2000) considered a different mixing-sensitive reaction scheme in a batch stirred reactor in which a pair of parallel-competitive reactions took place. Good agreement was obtained when the simulation results were compared with the original experimental data, implying that micro-mixing phenomena were actually negligible in their investigated system. On the other hand, macro-mixing phenomena should always be properly accounted for, for which CFD tools seemed particularly suited. For cases where results were not effectively explained in terms of macro-mixing inhomogeneities, Brucato *et al*. (2000) suggested a micro-mixing model to be coupled as sub-grid models to the CFD-derived macro-mixing frame (see Ranade and Bourne (1991) and Pipino and Fox (1994)).

5.4 Conclusions

With the ever decreasing computing costs and the continuous development of commercial codes for CFD, the simulation of three-dimensional flow fields in a stirred vessel is increasingly gaining acceptance as an alternative to the traditional modelling approaches. Predicted flow fields have shown good agreement with

the experimental data from the application of CFD simulations to the case of mixing tanks. Though quantitative discrepancies exist (often a problem of the spatial resolution as well as of turbulence models), CFD has been demonstrated to be a powerful tool for modelling reactive mixing. While mixing could be one of the key factors affecting the throughput of the type of commercially important processes such as ethoxylation, there has not been any known publication on the CFD application in the field of ethoxylation. Therefore, this research work attempted to initialise the building of a link between CFD and ethoxylation.

Hence, the objectives of the second stage of this research project were as follows:

"Integration of the previously developed kinetic model with the CFD technique to simulate an existing industrially operated stirred ethoxylation reactor, in order to rationalise the current reactor design, further determine the optimum operating conditions, and ultimately, provide a reliable tool for the exploration and design of new reactor systems."

Chapter 6

Description of a Numerical Model for a Stirred Ethoxylation Reactor

6.1 Introduction

This chapter presents the governing equations used in the numerical simulations of an ethoxylation reactor system. The ethoxylation system will be described as an incompressible, single-phase reactive flow with multiple chemical species under turbulent conditions. Expressions are also given for the ethoxylation exothermic heat. The numerical model was implemented in the commercial computational fluid dynamics software, CFX4.4.

6.2 Chemical kinetics

As discussed in Chapter 2, the chemical kinetics for the ethoxylation of an alkylphenol can be expressed by the evolution rate of product oligomers as in Equations 2. 22 to 2. 24 or the consumption rate of ethylene oxide as in Equation 2. 25. However, the determination of the former during an ethoxylation operation requires sample extraction at various degrees of ethylene oxide substitution - this is difficult to implement in the current set-up as discussed in Section 4.4.3. Therefore, the chemical kinetics was expressed in the numerical model in terms of the ethylene oxide consumption, in addition, with particular reference to the consumption in the propagation stage. Hence, the representation of the polymerisation in Equation 2. 3 was modified to facilitate the summation of total consumption of ethylene oxide during the propagation stage as follows

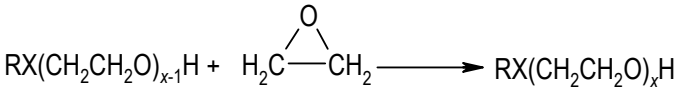

6. 1

where x, as defined previously, is not necessarily an integer and represents the number-average degree of polymerisation of ethylene oxide in the product, and $RX(CH_2CH_2O)_xH$ is the general formula representing the polyoxyethylene mixture. It was assumed that the concentration of an initiator was negligible in the propagation stage, particularly in the ethoxylation of an alkylphenol under the base-catalysed conditions. Therefore, the chemical kinetics for the consumption of ethylene oxide in Equation 2. 25 can be simplified to

$$\frac{d[\mathrm{EO}]_b}{dt} = k_p \cdot B^0 \cdot [\mathrm{EO}]_b$$

6. 2

where k_p, the reaction constant for the propagation reactions, is expressed in Arrhenius equation with the parameters obtained from the experiments performed in this work (Table 4. 4) and B^0 is the initial concentration of the catalyst (Section 2.5.2). The detailed derivation for Equation 6. 2 is given in Appendix A. 2.

In this model to be developed, Equation 6. 2 of the ethylene oxide consumption was integrated with CFX4.4 via a user-defined FORTRAN subroutine. Since the ethoxylation in the current mode of operation employed by HCA could be treated as a single-phase liquid mixing problem (Section 5.2.4), the corresponding numerical model was defined as an agitated single-liquid containing several chemical species. As Equation 6. 1 suggests, the polyoxyethylene mixture $RX(CH_2CH_2O)_xH$ is treated as a bulk liquid and hence, ethylene oxide is the sole chemical species in the model. Accordingly, the numerical model for the stirred ethoxylation reactor studied in this research project will be described as an incompressible, turbulent single-phase liquid mixing with chemical species undergoing heat and mass transfer in the following section.

6.3 Governing equations

The conservation equations of mass and momentum for an incompressible fluid are given as follows (Bird *et al*., 1960; AEA Technology, 1999):

$$\frac{\partial \rho}{\partial t} + \nabla \cdot (\rho U) = 0 \,, \tag{6. 3}$$

$$\frac{\partial}{\partial t}(\rho U) + \nabla \cdot (\rho U U) = \nabla \tau - \nabla p + S \,, \tag{6. 4}$$

where U is the mean velocity vector, represented by the components U_x, U_y, U_z, ρ the fluid density, p the pressure, S the momentum source term including contributions due to the body force and t is time. τ is the stress tensor:

$$\tau = \mu \left(\nabla U + (\nabla U)^T - \frac{2}{3} \mathbf{I} (\nabla U) \right), \tag{6. 5}$$

where μ is the molecular viscosity and **I**, the unity tensor. The energy transport equation solving for the total enthalpy H is:

$$\frac{\partial}{\partial t}(\rho H) + \nabla \cdot (\rho \mathrm{U} H) = \nabla \cdot (\lambda \nabla T) \,, \tag{6. 6}$$

where λ is the thermal conductivity and T is the temperature. The energy equation is more commonly described by transforming the temperature gradient to an enthalpy gradient:

$$\lambda \nabla T = \frac{\lambda}{C_p} \nabla H \,, \tag{6. 7}$$

where C_p is the specific heat at constant pressure as a function of temperature. The terms on the left hand side of the transport equations (Equations 6. 4 and 6. 6) represent, respectively, the transient term and the convection term. The right hand side terms are the diffusion term and a source or sink term representing creation and destruction of the conserved variable. Transient terms were retained only when the time-dependent calculation, e.g., sliding grid computation, was solved. They were not included in steady-state computations, such as the multiple frame of reference method.

The flow in a stirred ethoxylation reactor is turbulent (Re>10^4). Therefore, the numerical model is closed by the Reynolds averaging to the transport equations, combined with the standard k-ε model (Launder and Spalding, 1974); the diffusion term in the right hand side has a turbulent term added to the

molecular diffusive term. The effective viscosity μ_{eff} that is involved in the Reynolds-averaged momentum equation comprises a contribution from the turbulent diffusion term:

$$\mu_{eff} = \mu + \mu_T ,$$

6. 8

where μ_T is the turbulence viscosity or eddy viscosity and is formulated as below:

$$\mu_T = C_\mu \rho \frac{k^2}{\varepsilon} .$$

6. 9

The turbulence kinetic energy *k* and the turbulence dissipation rate ε are given by their transport equations as follows:

$$\frac{\partial}{\partial t}(\rho k) + \nabla \cdot (\rho U k) = \nabla \cdot ((\mu + \frac{\mu_T}{\sigma_k})\nabla k) + (G - \rho\varepsilon)$$

6. 10

$$\frac{\partial}{\partial t}(\rho \varepsilon) + \nabla \cdot (\rho U \varepsilon) = \nabla \cdot ((\mu + \frac{\mu_T}{\sigma_\varepsilon})\nabla \varepsilon) + \frac{\varepsilon}{k}(C_{\varepsilon 1} G - C_{\varepsilon 2} \rho \varepsilon)$$

6. 11

where σ is the corresponding turbulent Prandtl number of the conserved variable and *G* the turbulence generation rate. The values for the model constants used are standard C_μ =0.09; σ_k =1.00; σ_ε =1.3; $C_{\varepsilon 1}$ =1.44 and $C_{\varepsilon 2}$ =1.92 though some modified values C_μ =0.125 and $C_{\varepsilon 2}$ =1.60 were suggested by Abujelala and Lilley (1984) and used by Ranade and Joshi (1989b) in a stirred tank simulation.

Further, the transformation of the molecular diffusion term in the energy equation (Equation 6. 6) gives rise to the Reynolds averaged energy equation as follows:

$$\frac{\partial}{\partial t}(\rho H) + \nabla \cdot (\rho U H) = \nabla \cdot ((\frac{\lambda}{C_p} + \frac{\mu_T}{\sigma_H})\nabla H) .$$

6. 12

Here, various species are assumed to be mixed at the molecular level so that they share the same velocity, pressure and temperature fields as the carrier fluid. Once the flow pattern is established, the mass transport by convection and diffusion of a chemical species is described by mass fraction as follows:

$$\frac{\partial}{\partial t}(\rho Y_i) + \nabla \cdot (\rho U Y_i) = \nabla \cdot ((\Gamma_i + \frac{\mu_T}{\sigma_i})\nabla Y_i) + S_i ,$$

6. 13

where Y_i is the mass fraction of species *i* and is related to molar concentration X_i by

$$Y_i = \frac{W_i X_i}{\rho} ,$$

6. 14

where W_i is the molecular weight of species *i*. Γ_i is the molecular diffusion coefficient of species *i* through the mixture and $\frac{\mu_T}{\sigma_i}$ is the eddy diffusivity.

The mixture density ρ in the expressions above is calculated from:

$$\frac{1}{\rho} = \sum_{i=1} \frac{Y_i}{\rho_i} .$$

6. 15

The species source term S_i, representing the rate of creation or depletion due to all chemical reactions, is in dimensions of mass per volume per time:

$$S_i = W_i \sum_{j=1}^{N_R} n_{ij} R_j ,$$

6. 16

where n_{ij} is the overall stoichiometric coefficient for species *i* in reaction *j* and is positive for products and negative for reactants; R_j is the reaction rate for the *j*-reaction. As discussed in the previous section, the system containing reactions between different oligomers and ethylene oxide was simplified to a binary mixture of bulk polyoxyethylene mixture and ethylene oxide. One chemical reaction was solved (N_R=1) in the numerical model, with the reaction rate *R* evaluated by Equation 6. 2. That is, the depletion of ethylene oxide contributes to aggregated growth of the polyoxyethylene mixture.

The ethoxylation exothermic heat is taken into account by including a source term Q_R to Equation 6. 12 above:

$$\frac{\partial}{\partial t}(\rho H) + \nabla \cdot (\rho U H) = \nabla \cdot ((\frac{\lambda}{C_p} + \frac{\mu_T}{\sigma_H})\nabla H) + Q_R ,$$

6. 17

where

$$Q_R = -\sum_j^{N_R} R_j \Delta H_{Rj}(T),$$

6. 18

with H_{Rj} referring to the heat of reaction.

6.4 Solution procedures

6.4.1 Generic scalar convection-diffusion equation

As can be noticed, there are significant commonalities between the various transport equations described above (apart from the continuity equation), which can be written into a generic form with the conserved variable representing a velocity component, enthalpy (or temperature), mass fraction of a chemical species or a turbulence quantity:

$$\frac{\partial}{\partial t}(\rho\phi) + \nabla\cdot(\rho U\phi) = \nabla\cdot(\Gamma\nabla\phi) + S_\phi,$$

6. 19

where Γ is the relevant effective diffusion coefficient for variable ϕ (including the molecular contribution) and S_ϕ is the source or the sink term. The nature of a conservation equation is highly non-linear. Thus, numerical solution of the set of conservation equations follows the three-stage task as suggested by Ranade *et al*. (1989b): (1) translation of the partial differential equations (PDEs) into their discretised version in the form of a linear algebraic equation; (2) application of a suitable algorithm to handle various interactions and couplings, and (3) solving the resulting algebraic equations.

The method applied to solve the PDEs in CFX4.4 is the finite-volume method with a co-located grid arrangement. In the finite-volume method, the computational domain, which defines the area to be modelled, is meshed into a number of control volumes (Patankar, 1980; Versteeg and Malalasekera, 1995). Each control volume surrounds a fixed grid point where the conservation principles are applied in space. In this version of the CFX, the structured grid system is used, in which the control volumes or cells are hexahedral in shape as shown in Figure 6. 1. Each cell, defined by eight vertices, has six faces and in turn, six neighbouring cells (shown as uppercase letters in Figure 6. 1). Conservation variables are defined and stored at the centroid of the control volume (noted **P** in Figure 6. 1). The transport of flux quantities are through the cell faces between the neighbouring cells as indicated by lowercase letters.

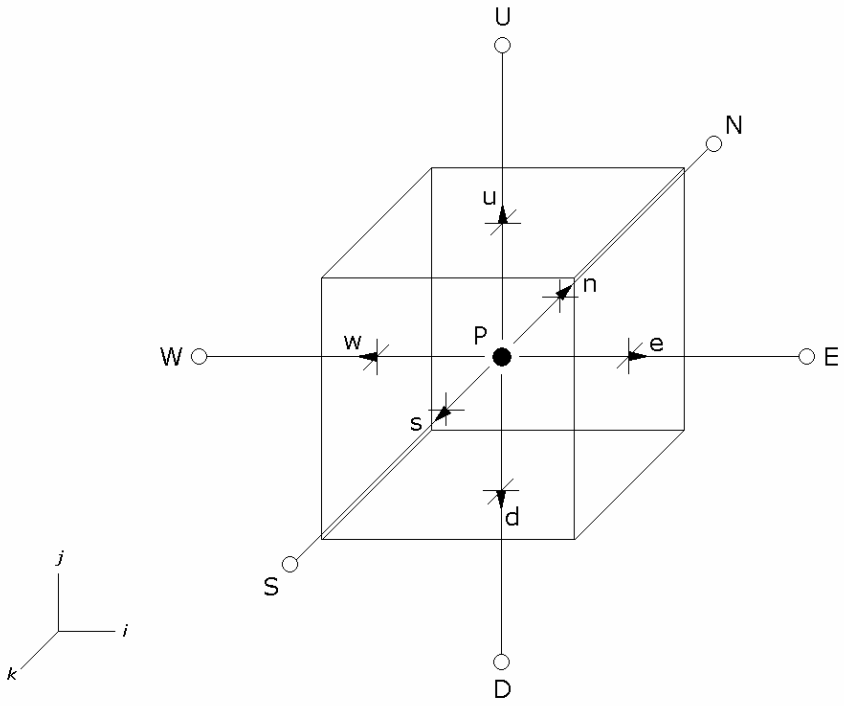

Figure 6. 1 A control volume for cell P.

A number of control volumes are grouped into a block. CFX4.4 allows a multi-block grid structure in which blocks adjacent to each other are glued together with the cells at the block junction joined in whole faces. However, blocks do not necessarily join at whole block faces. In a structured grid arrangement, each cell within a block is indexed with a unique identity in the local block coordinate (*i*, *j*, *k*) with its neighbouring cells labelled consecutively following the (*i*, *j*, *k*) directions.

6.4.2 Discretisation

The starting point for the computational procedures using the finite volume method is the integration of the generic scalar convection-diffusion over a control volume. The integration is further discretised into an algebraic expression which connects the conservative variable at the centroid of the control volume with its neighbours. When the number of control volumes becomes large, the solution of the discretised equations is expected to approach the exact solution of the differential equation.

Integration of the generic scalar convection-diffusion in Equation 6. 19 over a control volume (CV) yields:

$$\underbrace{\int_{CV}\frac{\partial}{\partial t}(\rho\phi)dV}_{\text{transient}}+\underbrace{\int_{CV}\nabla\cdot(\rho U\phi)dV}_{\text{advection}}=\underbrace{\int_{CV}\nabla\cdot(\Gamma\nabla\phi)dV}_{\text{diffusion}}+\underbrace{\int_{CV}S_{\phi}dV}_{\text{source/sink}}\quad .$$

6. 20

The volume integrals for the convection and diffusion terms are rewritten as integrals over the entire bounding surface of the control volume by using Gauss's divergence theorem which for a flux term *J* states that

$$\int_{CV}\nabla\cdot JdV=\int_{A}\mathrm{n}\cdot JdA\,,$$

6. 21

giving:

$$\int_{CV}\frac{\partial}{\partial t}(\rho\phi)dV+\int_{A}(\rho U\phi)\cdot\mathrm{n}dA=\int_{A}(\Gamma\nabla\phi)\cdot\mathrm{n}dA+\int_{CV}S_{\phi}dV\ .$$

6. 22

The accuracy of the solutions of the model equations is determined by how closely the discretised equations representing the original PDEs, in particular the treatment of the convection terms. It should be noted that the convection term has an inseparable connection with the diffusion term; the two terms are discussed as one unit. The following section briefly describes the differencing methods applied for each term in Equation 6. 22.

6.4.3 Differencing schemes

A one-dimensional array of control volumes is illustrated in the following figure to aid the understanding of various differencing schemes used in the numerical model described in this chapter:

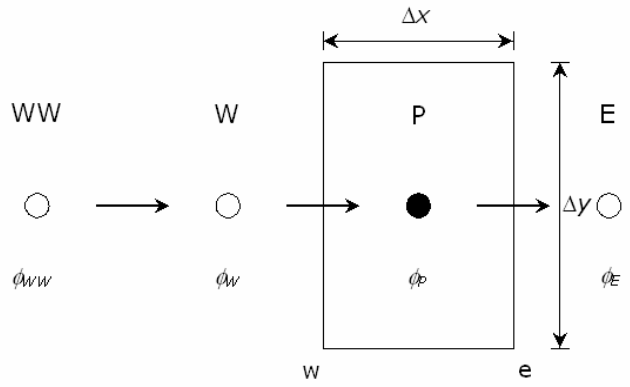

Figure 6. 2 Illustration of a one-dimensional control volume of P.

The nodes are labelled as WW, W, P and E in the direction of the flow with respect to the control volume P to be calculated. The faces encasing the control volume P are labelled as w and e, indicating the west and east faces. ϕ represents the conserved variable at a node or at a face with respect to the uppercase or lowercase subscript.

Starting with the most straightforward principle of differencing and interpolation, the central difference uses the arithmetic mean of the values at two nodes to approximate the value at the cell face between them. The discretisation of the convection term at the west face *w* of the control volume P by a central difference scheme is written as

$$\phi_w = \frac{(\phi_P + \phi_W)}{2} .$$

6. 23

For the diffusion term at west face *w*, using central difference to approximate the first derivative gives

$$(\Gamma A \nabla \phi)_w = \frac{\Gamma A_w}{\Delta x_w}(\phi_P - \phi_W) ,$$

6. 24

where A_w represents the area of the west face *w* and Δx_w represents the distance between the nodes W and P. This scheme is accurate to second-order and was initially thought to be the most natural discretisation scheme for the convection term. However, the scheme gives physically unrealistic results when the flow regime is outside the low Reynolds number flow. One remedy to overcome the weak formulation for the convective properties at the interface in the central difference method is the simple upwind difference with first-order accuracy. In the upwind difference method, the convective value of ϕ at the west face of the control volume P (ϕ_w) is replaced by the value of ϕ at the grid point on the upstream side of that face, that is, ϕ_W. The first-order accuracy makes the upwind scheme inherently prone to numerical diffusion errors (gross overestimate of the diffusion term), in particularly when the diffusion is almost absent in the flow.

The hybrid scheme is an improvement of upwind difference, which expresses the values at the cell faces using a combination of second-order central difference and first-order upwind difference. When the Peclet number (a measure of relative strengths of convection and diffusion) is less than or equal to two, the hybrid scheme is identical to the central difference. When the Peclet number is greater than two, the hybrid scheme reduces to the upwind difference but the diffusion is set to zero (Patankar, 1980). The advantage of using the hybrid scheme over the upwind difference is that the hybrid scheme does not share the shortcoming of the upwind difference described above and yet when dealing with low Reynolds

flows, the second-order central difference is used. The hybrid scheme is the default method used in CFX4.4.

Another possible improvement to the first-order accurate upwind difference is a higher order accurate differencing scheme. The quadratic upstream interpolation for convection kinetics (QUICK) is a third-order accurate upwind scheme that uses the values at two upwind nodes and one downstream node for cell face values. Brucato *et al*. (1998) tested both the QUICK and hybrid discretisation schemes for the convective terms when the grid independence was achieved in a stirred vessel simulation under the turbulent conditions. They found that the results obtained had little difference between the two; the effects of numerical diffusion associated with the upwind scheme were insignificant and the turbulent diffusion was largely dominant. The hybrid scheme was used throughout this work.

The transient term is discretised using the Euler implicit scheme

$$\int \frac{\partial}{\partial t}(\rho\phi)dV = \left[(\rho\phi)^{n} - (\rho\phi)^{n-1}\right]\frac{\Delta V}{\Delta t}$$

6. 25

where superscript *n*-1 denotes the previous time step and ΔV is the cell volume. This implies that all the terms in Equation 6. 22 are calculated at the current time step.

The source term of each model equation is linearised into the following form:

$$\int S_{\phi} dV = SU + SP\phi_{P}$$

6. 26

where *SP* must be non-positive as positive *SP* may cause divergence. For the positive variables, such as mass fraction of a chemical species Y_i, turbulence kinetic energy *k* and the energy dissipation ε, a further requirement is that *SU* must be always positive (Patankar, 1980).

6.4.4 Pressure-velocity coupling

The real difficulty in the calculation of the velocity field arises, as Patankar (1980) pointed out, in the unknown pressure field and yet pressure is not included in the governing equations but the pressure gradient is. Thus, the pressure field is to be obtained indirectly. Patankar and Spalding (1972) proposed an algorithm known as SIMPLE (semi-implicit method for pressure-linked equations) to couple the pressure and velocity fields, in which a pressure-correction equation is derived via a combination of continuity and momentum equations with some certain assumptions. The algorithm starts with a guessed pressure field. With this pressure field, it solves the momentum equation to obtain the velocity field, followed by the solution of the pressure-correction equation, then the corrections of both the pressure and velocity fields to enforce mass continuity. The algorithm continues to solve for other conserved variables,

such as temperature, concentration, turbulence parameters if they influence the flow field. The corrected pressure is now the pressure field to be used at the start of the procedure and the algorithm is repeated until a converged solution is obtained. For the current work, a modification of SIMPLE, SIMPLEC (Van Doormal and Raithby, 1984), is used. SIMPLEC (C for consistent) differs from SIMPLE in its derivation of a simplified momentum equation. The use of SIMPLEC is preferred because of its reduced sensitivity to the selection of under-relaxation factors as well as fewer requirements for under-relaxation.

6.4.5 Rhie-Chow interpolation method

The Rhie-Chow interpolation formula (Rhie and Chow, 1983) is used to prevent the checkerboard oscillations of the velocity and pressure fields caused by the use of weighted linear interpolation for the velocity components on control volume faces from those at control volume nodes. The formula is equivalent to the addition of a pressure-diffusion term.

6.4.6 Linear equation solvers

After the model equation (Equation 6. 19) is discretised and the treatment for interactions and couplings is chosen, the task of a numerical method that remains is to devise a suitable mechanism to solve the set of linear algebraic equations. Iterative solvers are preferred because of their storage requirements and ability to handle non-linearities (Patankar, 1980). The solver returns the updated values of a variable for next solution of the linearised equations and the process repeated until the convergence is achieved. CFX has several in-built solvers. For the stirred tank modelling in this work, the CFX default solver called block Stone's method, based on the strongly implicit procedure of Stone (1968), that solves the equations block by block is used. Block STONE is used for all equations including pressure, except for turbulence quantities where the line relaxation solver is used.

6.4.7 Additional model information

The following under-relaxation factors (default) are used: mean velocity vectors U_x, U_y, U_z, 0.65; pressure P, 1.0; enthalpy H, 1.0; turbulence kinetic energy k, 0.7; the turbulence dissipation rate ε, 0.7; and mass fraction Y_i, 1.0.

6.5 Conclusions

The governing equations for the numerical model for a stirred ethoxylation reactor were given in this chapter, including brief descriptions on the differencing schemes and solution procedures and references to the Rhie-Chow interpolation method and the pressure-velocity coupling algorithm.

The ethoxylation numerical model was solved using the finite-volume method with the hybrid discretisation scheme for the convection terms. The SIMPLEC algorithm was used to couple the pressure and velocity with Rhie-Chow interpolation to prevent the checkerboard oscillations due to the co-located grid system.

Chapter 7

Numerical Simulations of Ethoxylation Reactors

7.1 Introduction

The aim of the second stage of this research project as stated in Chapter 5 was to develop a CFD based process simulation model for a commercially operated stirred ethoxylation reactor to be used for optimising the productivity and for the design of a new reactor system. The model would incorporate the chemical kinetics established in the first stage of the research program with the physical transport processes to be studied in this stage including mass, heat and momentum.

As a part of the objectives outlined above was to determine the optimum operating conditions for the existing ethoxylation reactors, it was necessary to first pinpoint the rate-limiting factors and analyse the original design including the agitation and ethylene oxide injection systems. These were to be carried out prior to elaborating the reactor system into a CFD model.

The industrial reactor to be modelled is a reactor in the NIS A alkoxylation plant operated by Huntsman Corporation Australia (HCA). Its rate-limiting factor could be mixing (mass transfer), heat removal, or reactor pressure rating (mass transfer). Earlier investigation by HCA suggested that the mass transfer control primarily dominated the operation in the laboratory-scale autoclave. Additionally, the alkoxylation rates in the autoclave were up to five times faster than the rates in the industrial-scale reactors. Hence, the latter was assumed to operate under significant mass transfer control, even though the Reynolds number of the laboratory-scale autoclave will be shown later (in Section 7.2.5) to be at least one order of magnitude less than that of the industrial reactor. Moreover, mass transfer constraint arising from mixing was also used to explain the noticeable differences in alkoxylation rates between two NIS A reactors that were identical in size and design, but equipped with two different types of impellers. Thus,

based solely on these observations without thorough analysis, mixing was made the main scope of the study initially. Nevertheless, the postulation was largely based on years of operational experience: there was no solid, conclusive analysis in the form of formal documentation. Therefore, the identification of the rate-limiting factors should begin with an examination in detail of the reaction profile, where available, followed by a systematic and theoretically sound analysis of the reaction data.

In Section 5.2.4, it was suggested that the ethoxylation process in a stirred NIS A reactor could be treated as a single phase liquid mixing problem. This assumption was at odds with the literature discussed in Chapter 2 that treated ethoxylation as a gas-liquid reaction, in which ethylene oxide was present in the reactors as a gaseous reactant. It should be noted that while regarded as a single-phase liquid reaction, ethoxylation in this context did not necessarily involve resistance of inter-phase transfer between gas and liquid. An operational advantage to improve the asset productivity of the NIS A plant could be proposed as an outcome for this treatment: because the main reaction occurs in the bulk liquid, the higher the ethylene oxide concentration to be kept in the reaction mixture, the higher the reaction rate and the shorter the ethoxylation time would be. Therefore, the ideal situation would be ethylene oxide injection of 100% liquid into the reaction mixture all the way through the course of operation. To verify further the assumption of liquid ethylene oxide injection in a NIS A operation, a range of various operating conditions was numerically studied to compute the temperature of the ethylene oxide flow at the exit of the dip-leg pipe. A comparison of the corresponding ethylene oxide saturation pressure at the computed temperature with the system pressure would determine whether or not the ethylene oxide was boiling.

In determining the rate-limiting factors and analysing the reactor design, the definition of the scope of the CFD model became clearer. One of the main advantages of the CFD technique is its ability to examine the effect of process variations quickly and reliably. This is particularly useful for a process that involves hazardous materials and operations, where physical experimentation outside the operation perimeter is not always possible to perform. When the CFD model of a process is defined and carefully validated for the chosen conditions, it allows other modifications to be tested computationally. In the case of simulation of a NIS A ethoxylation reactor, the scope was to quantify the improvement in productivity in terms of ethylene oxide injection rates once the rate-limiting factor was identified.

The validation of the CFD model for an ethoxylation process will be undertaken in three stages. The first stage will model a single phase liquid agitation system based on the literature with experimental data on velocities, e.g., Wu and Patterson (1989). The second stage will implement the laboratory ethoxylation process into a CFD model, with the integration of the kinetic model established in Chapter 4. The third stage will extend the CFD model to incorporate the operating features in the industrial reactors.

When fully validated, process outcomes of the CFD model with new operating conditions becomes predictable. Further runs can then be conducted to determine the optimum operating conditions for the existing ethoxylation reactors as well as to explore the design specification for a new reactor.

To document the step-by-step debottlenecking of the operating limitations which leads to the optimisation of the existing NIS A reactors, this chapter begins with a thorough examination of the behaviour of several reaction variables, in particular those related to the three limiting aspects mentioned above. An initial analysis of the reaction data will point the way to the physical aspect that mainly constrains the current productivity. A further analysis is then performed to quantify the limitation that has been identified. As mentioned in the beginning of this chapter, the ethylene oxide injection system must be fully understood prior to the application of the CFD techniques into a stirred vessel. This helps to appropriately define the scope of the CFD model of a stirred ethoxylation reactor study. The later section of this chapter then presents the development of the working process model for an existing ethoxylation reactor, including the description of the CFD model and its validation against both laboratory and industrial data collected from HCA reactors. Once the identification of the current rate-limiting factor in the reactor operated by HCA is fully achieved and the optimum operating condition determined, a new reactor specification for substantially improving the reactor productivity may be suggested.

All simulations in this work are carried out using a commercial CFD code, CFX4.4.

7.2 Identification of the rate-limiting factor

The identification of the rate-limiting factor in the current NIS A alkoxylation plant is focussed on the following three areas: mixing, heat removal and reactor pressure rating. It seeks to shed light on the perceptions of the plant technical staff of HCA, that are (1) the noticeable differences in alkoxylation rates between two NIS A reactors that were identical in size and design, but equipped with two different types of impellers; (2) the alkoxylation rates in the laboratory autoclave were up to five times faster than the rates in the industrial NIS A reactors. In order to take appropriate measures in elucidating the causes for these observations, it was essential to be familiar with the underlying reactor design and operation scheme for each reactor system. The reader is advised to refer to Chapter 3 for the specification of the laboratory autoclave and the details of its operation. Therefore, the following section only includes an outline on the commercial NIS A alkoxylation plant and operations.

7.2.1 An overview of the NIS A plant and the operations

There are approximately 300 different nonionic surfactants which are manufactured in the NIS A alkoxylation plant of HCA at Botany. Major products include nonylphenol ethoxylates (N6, N9, N11, N40, ...) and fatty alcohol ethoxylates (12A3, 12A6, …). The NIS A alkoxylation plant comprises six industrial stirred reactors, two with a reactor capacity of $6m^3$ and the rest of $10m^3$. Each of the NIS A reactors is mechanically agitated by a single six-bladed pitched blade turbine (PBT), a dual-Lightnin A315 impeller or a dual-Rushton impeller. Unless otherwise mentioned, the PBTs used in the NIS A plant are all of six-bladed configuration. The reactors with the pitched blade turbine may also be fitted with a set of 2 or 4 welded extension blades as shown in the following figure:

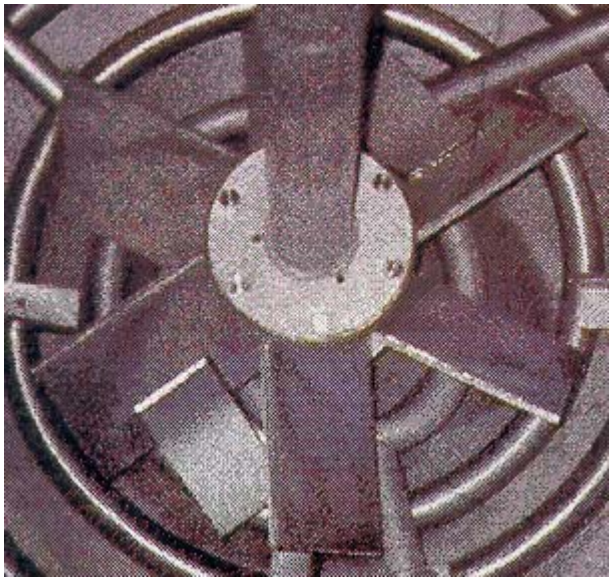

Figure 7. 1 The NIS A reactor with a single six-bladed pitched blade turbine with 2 extension blades.

Throughout this thesis, when we describe the NIS A reactor with the dual-Lightnin A315 impeller (Figure 5. 6 on page 89), we refer to it as QD2 whilst the reactor with the dual-Rushton impeller (Figure 5.8 on page 92) is referred to as QD3. Both QD2 and QD3 have a volumetric capacity of $6m^3$. The $10m^3$ reactors include QD1, stirred by a single PBT; QD4, a PBT with 2 extension blades as shown in Figure 7.1; QD5, a PBT with 4 extension blades; QD6, dual Lightnin A315s. A summary of the reactor configuration of the six NIS A stirred vessels is presented in Table 7. 1:

Table 7. 1 An overview of the NIS A reactor configuration.

	QD1	QD2	QD3	QD4	QD5	QD6
Dimensions						
Total capacity, m^3	10	6	6	10	10	10
Height, mm	3277	2807	3277	3277	3277	3277
Outside diameter, mm	2134	1829	1829	2134	2105	2105
Design						
Normal operating pressure, bar	3.62	3.62	3.62	3.62	3.62	3.62
Design pressure, bar	4.45	4.45	4.45	4.45	6.17	6.17
Design temperature, °C	200	200	200	200	200	200
Ethylene oxide peak flow rate, kg/min	28	18	18	28	28	28
Agitation method						
Agitator type	PBT	Lightnin A315	Rushton	PBT	PBT	Lightnin A315
Impellers (number of sets)	1	2	2	1	1	2
Top blades diameter, mm	none	812	711	none	none	913
Number of blades	N/A	3	18	N/A	N/A	3
Distance to next impellers, mm	N/A	900	500	N/A	N/A	900
Bottom blades diameter, mm	838	812	350	838	838	913
Number of blades	6	3	18	6 (2 ext.)	6 (4 ext.)	3
Distance off bottom, mm	460	305	315	400	400	380
Working (maximum) agitator speed, rpm	100	150	100	100	100	130

The operational scheme employed in the commercially operated NIS A reactors is outlined below. In the industrial ethoxylation, the reactor pressure and temperature are controlled by modulating both oxide flow and cooling water flow to achieve the desired settings. As described in Section 5.2.4, the ethylene oxide flow is maintained below a safety threshold as an operational precaution against the explosion hazard of the oxide at high temperature operation. To safeguard against the explosion hazard, nitrogen padding of 1 atmosphere pressure is inserted into the reactor at the start of an ethoxylation run. Accordingly, an explosive limit is calculated based on the partial pressure of the nitrogen present. The oxide flow is modulated such that the resulting concentration of oxide in the vapour space is kept marginally below the calculated explosive limit at all times. It should be noted that apart from the nitrogen padding initially inserted for the safety concern, the amount of nitrogen in the vapour space also originates from the nitrogen dissolution in the feed ethylene oxide due to the nitrogen padding in the ethylene oxide storage break tank. Because the semi-batch mode of operation is applied, the liquid level rises with the continuous insertion of ethylene oxide units into the hydrophobic reaction contents. The nitrogen partial pressure, inert to the reactions, increases as a result. Ultimately, a maximum safety margin obtained from the calculated explosive limit is reached which allows the flow of ethylene oxide injection to reach a maximum.

To best demonstrate the above operation scheme by graphical representations, the ethoxylation profiles in a NIS A reactor including the reaction temperature and ethoxylation rate are plotted against the reactor pressure in this thesis unless otherwise mentioned. It should also be noted that the ethoxylation rate is recorded as ethylene oxide mass flow rate in a typical plant batch report which also includes the data on the actual reactor pressure, nitrogen partial pressure and reactor temperature.

It can be seen from Table 7. 1 that the reactors of $10m^3$ capacity accommodate higher ethoxylation rates than the $6m^3$'s. A comparison of the reaction data sourced from both $6m^3$ and $10m^3$ batches for the same ethoxylate production suggests an explanation for this rate difference. In Figure 7. 2, the trend of the ethylene oxide partial pressure against the reactor pressure for an N4 production in QD2 ($6m^3$) and QD5 ($10m^3$) is compared. It should be noted that the ethylene oxide partial pressure was obtained from the difference between the total reactor pressure and the nitrogen partial pressure available from the plant batch report. It should also be noted that the last five digits following the reactor identification refer to the batch identification number in the HCA process database.

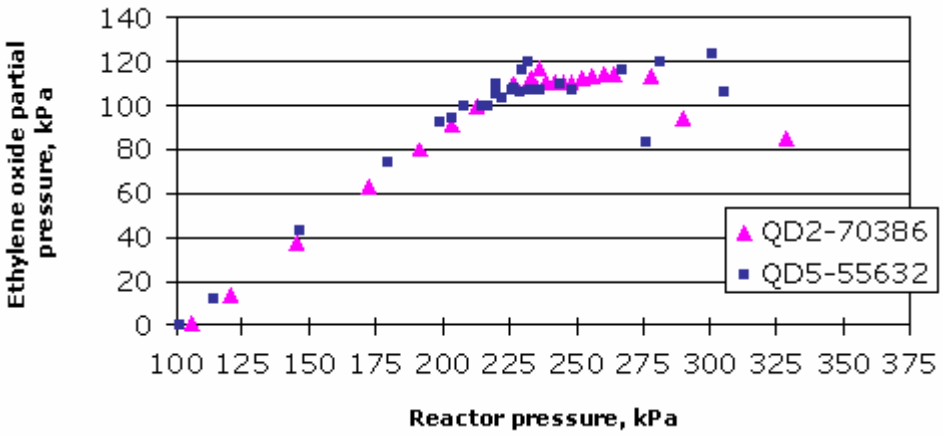

Figure 7. 2 Comparison of ethylene oxide partial pressure versus the reaction pressure in QD2 to that in QD5 for the N4 production.

Despite the obvious difference in the reactor sizes, the trend of the ethylene oxide partial pressure in response to the reactor pressure is almost the same in both reactors as can be seen in Figure 7. 2. This indicated that the corresponding ethylene oxide concentration in both volumes of the reaction mixture was kept at the same level. Since the larger reactor has a greater volume of reaction mixture, it allows higher ethylene oxide mass, hence higher ethylene oxide mass flow rate.

7.2.2 QD2 versus QD3

With the operation scheme employed in all NIS A ethoxylation operations, as described previously, HCA had noted differences in ethoxylation rates between two reactors that are identical in size but equipped with different agitator configurations. The most noticeable pair was QD2 and QD3, the former equipped with a dual-Lightnin A315 impeller and the latter with a dual-Rushton turbine. In this research project, QD2 and QD3 were therefore used as a means of examining the differences in performance. The reason advanced for the differences was the enhancement of the gas-liquid contacting by the use of the dual-Lightnin A315 impeller in QD2. This, however, was based on the consideration of the ethoxylation process as a typical gas-liquid reaction system.

Since this research project suggested ethylene oxide as a liquid reactant in HCA ethoxylation operation (see Section 5.2.4), the ethoxylation was regarded as a liquid reaction between miscible species. However, at this stage of the thesis, this was not yet justified. The most fundamental approach to explain the rate difference between the two reactors was to directly compare the reaction data of a NIS product that was manufactured under identical operating conditions in both reactors. For this purpose, a branched C12-C15 alcohol ethoxylate was chosen for the comparison of the reaction data in QD2 and QD3. Although the ethoxylation process addressed in this thesis has been focussed on nonylphenol ethoxylation,

the majority of the nonylphenol ethoxylates are manufactured in QD2 and other $10m^3$ reactors but not in QD3. For the purposes of this analysis, the use of an alcohol ethoxylation should not significantly affect the conclusions, since the manufacturing process was essentially the ethylene oxide condensation onto a hydrophobe as described in Section 2. 3, with similar hydrophobes being used in this case.

Figure 7. 3 plots the reaction data sourced from both QD2 and QD3 batches for the chosen branched C12-C15 alcohol ethoxylate. Six batches, three from each reactor manufactured during the Year 2002 were arbitrarily chosen for comparisons of the reaction data. It can be seen that the reproducibility of the reaction data in the industrial reactors was good. Normally, each batch required a few cycles of opening and closing the ethylene oxide valve to reach the desired number of ethylene oxide units in the product. Unless otherwise mentioned, all data readings were taken from the first cycle in the operation with a fresh hydrophobe charge as the starting material.

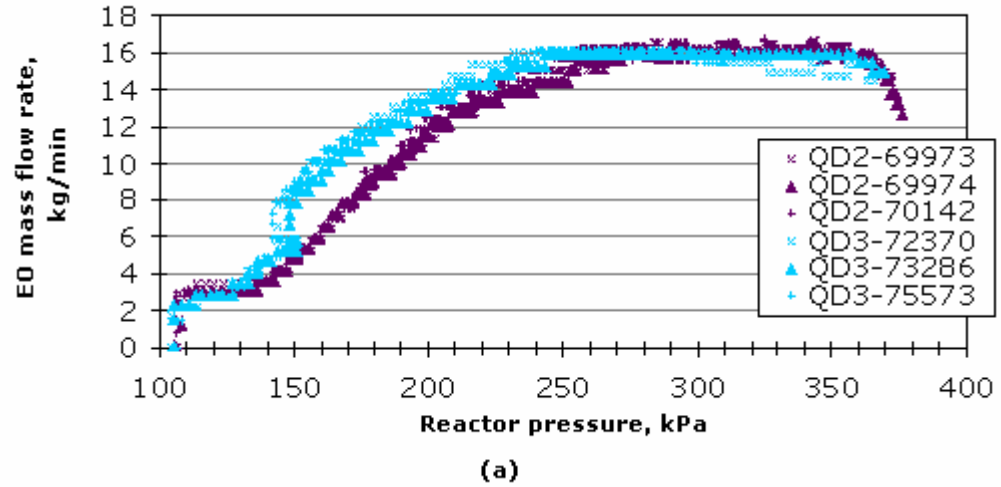

(a)

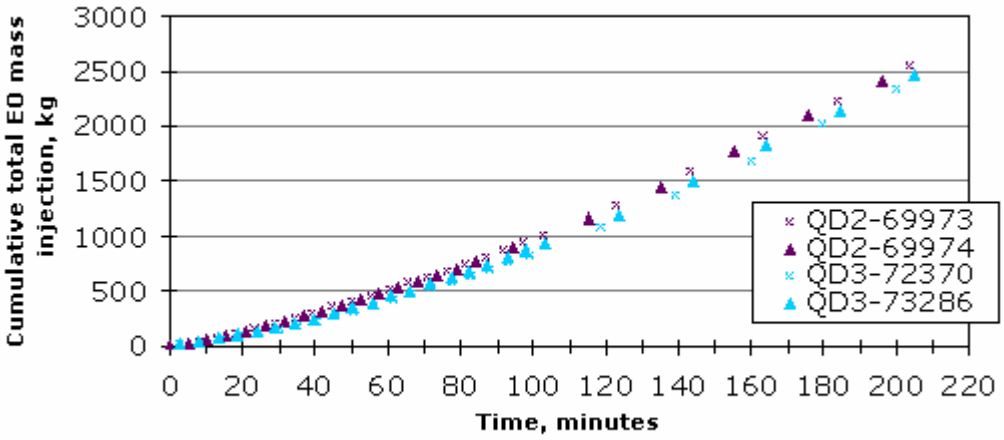

(b)

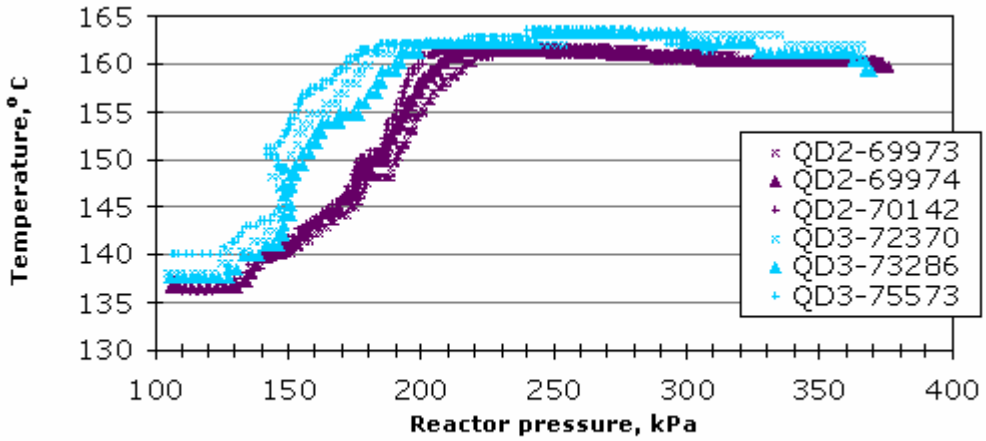

(c)

Figure 7. 3 Comparison of the reaction run data obtained from QD2 against that from QD3 using a branched C12-C15 alcohol batches: (a) ethylene oxide mass flow rate; (b) cumulative total ethylene oxide mass injected; (c) reaction temperature.

Given the perceived poorer QD3 performance, it was surprising to find the reactivities in both reactors alike in many points of comparison:

- the ethylene oxide mass flow rate in both reactors reached a maximum value about 16kg/min when the pressure was above a certain level as shown in Figure 7. 3(a);
- the plot of cumulative total ethylene oxide mass fed versus time in Figure 7. 3(b) did indicate higher mass injection in QD2 than in QD3 in the same period of time, however the difference was insignificant;
- the sigmoid behaviour of the temperature plot shown in Figure 7. 3(c) reflected the way in which the temperature was controlled: from a low initial value at the start of the operation, it was raised, with the aid of the reaction exothermic heat, to the desired reaction value according to the product specification. In this case, for the chosen alcohol ethoxylate, the production temperature was maintained at approximately 160°C.

Apart from the similarities, Figure 7. 3 also displayed the difference between the two groups of trends. As can be seen, the reaction trends did not entirely agree with one another at lower pressure: the ethylene oxide flow rate in QD3 increased considerably at about 150kPa, leading a higher trend compared to QD2. The cause for this was explained by the heat removal condition in QD3. As can be seen in Figure 7. 3(c), the temperature in QD3 was significantly higher than in QD2 at lower pressure, in particular, over the pressure range between 150 and 200kPa. This indicated a lower heat removal rate in QD3 at that stage. A series of occurrences was expected to follow this temperature rise, e.g., more vigorous reaction, resulting in a sharper drop in partial pressure of ethylene oxide, accompanying an increase in nitrogen partial pressure, finally leading to a higher calculated set-point for the explosive limit of ethylene oxide.

The similarities in the trends of the branched C12-C15 alcohol ethoxylation in QD2 and QD3 discussed above further suggested that the mixing related mass transfer rate was sufficiently alike between the dual-Lightnin A315 impeller and the dual-Rushton turbine. The use of a different impeller configuration, as in QD2 and QD3, apparently did not have a major consequence for the ethoxylation rate in this case. This supported our preference to adopt the geometrical arrangement of QD3 for the development of a CFD working model for the ethoxylation process as the aim for this stage of the research program. The main reason for choosing QD3 for modelling was because the impeller configuration of a radial flow impeller in terms of its geometrical implementation in a CFD model was relatively simple in comparison to that of an axial flow impeller, in the case of NIS A plant, a Lightnin A315 impeller or a pitched blade turbine with extension blades (see Figure 7. 1). Additionally, the experimental velocity distribution in a Rushton stirred vessel was readily available in the literature for validation. However, whilst this research project was concerned with the production of nonylphenol ethoxylates, their manufacture was not performed in QD3. Therefore, the following section attempts to draw a correlation between the data collected in QD2 from standard production for various nonylphenol batches, including N2, N4, N11,

N40 and N50, and the chosen C12-C15 alcohol ethoxylate in QD2/QD3. The main advantage of using a nonylphenol ethoxylate was its availability of the physical data as well as the chemical kinetics which was relatively complete, either in the literature, e.g., densities and ethylene oxide solubilities reviewed in Chapter 2, or in the kinetic model developed in Chapter 4. However, with the ethoxylates manufactured in QD3, e.g., polyethylene glycol 200 (PEG200) and the C12-C15 alcohol ethoxylate cited above, both their physical and chemical data were rather less available in the literature and experiments.

Figure 7. 4 presents the comparison of the reaction profiles from various nonylphenol batches with the chosen C12-C15 alcohol batch in QD2.

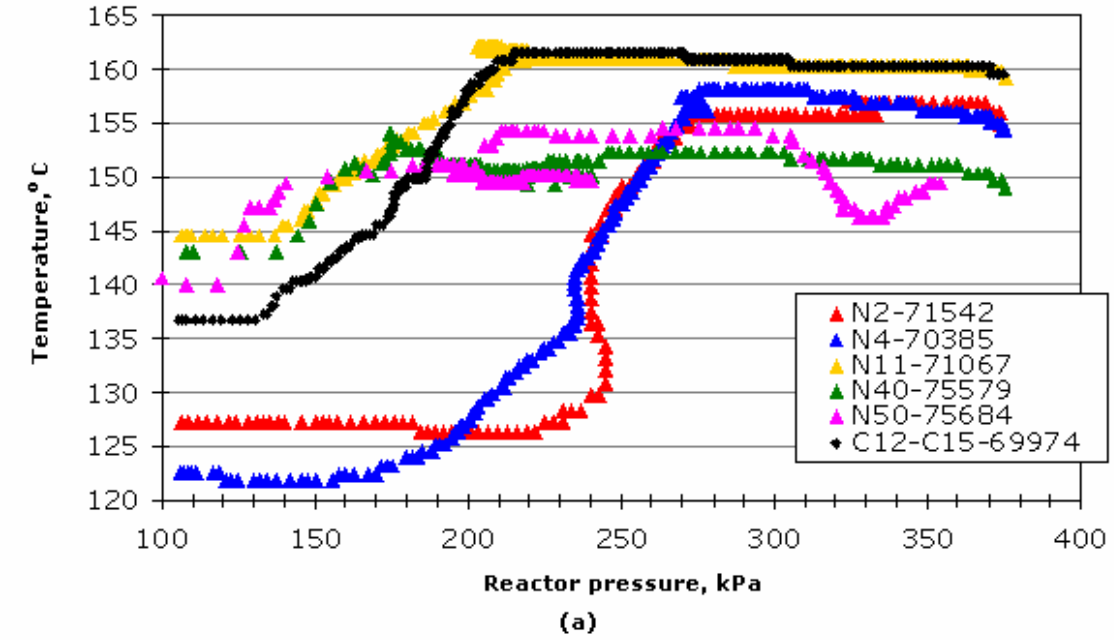

(a)

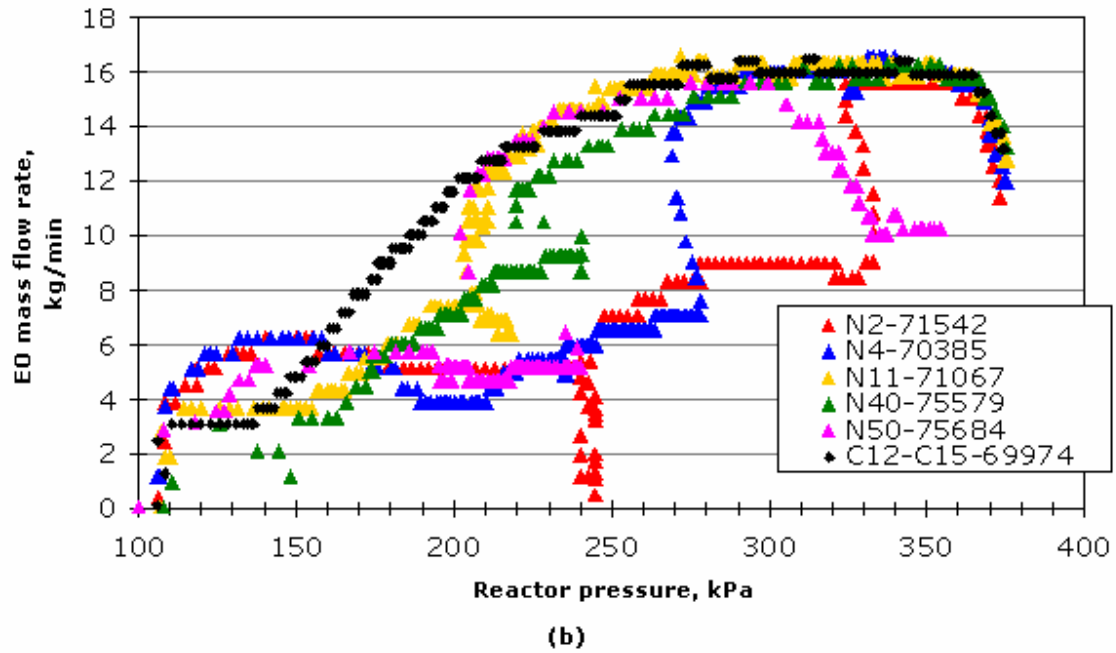

(b)

Figure 7. 4 Comparison of the reaction profiles from various nonylphenol batches with the chosen C12-C15 alcohol batch in QD2: (a) reaction temperature; (b) ethylene oxide mass flow rate.

Figure 7. 4(a) shows the trend of temperature recorded in each of the different production runs of nonylphenol ethoxylates with a comparison to that of the alcohol ethoxylate. Though the reactor temperature at which the ethoxylation operation began varied considerably for different products, the ethoxylation temperature was normally controlled within the range between 150 and 160°C. It can be seen that N11 and the alcohol ethoxylate displayed a similar trend for temperature (both at about 160°C), above approximately 220kPa.

The trends of ethylene oxide injection rate for the above mentioned production are presented in Figure 7. 4(b). It can be seen that the injection rate levelled off at a maximum of approximately 16kg/min in every nonylphenol batch of different numbers of ethylene oxide units at various levels of the reactor pressure. For example, for N2 manufacture, the injection rate had a slow build-up against pressure while for N50 manufacture, it reached the maximum value at the much lower pressure. The difference of the profile was related to the amount of the nitrogen padding of 1 atm initially inserted to keep ethylene oxide under explosive zone. The molar amount of nitrogen inserted in the padding varied considerably between nonylphenol ethoxylates with different number of adducts. Because the volume of the raw material charged at the start of each operation depended on the amount of ethylene oxide to be added in the final product, batches of high ethylene oxide adduct numbers started at low volume while batches of low adduct numbers started at high volume. That is, for the N50 batch, the volume of the raw material charged was approximately 20% of the reactor capacity; for the N2 batch, it was approximately 65%. The number of moles of nitrogen present in the initial padding in the N50 batch was about double that in the N2 batch. Accordingly, the ethylene oxide explosivity calculated based on the nitrogen pressure in the system was higher for N50 than for N2, resulting in the difference in the profile shown. The trend of the N11 batch was found closest to the C12-C15 alcohol ethoxylation since the volume of the starting hydrophobes was similar.

The trends of N11 and the branched C12-C15 alcohol ethoxylate in both QD2 and QD3 are further examined in Figure 7. 5 below.

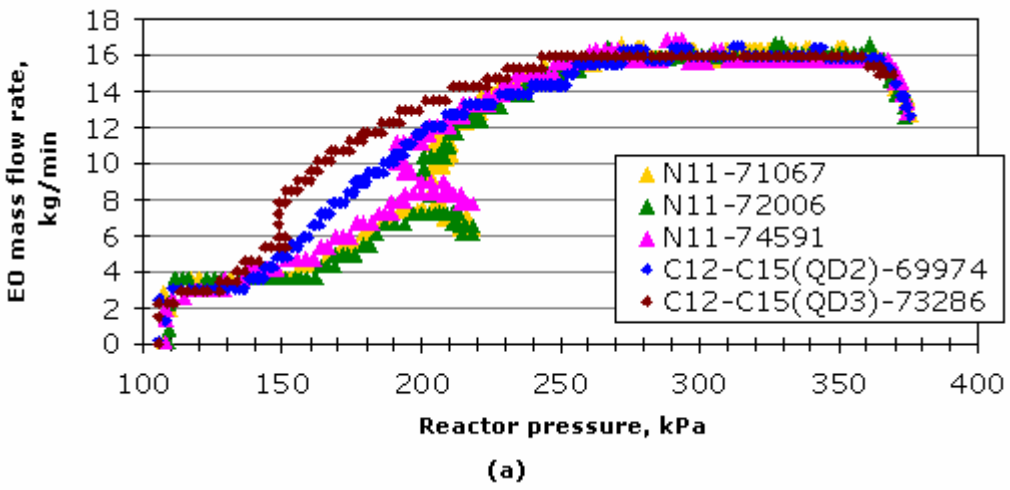

(a)

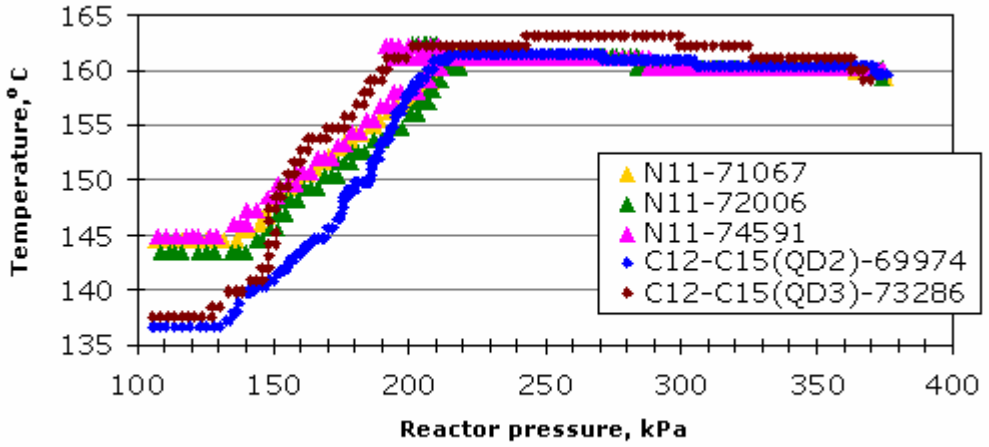

(b)

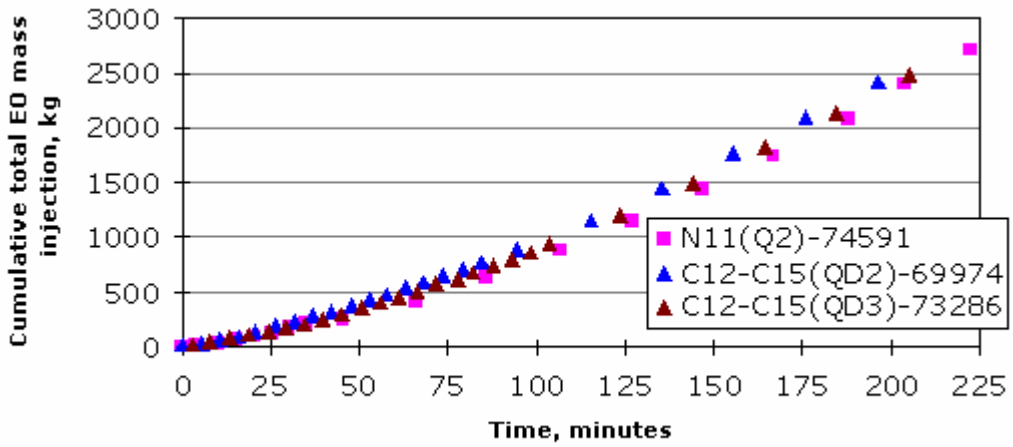

(c)

Figure 7. 5 Reaction profiles for nonylphenol ethoxylates and the chosen alcohol ethoxylate batches in QD2: (a) ethylene oxide mass flow rate; (b) reaction temperature: (c) cumulative total ethylene oxide mass injected, also with the alcohol ethoxylate batch in QD3.

It can be seen in Figures 7. 5(a) and (b), the trends for the ethylene oxide injection rate and temperature in these randomly chosen N11 batches followed a very steady path. It can also been seen that the operating conditions for both N11 in QD2 and the alcohol ethoxylate in either QD2 or QD3 batches were very similar. The cumulative total ethylene oxide mass plotted in Figure 7. 5(c) for the different products in the different reactors also agreed with one another very well. These comparisons confirmed that the mixing pattern and contacting induced by the dual-Lightnin A315 impeller (QD2) and the dual-Rushton turbine (QD3) had an insignificant effect on the ethoxylation rate. The maximum injection rate allowable, at approximately 16kg/min, was apparently product independent. Furthermore, the trends of ethylene oxide mass rate reaching a steady rate as shown in Figures 7. 3 to 7. 5 also indicated that the current NIS A reactors were limited either by heat removal in line with the cooling water capacity or reactor pressure rating attributed to the nitrogen padding. If this was not the case, then the injection rate should continue to increase until the maximum operating pressure was reached.

In summary, the reaction data between QD2 and QD3 were shown to be very comparable; only insignificant difference was found between the two (mainly at lower values of the reactor pressure). The reaction paths were particularly alike at higher values of the reactor pressure. The earlier perception of QD3 having poorer performance than QD2 was therefore dismissed.

The very similar reaction trends observed in QD2 and QD3 allowed us to interchange the reaction data despite the different flow patterns induced by the respective impeller configuration. That is, findings from a CFD simulation of QD3 would be applicable to the manufacture of nonylphenol ethoxylates in QD2. This assured us of our decision to model the Rushton impeller in preference to the Lightnin impeller because we could not model the Lightnin impeller due to its geometry complexity and the time constraints for this research project.

The following sections attempt to identify the role of the heat removal rate and the operating pressure in limiting the current operations.

7.2.3 Cooling capacity

Cooling in NIS A stirred reactors is provided by internal coils with high pressure cooling water (HPCW). During an ethoxylation run, the flow rate of HPCW varies in line with the demand through the adjustment of the cooling water control valve so that the reaction temperature is maintained at the set point. The cooling water has a maximum capacity of 7 tonnes per hour (tph) in QD2 and 8.4tph in QD3 when the control valve is fully open.

It was recorded that in QD2, the cooling water valve was 49% open with a flow rate of 3.9tph during the maximum ethylene oxide injection rate of 16kg/min in a production of nonylphenol ethoxylates at 160°C. While in QD3 for PEG200 manufacture at approximately 150°C, the valve was fully open to discharge the total cooling water capacity at the maximum oxide injection rate of 14.4kg/min. At the maximum ethylene oxide injection rate, the cooling water flow was not at its maximum, in particular, in QD2 operation. At the standard condition of 1atm, this could suggest that the cooling water was partially converted to steam and hence not the full flow of cooling water was needed. The fraction of cooling water converted to steam that the system could cope with then set the limit of the cooling capacity of the reactor system. However, the HPCW used has a line pressure of 960kPa (gauge), measured at the point where the cooling water lines from all the reactors return. This line pressure corresponds to a saturation temperature of 182.5°C and a latent heat of vaporisation of 2.0×10^6J/kg. A value of 112.1°C for the temperature rise was calculated for the nonylphenol batch in QD2 described above with the use of this HPCW. Since the HPCW has an inlet temperature at an ambient value, around 25°C, the exothermic heat from the reaction raises the cooling water outlet temperature in QD2 to approximately 136°C, which is below its saturation temperature of 182.5°C. Similarly in QD3, the full flow of the cooling water indicated that the temperature rise was smaller, emerging further below the saturation temperature.

Therefore, we concluded from the above-mentioned findings that the heat removal was not the capacity limiting factor to the current NIS A ethoxylation operations; the cooling water capacity was ample to provide the heat removal rate that was required.

Further, if the full flow of the HPCW was allowed to reach its saturation temperature, the maximum ethoxylation rate could be increased to 40kg/min in QD2 and 48kg/min in QD3 for manufacturing temperature at 160°C. These were at least double the current ethoxylation rate observed. The ethoxylation rate could be further increased to 163kg/min and 195kg/min in QD2 and QD3 respectively if the HPCW was fully converted to steam.

7.2.4 Reactor pressure rating

The fully automated reactor operation described in Section 7.2.1 is illustrated in the following figure:

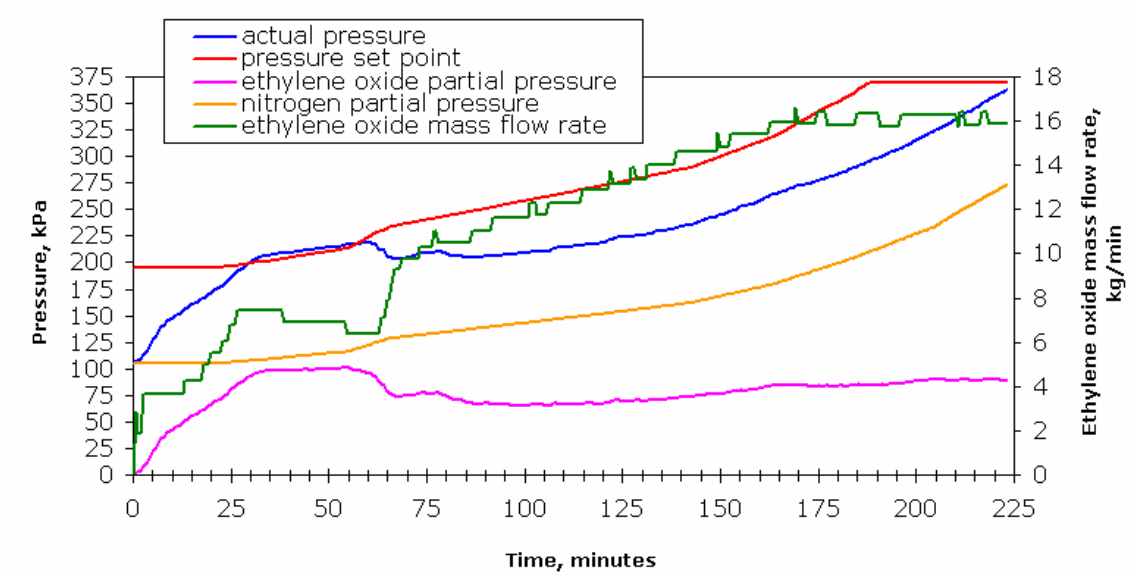

Figure 7. 6 The control scheme of the reactor pressure for a typical batch in a NIS A ethoxylation operation using the data of a nonylphenol batch in QD2.

The figure above shows the data of actual pressure, nitrogen partial pressure and ethylene oxide mass flow rate collected from a typical plant operation. The nitrogen partial pressure is calculated based on the initial reactor conditions and the varying reactor liquid volume, pressure and volume. The ethylene oxide partial pressure is derived from the difference between the actual pressure and the nitrogen pressure. The path of the desired pressure set point is determined from a relationship between the explosivity limit of ethylene oxide and the existing nitrogen pressure. The explosivity limit sets the allowable mass fraction of ethylene oxide in the vapour space and is calculated as a function of the higher liquid temperature. For example, for a nonylphenol batch the temperature value is taken as 160°C in the determination of the explosivity limit. The calculated set point increases as the batch progresses until an ultimate maximum set point is reached, which is currently 370kPa (absolute), as can be been in Figure 7.6. The actual pressure is manipulated in such a way that it is ramped from its current set point to a new desired set point by a pre-determined ramp rate in kPa/min. This probably explains the overshoot of the actual pressure between t=30 and 60 minutes as shown in Figure 7. 6. The pressure overshoot reflects directly onto the ethylene oxide injection rate with a decrease in the value. As also shown in Figure 7. 6, the initial rise in the reactor pressure is mainly due to the ethylene oxide partial pressure in line with the injection rate. After the initial hump, the partial pressure of ethylene oxide in the remainder of the operation does not vary significantly. Nitrogen partial pressure, on the other hand, continues to rise steadily with the progress of ethoxylation and the reduction of the vapour space from the build-up of the product. As mentioned earlier, the amount of nitrogen present in the vapour space originates from two sources: the

initial nitrogen padding and the nitrogen dissolved in feed ethylene oxide. The former originates from the nitrogen padding at the start-up of an operation that is used to safeguard against the ethylene oxide explosive hazards; the latter is due to the nitrogen padding in the storage tank of ethylene oxide, that is reported to be an average of 8.2×10^{-4} kilograms of nitrogen per kilogram of ethylene oxide (Khuu, 2002). In the semi-batch operation with the liquid level continuously rising, nitrogen, being inert, increases in pressure with the extent of the reaction. Since the overall reactor pressure is ramped towards the maximum pressure set point, the increase in nitrogen pressure ultimately limits the amount of ethylene oxide allowed in the system, leaving a relatively flattened profile for ethylene oxide partial pressure as seen in Figure 7. 6. Consequently, the amount of ethylene oxide retained in the liquid is limited and hence the injection rate reaches a limit. Therefore, it is concluded that the current ethoxylation rate in the NIS A operation is reduced by the use of nitrogen padding.

7.2.5 Laboratory autoclave versus industrial NIS A reactor[1]

It became clear that the reactor pressure rating is the major constraint to the current asset productivity of the industrial NIS A plant, and mixing-induced mass transfer and cooling water capacity are not rate limiting. Therefore, the design pressure of the reactors is the main factor behind the differing rates displayed between the laboratory autoclave and the full-scale industrial reactors.

As shown in Table 7. 1, the design pressure for a NIS A reactor is 4.45 bar or 6.17 bar (absolute), with the normal operating pressure kept under 3.62 bar (absolute). These values are compared to the maximum working pressure of 6 bar and the normal operating pressure of 4 bar for the 2-litre autoclave listed in Table 3. 1. The same normal operating pressure of 4 bar (absolute) also applies to the 4-litre, 10-litre and 20-litre autoclaves. With the specifications of higher normal operating pressure, the autoclave reactors clearly allow a higher ethylene oxide concentration in the system. Furthermore, it should be noted that an initial nitrogen padding, when inserted, corresponds to a lower nitrogen amount in a autoclave than that in a NIS A reactor[2]. That is, the ethylene oxide partial pressure is higher in the autoclave reactor. As a result, higher ethoxylation rates were observed in the laboratory operation.

[1] The impeller Reynolds numbers for the laboratory autoclave and the industrial reactor QD3 are 1.3×10^{4} and 3.8×10^{5} at their working agitator speeds of 1700rpm and 100rpm respectively. The working fluid used in this case is an N2 batch at 155°C with ρ=893kg/m^3, μ=1.96×10^{-3}kg/ms.

[2] According to ideal gas law, when $P_1 = P_2$ and $T_1 = T_2$, $\frac{n_1}{V_1} = \frac{n_2}{V_2}$. But $V_1 < V_2$, then $n_1 < n_2$.

7.3 Ethylene oxide injection system

The mode of ethylene oxide injection in both the laboratory autoclave and the industrial NIS A reactors was discussed in Sections 5.2.4 and 7.2.1 above. In both set-ups, a dip-leg pipe is used as the means for ethylene oxide injection. The pipe has its top end open to a line from the ethylene oxide storage and the other end extending to near the base of the reactor vessel. It was proposed that the use of a dip-leg pipe for ethylene oxide injection raised the possibility that the ethoxylation process in the current operation was essentially a single-phase liquid mixing and hence a liquid reaction between miscible species. This type of the reaction system is preferred in commercial operations of HCA because keeping ethylene oxide as a liquid in the reaction mixture avoids the mass transfer problem from vapour into the liquid. Furthermore, the higher the ethylene oxide concentration in the reaction mixture, the higher the rate of the ethoxylation and the shorter the time it takes.

The assumption of liquid ethylene oxide injection appeared to be true in the autoclave laboratory as discussed earlier in Section 5.2.4. This section is concerned with determining the state of ethylene oxide injection system in the NIS A operation. The ethylene oxide injection will be described as a single-phase liquid system subjected to heat input from the surrounding medium. The effects of pipe sizes, ethylene oxide injection rates and bulk reaction temperature on the exit flow temperature will be numerically investigated. The saturation pressure corresponding to the computed exit temperature will be compared with the system pressure to determine whether the ethylene oxide boils.

The dip-leg pipe used in the NIS A reactors is a stainless steel pipe. The specification of the pipes studied in this section is summarised in Table 7. 2. Two nominal sizes of the dip-leg pipes are used with respect to the reactor sizes.

Table 7. 2 Specifications of the dip-leg pipes used in the NIS A reactors.

	Nominal pipe size, mm	
Steel pipe Sc 40s dimensions	**40**	**50**
Used in reactors	QD2, QD3	QD1, QD5
Inner diameter $d_{i.d.}$, mm	40.9	52.5
Pipe wall thickness t_w, mm	3.7	3.9
Length L, m	2.7	3.2
Cross-sectional area A_x, mm^2	1314	2165

The peak rate of ethylene oxide flow experienced through the pipe was reported to be no more than 18kg/min for the 40mm pipe in QD2 and QD3 and 28kg/min for the 50mm pipe in QD1 and QD5 (see Table 7. 1).

7.3.1 Operating conditions

A real time measurement was taken when the flow controller valve on the ethylene oxide line was opened for a period of time. At the time of measurement, only QD2 was in use. The upstream line coming from the ethylene oxide storage break tank just before the feed controller valve to the reactor was measured at a temperature of 17.8°C and an absolute pressure at about 570kPa. At this line pressure, the corresponding saturation temperature is approximately 63.5°C. Therefore, ethylene oxide before the feed controller valve was confirmed as liquid. It is also possible that the ethylene oxide temperature at this point could reach 30°C in a hot day. However, only the first slug of ethylene oxide injected may be 30°C but the bulk that follows is less than 20°C since the temperature of ethylene oxide in the header is almost always under 20°C (15-20°C). The reactor QD2, at the time of measurement, had an ethoxylation rate, i.e., an ethylene oxide flow rate, of 11kg/min and a pressure at 166 kPa. The reactor temperature was not taken at the time of measurement but it should be within the normal operation range between 140 and 160°C.

At the flow rate mentioned above, the flow is turbulent since the Reynolds number Re_d is amounted to approximately 2.0×10^4 where Re_d is defined as

$$Re_d = \frac{\rho u_m d_{\text{i.d.}}}{\mu} \qquad \textbf{7. 1}$$

where ρ is the fluid density, u_m the mean velocity, $\rho u_m = \frac{\dot{m}}{A_x}$, where $\dot{m}$ =mass rate of the flow, A_x= cross-sectional area of the pipe; $d_{\text{i.d.}}$ is the pipe diameter and μ, the fluid viscosity.

7.3.2 Numerical implementation

The governing equations used for the flow simulation in a dip-leg pipe were presented in Chapter 6. The model geometry and model boundary conditions are to be described below.

7.3.2.1 Model geometry

The dip-leg pipes used in the industrial reactors consist of a long straight body for most of the reactor height and a bent section, which extends to below the bottom-most impeller as can be seen in Figure 7. 7. The bent section has a length less than 10% of the total pipe length. Replacing the bend with a straight section of equivalent length simplified the construction of the model geometry which was further reduced

to a small sector in the computational model due to the symmetry. As the residence time of the fluid in the bent section would be small, the simplification was considered to be insignificant for the flow profile and the heat transfer treatment. A straight pipe of equivalent length was simulated instead.

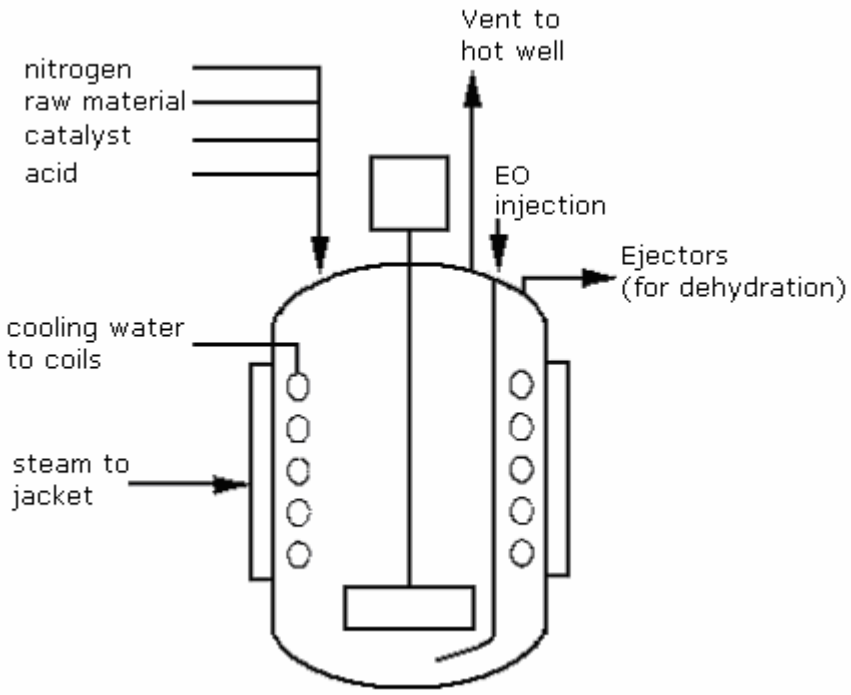

Figure 7. 7 The arrangement of the dip-leg pipe in a simplified NIS A reactor configuration.

Due to the symmetry of a straight pipe, only a sector with a central angle $\theta = 5°$ of the domain was modelled. This simplified the model to a two-dimensioned geometry and reduced the computational expenses significantly. Figure 7. 8 illustrates the geometry used in the numerical computation. The computational domain was also extended to a region below and adjacent to the actual pipe, representing a bulk temperature medium surrounding the pipe (see Figure 7. 8(b)).

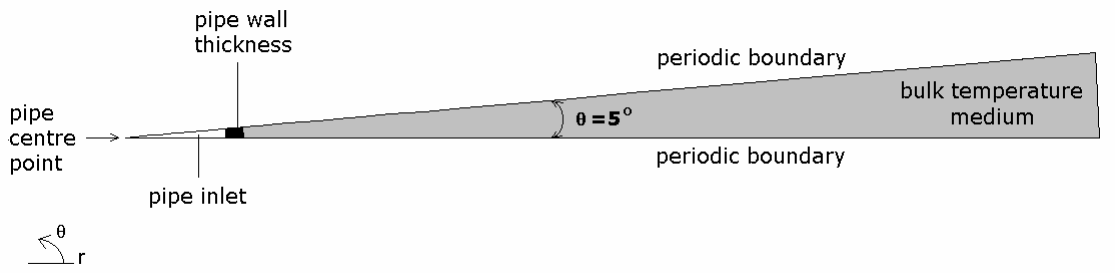

(a)

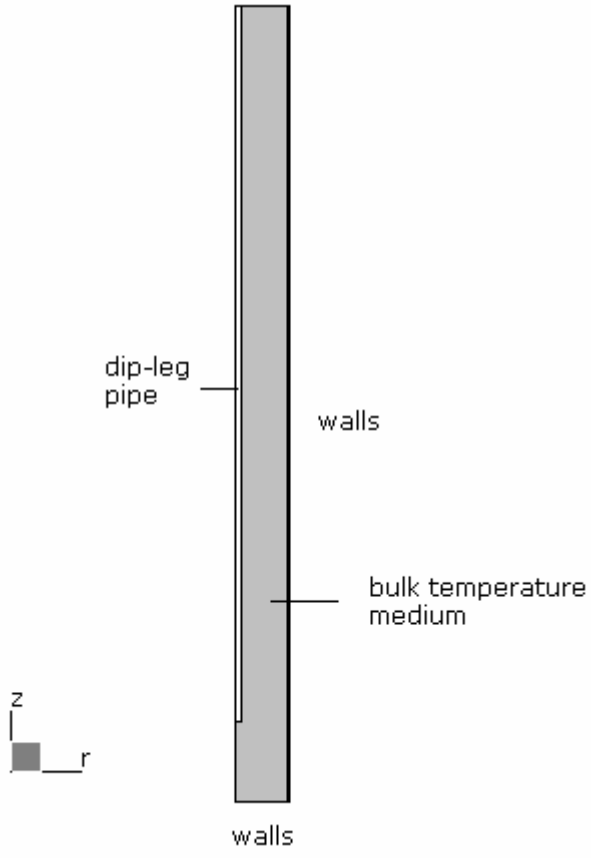

(b)

Figure 7. 8 Computational domain for the 2-D pipe sector simulated: (a) top view; (b) side view.

7.3.2.2 Model boundary conditions

Centre axis

In the physical space for the geometry construction, the vertices of the control volume and coordinates were expressed in the Cartesian framework. Therefore, the sector of the pipe to be modelled was transformed into a rectangular block: *x* coordinate for the vertical length of the computational domain; *y* coordinate for the radius; *z* coordinate for the circumferential length. The rectangular block was then wrapped around the plane of the centre axis (*y*=0), which was defined as symmetry plane. The symmetry plane was considered as frictionless.

Periodic boundaries

In the two-dimensional pipe sector, two periodic boundaries were defined at the top and the bottom vertical planes in Figure 7. 8(a) of the computational domain.

Conducting solid

The pipe wall thickness was defined as a conducting solid in order to compute the temperature gradient across the actual pipe wall as a result of being sandwiched between the cold and hot fluids. The physical properties of the conducting solid were defined as pipe of specification AS304.

Ethylene oxide liquid inlet

The boundary condition at the pipe entrance was defined as

$$u_m = \frac{\dot{m}}{\rho_{EO} A_x} \qquad \textbf{7. 2}$$

where $\dot{m}$ and A_x are as defined in Equation 7. 1, and ρ_{EO} is the density of the ethylene oxide liquid.

Outflow boundary

The top surface of the bulk hydrophobic mixture temperature medium was defined as an outflow boundary with zero gradient across the interface.

Walls

By default in CFX4.4, walls are defined on the domain boundary adjacent to fluid cells, where no other boundary type has been specified, and between fluid cells and solid cells. In the model geometry of the pipe sector simulated, walls occur at outer and bottom surfaces of the bulk temperature medium (see Figure 7. 8(b)) and at the surfaces between the conducting solid cells, defined above for the pipe thickness, and the fluid cells. A no-slip condition was applied at all walls in contact with the fluids. The

walls at outer and bottom surfaces of the bulk temperature region were specified with the fixed reaction temperature. The heat transfer through the walls adjacent to the pipe thickness was computed by the continuity of temperature and heat flux at the interface. A standard wall function was applied with the use of the k-ε model.

Grids

Grid independence was achieved when the pipe radius was modelled with 15×1 cells with a geometric progression factor of 1.05 in the radial direction with decreasing cell width from the centre axis towards the inner pipe surface; the pipe wall with 4×1 cells and the pipe length with 320 cells, both with a uniform distribution.

7.3.3 Constant bulk temperature scenario

The bulk temperature medium referred to as the extended domain in this study was in reality, partially in gaseous contact in the upper section and the rest in liquid contact. During an ethoxylation operation, the temperature in the gas region was likely to be a few degrees lower than the liquid region since the gaseous components had lower conductivity than the liquid. In addition, the gas region was in contact with cooling water passes while the liquid region was maintained at a fixed temperature, modulated by a balance between the exothermic heat and the cooling water heat removal. By assuming a constant temperature in the whole bulk medium, that is, no temperature variation and no differentiation of the physical properties between the gas and liquid, the results obtained represented the upper limit of the temperature that ethylene oxide could reach at the exit of the pipe.

Using the scenario described above, the modelling of the dip-leg pipe took into account the effects of bulk reaction temperature and ethylene oxide injection rates on the exit ethylene oxide temperature, which in turn determined its state. The variation in ethylene oxide inlet temperature was not considered in this study since the inlet temperature was always kept between 15 and 20°C. The real time measurement at 17.8°C described above in Section 7.3.1 was used for the ethylene oxide entrance temperature in the simulations. An overview of the simulations performed for the ethylene oxide dip-leg pipe is given in Table 7. 3.

Table 7. 3 Overview of the conditions in the cases studied.

Case	a	b	c	d	e	f
Pipe nominal size, mm	40	40	40	50	50	50
EO averaged flow rate, $\dot{m}$, kg/min	11	11	16	11	11	28
Bulk reaction temperature, °C	140	160	160	140	160	160
Comment	real	real	sim	sim	sim	sim

Note: real= actual operation condition; sim= simulated conditions.

The computational strategy adopted was such that the steady state computation was applied first to establish the flow profile in the pipe without heat transfer. Once the flow profile was established, the energy calculations were then activated with the transient computation. To maintain the bulk temperature field at constant, a user-defined FORTRAN subroutine was called to overwrite the temperature field at the beginning of each time step calculation.

7.3.4 Results

7.3.4.1 Empirical correlation

In order to validate the CFD simulations of ethylene oxide flow in the dip-leg pipe, the numerically computed (CFD) results were compared with the values derived from empirical correlations. Since cases *a* and *b* represent the actual operation conditions, their predicted results are compared with the values calculated from an empirical correlation. There are a number of correlations proposed for forced-convection flow in a pipe depending on the types of the flow and pipe length to diameter ratio $L/d_{\text{i.d.}}$ (Holman, 1989). Given that the ethylene oxide flow in the dip-leg pipe is turbulent as indicated by the Reynolds number calculated earlier and the ratio $L/d_{\text{i.d.}}$, according to the specification in Table 7. 2, has a value greater than 60, the following empirical correlation proposed by Nusselt for undeveloped turbulent flow in the entrance region in smooth pipes applies:

$$Nu_d = 0.036 Re_d^{0.8} Pr^{1/3} \left(\frac{d_{\text{i.d.}}}{L}\right)^{0.055} \text{ for } 10 < \frac{L}{d_{\text{i.d.}}} < 400 \qquad \textbf{7. 3}$$

where Nu_d is the Nusselt number, defined as $Nu_d = \frac{h d_{\text{i.d.}}}{\lambda}$, in which h is the heat transfer coefficient; λ is the thermal conductivity of the fluid; Pr is the Prandtl number $Pr = \frac{C_p \mu}{\lambda}$, in which C_p is the specific heat and μ is fluid viscosity. The properties in the above equations are evaluated at the mean bulk temperature. The correlation represents the data within $\pm$ 25%. The total heat transfer q is then expressed as follows:

$$q=hA(T_w-T_b)_{av}=\dot{m}\,C_p(T_{b2}-T_{b1}) \qquad \textbf{7. 4}$$

where A is the total surface area for heat transfer, T_w and T_b are the wall and fluid bulk temperatures and (T_{b2}-T_{b1}) is the fluid bulk temperature difference. The evaluation of T_w and T_b normally requires a suitable averaging process since both vary along the length of the pipe. In this case, T_w referred to the temperature of the inner pipe surface. Since the constant heat flux condition was only applied to the outer surface of the pipe, T_w was unknown and for simplicity, taken as the midpoint of the fluid temperatures on either side of the pipe in the calculation. Detailed calculations are given in Appendix C. The empirical correlation estimated an exit temperature of 44.7°C for case *a* and 49.3°C for case *b*.

The effect of varying pipe diameters was also investigated by the empirical correlation. By an increase in the pipe nominal size from 40mm to 50mm while keeping the rest of operating conditions the same, the exit temperature was reduced to 40.1°C for case *a* and 43.9°C for case *b* from the previously calculated values of 44.7°C and 49.3°C for case *a* and case *b* respectively (see details of the calculation in Appendix C). These results indicated that the heat transfer rate could be effectively reduced under the same flow conditions with the use of larger dip-leg pipe.

7.3.4.2 Simulation results

The simulations were run on a Compaq XP-1000 machine and required on average, a total of about 325 steady state iterations to reduce the residual by at least 10^{-4} times and 12.77 seconds of computational time for 1.0 second of real time with a model time step of 0.05 second.

After t=180 seconds by the transient calculation, the temperature at any random point on the exit plane of the pipe became steady. The results presented in this study were taken at t=300 seconds. The layer of the fluid in contact with the heated pipe wall was expected to be at higher temperature than that in the bulk with no contact with the pipe wall. Therefore, the computational results were represented as the average of the temperature field at the pipe exit plane. The results predicted from the numerical simulation with the boundary conditions specified in Table 7. 3 are tabulated in Table 7. 4 below. This table also presents the saturation pressure corresponding to the exit temperature computed in each case.

Table 7. 4 Computational results for each case studied in Table 7. 3.

Case	a	b	c	d	e	f
Averaged exit temperature, °C	41.3	45.1	38.6	41.1	44.9	32.8
Corresponding saturation pressure, kPa	301	339	277	299	337	229

The computational results agreed well with the empirical calculations (Section 7.3.4.1). The discrepancy was less than 10%, even though Nusselt's empirical correlation has a 25% error.

The mechanism of boiling depends on the relative values of the vapour pressure of the liquid P^* and the total system pressure P_{system}. That is, boiling occurs if $P^* \geq P_{system}$, where P_{system} is the total of the reactor pressure plus the hydrostatic pressure of the reaction mixture at the depth of the pipe exit point. In the case of the 40mm pipe, the hydrostatic pressure, depended on the liquid heights, was estimated to be between 10-20kPa based on a hydrophobic mixture density of 900kg/m^3. Therefore, the total system pressure according to the real measurement given in Section 7.3.1 was no more than 190kPa. When this value was compared to the saturation vapour pressure at the exit temperature showed in Table 7. 4 for actual operation conditions in cases *a* and *b*, the ethylene oxide should boil at a latent heat of vaporisation of 5.47×10^5 J/kg. In fact, at this system pressure, ethylene oxide would boil when its exit temperature was above approximately 27.5°C. From these results, the injection of ethylene oxide at the flow rate of 11kg/min in the 40mm pipe should exit partially gaseous. This deduction was also applicable to the 50mm pipe at an ethylene oxide flow rate of 11kg/min as in cases *d* and *e* if a reactor pressure was also 166kPa. Nevertheless the temperature values obtained in Table 7. 4 were based on an ideal environment in which the bulk temperature medium was maintained perfectly at the set constant, whilst temperature differentiation might exist between the gas and liquid in the upper and lower parts of the reactor respectively.

The effect of the ethylene oxide peak rate on the exit temperature of the injection was studied in cases *c* and *f* for the 40mm and 50mm pipes respectively. With the increase in the flow rate of ethylene oxide injection, as in moving from case *b* to case *c* in the 40mm pipe and from case *e* to case *f* in the 50mm pipe, it can be seen (in Table 7. 4) that the exit temperature dropped which in turn should lead to a correspondingly lower saturation vapour pressure. This indicated that so long as the reactor pressure reached, approximately, 280kPa in QD2/QD3 and 230kPa in QD1/QD5, boiling would not take place since the saturation vapour pressure was less than the total system pressure. As was also observed earlier, it was found that in Figures 7. 3(a) and 7. 4(b) the peak rate of ethylene oxide injection in QD2 occurred when the system pressure was above 270kPa for the production of the C12-C15 alcohol ethoxylates and above 300kPa for most of the nonylphenol ethoxylates, apart from N2 and N50. Summing up these results, it was concluded that when the ethylene oxide feed reached its maximum rate, boiling was unlikely to take place.

7.3.5 Concluding remarks

In conclusion, the results above clearly indicated that when the ethylene oxide injection rate reached its maximum, the reactor pressure was high enough to prevent the ethylene oxide from boiling. That is, ethylene oxide injected from the dip-leg pipe could be assumed to be liquid. After the injection, ethylene oxide was dissolved within the bulk hydrophobic mixture, with minimal amount of boiling. Under these specified conditions, the ethoxylation essentially became a liquid phase reaction. Additionally, the results also demonstrated that the boiling of ethylene oxide could be reduced with the use of a larger dip-leg pipe.

7.4 Scope of numerical model for ethoxylation

The application of numerical modelling to an ethoxylation reactor would enable us to assess the effect of operational variation on the process parameters quickly and safely. A validated CFD model could provide a robust tool for the tests of process modifications. In the case of the numerical modelling of a commercially operated ethoxylation reactor, the aim was to quantify the improvement in productivity in terms of ethylene oxide injection rates after the operational limitations were understood and identified.

We have thus far examined the roles of the three possible rate limiting factors in the ethoxylation process performed in a NIS A stirred reactor of HCA. They were mixing effectiveness, heat removal and reactor pressure rating. We have established that (1) the mixing pattern due to a dual-axial or a dual-Rushton impeller had little effect on the ethoxylation behaviour under the current operation mode, and that the data in QD2 and QD3 of NIS A plant was interchangeable (Section 7.2.2); (2) the cooling capacity of the high-pressure cooling water used was sufficient to provide the cooling required for at least a twofold increase in the current ethoxylation rate (Section 7.2.3), and (3) the current ethoxylation productivity at the Botany alkoxylation plant was limited by the use of nitrogen padding (Section 7.2.4).

We have also established that when the reactor pressure exceeded a certain level, the ethylene oxide injected was fully liquid (Section 7.3.4.2). This enabled us to select a zone in an ethoxylation process to be modelled by the CFD technique. The zone was chosen in which the ethylene oxide injection was fully liquid into the reaction mixture. This occurred when the ethylene oxide injection rate was constant at its maximum value and above a certain reactor pressure (over 300kPa). Within this pre-assigned zone, the bulk liquid where the main reaction took place was simplified to an agitated single-liquid containing several chemical species. That is, in this research project, we did not model ethoxylation as a gas-liquid reaction. This is mainly due to the fact that at the pre-assigned zone, the ethylene oxide injected into the reaction mixture is liquid, and as a result, there is no need to deal with the complexity of modelling a gas-liquid reaction.

It was necessary to further simplify the numerical model to a fixed liquid height-to-diameter ratio. The reason for this simplification was that in the semi-batch operation, the liquid content expanded with the extent of the reaction. To incorporate this feature in the corresponding numerical model, a moving boundary needs to be included. Due to the time limitations in this research project, we did not explore this modelling technique that could potentially address the continuous liquid growth. Therefore, a single artificial outlet was designated at the free surface in the model (as will be shown later in Figure 7. 18(b)). This was included to satisfy the mass balance, compensating for the simplification that the liquid height remained constant during the computation.

7.5 Boundary conditions for the stirred ethoxylation reactors

Two of the numerical approaches using the rotating coordinate system discussed in Section 5.3.2 were used for the simulation of the stirred tanks in this research work. They were the multiple frames of reference (MFR) and sliding grid (SG) methods. This section defines the boundary conditions relevant to the simulation of a stirred ethoxylation reactor investigated in this research project.

7.5.1 Unmatched grid boundary

The interface between the inner block encasing the rotating impeller and the outer block encasing the stationary baffles in the rotating coordinate system was defined as an unmatched grid boundary. An unmatched grid boundary means, in the SG calculation, the grids from the blocks at either side of the interface are allowed to move relative to each other at the interface; in the MFR calculation, the blocks are in different frames of reference. In a typical geometry, a stirred vessel was divided into two blocks as described above. An unmatched grid boundary was imposed at a vertical plane between the outer-most edge of the impeller blade and the inner edge of the baffle plate. In this research work, the exact location for the unmatched grid boundary depended on the location of the injection of ethylene oxide - if it was included in the model. For example, in the simulation of a stirred vessel with no injection, an unmatched grid boundary was placed at the halfway plane between the outer edge of the impeller blade and the inner edge of the baffle plate. In the industrial NIS A reactor, the injection of ethylene oxide was directly beneath the lower impeller approximately midway between the impeller and the reactor base. Therefore, in addition to the unmatched grid boundary that vertically separated the blocks containing the impeller and the baffles, a second unmatched grid boundary was imposed between the injection point and the lower edge of the impeller blade. That is, the rotating block was totally excluded from association with any part of the vessel base.

To aid convergence and minimise numerical error, the cell spacing in the azimuthal direction at an unmatched grid boundary was fixed at 5° a cell. The time step was chosen such that the relative motion between the two blocks was exactly one azimuthal grid cell per time step.

7.5.2 Symmetrical axis

In the physical space for the geometry construction in the Cartesian framework, the cylindrical vessel was transformed into a rectangular block. That is, *x* coordinate represented the liquid height; *y* coordinate the radius of the vessel; *z* coordinate the circumference. To avoid the grid singularity at the centre axis which might cause numerical problems, a circle of 1mm radius was taken out from the model geometry. The rectangular block was then wrapped around the plane of the centre axis (y=0.001m), which was defined as a frictionless symmetry plane.

7.5.3 Periodic boundaries

Two periodic boundaries were defined in the rectangular block described above; z=0 and z=π for a half-tank geometry or z=2π for a whole tank geometry.

7.5.4 Walls

A flat, free surface was assumed at the top of the fixed liquid height and imposed as free-slip conditions. All other solid surfaces including impeller blades, shaft, baffle plates and vessel walls were defined by standard wall functions with no-slip conditions. An anti-rotational movement, negative in magnitude to the angular velocity of the impeller, was necessarily imposed at the part of the vessel base that was included in the central rotating block to prevent it from rotating with the grids. This did not need to be defined when there was an unmatched grid boundary separating the impeller and the vessel base.

When the temperature field in the computational domain was also solved, the walls adjacent to the cooling water coils were specified with constant heat flux given by the following equation:

$$Q_{\mathrm{w}} = -\frac{H_R(T) \times \frac{dm_{\mathrm{EO}}}{dt}}{A_{\mathrm{w}}} \qquad \textbf{7. 5}$$

where $H_{\mathrm{R}}(T)$= heat of reaction in J per kilogram of ethylene oxide and is a function of temperature, $\frac{dm_{\mathrm{EO}}}{dt}$ = averaged ethoxylation rate in kg/s and A_{w}= total area of the wall in adjacent to cooling water coils. The heat flux is negative because heat is removed from the system. The ethoxylation rate was an averaged value calculated from the period of ethoxylation to be described by the numerical model.

7.5.5 Ethylene oxide injection

In the case of the laboratory autoclave, the injection of ethylene oxide mass was by manually opening and closing the oxide valve as described in Chapter 3. The injection process was intermittent and the disturbance to the flow was considered insignificant (an averaged ethylene oxide flow rate at 0.03m/s compared to the impeller tip velocity at 2.85m/s at 1700rpm). For simplicity, any impact of the injection on the flow field was ignored. Therefore, the ethylene oxide mass in the simulation model was represented by a number of cells, equivalent to the volume of the injected mass, at the location where it was injected. In simulations of the industrial reactor where ethylene oxide injection was continuous, a continuous supply of ethylene oxide into the reaction mixture was maintained with a rate given by Equation 7. 2. For both the laboratory scale and industrial scale ethoxylation reactors investigated, a single inlet of ethylene oxide injection was used. Therefore, for modelling the reactive flow, a whole tank of 360° was necessarily used.

7.5.6 Outflow boundary

Due to the single inlet for injection of ethylene oxide and fixed liquid height to diameter ratio in the model, a small outlet was artificially created for mass conservation purposes. This single outlet created at the outer-rim of the free surface (shown later in Figure 7. 18(b)) was believed to have no major consequences for disruption of the flow field generated by the impeller rotations.

7.5.7 Frozen field computation

A time dependent computation was required for calculations of species concentration distribution in a mixing reactor. However, a time-resolved simulation such as the sliding grid calculation was unnecessarily time consuming for a potentially long transient computation. Hence, a two-stage computation was adopted as a compromise strategy: the first stage solved the momentum transfer and the turbulence fields; the second stage solved the species concentration equation with the flow field “frozen” by deactivating the solver for momentum transfer, as described by Jaworski *et al*. (2000) for computing tracer homogenisation in a dual-Rushton stirred tank.

7.6 CFD simulations of single phase liquid stirred flow

This section contains two parts. The first part is concerned with the validation of the CFD simulation of a single-phase liquid flow system in a stirred vessel without chemical reactions. The second part addresses the grid sensitivity assessment for the CFD model for both the laboratory and industrial reactors of HCA studied in this research project. Unless mentioned otherwise, all results presented from this section onwards were taken in a vertical plane halfway between two baffles.

7.6.1 Literature data

The literature experimental data to be simulated in the present study is summarised in Table 7. 5.

Table 7. 5 Summary of the single-phase liquid flow simulated in the present study.

Geometry	Experimental data	Methods used
A. Single Rushton turbine, $D/T=\frac{1}{3}$, $C/T=\frac{1}{3}$	Mahouast *et al*. (1987), cited in Brucato *et al*. (1998) Wu and Patterson (1989)	MFR, SG
B. Dual Rushton turbine, $D/T=\frac{1}{3}$, $C_1=C_2=C_3=\frac{1}{3}T$	Rutherford *et al*. (1996a)	SG

7.6.1.1 Single Rushton turbine

The computational reproduction of the experimental data of Mahouast *et al*. (1987), cited in Brucato *et al*. (1998), and Wu and Patterson (1989) on the mean velocities and total turbulent kinetic energy of a single-phase liquid flow in a Rushton turbine stirred vessel is presented in Figures 7. 9 and 7. 10. The experimental data of Wu and Patterson (1989) was obtained from the LDV measurements on the turbulent flow in the stirred tank, filled with water as working fluid, of a diameter T=0.27m and a liquid height equal to the tank diameter ($Z=T$). There were four baffles that were equally-placed around the tank, each with a width $T/10$. The Rushton turbine, of a standard configuration with a diameter about one-third of the tank diameter ($D=T/3$), was placed at a distance $C=T/3$ from the tank base. The impeller speed used was 200rpm (U_{tip}=0.974m/s), corresponding to an impeller Reynolds number of 2.9×10^4. The computational domain contained 180° of the tank and was discretised into $74\times57\times36$ ($z\times r\times\theta$) cells, in which the impeller was modelled with $8\times12\,(z\times r)$ cells. The thickness of the blade was treated as a thin surface. The simulation results with the use of the SG and MFR techniques are both presented in the comparison with the experimental mean velocities.

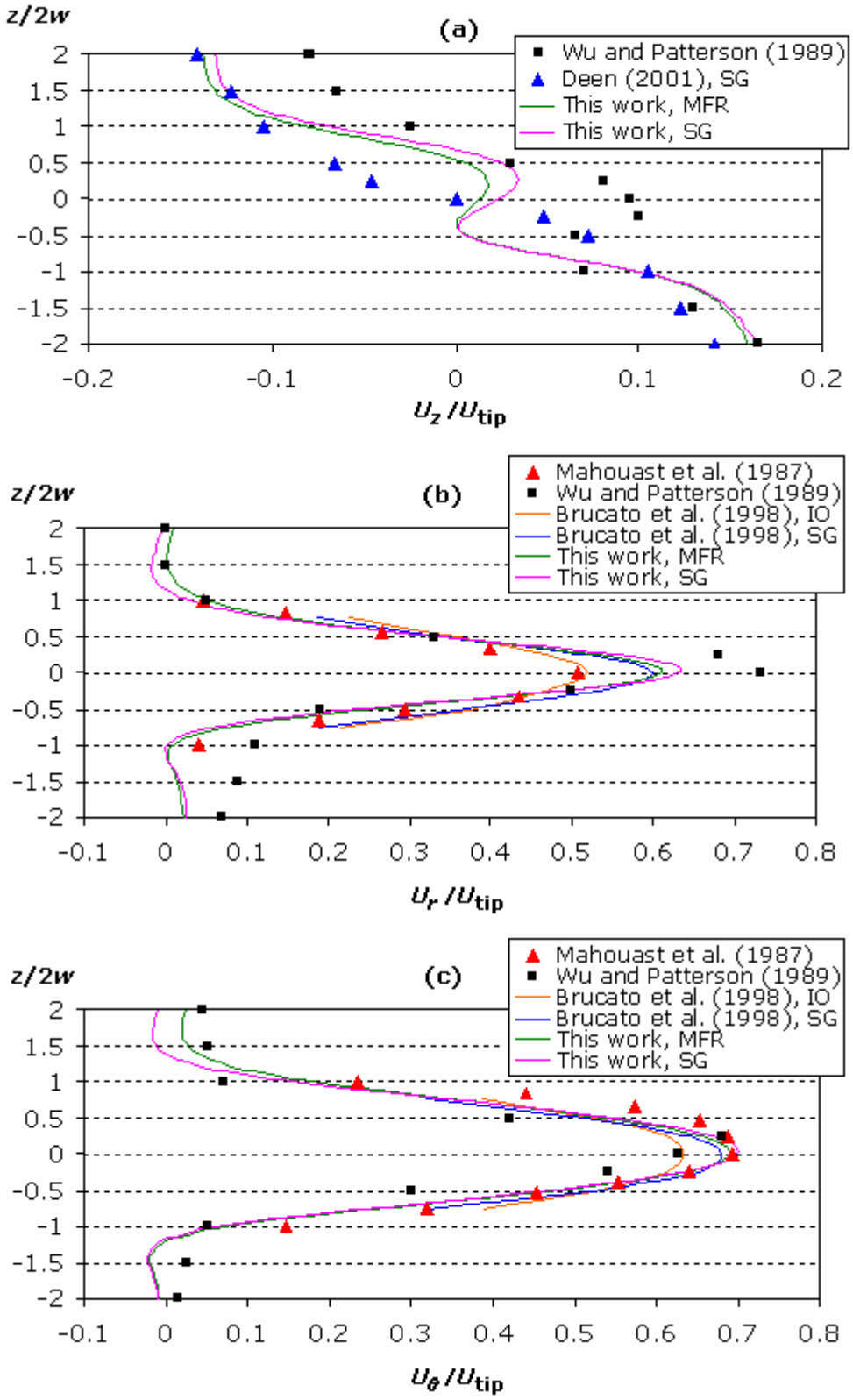

Figure 7. 9 Axial profiles of the mean liquid velocities measured at a vertical line just off the impeller blade, at *r*/*R*=0.37, a radial distance of 0.37 of the tank radius *R*: (a) axial velocity; (b) radial velocity; (c) tangential velocity. Symbols: (▲) experimental results by Mahouast *et al.* (1987), cited in Brucato *et al.* (1998); (▪) experimental results by Wu and Patterson (1989); (▲) predictions by Deen (2001). Solid lines: predictions, IO and SG techniques by Brucato *et al.* (1998); predictions obtained from this work by MFR and SG techniques.

In Figure 7. 9, the axial profiles of the mean radial, tangential and axial velocities in the vicinity of the impeller are shown; the velocities are normalised with the impeller tip velocity U_{tip}; the axial distance, from the centre of the impeller blade, is normalised with half of the blade width $w/2$. The simulation results were also compared with the results of Brucato *et al*. (1998) obtained from both the inner-outer (IO) and the SG methods and those of Deen (2001) by the SG technique. The simulation trends in Figure 7. 9 corresponded very well with both the experimental and the computational data from the literature cited. As can be seen in Figure 7. 9, the simulation results predicted a maximum radial and tangential velocities located above the centreline of the impeller ($z/2w>0$), capturing the upward inclination of the impeller discharge stream displayed in the experimental data. The transient computation of SG method improved the results slightly from that of the steady-state computation of MFR. The SG method also showed a significant improvement over the steady-state IO method.

The plot of the total turbulence energy k normalised with U_{tip}^2 is shown in Figure 7. 10. As can be seen in this figure, the trend of the simulation results obtained in this work was in good agreement with that obtained by Brucato *et al*. (1998). However, both sets of the simulation results under-predicted the turbulence energy in the near impeller region severely. As discussed in Section 5.3.4, it was due to the inherent assumption of the k-ε model that the turbulence in the impeller vicinity was local isotropic.

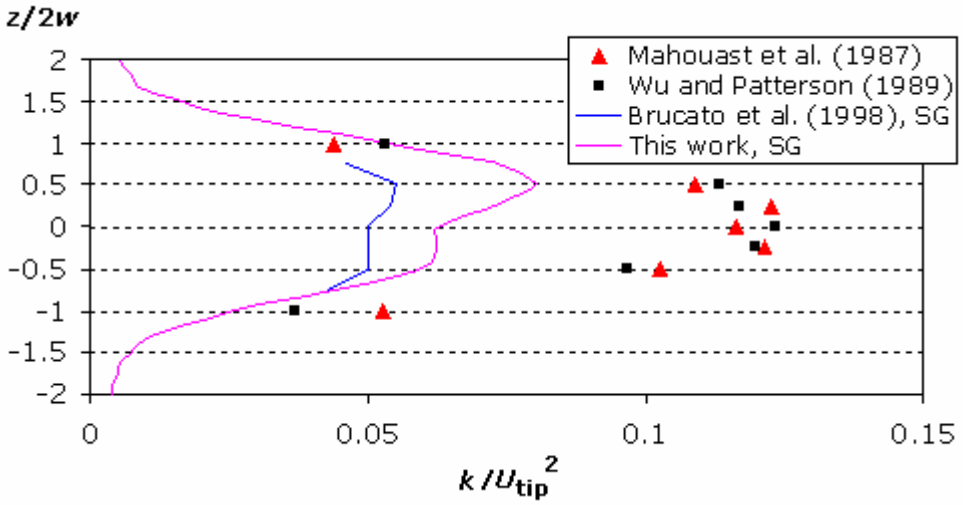

Figure 7. 10 Axial profile of the turbulence energy k measured at a vertical line near the blade edge (at r/R=0.37).

The typical flow field generated by a single Rushton impeller with the above arrangement (geometry A in Table 7. 5) is illustrated in Figure 7. 11. The characteristic two ring vortices, one above and one below the impeller, are clearly depicted in the *r-z* plane vector plot. The location of the recirculation centre for the upper and lower characteristic loop agreed very well with the literature data, e.g. Middleton *et al*. (1986) and Brucato *et al*. (1998). The upwards skewed jet emerging from the turbine was also evident in both the *r-z* plane vector plot and the contour map, which was due to the non-symmetrically located impeller and the free surface at the top of the tank, as noted by Wu and Patterson (1989). The maximum velocity magnitude was found in the outflow of the impeller, which was primarily radial with a velocity magnitude at approximately 80% of the impeller tip velocity (U_{tip}=0.972m/s). The velocity magnitudes in most of the reactor zones above and below the impeller were low with less than 20% of the tip velocity. The fluid movement was minimal in the regions containing the two recirculation centres and the zone below the centre of the impeller towards the vessel base where the velocity was less than 10% of the impeller tip velocity.

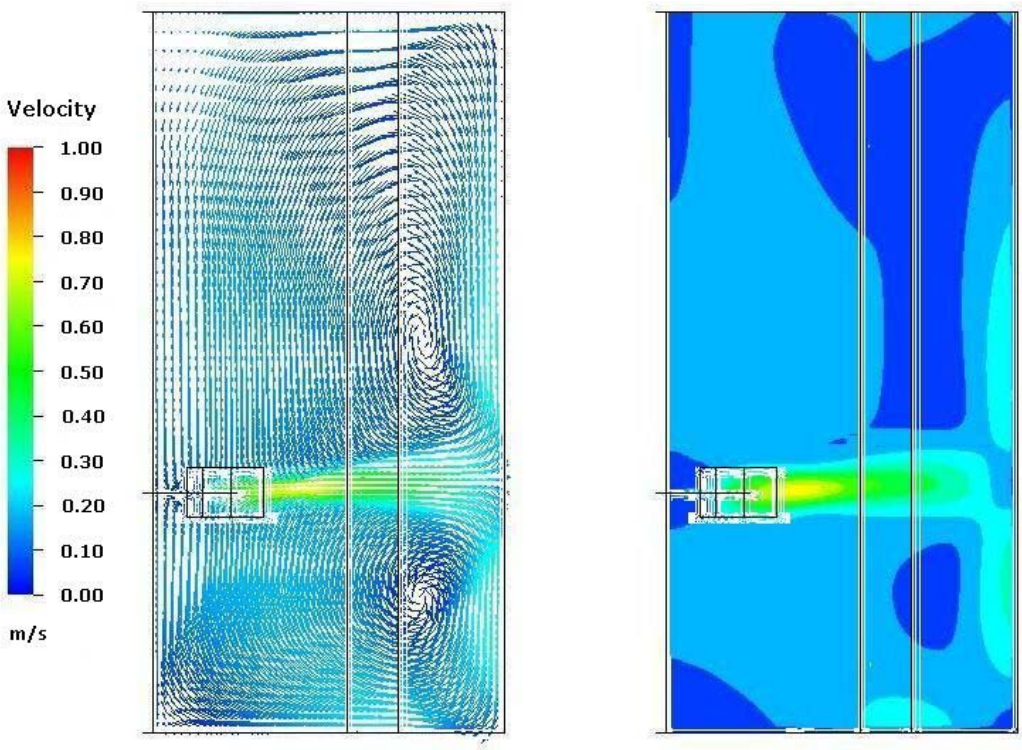

Figure 7. 11 Simulated *r-z* plane vector plot and contour map for the mean velocities in the single Rushton stirred reactor of Wu and Patterson (1989).

7.6.1.2 Dual-Rushton impeller

As discussed in Section 5.2.3.2, the dual-Rushton impeller in the NIS reactor A is arranged with the lower impeller clearance $C1$ at $0.172T$ above the base of the vessel and the separation between the impellers $C2$ at $0.273T$. According to Rutherford *et al*. (1996a), this arrangement was potentially a "merging" flow pattern since $C1>0.17T$ and $C2<0.385T$ if the two impellers were of the same size. Figure 7. 12 reports the axial profiles of the radial velocity for a merging flow pattern in a dual-Rushton stirred vessel used by Rutherford *et al*. (1996a) at different radial locations: $r=0.18T$ (immediately outside the blade edge); $0.25T$ and $0.39T$ (close to the radial location of the baffle edge). In this figure, both the experimental and simulation results are shown: the experimental profiles were obtained from Rutherford *et al*. (1996a); the simulation results were obtained from the fully predictive SG method by Micale *et al*. (1999) and this work. It should be noted that the experimental profiles were obtained from Micale *et al*. (1999) who took the data by reading off the published vector plots of Rutherford *et al*. (1996a). Therefore, the experimental data should be used with some caution. The flow was generated in a stirred vessel of 100mm in diameter by two standard Rushton impellers, each with a diameter of $D=T/3$. The impeller blade of width $D/4$ and height $D/5$ had the same thickness as the disk of 1.65mm. The liquid height was equal to the tank diameter and the impellers were equally placed along the tank axis, i.e., $C1=C2=C3=T/3$. Four baffles were equally placed around the tank, each of width $T/10$. The flow had a Reynolds number of 4.0×10^4 at an impeller rotation speed of 2165rpm (U_{tip}=3.77m/s). The thickness of the blades and disks was modelled as solid blocks with the above dimension. Due to the symmetry of the geometry, half of the vessel was modelled. The computational grids used were consistent with those of Micale *et al*. (1999); each impeller blade was modelled with $7\times8\times2$ cells and the total computational domain with $86\times42\times36$ cells in axial, radial and azimuthal direction respectively.

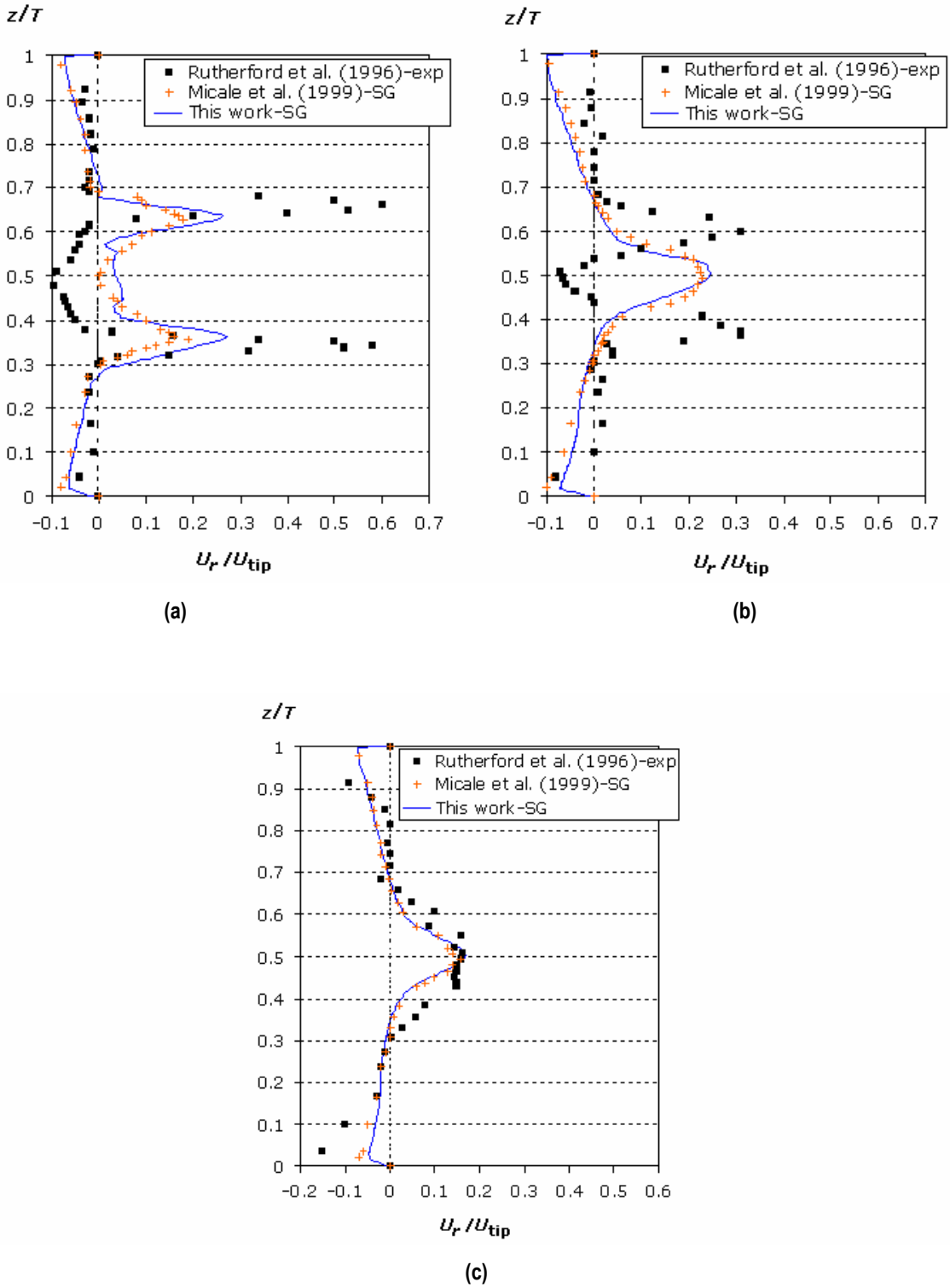

Figure 7. 12 Axial profiles of radial velocity at various radial locations in a merging flow simulation: (a) *r*=0.18*T*; (b) *r*=0.25*T*; (c) *r*=0.39*T*. Symbols: (▪) experimental results (Rutherford *et al.*, 1996); (+) predictions, SG technique (Micale *et al.*, 1999). Solid lines: predictions obtained in this work, SG technique.

As can be seen in Figure 7. 12, at various radial locations along the central line of the impeller, the axial distributions of the radial velocity by SG predictions in this work corresponded very well with those of Micale *et al*. (1999); the locations of the peak radial velocities and the shape of the distributions. However in the comparison of the simulation results to the experimental data of Rutherford *et al*. (1996a), the radial velocity that was very close to the impeller periphery, i.e., at r=0.18T, was severely under-predicted as shown in Figure 7. 12(a). Additionally, the radial velocity at the intermediate distance from the impeller edge, r=0.25T, was also not so well predicted (see Figure 7. 12(b)). As noted by Micale *et al*. (1999), the experimental data of the radial velocity at this location showed the two streams remained separated with a central reverse flow region, while the simulations yielded outflow in the vessel mid-height. The simulations only predicted a satisfactory agreement with the experimental data at a distance further away from the impeller blade where the two discharged streams from the impellers had completely merged as shown in Figure 7. 12(c). The inherent shortcoming of the k-ε model for such flow with strong streamline curvature as discussed in Section 5.3.3 was even more evident in the axial profiles of the turbulence energy k plotted in Figure 7. 13. At both the radial locations, the turbulence level given by the SG technique was significantly lower along most of the vessel height as shown in the figure. As can be seen in Figure 7. 13(a), the simulation profiles in this work were mostly in good agreement with those by Micale *et al*. (1999), except for the region between the impeller at r=0.18T. The data of Micale *et al*. (1999) displayed an over-prediction of k while the results of this work corresponded very well with the experimental data. The results of this work also exhibited the trend displayed in the experimental data with double peaks just off the impeller edges, however with the values under-predicted.

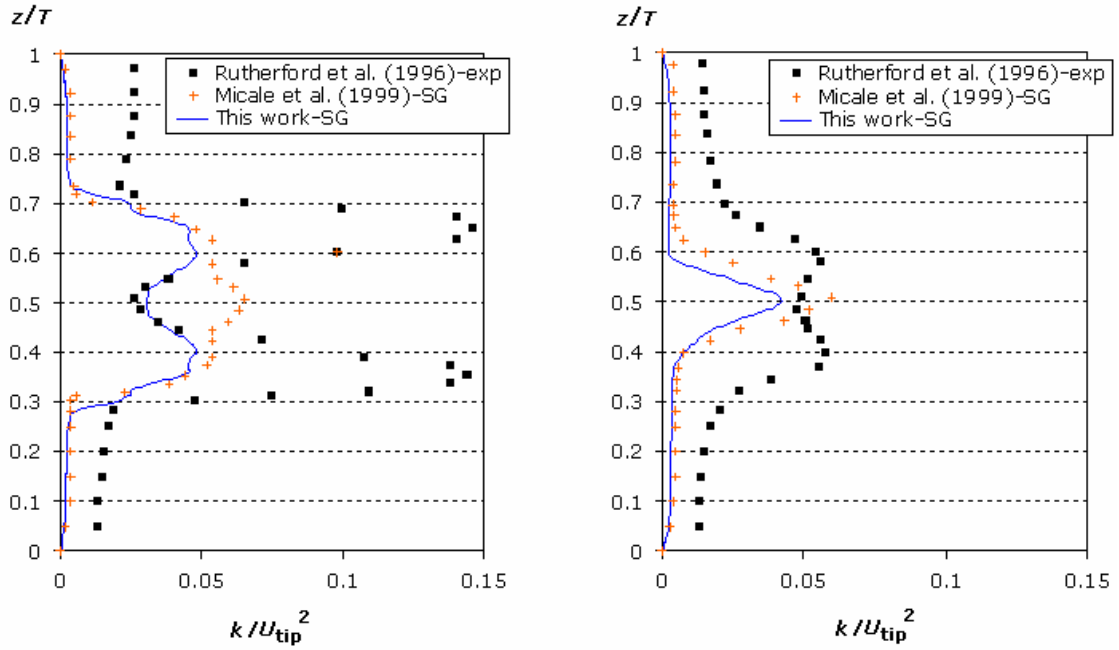

Figure 7. 13 Comparison of axial profiles of the turbulence energy at different radial distances in a merging flow simulation: (a) *r*=0.18*T*; (b) *r*=0.25*T*. Symbols: (▪) experimental results (Rutherford *et al*., 1996); (+) predictions, SG technique (Micale *et al*., 1999). Solid lines: predictions obtained in this work, SG technique.

Figure 7. 14 shows the *r-z* plane vector plot of the mean velocities in the merging flow pattern observed by Rutherford *et al*. (1996a). The centre of the recirculation zones and the flow pattern corresponded very well with the literature data, from either the experiments (Rutherford *et al*., 1996a) or the simulation (Micale *et al*., 1999). The impeller discharge streams met at the mid-way in the zone between the impellers at an angle of approximately 65° to the horizontal. It differed from the 35° merge observed in the experimental measurements of Rutherford *et al*. (1996a), however it was similar to the prediction of Micale *et al*. (1999) with the SG method. The result was a consequence of excessive convergence of the two impeller streams in the numerical computation as explained by Micale *et al*. (1999).

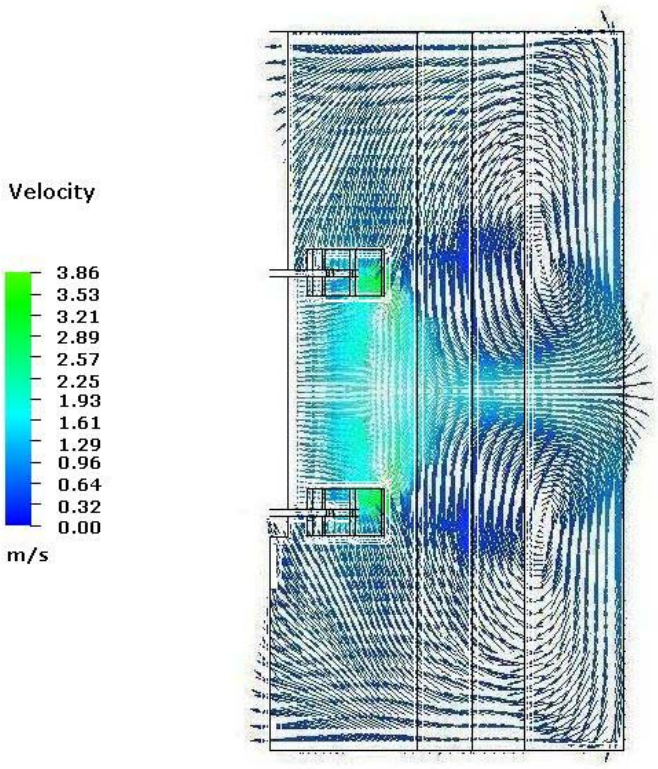

Figure 7. 14 Simulated *r-z* plane vector plot for the mean velocities in the merging flow pattern induced by the dual-Rushton impeller of Rutherford *et al*. (1996a).

7.6.1.3 Concluding remarks

On the whole, the qualitative features of the literature data of the mean flow field in a vessel stirred by either single-Rushton turbine or dual-Rushton impeller were very well reproduced. The quantitative comparisons showed some discrepancies. The major discrepancy was the under-prediction of the turbulence energy due to the deficiencies of the k-ε turbulence model, which was commonly reported in most of the simulation work as discussed in Section 5.3.4.

7.6.2 Grid sensitivity assessment

Grid sensitivity tests were conducted for both the laboratory-scale and industrial reactors by assessing the effect of grid sizes on the mean velocities. For each reactor, the grid density was varied from coarse to fine by increasing the number of cells mainly radially and axially at the impeller blades and the immediate vicinity of the impeller, where the flow was most turbulent. The azimuthal cell spacing was set constant at 5°, i.e., a total of 72 cells in a complete revolution of 360°. Grid independency was said to be achieved when any further increase in the number of cells did not adversely affect the simulation results; the optimum grid size avoided any unnecessarily prolonged computational effort required for simulations with large number of cells. It should be noted that the model geometry used for the grid sensitivity assessment did not necessarily include the ethylene oxide injection. As was shown by Chiu *et al*. (2002), the presence of a dip-leg pipe near the edge of the baffle had insignificant impact on the flow characteristics in the vicinity of the impeller, especially when the injection rate was low compared to the impeller tip velocity. For example, in the case of QD3 operation, the ethylene oxide injection rate was approximately 0.23m/s, while the impeller tip velocity was 3.72m/s. With the omission of the dip-leg pipe, only half of the tank was required in the model due to the symmetry of the geometry. In addition, for simplicity, all the impeller blades and disks were modelled as thin surface from hereon.

Since only the flow at the final, time periodic state was of concern, the time-resolved simulation by the SG technique was unfavourable and unnecessary in terms of time and computer power expenses for flow starting from rest. Therefore, in order to overcome the flow starting from stationary in all simulations, the steady-state computation by the MFR method was used to establish the flow field. The MFR computation was aimed at achieving a reduction in mass flow residue by a factor of 10^{-5} (normalised by its value after the second iteration) or at the convergence of 2000 SIMPLEC iterations. The SG calculation then carried the computation further to refine the flow data until the time-periodic condition was attained.

7.6.2.1 Laboratory-scale reactor

The grid sensitivity assessment for the laboratory-scale reactor was performed for the two-litre autoclave reactor used in the kinetic experiments described in Chapter 3. An illustration of the reactor geometry is shown in Figure 7. 15. The vessel had a diameter T=0.089m and an aspect ratio of 3.7. Two full height baffles, each one-twentieth of the tank diameter in width, were suspended against the tank wall at 180° apart. The vessel was equipped with a 6-bladed Rushton turbine with a diameter D=0.36T, placed at a distance C=T/2 off the centre of the dished vessel base. The blade height w was 0.32D and the blade width l was 0.25D. The impeller was rotated at N = 1,700rpm, corresponding to a Reynolds number of 7,000 and an impeller tip velocity of 2.85m/s with a working fluid of the properties based on the reaction mixture used in the kinetic run kin.4a in Table 4. 3 (at 125°C, the fluid composed of nonylphenol with 2.77 moles of ethylene oxide has a density of 928kg/m^3 and viscosity of 4.0×10^{-3}kg/ms). Although the Reynolds number gave a transition flow regime for this flow where it was turbulent at the impeller region and laminar in remote parts of the vessel (Perry and Green, 1984), for simplicity, the k-ε turbulence model was still assumed to be applicable in this flow and used in the numerical model. An ethylene oxide dip-leg pipe of diameter about 2mm was placed at a distance 0.125T from the tank wall at a plane halfway between the baffles and length-wise extended through to the mid-way between the impeller and the tank base, that is, to C/2. Figure 7. 15(b) gives a view at a horizontal plane on the relative locations between the baffles, dip-leg pipe and the impeller.

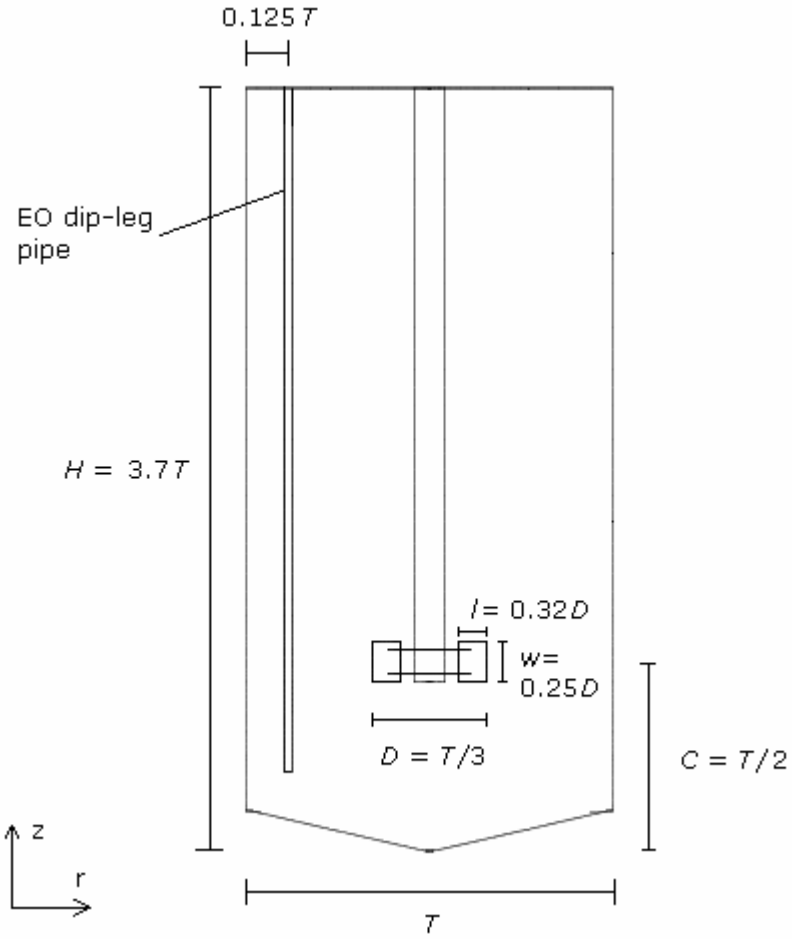

(a)

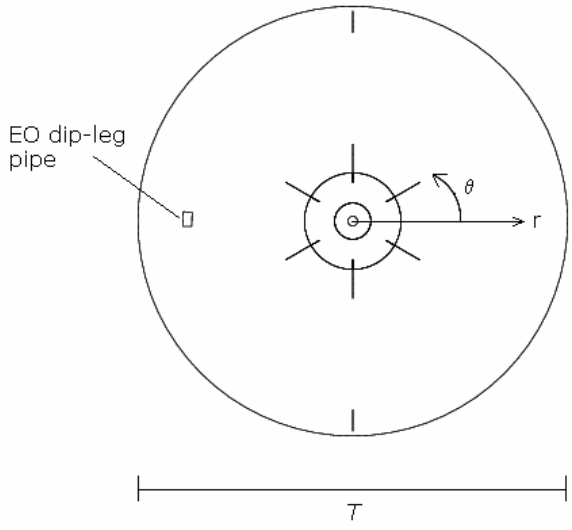

(b)

Figure 7. 15 Model geometry of the two-litre laboratory reactor: (a) front view; (b) top view.

The liquid height used in the grid independency study for the two-litre reactor was twice the tank diameter (Z=2T). As mentioned earlier, the physical presence of the dip-leg pipe was not included in the grid sensitive study - 180° of tank was modelled. Table 7. 6 presents an overview of the grid information on each grid density studied in this grid independency test.

Table 7. 6 Overview of the computational grids used for the grid-independency assessment for the 2-litre autoclave.

Grid density	Coarse	Medium	Fine
Cells along z	41	69	80
Cells along r	17	32	50
Cells along θ	36	36	36
Cells in blade $(z \times r)$	5×4	10×8	15×12
Overall grid cells	25,092	79,488	144,000

The computational strategy adopted to achieve the final time-periodic state of the flow was implemented in the following steps similar to that proposed by Brucato *et al*. (1998). Firstly, the MFR approach was used to reduce the mass residual to a value of 1.0×10^{-4} (normally achieved a reduction by 10^{-4} or 10^{-5} when normalised with the residual value after the second iteration) or the convergence results after 2000 SIMPLEC iterations. Next, the SG method was applied for the flow field established earlier by the MFR computation for an overall computation of 125 revolutions. However, the first 100 rotations of the transient calculation were computed with a very coarse time step: *dt* of 1 revolution period. The last 25 revolutions continued to compute the flow parameters with a much finer time step at *dt* equal to one-seventy second of a cycle. That is, the inner block at the unmatched boundary with the outer block slid exactly one azimuthal cell per time step. The time-periodic results taken at the end of 130 revolutions for different grid densities are presented in Figure 7. 16. In this figure, the axial and radial profiles of the axial velocity are shown at a line 0.5mm next to and below the impeller blade edge respectively.

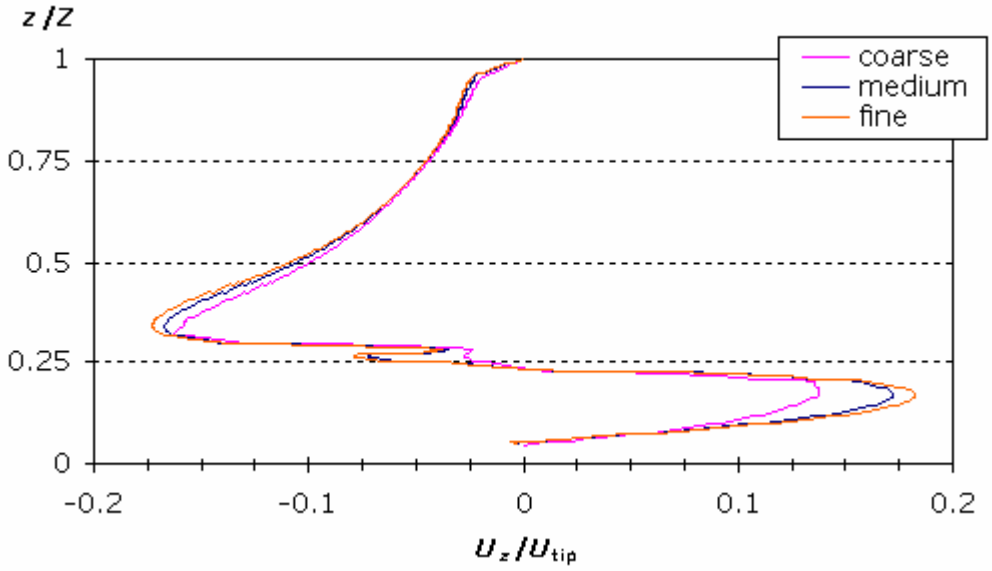

(a)

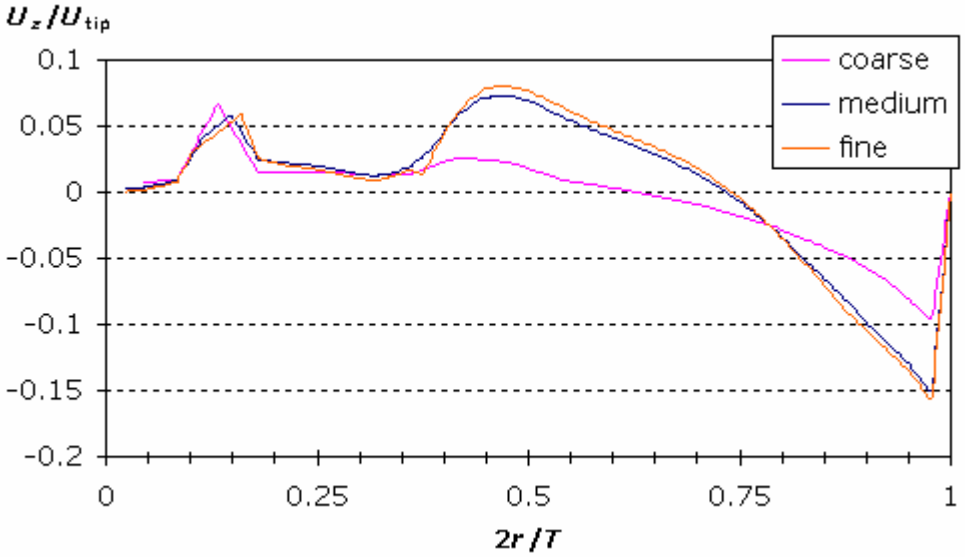

(b)

Figure 7. 16 Illustration of the influence of the grid resolutions. (a) Axial profile of the axial velocity at a clearance of 0.5mm away from the blade edge. (b) Radial profile of the axial velocity at 0.5mm below the blade edge.

The discontinuity at the start of the trend in the plot of the axial profile (Figure 7. 16(a)) arose because of the dished shape of the vessel base; in the plot of the radial profile (Figure 7. 16(b)), it occurred where the narrow hole below the central shaft was removed to avoid the grid singularity at the axis. As shown in Figure 7.16, apart from the case of the coarse grid resolution which under-estimated largely the velocities at most places, the deviation between the two finer grids was marginal (by 7% at most). Therefore, it can be considered that the medium grid resolution of 79,488 cells was sufficient to

obtain grid independent results. It should be noted that for the CFD simulations with the inclusion of chemical reactions to be presented in the next section, the geometry of the whole tank at ~160,000 cells was used due to the single inlet of injection of ethylene oxide.

The vector plot of the mean velocity in an *r-z* plane midway between the two baffles for the flow generated in the laboratory autoclave at the kinetic condition used is shown in Figure 7. 17. As can be seen in the figure, the characteristic "figure-eight" pattern, typically with two distinctive recirculation zones, was poorly defined in this case. At a rotational speed of 1700rpm, the resulting impeller discharge flow impinged forcefully onto the tank wall due to the short clearance between the impeller and the wall (4.45cm). When the impeller discharge stream met the wall, it pushed the local flow to three separate directions, two sideways to the upper and lower sections of the reactor and one in direct reverse to the impeller stream. The reverse flow interfered with the downstream flow of the impeller discharge which separated into two streams, each forming a circulation loop, one to the upper and one to the lower part of the vessel. As for the two sideways streams, with sufficient momentum remaining after the impact, the streams did not travel along the vessel wall that normally extended to either side of the vessel space. Instead, the flow followed a circular trajectory around the circulation centre, back to the low-pressure zone behind the impeller blade. The top stream entered the low-pressure zone from top of the impeller at an angle to the blade edge; the bottom stream entered from below the inner blade edge with a portion drawn into the space between the inner blade edge and the shaft. These entrance flows at an angle into the low-pressure zone behind the impeller blade were believed to account for the ripples observed in Figure 7. 16.

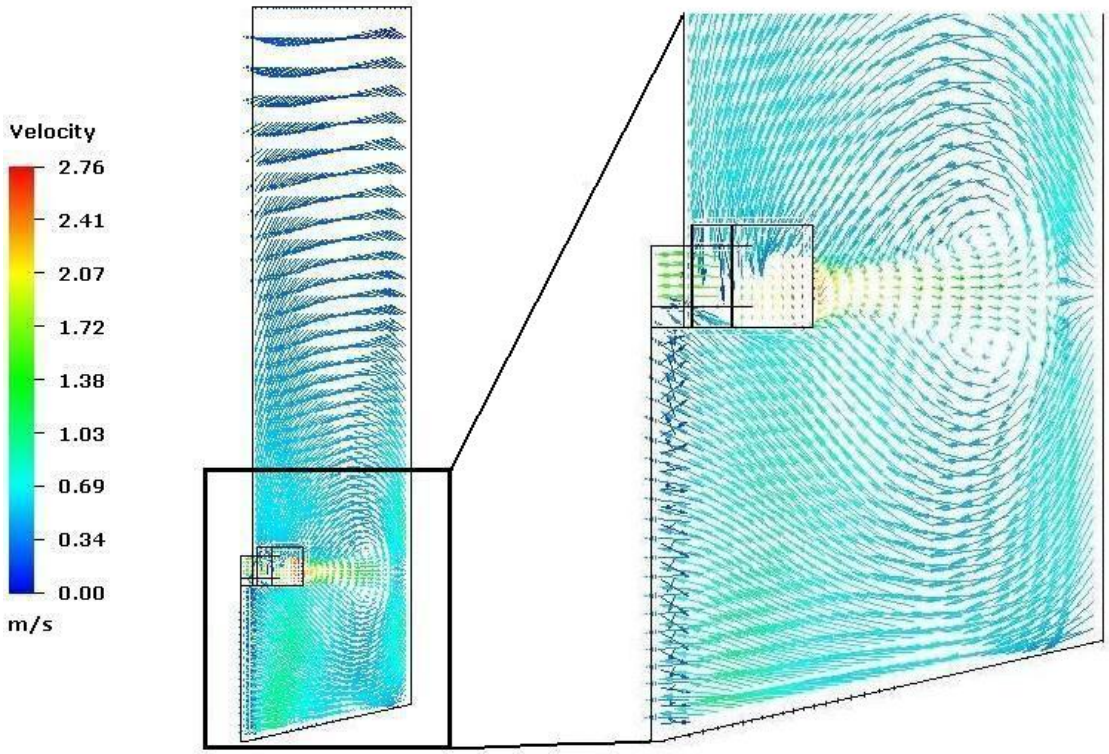

Figure 7. 17 Vector plot of a *r-z* plane, θ=90° halfway between two baffles.

7.6.2.2 Industrial NIS A reactor

The NIS A reactor with the dual-Rushton impeller as described in Table 7. 1 is illustrated in Figure 7. 18. Each of the Rushton impellers is of the standard configuration. Four baffles, each of one-tenth of the tank diameter, are placed 90° apart around the tank. In the grid sensitivity assessment, the liquid height was 93% of the tank diameter. The working fluid used was nonylphenol with 11 moles of ethylene oxide at 150°C, of density 960kg/m^3 and viscosity 5.2×10^{-3}kg/ms. The impeller speed was set at 100rpm, corresponding to a Reynolds number of 156,000 and an impeller tip velocity of 3.72m/s and 1.83m/s for the top and bottom impeller respectively. The physical presence of the injection pipe was not included in the model. Therefore, due to the geometrical periodicity, 180° of the tank was used. Four grid resolutions were tested, mainly increasing the number of cells in the top impeller blades. Details of the grid information in each case can be found in Table 7. 7. The computational strategy adopted to attain the final time-periodic flow was similar to that used in the grid sensitivity test for the laboratory autoclave; the MFR method was applied first to overcome the start-up of the flow pattern from fluid at rest, followed by the SG calculation for 130 complete revolutions. Of the 130 rotations by the SG computation, the first 100 rotations was run at a time step equal to one complete cycle of rotation and the last 30 rotations at the time step equal to 1/72nd of a cycle. Figure 7. 19 shows the effects of grid resolutions on the axial and radial profiles of the axial velocity at a line in the immediate impeller periphery in the final, time periodic flow.

Table 7. 7 Overview of the computational grids used for the grid-independency assessment for the industrial scale autoclave.

Grid density	Very coarse	Coarse	Medium	Fine
Cells along z	62	74	76	78
Cells along r	36	36	36	36
Cells along θ	27	33	38	44
Cells in the top blade $(z\times r)$	4×6	4×8	6×10	8×12
Cells in the bottom blade $(z\times r)$	2×4	4×4	4×4	4×6
Overall grid cells	60,264	85,248	103,968	123,552

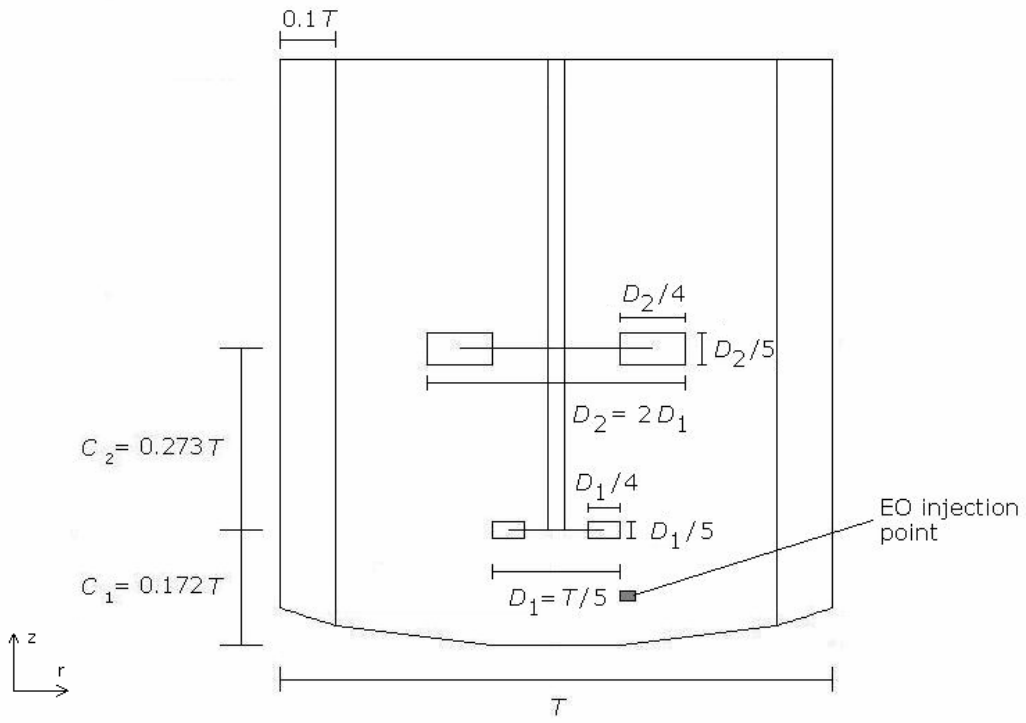

(a)

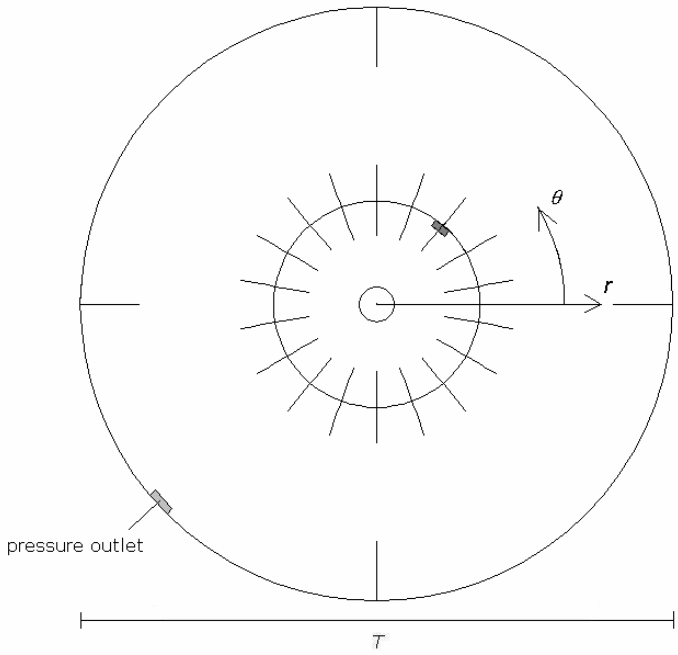

(b)

Figure 7. 18 Model geometry of the industrial reactor stirred by a dual-Rushton impeller: (a) front view; (b) top view, only showing the top impeller.

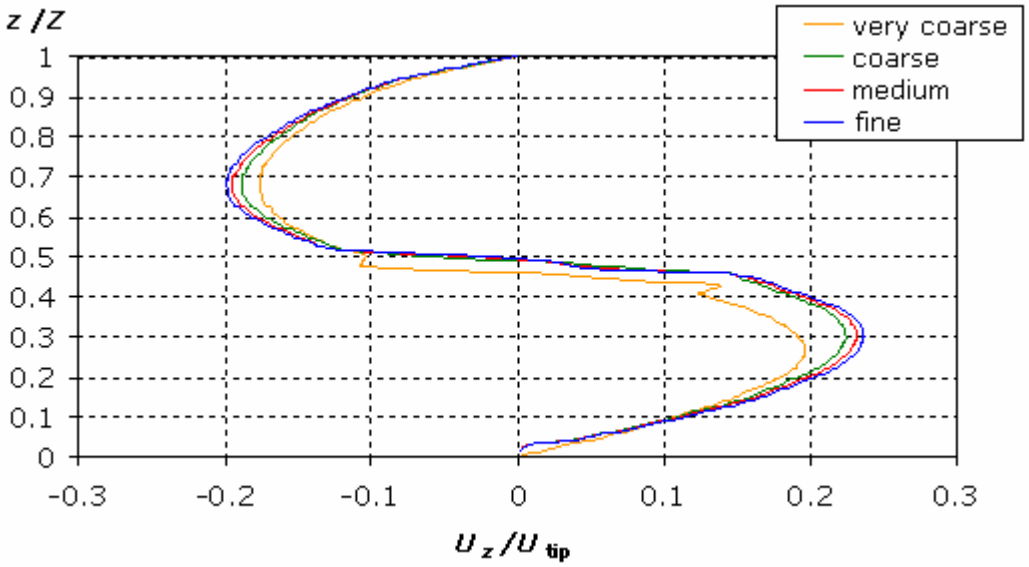

(a)

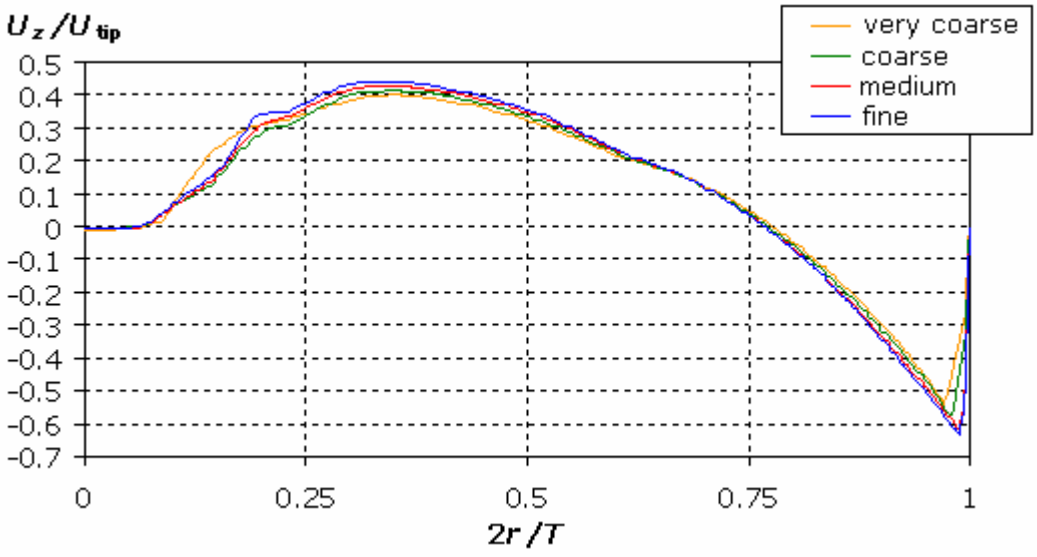

(b)

Figure 7. 19 Effects of grid resolutions on (a) axial profile of axial velocity at a vertical line 4.5mm outside the top blade edge; (b) radial profile of axial velocity at a horizontal line 5mm below the bottom blade edge.

Figure 7. 19(a) shows the axial profile of the axial velocity at a vertical line 4.5mm outside the top blade edge. As can be seen in this figure, apart from the very coarse grid resolution that largely under-predicted the intensity of the velocity at the recirculation zones, the three finer grids predicted the flow with marginal difference; 6% at most between coarse and fine grids; 3% between medium and fine grids. While in the radial profile of the axial velocity at 5mm below the bottom blade impeller edge as shown in Figure 7. 19(b), the deviation between different grid resolutions was small, even when the number of the cells was increased threefold from a very coarse to a fine grid. Hence, the medium grid resolution at ~104,000 cells was considered sufficient to achieve the grid independent results. That is, a total of approximately 208,000 cells will be used for the computational domain of a 360° tank geometry.

As can also be noted in Figure 7. 19(a), the axial profile of the axial velocity resembled that of a single-Rushton stirred reactor with two recirculation zones, one above and one below the impeller of which the centre line was about 0.5*T*. The effect of the bottom impeller of the smaller diameter on the axial velocity was hardly noticeable in the figure at its off-bottom clearance of 0.172*T*. A further examination on the vector plot at a vertical plane mid-way between two baffles confirmed the existence of only two recirculation zones about the top impeller (see Figure 7. 20 below).

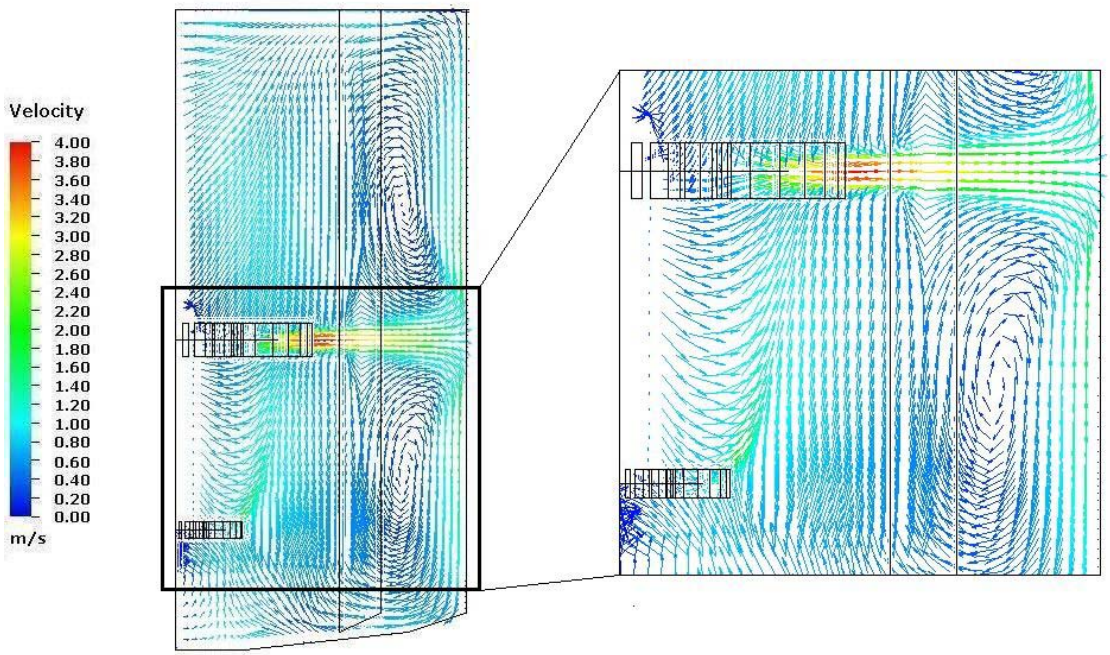

(a)

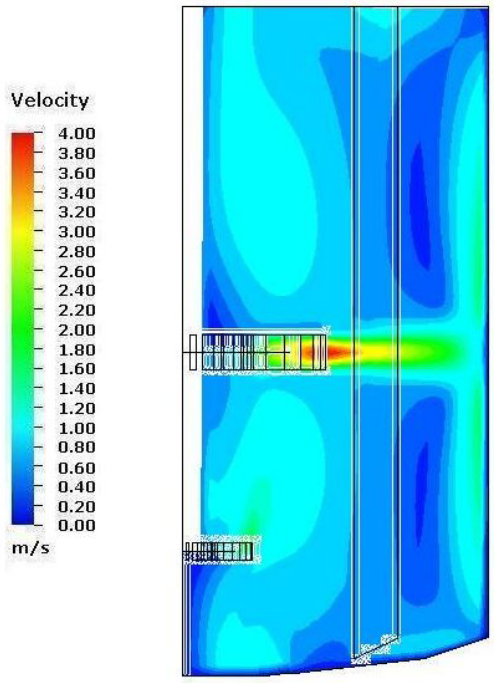

(b)

Figure 7. 20 Velocity field in the dual-Rushton stirred reactor: (a) the *r-z* plane vector plot, (b) the contour map.

As discussed earlier in Section 5.2.3.2, a stable merging flow pattern generated by two Rushton impellers with the same size would have two large ring vortices formed around each impeller, right and left to the impeller and therefore, four large ring vortices (refer to Figure 5. 9(b)). Within the zone between the two impellers, the impeller streams should follow a near straight-line at 45° toward one another and merge at mid-way of the zone (in the case C_1=C_2=1/3T). However, the bottom impeller of the dual-Rushton impeller investigated in the present study is half the size of the top one. Hence, the resulting flow pattern differed considerably from what was expected as a merging flow pattern discussed above. As is shown in Figure 7. 20, the outflow from each impeller did not follow the path that moved towards one another and merge at the mid-way of the zone between the impellers. The top impeller discharge retained a strong radial velocity component which impinged onto the vessel wall and split into two streams, while the bottom impeller discharge was swept axially upwards, towards the top impeller by the recirculation flow of the top impeller blades entering from below. Overall, there were two large ring vortices identified in the side of tank geometry shown in Figure 7. 20 for this merging flow pattern, which was similar to that of a single Rushton impeller. These two large vortices, one above and one below the top impeller, were generated from the impeller discharge stream of the top impeller. The deflected outflow from the bottom impeller merged with the recirculation flow of the top impeller which enhanced the returning flow into the low pressure regions behind the top impeller blades. The maximum velocity magnitude of the impeller outflow due to the merge was each found close to 100% of its impeller tip velocity. In most of the reactor zones, the velocity magnitudes were about 20% of the impeller tip velocity of the large impeller. The presence of the small impeller at a lower off-bottom clearance significantly improved the flow movement in the region below the impeller adjacent to the vessel base where normally a dead pocket would have been observed with the velocity magnitude less than 10% of the tip velocity (see Figure 7. 20(b)).

7.7 Ethoxylation validations

The validation of the CFD model for an ethoxylation process was carried out in two parts. The first part involved the integration of the kinetic model previously established in the laboratory autoclave into the CFD simulation with the use of the experimental data collected from the kinetic runs in Chapter 4. The temperature range of the flow field considered in the CFD model for the laboratory-scale reactor was between 88 and 130°C. The second part extended the CFD simulation to an industrial ethoxylation reactor operated at higher temperatures, about 140-160°C. The simulation for the industrial reactor also incorporated the ethylene oxide injection system that was analysed in Section 7. 3.

7.7.1 Laboratory-scale reactor

The validation study for the laboratory autoclave was based on the kinetic experiments presented in Chapter 4, where a series of ethoxylation runs was conducted at different reaction temperatures. To facilitate the selection of a frame in an ethoxylation run for numerical simulation, the injection process of ethylene oxide mass was sliced into a series of snapshots. The frame of a snapshot was taken as the interval between a pair of consecutive additions of ethylene oxide. That is, starting from the opening of the ethylene oxide feed valve through its closing for that addition until it opened again for the following addition. Only the snapshots situated along the propagation step of the ethoxylation run were of interest for the numerical studies. One snapshot from each kinetic run was then chosen for simulation at which the reaction contents height (Z) to autoclave diameter ratio (T) was either at 1.5 or 2. The numerical models investigated different combinations of Z to T ratios and temperatures, for which the solutions for temperature field were obtained by taking care of the heat transfer between the reaction exothermic heat and the heat removal by the cooling coil (Section 7.5.4). The simulation computed the amount of ethylene oxide reacted for the chosen snapshot. Since the amount of ethylene oxide injected within a snapshot represented the amount of consumption within that snapshot because of the fixed pressure used in the operations, these results were validated against the experimentally measured values. Table 7. 8 outlines the cases modelled and their boundary conditions used.

Table 7. 8 Overview of the model and the boundary conditions.

	Liquid height to tank diameter ratio			
	Z/*T*=1.5	*Z*/*T*=2		
Kinetic run no.	kin.1a	kin.2b	kin.3a	kin.4a
Temperature, °C	88	99.5	115	125
Heat of reaction (J/kg EO)	-1.888×10^{6}	-1.888×10^{6}	-1.891×10^{6}	-1.893×10^{6}
Cooling heat flux, W/m^2	-1.46×10^{3}	-2.49×10^{1}	-1.06×10^{3}	-4.01×10^{3}
Viscosity, kg/ms	0.0113	0.0075	0.0047	0.004
Impeller Reynolds number	2,400	3,600	5,600	6,800
EO mass injected at the chosen snapshot, g	4.95	4.9	6.62	6.12
EO mass fraction initialised, $Y_{EO}(0)$	0.071	0.001	0.015	0.032
Time interval of the chosen snapshot, s	180	120	60	60

The heat flux imposed on the walls near the cooling coils in the numerical model was taken based on an averaged ethylene oxide injection rate from a period of time during the propagation step instead of a value calculated locally within that snapshot. The low temperatures used in the above experiments ensured the chemical kinetics regime was in control. Consequently, the reaction mixture was relatively viscous and the resulting impeller Reynolds numbers fell into the transition flow regime. Although the flow in the kinetic runs was not fully turbulent, for simplicity, the k-ε turbulence model was assumed to be applicable and used in the numerical model.

Because of the single injection of ethylene oxide, the whole tank geometry of 360° was used. A two-step computation strategy was applied. The first step established the time periodic flow induced by the impeller with species and temperature equations deactivated. Once the flow field was established, the second step applied the frozen field approach (Section 7.5.7) to solve for the enthalpy and the species concentration equations with the hydrodynamic equations off. The initial conditions at the start of the frozen field computation set a uniform species concentration for ethylene oxide and temperature at the reaction value in every cell. The value of ethylene oxide mass fraction initialised at the beginning of the frozen field calculation was derived from a subtraction of the amount of ethylene oxide in the vapour space and the amount consumed in the ethoxylation from the total cumulative ethylene oxide mass and then divided the value by the total mass of the reaction content. The species concentration was solved as mass

fraction term as described in Chapter 6. A number of cells in volume equivalence to the amount of ethylene oxide injected during the chosen snapshot were also initialised at the location of injection. This was used with the assumption that the intermittent nature of the ethylene oxide injection had no major disturbances on the flow generated by the impeller at an impeller tip velocity of 2.83m/s by the rotational speed of 1,700rpm as mentioned in Section 7.5.5. The temperature of the ethylene oxide mass initialised was assumed as 25°C. This value would later be proven to be insensitive to the overall temperature field distribution since the reaction was highly exothermic and quickly evened the temperature difference. The simulation was then run for 60 to 180 seconds of real time, depending on the size of the time interval of the snapshot listed in Table 7. 8. A model time step sensitivity test was conducted in calculations of species and temperature distribution with the time step size varying between 0.01s and 0.05s. It was found that the difference in the results with the use of the smallest time step at 0.01s and the largest time step of 0.05s was negligible. Hence, the model time step size of 0.05s was used. The transient computations for the species and temperature calculations were performed at eight SIMPLEC iterations per time step and took an average of 360s on Compaq XP1000 machines to simulate 1s of the real time.

The predicted results for the amount of ethylene oxide reacted within the chosen snapshot were given in Table 7. 9. These results compared very well with the experimental values specified in Table 7. 8; the discrepancy was less than 15%. The discrepancy between the simulated and experimental results could be accounted for by (1) the accuracy of the kinetic model: mean Arrhenius parameters of propagation step carried an accuracy of 5-24% as discussed in Chapter 4; (2) heat treatment in the numerical model: the numerical model took a rather ideal approach for temperature calculation. First, the computation domain was entirely initialised with a uniform temperature, except for the few cells designated for ethylene oxide mass injection. The uniform temperature field assumed no temperature variations in the reactor, in which the computational cells in contact with the cooling coils would be lower in value. Additionally, in the experimental operation, the cooling water flow control was in line with the reaction rate. In other words, the heat removal rate in the real system was not perfectly maintained at the set constant throughout the entire process, or at any particular snapshot. In contrast, the simulation model used a constant, averaged heat removal rate. These two factors were the major contributions to the higher ethoxylation rate observed in the simulation results.

Table 7. 9 Model prediction results for the laboratory ethoxylation.

	Liquid height to tank diameter ratio			
	Z/*T*=1.5	*Z*/*T*=2		
Kinetic run no.	kin.1a	kin.2b	kin.3a	kin.4a
Simulated EO mass reacted, g	4.36	4.98	6.99	6.20

The contour maps on the spatial distribution of the ethylene oxide mass fraction in the bulk liquid (Y_{EO}) and the reaction content temperature are given in Figures 7. 21 to 7. 24. The mid-plane between the two baffles was also through the centre of ethylene oxide injection pipe (See Figure 7. 15(b)). The distribution of ethylene oxide mass fraction within the first four seconds of the real time in the frozen field computation is shown in Figure 7. 21. The spatial distribution for every one second interval was plotted based on the local range of that interval. It can be seen that at the end of the fourth second, the ethylene oxide mass was thoroughly dispersed through the entire vessel; the variation in mass fraction at various reactor places was less than 10^{-4} kg of ethylene oxide per kg of the total reaction liquid content. As expected, the dispersion of the ethylene oxide mass followed the flow pattern shown in Figure 7. 17. Since the ethylene oxide mass patch was initialised at the bottom section of the vessel near the wall below the outflow of the pipe, the dispersion of the ethylene oxide mass first took place through the circulatory flow in the bottom part of the vessel and gradually dispersed to the upper part of the vessel through the impeller discharge stream. Hence, the lower section of the vessel achieved the homogeneity in the ethylene oxide distribution ahead of the upper section of the vessel (see the plot in 2s). Figure 7. 22 shows the variation of ethylene oxide mass distribution in every 10s into the ethoxylation based on the global range of the mass fractions between 10s and 60s. As can be seen against the colour legend, the concentration of ethylene oxide decreased with time due to the consumption in ethoxylation. By the end of 50s, the amount of ethylene oxide injected was very much exhausted as the mass fraction returned to the initialised value at approximately 0.032. By the end of 60s, the ethylene oxide concentration dropped below the initialised value, which indicated a pressure drop in ethylene oxide partial pressure in the vapour space. This reflected truly the operation scheme carried out for the laboratory autoclave described in Section 3.4.3 in Chapter 3. The feed of ethylene oxide was introduced whenever a pressure drop of 15-25kPa was observed and the subsequent amount injected was to maintain the pressure at the operating set constant.

The temperature distribution of the first two seconds of real time and the entire 60s interval of the chosen snapshot simulated are shown in Figures 7. 23 and 7. 24. As can be seen in Figure 7. 23 for the first 2s of the distribution, the cold fluid of ethylene oxide injection at 25°C lowered the initial temperature value by about 2°C in the bottom section of the reactor in the first 0.5s. The cold fluid also started to spread into the near wall of the top section of the reactor. The apparent temperature differentiation within the reactor lasted only for another 1.5s. By the end of 2s, the temperature appeared to be uniform in most of the reactor, apart from the near regions of the walls at the free surface, reactor base and dip-leg pipe which were assigned constant temperature at the reaction temperature. In Figure 7.24 for the entire interval of the simulation, it is evident that the temperature gradually rises from initially 1°C below the reaction temperature at the end of 5s to 1°C above at the end of 60s, possibly due to the assumed average constant heat removal rate used being higher than the actual during the chosen snapshot. However, the variation in the simulated results was well in the range allowed for in the temperature

controlled experiments. The results also corresponded well to an experimental observation that the temperature of the entire system during an injection, bringing in cold fluid, was lowered by a few degrees before the exothermic heat was released.

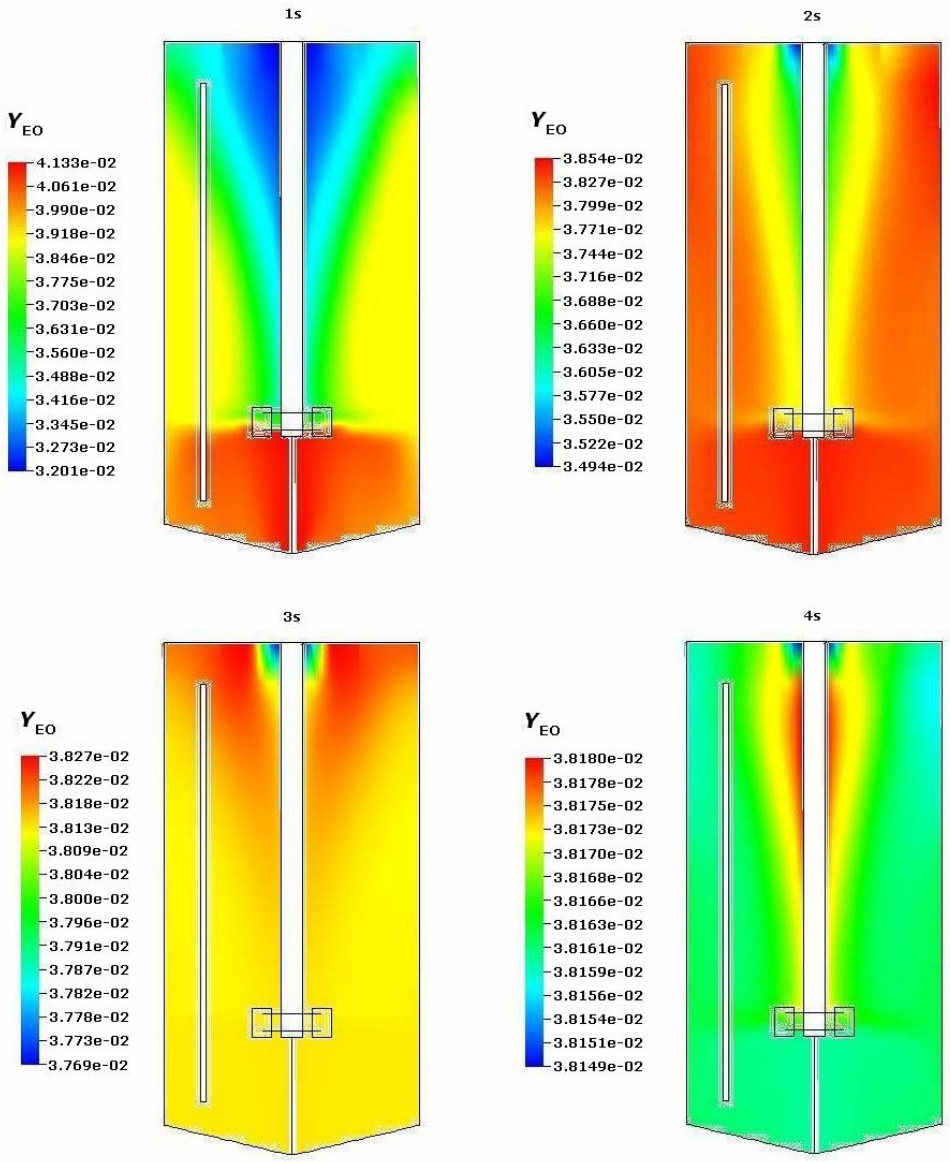

Figure 7. 21 Variation of the spatial distribution of ethylene oxide mass fraction Y_{EO} with time for the first 4s in the chosen snapshot.

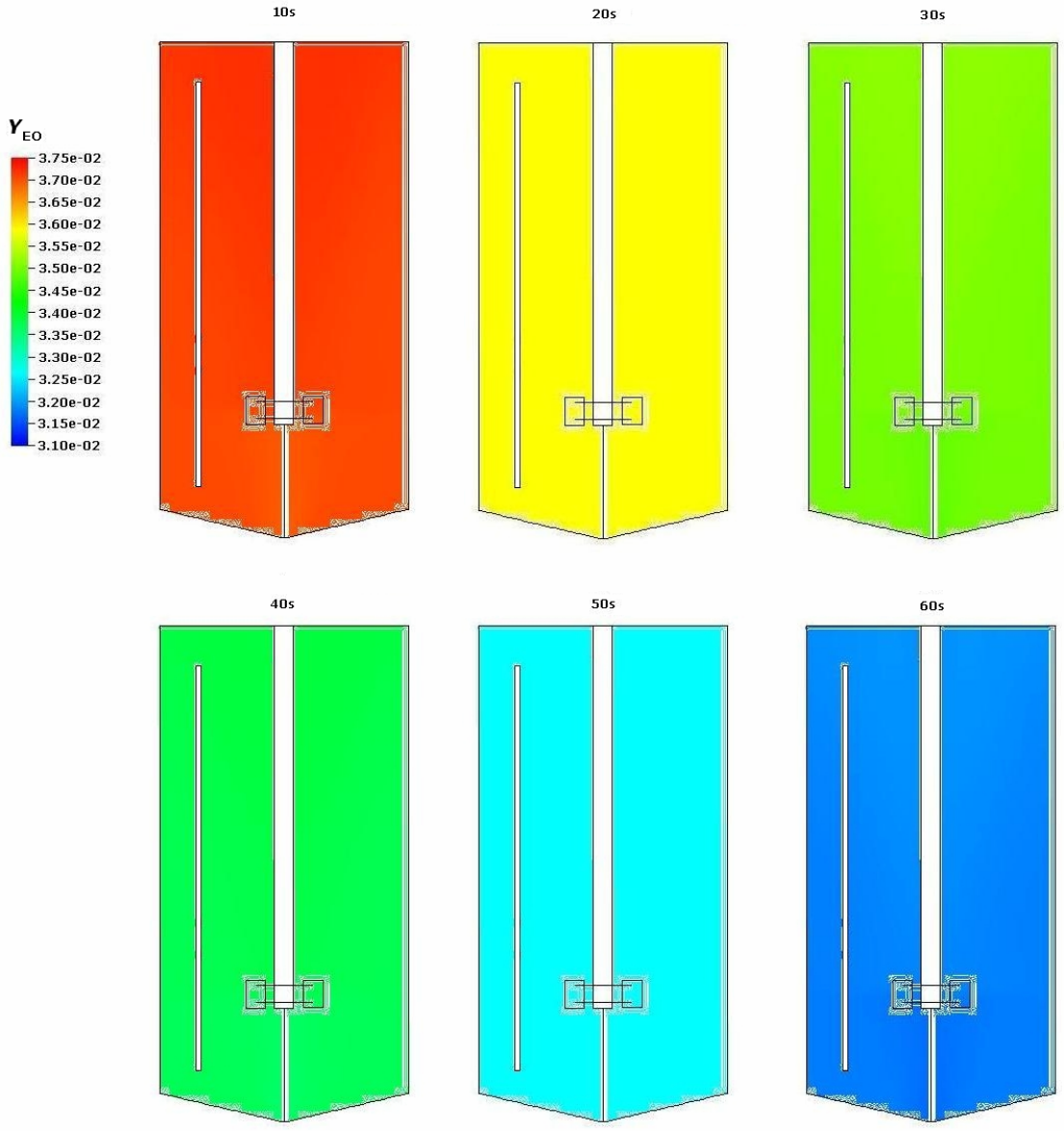

Figure 7. 22 Progress of ethylene oxide mass fraction Y_{EO} at 10s interval through the entire interval of the chosen snapshot. Note that the concentration scale in this figure is different to Figure 7. 21.

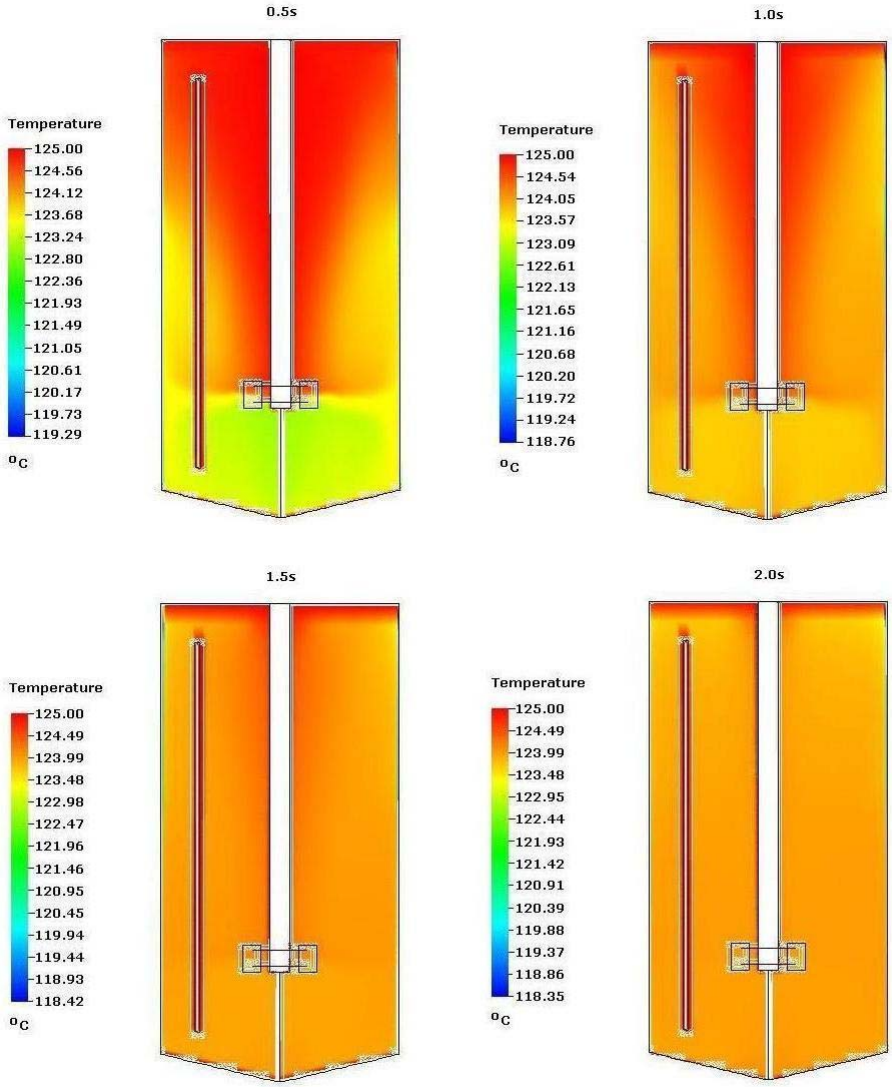

Figure 7. 23 Variation of the spatial distribution of temperature with time for the first 2s of the chosen snapshot.

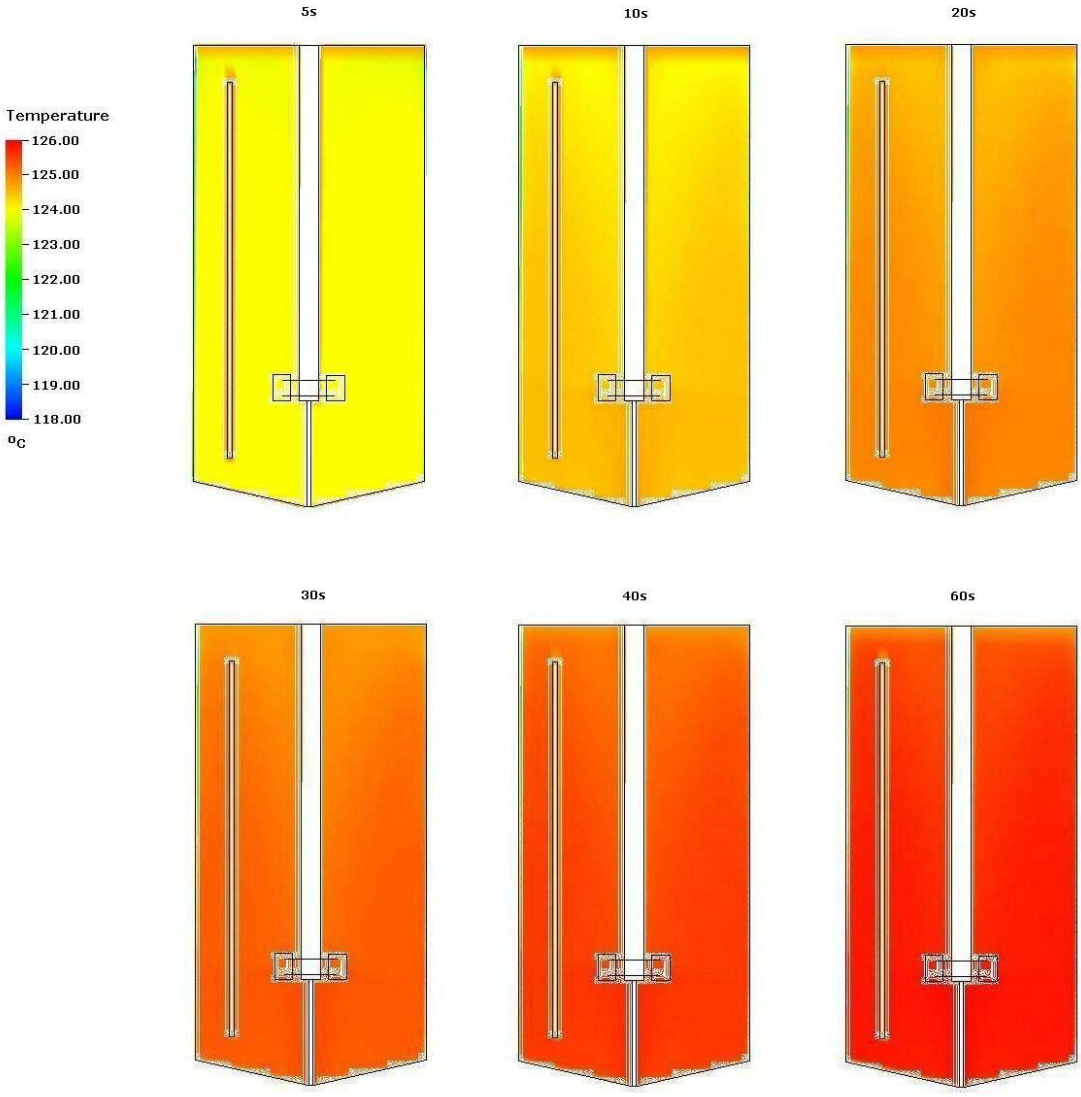

Figure 7. 24 Variation of the spatial distribution of temperature with time for the full interval of the chosen snapshot.

7.7.2 Industrial NIS A reactor

A different approach was adopted for the validation of the industrial ethoxylation simulation to that of the autoclave simulation discussed above. In the laboratory kinetic experiments, the pressure was fixed at a set value (see Table 4. 3) and therefore the ethylene oxide injection was intermittent to maintain the pressure at the constant value. Whereas in the industrial operation, the pressure of the reactor was gradually ramped up by continuous injection of ethylene oxide towards the maximum operating pressure as illustrated in Figure 7. 6. As discussed in Section 7. 4, for modelling the commercially operated ethoxylation process a snapshot should be chosen when the ethylene oxide injection rate had reached the current maximum and at a total pressure above 320kPa for ethylene oxide to remain liquid injection. The computational model incorporated the dispersion of the continuous ethylene oxide injection with the chemical reactions in the reaction mixture at the kinetics estimated at the industrial operating temperature and computed the time-variant ethylene oxide concentration. The results were then checked against the ethylene oxide concentration corresponding to the observed ethylene oxide partial pressure derived from the difference between the total reactor pressure and nitrogen partial pressure recorded in the plant batch report. The validation study modelled three different nonylphenol ethoxylates production batches, each with different liquid-height-to-tank-diameter ratios. The batches studied included N2, N11 and N40 productions. Table 7. 10 presents the operating conditions applied in each production and the model boundary conditions used in the CFD model based on a pre-selected snapshot according to the scope defined in Section 7. 4.

Table 7. 10 Overview of the operating and the initial boundary conditions of the batch productions studied by CFD simulation.

Batch ID	N2-71542	N11-74591	N40-75579
Operating conditions			
Starting nonylphenol, kg	3639	1627	582
Reaction temperature, °C	156.9	160.3	151.0
Reactor conditions at the chosen snapshot			
EO mass flow rate, kg/min	15.60	15.73	16.26
At t = 0 minute			
Total reactor pressure, kPa	326.5	322.6	338.0
Nitrogen partial pressure, kPa	244.5	244.0	212.0
At t = 10 minutes			
Total reactor pressure, kPa	351.8	343.2	351.3
Nitrogen partial pressure, kPa	289.9	266.0	225.7
Initial model boundary conditions			
Z/T	1.37	1.14	0.93
Averaged EO adducts, N_{EO}	1.31	7.33	25.91
EO mass fraction, $Y_{EO}(0)$	1.16×10^{-2}	8.98×10^{-3}	9.20×10^{-3}

The experimental details of the pressure variation recorded in the batch run report during the simulated snapshot in the above batch runs are given in Appendix D. Attempts had been made to include heat calculations in the simulation of the industrial process but were eventually abandoned. It was found that the use of an averaged heat removal rate estimated in Equation 7. 5 could not represent accurately the cooling capacity used during the process in reality since the cooling water flow rate was adjusted with the ethoxylation rate to best maintain the temperature at the desired value. It was also not correct to assume a uniform temperature across the entire computational domain for simplicity as the initial boundary condition of the numerical model. The cooling water coils used in the industrial reactors extend to the circumferential wall and the base of the tank. The initialisation of the uniform temperature for the whole of the computational cells could not justify the temperature of the cells in contact with the cooling coils. The use of a global temperature value was likely to overestimate the temperature in those places.

Consequently, the numerical model with the inclusion of the heat calculation gave rise to an over-shoot in the extent of ethoxylation. On the other hand, assuming a fixed heat removal rate turned out to be insufficient for the additional exotherm from the over-shoot of the reaction activity. Hence the computation returned an even higher temperature field. The solution to this problem would be to use a local temperature value in the areas where the cooling coils were placed, and implement a variable heat removal rate in line with the reaction extent. However this was not feasible within the time frame for this research project.

Alternatively, the temperature problem in the numerical model was overcome by assuming perfect heat removal. This was reasonable because it was known the operation at the maximum ethylene oxide mass rate was carried out isothermally with ample cooling capacity.

The computational strategy applied for the numerical model for the industrial NIS A reactor followed the same two-stage procedures used for most of the numerical models described in this thesis. The first stage involved both the MFR and SG methods to establish the flow pattern without solving the species mass transfer. In the flow establishment, the MFR method was performed first for a closed system without an injection to establish the flow from rest. The SG method was applied next to refine the flow variables and also to include the ethylene oxide injection (see Figure 7. 18(a)), however with the inlet composition of the initialised ethylene oxide concentration in the bulk reaction mixture. To satisfy mass balance, a single artificial outlet at the free surface was included in the model (see Figure 7. 18(b)). This compensated for the simplification that the liquid height remained constant during the snapshot. When the final, time-periodic flow at a monitoring location in the reactor, normal from the edge of an impeller blade, was achieved, the second stage of the computation procedure of the frozen field calculation began. The hydrodynamic equations were deactivated and the species concentration including the chemical reaction was switched on.

The comparison of the predicted mass fraction of ethylene oxide in the total liquid obtained from the numerical simulation with the experimental values is given in Figure 7. 25. The experimental ethylene oxide mass fraction referred to the ethylene oxide solubility in the polyoxyethylene mixture. By assuming the gas phase ethylene oxide reached near instantaneous equilibrium with the liquid phase, the ethylene oxide mass fraction was related to the temperature, ethylene oxide vapour pressure and averaged ethylene oxide adducts in the system by the Wilson method as discussed in Section 2.5.3.2. In the Wilson method, the ethoxylation reactor system was regarded as a pseudo-binary system of the polyoxyethylene mixture and ethylene oxide; the nitrogen solubility in the polyoxyethylene mixture was negligible.

In the N2 and N40 batches studied (Figures 7. 25(a) and (c)), the total pressure and nitrogen pressure recorded indicated a decrease in partial pressure of ethylene oxide in the chosen 10 minutes for the modelling (see Appendix D). The conversion of the partial pressure by the Wilson method into the ethylene oxide mass fraction showed a trend of a linear tendency in the experimental data, while the simulation predicted an exponential decrease due to the first-order dependency to ethylene oxide concentration as given in Equation 2. 25. During the chosen 10-minute slot, the agreement between the two results was satisfactory. The major sources of discrepancies were believed to be in association with (1) the accuracy of the Wilson method, which had a reported value of 17% (Di Serio *et al*., 1995); (2) the use of the mean Arrhenius parameters for the propagation step, which had an accuracy of 5-24% as discussed in Chapter 4. In the N11 batch studied, the ethylene oxide pressure fluctuated within 2kPa as can be seen in Appendix D. The Wilson method interpreted this fluctuation with little variation in the ethylene oxide mass fraction (Figure 7. 25(b)). This profile could be depicted with a straight line with a small inclination. After the initial drop, the simulation predicted a constant mass fraction of ethylene oxide which was seen to describe the experimental mass fraction very well within the chosen time slot.

The distribution of the ethylene oxide mass fraction in a complete revolution is shown in Figure 7. 26. The plot follows the trace of ethylene oxide from its point of injection to a full revolution of 360° through a series of consecutive angular displacements of 45°.

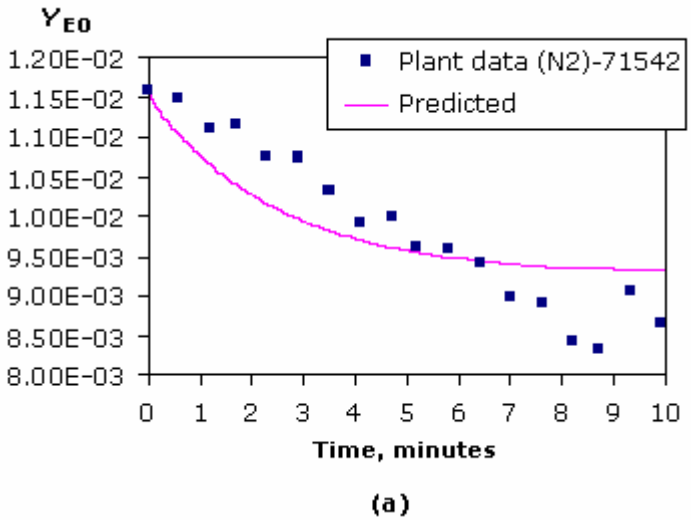

(a)

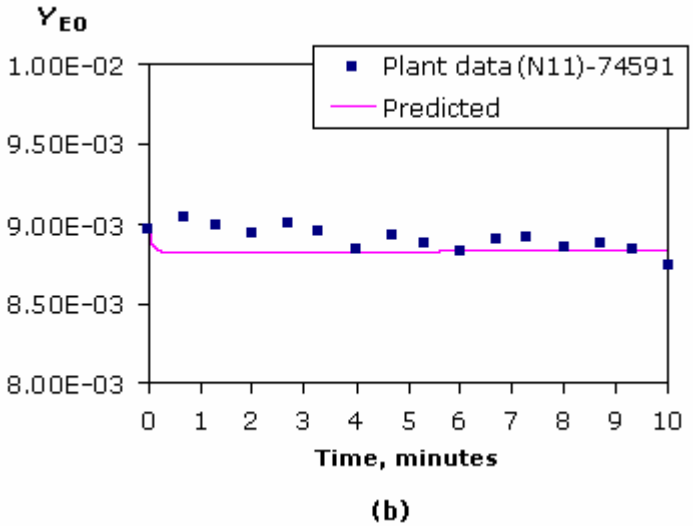

(b)

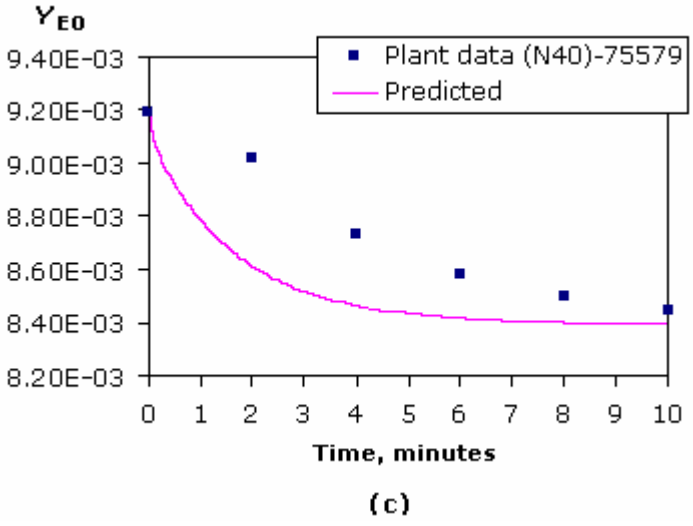

(c)

Figure 7. 25 Comparison of the predicted and experimental mass fraction of ethylene oxide of the batch runs listed in Table 7. 10: (a) N2-71542; (b) N11-74591; (c) N40-75579. Values for the experimental deduced mass fraction are given in Appendix D.

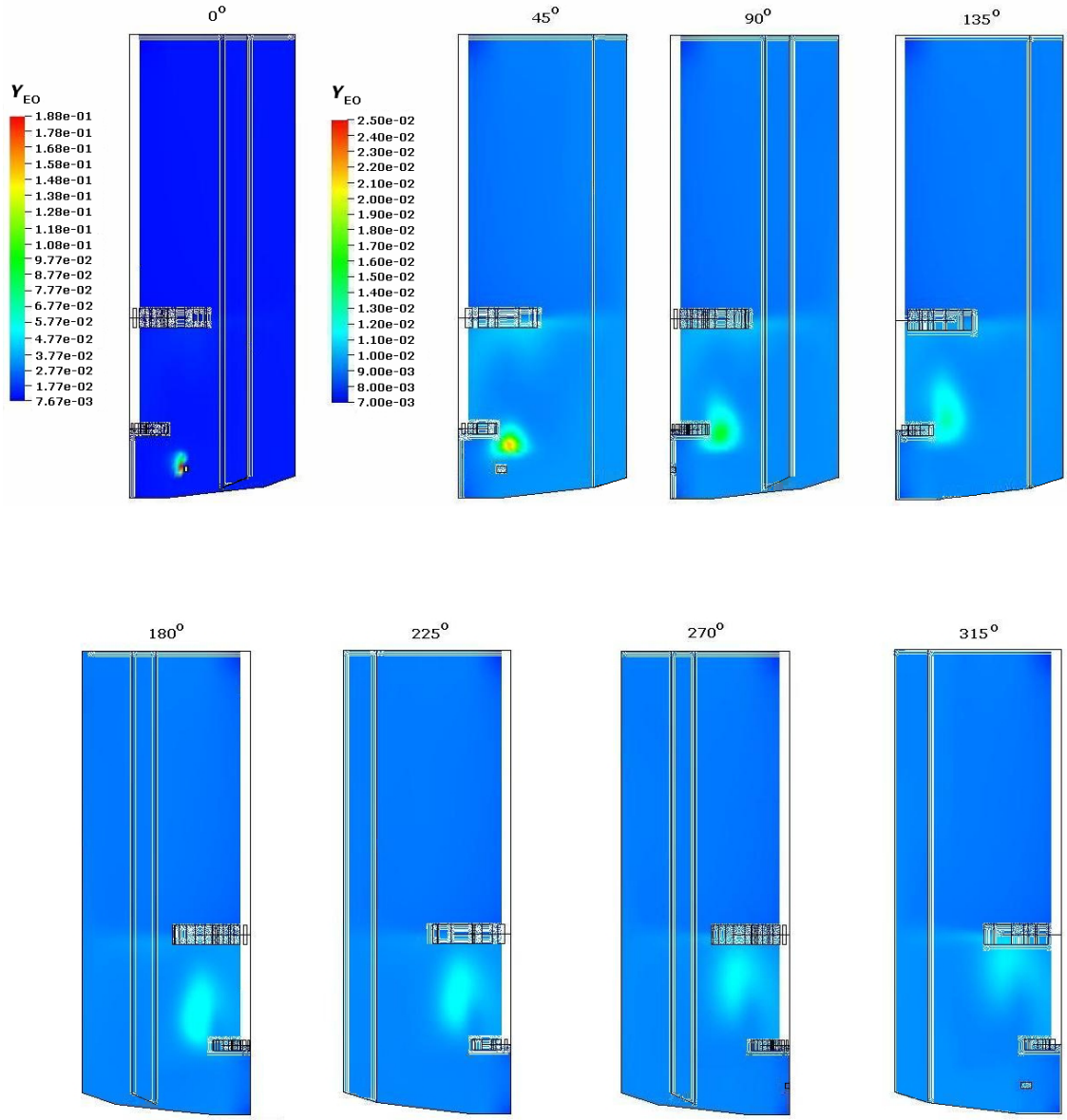

Figure 7. 26 Contour maps showing the progress of ethylene oxide mass fraction (Y_{EO}) at various angular planes relative to the centre of the injection point in the N11 batch run reported in Table 7. 10.

The first contour map in Figure 7. 26 plots the plane with the injection point. In this plot, the mass fraction was plotted against the local range of that plane. For the rest of the contour maps, the mass fraction was plotted against the global range of the concentration values in the 45° and 315° displacement after the injection plane. As shown in Figure 7. 7, the outflow of the dip-leg pipe was positioned towards the centre axis of the reactor vessel. Since the location of the injection point lay on the course of the recirculation flow into the lower pressure of the upper impeller (see Figure 7. 20(a)), the trace of unreacted ethylene oxide followed the recirculation pattern into the lower pressure regions of the impeller. From there onwards, it spread into the upper portion of the vessel. Most of the unreacted ethylene oxide, however, localised in the lower portion of the reactor. As is shown in the contour maps of 45° through to 315° planes, a shade of higher mass fraction in the shape of a kidney bean can be discerned at the lower half of the vessel. It should also be noted that even though the concentration of ethylene oxide was higher in the lower part of the vessel, the difference throughout the reactor was very small.

7.7.3 Concluding remarks

We have successfully validated the CFD model for a stirred ethoxylation reactor against the experimental data from both the laboratory autoclave and the industrial NIS A operations. The validation also verified the kinetics developed in the first stage of this research program and the assumption of liquid ethylene oxide injection under the certain specified conditions.

7.8 Increasing capacity

We have identified that the reactor pressure rating and the presence of nitrogen padding are limiting the ethylene oxide partial pressure in the current NIS A ethoxylation operations (Section 7.2.4). This section explores any opportunity for increasing the ethoxylation capacity. Two aspects were addressed: (1) the determination of the optimum ethoxylation rate under the current design specification; (2) explorations of the design specification for a new reactor if, for example, the ethylene oxide injection rate was increased up to 45 kg/min, that is, nearly three times the current injection rate. These studies were performed on the assumption that the existing cooling capacity was sufficient to cope with the rate increases. That is, all simulation runs presented in this section were performed for an isothermal reactor system. It should be noted that the earlier investigation on the cooling water capacity in Section 7.2.3 had suggested the cooling capacity was able to sustain up to 10 times the current ethoxylation rate if the high pressure cooling water was fully converted to steam.

As outlined in Table 7. 1, the design pressure for the $6m^3$ reactors is 4.45 bar and the normal operating pressure is kept below 3.62 bar. At this normal operating pressure, the current maximum

ethoxylation rates for both the QD2 and QD3 reactors were recorded at approximately 16kg/min. To determine the maximum ethoxylation rate at the limit of the current reactor design pressure, the ethylene oxide injection rate in the above-validated CFD model was allowed to increase until the design pressure was met. Table 7. 11 summarises various ethylene oxide injection rates studied and the corresponding pressure required for the reactor specification, using the N11 batch reported in Table 7. 10 as the basis of the model: the same initial model boundary conditions were used.

Table 7. 11 Summary of various ethylene oxide rates used in the optimisation study and the predicted results for total reactor pressure required.

EO injection rate, kg/min	Y_{EO}, kg EO/ kg total liquid	P_{EO}, kPa	P_{N_2} ,kPa	P_T, kPa
18	1.01×10^{-2}	89.15	280.77	369.92
20	1.13×10^{-2}	99.37	285.52	384.89
22	1.24×10^{-2}	109.20	290.21	399.41
25	1.40×10^{-2}	124.13	297.17	421.29
30	1.69×10^{-2}	150.70	359.32	510.02
35	1.96×10^{-2}	174.99	384.92	559.91
40	2.24×10^{-2}	200.06	410.09	610.15
45	2.49×10^{-2}	223.5	461.75	685.25

The ethylene oxide mass fraction Y_{EO} was computed by the CFD model previously developed in Section 7.7.2. The partial pressure of ethylene oxide P_{EO} was interpreted by the Wilson method based on the inputs of the mass fraction predicted, the reaction temperature and an estimated mean ethylene oxide adduct number N_{EO}. It was assumed that the gas and liquid phase ethylene oxide reached instantaneous equilibrium. The nitrogen pressure P_{N_2} was the total pressure exerted by the initial nitrogen padding and the nitrogen dissolution in the ethylene oxide feed (an average of 8.2×10^{-4} kg N_2/kg EO as mentioned in Section 7.2.4). The summation of the ethylene oxide partial pressure and the total nitrogen pressure gave the total reactor pressure. For the ethylene oxide injection rate below 25kg/min, the results for the ethylene oxide mass fraction were taken at the end of 10-minute simulation runs, otherwise the results were taken at the end of 15- minute runs for the higher injection rates. The results are summarised in Figure 7. 27 below.

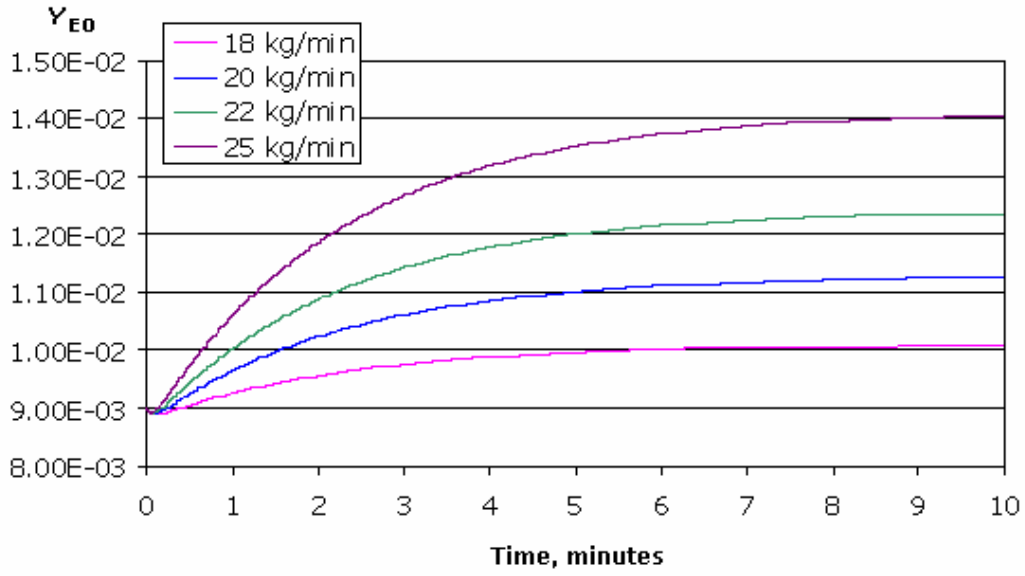

(a)

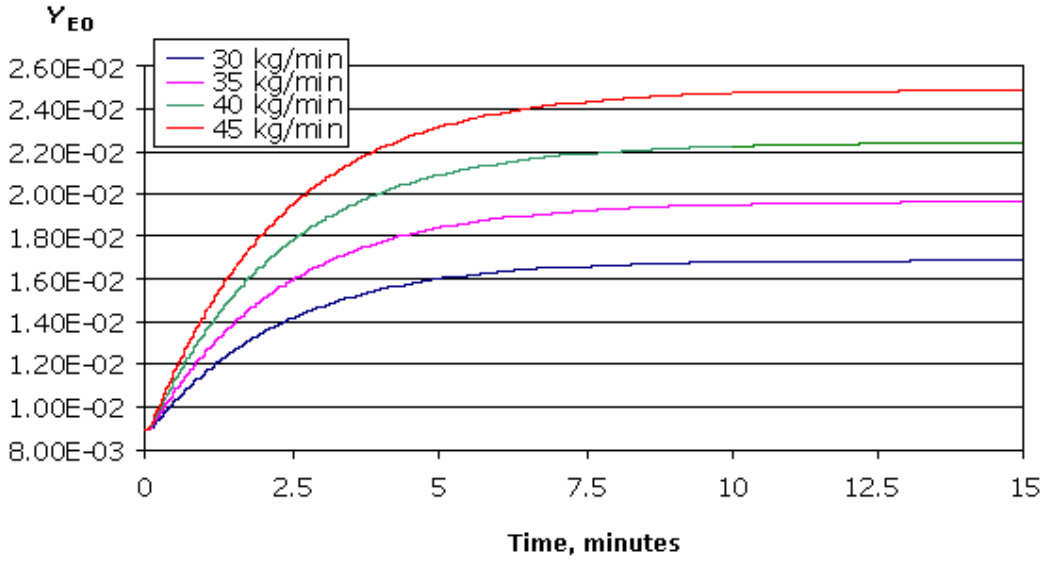

(b)

Figure 7. 27 Profiles of predicted ethylene oxide mass fraction due to various ethylene oxide injection rates: (a) a 10-minute run time; (b) a 15-minute run time.

As mentioned earlier in Section 7.7.2, at the ethylene oxide injection rate of 15.73kg/min in the N11 batch simulated, Y_{EO} was nearly invariant with time (see Figure 7. 25(b)). Thus, any injection rate higher than 16kg/min would lead to an increase in the ethylene oxide mass in the reaction mixture from its initial value which eventually levelled off with the progress of the reaction as shown in the figure above. It should be noted that in those simulation runs reported in Table 7. 11, the initial value of Y_{EO} used was that of the N11- batch listed in Table 7. 10.

The results of the total reactor pressure in Table 7. 11 indicated that the ethylene oxide injection rate could be raised to approximately 25 kg/min at the current design pressure of 4.45 bar. However, the current maximum operating pressure is kept at about 0.8 bar below the design pressure (3.62 bar versus 4.45 bar). This is based on a decision to have a good margin of safety during a potentially hazardous operation.

Further, the results from the simulation runs using an injection rate above 25 kg/min indicated the likely new required pressure rating (above 4.45 bar) of the reactors. For example, if the ethylene oxide injection rate were to increase to 45 kg/min, the normal operating pressure required was nearly 7 bar.

7.9 Conclusions

The ethoxylation process in a commercially operated industrial reactor was thoroughly examined in this stage of the research project.

Numerical simulations of the ethylene oxide liquid flow in the dip-leg pipe were presented. This enabled a better understanding of the state of ethylene oxide in the dip-leg pipe which led to the finding that above a certain reactor pressure and ethylene oxide injection rate, the ethylene oxide injection was essentially liquid. Hence, a single phase reaction system was established. Moreover, the use of a larger pipe would help to reduce the boiling of ethylene oxide, which in turn enhances the asset productivity through higher ethoxylation rate and shorter ethoxylation time as a result of higher ethylene oxide concentration in the bulk reaction mixture.

Key factors affecting the current asset productivity of the ethoxylation plant were examined which included mixing efficiency with respect to agitator configuration, heat removal rate and reactor pressure rating. It was found that the flow characteristics induced by different agitator configurations was insignificant in influencing the current ethoxylation behaviour; the existing heat removal capacity was sufficient to sustain at least double the current reaction rate observed, and the reactor pressure rating and the presence of nitrogen padding were the rate-limiting factors in the current NIS A ethoxylation operations. Consequently, the asset productivity could be improved by increasing the reactor pressure rating: an

increase in the design pressure of the reactor increases the bulk ethylene oxide concentration and hence, the ethoxylation rate.

A CFD model for the reactive flow in a stirred ethoxylation reactor was developed. The CFD predictions showed that the rate of ethoxylation could be improved by 50% under the current design specification if it was operated closer to the design pressure limit. The CFD model was further used to aid the exploration of a new reactor specification with the asset productivity increased to approximately three times the current performance.

Chapter 8

Conclusions and Recommendations

8.1 Conclusions

This thesis has presented a thorough analysis of rate phenomena involved in the manufacture of nonionic surfactants in the NIS A alkoxylation stirred tank reactors at the Botany surfactants plant of Huntsman Corporation Australia (HCA). Through a better understanding of the interactions between chemical kinetics and various physical transport processes in the ethoxylation operation, measures for enhancing the productivity were identified and recommended.

8.1.1 Kinetic modelling

In the context of the kinetic modelling, base-catalysed ethoxylation of nonylphenol in a stirred reactor was characterised as a sequence of interfacial mass transfer followed by liquid-phase reaction. To generate the kinetic data, experiments were performed in a 2-litre stirred laboratory autoclave. Experimental conditions employed to ensure the generation of reliable kinetic results included the confirmed absence of mass transfer resistance (high stirrer speed) and a relatively low reaction temperature (in the range of 80-125°C). It was found that to integrate the experimental data into a kinetic model for a description of the ethoxylation behaviour, the non-ideal features occurring during the operation needed to be characterised. This referred particularly to the presence of nitrogen.

The presence of nitrogen pressure reduced the partial pressure of ethylene oxide in the reactor, which subsequently reflected on the ethylene oxide solubility in the reaction mixture, and so the reaction rate. Nitrogen pressure was deduced to originate from its solubility in ethylene oxide in the storage cylinder where nitrogen was used for the pressurisation. It entered the vessel with ethylene oxide injection and accumulated in the vapour space during the course of the ethoxylation. The average nitrogen solubility

was experimentally determined as 0.0025kg N_2/kg EO in the ethylene oxide storage cylinder used in the laboratory autoclave.

The intrinsic reaction rates determined from the kinetic experiments were analysed based on a reduced ethylene oxide pressure and further expressed in forms of Arrhenius equation. The experimentally derived Arrhenius parameters agreed very well with those reported by Di Serio *et al*. (1995). A mathematical model using this kinetic information was developed for ethoxylation in the well-stirred laboratory autoclave. The model integrated the changes of ethylene oxide solubility, liquid density and volume and accumulation of nitrogen pressure with progress of ethoxylation into a rigorous kinetic model. The kinetic model was capable of closely predicting the ethoxylation behaviour and allowed the determination of the ethoxylation kinetics in the industrial-scale reactors.

8.1.2 Process optimisation and CFD simulations

An important assumption was made prior to developing the ethoxylation operations of HCA into a CFD process model. Because of the use of a dip-leg pipe for the path of ethylene oxide injection in HCA reactors, the ethoxylation process was treated as miscible liquids mixing followed by chemical reaction. This assumption was applicable in the laboratory autoclave operation presented in Chapter 3. Since the injections of ethylene oxide were controlled to a rate such that the system pressure was maintained constant during the ethoxylation, the rate simply represented the maximum allowable injection of ethylene oxide at that system pressure. The amount in each ethylene oxide injection was limited to the corresponding ethylene oxide solubility in the bulk liquid. If ethylene oxide injection exceeded the threshold, boiling would occur as the saturation vapour pressure exceeded the system pressure. A similar mode of operation was employed in the industrial-scale NIS A reactor. Ethylene oxide feed rates were adjusted in a way that the ethylene oxide vapour pressure was kept below the explosive limit, set according to the presence of nitrogen pressure. Estimation of the ethylene oxide gas content to the total injected found that a maximum of about 6% of ethylene oxide liquid was converted to ethylene oxide gas, indicating that the majority of the ethylene oxide injected remained in the bulk liquid. Further, CFD simulations of the ethylene oxide liquid flow in the dip-leg pipe used in a NIS A reactor showed that above a certain reactor pressure and ethylene oxide mass flow rate, the ethylene oxide injection was essentially liquid. The finding was particularly applicable when the ethylene oxide feed rate reached its maximum at which boiling was unlikely to take place.

The advantage of treating ethoxylation as a single-phase liquid reaction obviated the need to deal with the complexities of inter-phase transfer between gas and liquid. Moreover, keeping the ethylene oxide injected as a liquid in the bulk liquid gave rise to an operational benefit in terms of the asset productivity of the commercial reactors. The more ethylene oxide injection remained liquid in the reaction mixture (where the main reaction takes place), the higher the ethoxylation rate and the shorter the operation time. The

optimum situation would be ethylene oxide injection of 100% liquid all the way through the course of operation. The study of the effects of various pipe sizes on the heat transfer rate indicated that an increase in pipe size reduced the heat transfer rate. To minimise boiling, pipes of larger diameter were recommended.

Three possible rate-limiting factors in the NIS A operations were examined: mixing (mass transfer), heat removal, and reactor pressure rating (mass transfer). Mixing of the reaction contents in NIS A reactors is achieved by means of mechanical agitators. Different impeller configurations induce different flow patterns, which may result in a distinct reaction rate response. Comparisons of the reaction data were made between two NIS A reactors of the same size but equipped with different types of impellers for the production of the same nonionic surfactant. Although the dual Lightnin A315 impellers and the dual Rushton impellers induce different flow characteristics, the ethoxylation rates between the two differ only insignificantly. This suggested that the ethoxylation behaviour in the current mode of operation is insensitive to the agitator configurations used.

Heat removal in NIS A reactors is achieved by internal coils circulated with high pressure cooling water (HPCW). The HPCW capacity was found to be sufficient for at least double the current ethoxylation rate observed. Therefore, it is not the rate-limiting factor to the current NIS A ethoxylation operations. Further, it was found that the cooling capacity was able to provide heat removal for up to 10 times the current ethoxylation rate if the HPCW was fully converted to steam.

The reactor pressure rating and the presence of nitrogen padding were identified as the rate-limiting factors in the current NIS A ethoxylation operations. In the industrial-scale operation, nitrogen padding of 1 atm is inserted into the reactor at the start of an ethoxylation run to safeguard against ethylene oxide explosive hazards. Apart from this nitrogen padding used, additional nitrogen comes in with liquid ethylene oxide feed due to its solubility in the ethylene oxide storage break tank (at an average of 8.2×10^{-4} N_2/kg EO). Inert to the reaction, nitrogen ends up in the reactor vapour space and accumulates with the progress of ethoxylation in the semi-batch operation, ultimately pushing the total pressure past the operating pressure limit of the reactor. Therefore, the asset productivity could be improved by an increase in the reactor pressure rating: an increase in the design pressure of the reactor increases the ethylene oxide concentration in the bulk.

Three-dimensional, transient numerical simulations of the flow in a baffled reactor agitated by a single- or a dual-Rushton impeller were presented. The turbulence parameters were modelled with k-ε turbulence model. The relative motion between the rotating impeller and the stationary baffles were described by a steady-state calculation of multiple frames of reference (MFR) method followed by a time-dependent calculation of sliding grid (SG) method. The MFR method was used to overcome the flow

starting from still; the SG computation was to refine the flow data until the time-periodic condition was attained.

The simulations of the flow without chemical reactions were reproduced and agreed very well with the qualitative features of the experimental velocity data of Mahouast *et al*. (1987) and Wu and Patterson (1989) for a single-Rushton stirred vessel and Rutherford *et al*. (1996a) for a dual-Rushton stirred vessel. Good qualitative agreements were also obtained with the numerical results obtained by Brucato *et al*. (1998) and Micale *et al*. (1999) for the flow in the single- and the dual-Rushton stirred vessel respectively. The quantitative comparisons displayed some discrepancies, mainly due to the under-prediction of the turbulence energy, an inherent shortcoming associated with the use of the k-ε turbulence model.

The numerical model for the flow in an ethoxylation stirred reactor of HCA was described as turbulent mixing of an incompressible single-phase (hydrophobe substrate) fluid with a single chemical species (ethylene oxide). Simulations were performed for the ethoxylation flow in the 2-litre laboratory-autoclave used in the kinetic experiments, which was stirred by a single-Rushton impeller, as well as for a $6m^3$ NIS A reactor equipped with a dual-Rushton turbine. The former took into account the ethoxylation exotherm in the numerical model and the latter was carried out isothermally. The computed results of both the ethylene oxide consumption and the spatial distribution of temperature compared very well with the experimental measurements in the laboratory-autoclave operations. Good agreement was also reached between the simulated and experimental data on the changes of ethylene oxide mass fraction in the bulk liquid with time in the industrial NIS A operations.

The CFD process model, now validated, was used to explore any opportunity for increasing the ethoxylation capacity through reactor pressure rating in the NIS A reactor. Two aspects were addressed: the determination of the optimum ethoxylation rate under the current design specification and explorations of the design specification for a new reactor when, for example, the ethylene oxide injection rate was increased to three times the current maximum. The simulations found that the ethylene oxide injection rate could be raised by about 50% of the current capacity if the reactor pressure was operated closer to the current design pressure (4.45 bar). Nevertheless, keeping the operating pressure (3.62 bar) at about 0.8 bar below the design pressure allows for a good margin of safety for the potentially hazardous operation. If the ethylene oxide injection rate were increased to three times its current rate, the new normal operating pressure would need to be about 7 bar.

8.2 Recommendations

Two areas relating to the industrial operations are recommended as a future study to this research project for improvements on the asset productivity of the NIS A ethoxylation plant. Firstly, the determination of a least diameter size required for a dip-leg pipe which ensures minimal or, ultimately, zero boiling of ethylene oxide injection in the commercially operated NIS A reactors. Secondly, extension of CFD simulations of the flow in a stirred vessel equipped with an axial flow impeller, including Lightnin A315 impeller and pitched-blade turbine.

As mentioned above, the more the ethylene oxide injection remained liquid in the reaction mixture, the higher the ethoxylation rate and the shorter the ethoxylation time. The optimum situation is aimed at a 100% liquid ethylene oxide injection into the reaction mixture during the entire course of an operation. In the existing operations, only when the ethylene oxide injection rate has reached its current maximum, boiling is unlikely to occur. However, before the maximum injection rate is reached, the injection outflow from the dip-leg pipe is, possibly, partially boiling. To suppress the boiling, the ethylene oxide saturation pressure should always be kept below the system pressure; the heat transfer rate to the pipe flow must be reduced. From the study on the effect of pipe sizes on the heat transfer rate, it was found that the use of larger pipe of the same length reduced notably the heat transfer rate and resulted in a lower exit temperature of the flow. The study indicated that with the right selection of the pipe dimension, boiling could be effectively minimised. It is recommended that further calculations by the Nusselt empirical correlation, together with CFD simulations, be performed to determine the minimum pipe diameter required for ethylene oxide injection to remain liquid.

The NIS A reactor modelled in the present study for nonylphenol ethoxylation production batches was stirred by a set of Rushton impellers, although the manufacture of nonylphenol ethoxylates was never carried out in that NIS A unit. Since we have established that the ethoxylation behaviour in the current operations was insensitive to the agitator type, the reaction data between a dual-Lightnin A315 stirred reactor and a dual-Rushton one was interchangeable. Therefore, the Rushton stirred reactor was simulated based on a choice made from the convenience of its model geometry construction and the extensive availability of its literature flow data. It is recommended that the CFD simulations be extended to describe the reactor stirred by the dual-Lightnin A315 impeller and a larger reactor ($10m^3$) with pitched-blade turbine where experimental data for nonylphenol ethoxylates are recorded. Although the flow data available for Lightnin A315 impeller to date is still scarce in the open literature, validation of the simulation results could be made on power number N_P and impeller flow number N_{QP}. For the case with increased ethylene oxide injection rate due to increased reactor pressure rating, various feed locations with respect to the flow structure can be tested on the basis where ethylene oxide injection is most effectively dispersed into the reaction mixture. This is important as the accumulation of a large amount of unreacted

ethylene oxide in the system gives rise to potential hazards if the reaction gets out of control. It is also proposed to perform simulations with the use of a sparger ring for dispersion of ethylene oxide injection. Recommendations can be made based on the effectiveness of dispersal of ethylene oxide compared to that of a dip-leg pipe.

Further work could also be carried out with simulations using different turbulence models. Since the k-ε model used in this research project suffices only to resolve macro-mixing features, an appropriate turbulence model needs to be applied for systems with micro-mixing or meso-mixing features, a choice to be made dependent on the relative timescale between reaction and mixing.

Bibliography

Part I Kinetic modelling

Boyd, D. R. and Marle, E. R. (1914) The velocities of combination of sodium derivatives of phenols with olefine oxides. *J. Chem. Soc.* **105**, 2117-2139.

Boyd, D. R. and Thomas, D. F. (1919) The velocities of combination of sodium derivatives of phenols with olefine oxides. Part II. *J. Chem. Soc.* **115**, 1239-1243.

Carpentier, J. C. (1981) Mass transfer rates in gas-liquid absorbers and reactors. In *Advances in Chemical Engineering*, vol. **II**. New York, USA: Academic Press, pp 1-133.

Davidsohn, A. S. and Milwidsky, B. (1987) *Synthetic Detergents*. Great Britain: Longman Scientific and Technical.

Di Serio, M. (1998) Private communication.

Di Serio, M., Di Martino, S. and Santacesaria, E. (1994) Kinetics of fatty acids polyethoxylation. *Ind. Eng. Chem. Res.* **33**, 509-514.

Di Serio, M., Tesser, R., Felippone, F. and Santacesaria, E. (1995) Ethylene oxide solubility and ethoxylation kinetics in the synthesis of nonionic surfactants. *Ind. Eng. Chem. Res.* **34**, 4092-4098.

Di Serio, M., Vairo, G., Iengo, P., Felippone, F. and Santacesaria, E. (1996) Kinetics of ethoxylation and propoxylation of 1- and 2-Octanol catalysed by KOH. *Ind. Eng. Chem. Res.* **35**, 3848-3853.

Dimiccoli, A., Di Serio, M. and Santacesaria, E. (2000) Key factors in ethoxylation and propoxylation technology. In *Proceedings of 5th World Surfactants Congress*, 2000. **1**, 99-110. Firenze, Italy.

Ethylene Oxide User's Guide (1999) Old World Industries, The Dow Chemical Company, Shell Chemical Company, Sunoco, Inc. and Equistar Chemicals, LP.

Gee, G., Higginson, W. C., Levesley, P. and Taylor, K. J. (1959a) Polymerisation of epoxides. Part I. Some kinetic aspects of the addition of alcohols to epoxides catalysed by Sodium Alkoxides. *J. Chem. Soc.* 1338-1344.

Gee, G., Higginson, W. C. and Merrall, G. T. (1959b) Polymerisation of epoxides. Part II. The polymerisation of ethylene oxide by Sodium Alkoxides. *J. Chem. Soc.* 1345-1352.

Hall, C. A. and Agrawal, P. K. (1990) Separation of kinetics and mass-transfer in a batch alkoxylation reaction. *The Canadian Journal of Chemical Engineering* **68**, 104-112.

Ingold, C. K. (1953) *Structure and Mechanism in Organic Chemistry*. London: Cornell University Press.

Ishii, Y., Nishikawa, Y. and Kimura, K. (1962) *Kogyo Kagaku Zasshi* **65**, 1365-1367.

Ishii, Y. and Ozeki, N. (1960) *Kogyo Kagaku Zasshi* **63**, 1387-1390.

Karsa, D. R. (1987) *Industrial applications of surfactants. The proceedings of a symposium organised by the North West Region of the Industrial Division of the Royal Society of Chemisty*. London, England: The Royal of Chemistry, Burlington House.

Kirk-Othmer Encyclopaedia of Chemical Technology, 4th ed., vol. **2**, Howe-Grant, M. (ed.) New York, USA: John Wiley and Sons 1992.

Kirk-Othmer Encyclopaedia of Chemical Technology, 4th ed., vol. **9**, Howe-Grant, M. (ed.) New York, USA: John Wiley and Sons 1994.

Lowe, A. J. and Weibull, B. (1954) Discussion on the paper presented by Patat, F. Cremer, E. and Bobleter, O. J. *J. Polym. Sci.* **12**, 493-496.

Miller, S. A., Bann, B. and Thrower, R. D. (1950) The reaction between phenol and ethylene oxide. *J. Chem. Soc.* 3623-3628.

Myers, D. (1988) *Surfactant Science and Technology*. New York, USA: VCH Publishers, Inc.

Nace, V. M. (1996) *Nonionic Surfactants. Polyoxyalkylene Block Copolymers*. New York, USA: Marcel Dekker.

Ngian, K. F. (2002) Private communication.

Olson, J.A. (1977) Solubility of nitrogen, argon, methane, and ethane in ethylene oxide. *J. Chem. Eng. Data* **22**, 326-329.

Parker, R. E. and Isaacs, N. S. (1959) Mechanisms of epoxide reactions. *Chem. Rev.* **59**, 737-799.

Patat, F., Cremer, E. and Bobleter, O. (1952) Zur kinetik der polykondensation von athylenoxyd au phenol. *Monatsh. Chem.* **83**, 322

Patat, F., Cremer, E. and Bobleter, O. (1954) Zur frage der anionpolymerisation, II. Die addition von athylenoxyd an phenol. *J. Polym. Sci.* 489-492.

Patat, F. and Wojtech, B. (1960) Die kondesation von athylenoxyd au phenol. *Makromol. Chem.* **37**, 1

Patel, N. C. and Young, M. A. (1993) Measurement and prediction of liquid equilibria for a reactive system: application to ethylene oxide + nonylphenol. *Fluid Phase Equilibria* **82**, 71-78.

Porter, M. R. (1994) *Handbook of Surfactants*. London: Blackie Academic & Professional.

Prausnitz, J. M. (1980) *Computer calculations for multicomponent vapour-liquid and liquid-liquid equilibria*. New York, USA: Prentice Hall.

Sakai, S. and Ishii, Y. (1959) *Kogyo Kagaku Zasshi* **62**, 413-417.

Santacesaria, E., Di Serio, M., Garaffa, R. and Addino, G. (1992a) Kinetics and mechanisms of fatty alcohol polyethoxylation. 1. The reaction catalysed by potassium hydroxide. *Ind. Eng. Chem. Res.* **31**, 2413-2418.

Santacesaria, E., Di Serio, M., Garaffa, R. and Addino, G. (1992b) Kinetics and mechanisms of fatty alcohol polyethoxylation. 2. Narrow-range ethoxylation obtained with barium catalysts. *Ind. Eng. Chem. Res.* **31**, 2419-2421.

Santacesaria, E., Di Serio, M., Lisi, L. and Gelosa, D. (1990) Kinetics of nonylphenol polyethoxylation catalysed by potassium hydroxide. *Ind. Eng. Chem. Res.* **29**, 719-725.

Santacesaria, E., Di Serio, M. and Tesser, R. (1995) Role of ethylene oxide solubility in the ethoxylation processes. *Catalysis Today* **24**, 23-28.

Santacesaria, E., Iengo, P. and Di Serio, M. Catalytic and kinetic effect in ethoxylation processes. In *Annual Surfactant Review*

Satkowski, W. B. and Hsu, C. G. (1957) Polyoxyethylation of alcohol. *Ind. Eng. Chem.* **49**, 1875-1878.

Shell Chemicals (2000) *Alcohol-Based Surfactants: Thoughts on the European scene from a global perspective*. In CESIO 2000

Schick, M. J. (1967) *Nonionic Surfactants*. Surfactant Science Series, vol. **1**. New York, USA: Mercel Dekker, Inc.;

Schonfeldt, N. (1969) *Surface Active Ethylene Oxide Adducts*. London: Pergamon Press.

Schmitt T. M. (2001) *Analysis of Surfactants*. Surfactant Science Series, vol. **96**. New York, USA: Mercel Dekker, Inc.

Ullmann's Encyclopaedia of Industrial Chemistry, 5th ed., vol. **A.19**. Elvers, B., Hawkins, S. and Schulz, G. (eds.), Weinheim: Wiley-VCH Publishers, Inc. 1991.

Van Dierendonck, L. L.; Zahradnik, J. and Linek, V. (1998) Loop Venturi Reactor-A feasible alternative to stirred tank reactors? *Ind. Eng. Chem. Res.* **37**, 734-738.

Van Os, N. M. (1998) *Nonionic Surfactants*: *Organic Chemistry*. Surfactant Science Series, vol. **72**. New York, USA: Marcel Dekker, Inc.

Yang, K., Nield, G. L. and Washecheck, P. H. (1980), U.S. Patent 4,210,764 to Conoco, I., Barium oxide/cresylic acid catalysed ethoxylation.

Part II CFD simulations

Abbott, M. B. and Basco, D. R. (1989) *Computation Fluid Dynamics: an Introduction to Engineers*. 425. Great Britain: Longman Scientific and Technical.

Abujelala, M. T. and Lilley, D. G. (1984) Limitations and empirical extensions of the *k-*ε model as applied to turbulent confined swirling flow. *Chem. Eng. Commun.* **31**, 223-236.

AEA Technology (1999) *CFX-4.4:Solver.* Oxfordshire, UK: AEA Technology plc.

Armenante, P. M., Nagamine, E. U. and Susanto, J. (1998) Effect of low off-bottom impeller clearance on the minimum agitation speed for complete suspension of solids in stirred tanks. *Chem. Eng. Sci.* **53**, 1757-1775.

Aubin, J., Mavros, P., Fletcher, D. F., Bertrand, J. and Xuereb, C. (2001) Effect of axial agitator configuration (up-pumping, down-pumping, reverse rotation) on flow patterns generated in stirred vessels. *Chem. Eng. Res. Des.* **79**, 845-856.

Bakker, A., Haidari, A. H., Oshinowo, L. M. (2001) Realise greater benefits from CFD. *Chem. Eng. Progr.* **97**, 45-53.

Bakker, A. and Van den Akker, A. (1994) Single-phase flow in stirred reactors. *Chem. Eng. Res. Des.* **72**, 583-593.

Bartels, C., Breuer, M., Wechsler, K. and Durst, F. (2002) Computational fluid dynamics applications on parallel-vector computers: computations of stirred vessel flows. *Computers & Fluids* **31**, 69-97.

Bird, R. B., Stewart, W. E. and Lightfoot, E. N. (1960) *Transport Phenomena*. New York, USA: John Wiley and Sons.

Brucato, A., Ciofalo, M., Grisafi, F. and Micale, G. (1994) Complete numerical simulation of flow fields in baffled stirred vessels : the inner-out approach. *IChemE Symposium Series* 155-162.

Brucato, A., Ciofalo, M., Grisafi, F. and Micale, G. (1998) Numerical prediction of flow fields in baffled stirred vessels: a comparison of alternative modelling approaches. *Chem. Eng. Sci.* **53**, 3653-3684.

Brucato, A., Ciofalo, M., Grisafi, F. and Tocco, R. (2000) On the simulation of stirred tank reactors via computational fluid dynamics. *Chem. Eng. Sci.* **55**, 291-302.

Chiu, Y. N., Naser, J., Ngian, K. F. and Pratt, K. C. (2002) Optimisation of an ethoxylation stirred reactor. In *Proceedings of the 9th APCChE Congress and CHEMECA 2002*, Christchurch, New Zealand.

Ciofalo, M., Brucato, A., Grisafi, F. and Torraca, N. (1996) Turbulent flow in closed and free-surface unbaffled tanks stirred by radial impellers. *Chem. Eng. Sci.* **51**, 3557-3573.

Daskopoulos, P. and Harris, C. K. (1996) Three-dimensional CFD simulations of turbulent flow in baffled stirred tanks: an assessment of the current position. *IChemE Symposium Series* **140**, 1-13.

Deen, N. (2001) An experimental and computational study of fluid dynamics in gas-liquid chemical reactors. PhD thesis, Aalborg University.

Derksen, J. J. and Van den Akker, A. (1999) Large-eddy simulations on the flow driven by a Rushton turbine. *AIChE J* **45**, 209-219.

Dyster, K. N., Koutsakos, E., Jaworski, Z. and Nienow, A. W. (1993) LDA study of the radial discharge velocities generated by a Rushton turbine: Newtonian fluids, $Re \geq 5$. *Chem. Eng. Res. Des.* **71**, 11-23.

El-Wazzan, Y. J. E. (1997) The prediction of swirling recalculating flow and the fluid flow and mixing in a stirred tank. PhD thesis, University of London.

Fokema, M. D., Kresta, S. M. and Wood, P. E. (1994) Importance of using the correct impeller boundary conditions for CFD simulations of stirred tanks. *Can. J. Chem. Eng.* **72**, 177-183.

Gosman, A. D., Lekakou, C., Politis, S., Issa, R. I. and Looney, M. K. (1992) Multidimensional modeling of turbulent two-phase flows in stirred vessels. *AIChE J* **38**, 1946-1956.

Harnby, N., Edwards, M. F. and Nienow, A. W. (1985) *Mixing in the Process Industries*. London: Butterworth & Co (Publishers) Ltd.

Harris, C. K., Roekaerts, D., Rosendal, F. J. J., Buitendijk, F. G. J., Daskopoulos, P., Vreenegoor, A. J. N. and Wang, H. (1996) Computational fluid dynamics for chemical reactor engineering. *Chem. Eng. Sci.* **51**, 1569-1594.

Hockey, R. M. and Nouri, J. M. (1996) Turbulent flow in a baffled vessel stirred by a 60° pitched blade impeller. *Chem. Eng. Sci.* **51**, 4405-4421.

Holman, J. P. (1989) Heat Transfer, SI Metric Edition. 273-287. New York, USA: McGraw-Hill Book Company.

Hudcova, V., Machon, V. and Nienow, A. W. (1989) Gas-liquid dispersion with dual Rushton turbine impellers. *Biotechnology and Bioengineering* **34**, 617-628.

Ibrahim, S. and Nienow, A. W. (1995) Power curves and flow pattern for a range of impeller in Newtonian fluid: $40<Re<5x10$. *Chem. Eng. Res. Des.* **73**, 485-491.

Jaworski, Z., Bujalski, W, Otomo, N. and Nienow, A. W. (2000) CFD study of homogenization with dual Rushton turbines—comparison with experimental results Part I: Initial studies. *Chem. Eng. Res. Des.* **78**, 327-333.

Jaworski, Z., Dyster, K. N., Moore, I. P. T., Nienow, A. W. and Wyszynski, M. L. (1997) The use of angle resolved LDA data to compare two differential turbulence models applied to sliding mesh CFD flow simulations in a stirred tank. *Recents Progres en genie des Procedes* **11**, 187-194.

Jaworski, Z., Nienow, A. W. and Dyster, K. N. (1996) An LDA study of the turbulent flow field in a baffled vessel agitated by an axial down-pumping hydrofoil impeller. *Can. J. Chem. Eng.* **74**, 3-15.

Jaworski, Z., Nienow, A. W., Koutsakos, E., Dyster, K. N. and Bujalski, W. (1991) An LDA study of turbulent flow in a baffled vessel agitated by a pitched blade turbine. *Chem. Eng. Res. Des.* **69**, 313-320.

Jenne, M. and Reuss, M. (1999) A critical assessment on the use of k-ε turbulence models for simulation of the turbulent liquid flow induced by a Rushton-turbine in baffled stirred-tank reactors. *Chem. Eng. Sci.* **54**, 3921-3941.

Khuu, S. (2002) Advanced operational analysis of an industrial nonionic surfactant reactor. PhD thesis, Sydney University.

Kresta, S. M. and Wood, P. E. (1991) Prediction of three-dimensional turbulent flow in stirred tanks. *AIChE J* **37**, 448-460.

Kresta, S. M. and Wood, P. E. (1993) The mean flow field produced by a 45° pitched blade turbine: changes in the circulation pattern due to off bottom clearance. *Can. J. Chem. Eng.* **71**, 42-53.

Launder, B. E. and Spalding, D. B. (1974) The numerical computation of turbulent flows. *Computer Methods in Applied Mechanics and Engineering* **3**, 269-289.

Lee, K. C., Ng, K., Yianneskis, M., Lange, F. and Sanatian, R. (1996) Sliding mesh predictions of the flows around Rushton Impellers. *IChemE Symposium Series* 47-58.

Lee, K. C. and Yianneskis, M. (1998) Turbulence properties of the impeller stream of a Rushton turbine. *AIChE J* **44**, 13-24.

Luo, J. Y., Gosman, A. D., Issa, R. I., Middleton, J. C. and Fitzgerald, M. K. (1993) Full flow field computation of mixing in baffled stirred vessels . *Chem. Eng. Res. Des.* **71**, 342-344.

Luo, J. Y., Issa, R. I. and Gosman, A. D. (1994) Prediction of impeller induced flows in mixing vessels using multiple frames of reference. *IChemE Symposium Series* 549-556.

Mahmoudi, S. M. and Yianneskis, M. (1992) The variation of flow pattern and mixing time with impeller spacing in stirred vessels with two Rushton impellers. *Fluid Mechanics of Mixing: Modelling, Operations and Experimental Techniques* 11-18.

Mahouast, M., David, R. and Cognet, G. (1987) Caracterisation des champs hydrodynamique et de concentration dans une cuve agitee standard alimentee en continu. *Entropie* **133**, 7-17.

Mao, D. M., Feng, L. F., Wang, K. and Li, Y. L. (1998) The mean flow field generated by a pitched blade turbine: changes in the circulation pattern due to impeller geometry. *Can. J. Chem. Eng.* **75**, 307-316.

Mavros, P. (2001) Flow visualisation in stirred vessels. A review of experimental techniques. *Chem. Eng. Res. Des.* **79**, 113-127.

Mavros, P. and Baudou, C. (1997) Quantification of the performance of agitators in stirred vessels: Definition and use of an agitation index. *Chem. Eng. Res. Des.* **75**, 737-745.

Mavros, P., Xuereb, C. and Bertrand, J. (1996) Determination of 3-D flow fields in agitated vessels by laser-Doppler velocimetry: Effect of impeller type and liquid viscosity on liquid flow patterns . *Chem. Eng. Res. Des.* **74**, 658-668.

Mavros, P., Xuereb, C. and Bertrand, J. (1998) Determination of 3-D flow fields in agitated vessels by Laser-Doppler velocimetry: Use and interpretation of RMS velocities. *Chem. Eng. Res. Des.* **76**, 223-233.

Micale, G., Brucato, A., Grisafi, F. and Ciofalo, M. (1999) Prediction of flow fields in a dual-impeller stirred vessel. *AIChE J* **45**, 445-464.

Middleton, J. C., Perice, F. and Lynch, P. M. (1986) Computations of flow fields and complex reaction yield in turbulent stirred reactors and comparison with experimental data. *Chem. Eng. Res. Des.* **64**, 18-21.

Montante, G., Lee, K. C., Brucato, A. and Yianneskis, M. (1999) An experimental study of double-to-single-loop transition in stirred vessels. *Can. J. Chem. Eng.* **77**, 649-659.

Ng. K., Fentiman, J., Lee, K. C. and Yianneskis, M. (1998) Assessment of sliding mesh CFD predictions and LDA measurements of the flow in a tank stirred by a Rushton impeller. *Chem. Eng. Res. Des.* **76**, 737-747.

Nouri, J. M. and Whitelaw, J. H. (1990) Flow characteristics of stirred reactors with Newtonian and non-Newtonian fluids. *AIChE J* **36**, 627-629.

Oldshue, J. Y. (1983) Fluid mixing technology and practice. *Chem. Eng.* **90**, 82-108.

Oldshue, J. Y. (1989) Fluid mixing in 1989. *Chem. Eng. Progr.* **85** , 33-42.

Oldshue, J. Y. and Herbst, N. R. (1990) A Guide to Fluid Mixing. N. Y. Mixing Equipment Company.

Patankar, S. V. (1980) *Numerical Heat Transfer and Fluid Flow*. Washington, DC: Hemisphere Publishing Corp.

Patankar, S. V. and Spalding, D. B. (1972) A calculation procedure for heat, mass and momentum transfer in three-dimensional parabolic flows. *Int. J Heat Mass Transfer* **15**, 1787-1806

Perry, R. H. and Green, D. (1984) Perry's Chemical Engineers' Handbook, 6th ed. New York, USA: McGraw-Hill Inc.

Pipino, M. and Fox, R. O. (1994) Reactive mixing in a tubular jet reactor: A comparison of PDF simulations with experimental data. *Chem. Eng. Sci.* **49**, 5229-5241.

Placek, J., Tavlarides, L. L. and Smith, G. W. (1986) Turbulent flow in stirred tank, Part II: A two-scale model of turbulence. *AIChE J* **32**, 1771-1786.

Ranade, V. V. (1997) An efficient computational model for simulating flow in stirred vessels: a case of Rushton turbine. *Chem. Eng. Sci.* **52**, 4473-4484.

Ranade, V. V. and Bourne, J. B. (1991) Reactive mixing in agitated tanks. *Chem. Eng. Commun.* **99**, 33-53.

Ranade, V. V. and Joshi, J. B. (1989) Flow generated by a pitched blade turbines I: Measurements using laser Doppler anemometer. *Chem. Eng. Commun.* **81**, 197-224.

Ranade, V. V. and Joshi, J. B. (1989) Flow generated by a pitched blade turbines II: Simulation using k-ε mode. *Chem. Eng. Commun.* **81**, 225-248.

Ranade, V. V. and Joshi, J. B. (1990) Flow generated by a disc turbine: Part II Mathematical modelling and comparison with experimental data. *Chem. Eng. Res. Des.* **68**, 34-50.

Ranade, V.V. and Van den Akker, A. (1994) A computational snapshot of gas-liquid flow in baffled stirred reactors. *Chem. Eng. Sci.* **49**, 5175-5192.

Rhie, C. M. and Chow, W. L. (1983) A numerical study of the turbulent flow past an aerofoil with trailing edge separation. *AIAA J* **21**, 1525-1532.

Rutherford, K., Lee, K. C., Mahmoudi, S. M. and Yianneskis, M. (1996) Hydrodynamic characteristics of dual Rushton impeller stirred vessel. *AIChE J* **42**, 332-346.

Rutherford, K., Mahmoudi, S. M., Lee, K. C., Yianneskis, M. (1996) The influence of Rushton impeller blade and disk thickness on the mixing characteristics of stirred vessels. *Chem. Eng. Res. Des.* **74**, 369-378.

Schafer, M., Yianneskis, M., Wachter, P. and Durst, F. (1998) Trailing vortices around a 45° pitched-blade impeller. *AIChE J* **44**, 1233-1246.

Stoots, C. M. and Calabrese, R. V. (1995) Mean velocity field relative to a Rushton turbine blade. *AIChE J* **41**, 1-11.

Tabor, G., Gosman, A. D. and Issa, R. I. (1996) Numerical simulation of the flow in a mixing vessel stirred by a Rushton turbine. *IChemE Symposium Series* **140**, 25-34.

Tatterson, G. B. (1991) *Fluid Mixing and Gas Dispersion in Agitated Tanks*. New York, USA: McGraw-Hill Inc. 208-222.

Tatterson, G. B. (1994) *Scaleup and Design of Industrial Mixing Processes.* New York, USA: McGraw-Hill Inc.

Van Doormal, J. P. and Raithby, G. D. (1984) Enhancement of the SIMPLE method for predicting incompressible fluid flows. *Numer. Heat Transfer* **7**, 147-163.

Van't Riet, K. and Smith, J. M. (1973) The behaviour of gas-liquid mixtures near Rushton turbines blades. *Chem. Eng. Sci.* **28**, 1031-1037.

Versteeg, H. K. and Malalasekera, W. (1995) *An Introduction to Computational Fluid Dynamics: The Finite Volume Method.* Harlow, England: Pearson Education Limited.

Wechsler, K., Breuer, M. and Durst, F. (1999) Steady and unsteady computations of turbulent flows induced by a 4/45° pitched blade impeller. *J. Fluids Eng.* **121**, 318-329.

Wu, H. and Patterson, G. K. (1989) Laser-Doppler measurements of turbulent-flow parameters in a stirred mixer. *Chem. Eng. Sci.* **44**, 2207-2221.

Yianneskis, M., Popiolek, Z. and Whitelaw, J. H. (1987) An experimental study of the steady and unsteady flow characteristics of stirred reactors. *J. Fluid Mech.* **175**, 537-555.

Nomenclature

Symbols

Part I Kinetic modelling

A	Pre-exponential factor ($cm^3mol^{-1}s^{-1}$)
E	Activation energy ($calmol^{-1}$; $Jmol^{-1}$)
R	Universal gas constant ($calmol^{-1}K^{-1}$; $Jmol^{-1}K^{-1}$)
T	Temperature (K)
B^0	Initial concentration of the catalyst ($molcm^{-3}$)
$[EO]_{if}$	Ethylene oxide interface concentration ($molcm^{-3}$)
$[EO]_b$	Ethylene oxide bulk concentration ($molcm^{-3}$)
H	Henry's Law constant, reciprocal of the partition coefficient K
J	Mass transfer rate ($molcm^{-3}s^{-1}$)
K_i	Partition coefficient for ethylene oxide at T_i (atm)
Ke	Equilibrium constant for proton-exchange reaction (-)
Ke_{NP}	Equilibrium constant for the proton exchange between the initiator and subsequent polyoxyethylene adducts (-)
k_i	Second-order rate constant for the initiation reaction ($cm^3mol^{-1}s^{-1}$)
k_La	Liquid-side of volumetric mass transfer coefficient (s^{-1})
k_p	Second-order rate constant for the propagation reactions ($cm^3mol^{-1}s^{-1}$)
m_0	Total initiator concentration ($molcm^{-3}$)
m_i	Total oligomer concentration of i^{th} ethylene oxide adducts ($molcm^{-3}$)
MW	Molecular weight (g/mol)
N_{EO}	Mean number of ethylene oxide adducts per mole of initiator (-)
n	Numbers of polyoxyethylene products (-)
n_{N_2}	Number of moles of nitrogen (mol)
P_{EO}	Vapour pressure of ethylene oxide (kPa)
P°_{EO}	Saturation vapour pressure of ethylene oxide (kPa)
P_{N_2}	Partial pressure of nitrogen (kPa)
P_T	Total reactor pressure (kPa)
R^0	Total concentration of the initiator ($molm^{-3}$)
$S_{N_2,EO}$	Solubility of nitrogen in ethylene oxide (kg N_2/kg EO)
t_{max}	Length of reaction time (s)

Δt	Time step (s)
V_G	Volume of the gas in the reactor (m^3)
V_L	Volume of the liquid in the reactor (m^3)
W_{SUM_CYL}	Cumulative weight withdrawn from the ethylene oxide cylinder (kg)
W_{SUM_EO}	Cumulative weight of ethylene oxide (kg)
$W_{SUM\_N_2}$	Cumulative weight of nitrogen dissolved in ethylene oxide feed (kg)
X_{EO}	Molar fraction of ethylene oxide (-)
x_i	Molar fraction *i* (-)

Part II Process optimisation and CFD simulations

A	Total surface area for heat transfer (m^2)
A_x	Pipe cross-sectional area (m^2)
B	Body force
C	Impeller clearance, measured from the tank bottom to the horizontal centreline of the impeller blades (m)
C_p	Specific heat at constant pressure ($Jkg^{-1}°C^{-1}$)
$C_{\varepsilon 1}$	Model constant k-ε model (-)
$C_{\varepsilon 2}$	Model constant k-ε model (-)
C_μ	Model constant k-ε model (-)
D	Impeller diameter (m)
$d_{i.d.}$	Inner pipe diameter (m)
G	Generation of turbulence kinetic energy ($kgm^{-1}s^{-3}$)
H	Total enthalpy (Jkg^{-1})
H'	Impeller velocity head (m)
H_{Rj}	Heat of reaction ($Jmol^{-1}$)
h	Heat transfer coefficient ($Wm^{-2}°C^{-1}$)
I	Unity tensor (-)
k	Turbulence kinetic energy (m^2s^{-2})
L	Length of pipe (m)
$\dot{m}$	Mass rate of pipe flow (kgs^{-1})
N	Impeller rotational speed in revolutions per second (rps)
N_R	Number of chemical reactions (-)
n_{ij}	Overall stoichiometric coefficient for species *i* in reaction *j* (-)
P	Power input (W)
P^*	Saturation vapour pressure of liquid (kPa)

p	Pressure (Pa)
Q_C	Total circulation rate (m^3s^{-1})
Q_p	Primary pumping capacity (m^3s^{-1})
Q_R	Energy source term due to chemical reactions (J)
q	Total heat transfer (W)
R	Chemical reaction rate ($mols^{-1}$)
r	Position in the radial direction
S	General source or sink term per unit volume per time
S_i	Source term for species i
SU	Constant source term
SP	Linear gradient source term
T	Tank diameter (m); temperature (K)
T_b	Fluid bulk temperature (°C)
T_r	Torque (kgm^2s^2)
T_w	Temperature of the inner pipe surface (°C)
t	Time (s)
t_b	Blade thickness (m)
t_d	Disc thickness (m)
t_w	Pipe wall thickness (m)
U	Mean velocity vector (U_x, U_y, U_z) (ms^{-1})
$\hat{U}$	Volume-weighted average velocity (ms^{-1})
U_{tip}	Impeller tip velocity (ms^{-1})
u_m	Mean velocity of pipe flow (ms^{-1})
u'_x, u'_y, u'_z	Fluctuating velocity components (ms^{-1})
V_{ij}	Liquid volume surrounding measuring point (m^3)
W_i	Molecular weight of species i ($kgkmol^{-1}$)
w	Impeller blade width (m)
X_i	Molar fraction of species i (-)
Y_i	Mass fraction of species i (-)
Z	Static liquid depth (m)
z	Position in the axial direction

Greek symbols

ε	Energy dissipation rate (m^2s^{-3})
Γ	General diffusion coefficient
γ	Concentration ratio between the of an un-dissociated polyethoxylate and its dissociated ion (-)
γ_1, γ_2	Wilson method activity coefficients
Λ_{12}, Λ_{21}	Wilson method interaction parameters
λ	Thermal conductivity ($Wm^{-1}°C^{-1}$)
μ	Molecular viscosity ($kgm^{-1}s^{-1}$)
μ_{eff}	Effective viscosity ($kgm^{-1}s^{-1}$)
μ_T	Turbulent viscosity ($kgm^{-1}s^{-1}$)
π	Pi
ρ	Density (kgm^{-3})
θ	Position in the tangential direction
σ	Turbulent Prandtl number
σ_k	Model constant k-ε model (-)
σ_ε	Model constant k-ε model (-)
τ	Stress tensor ($kgm^{-1}s^{-2}$)
ω	Shaft rotational speed (s^{-1})

Dimensionless numbers

η_C	Circulation efficiency number, $\eta_C = (N_C/N_P)(D/T)^4$
η_p	Pumping effectiveness, $\eta_P = N_{QP}/N_P$
I_g	Agitation index, $I_g = 100\hat{U}/U_{tip}[\%]$
N_C	Circulation flow rate number, $N_C = Q_C/ND^3$
N_P	Power number, $N_p = P/\rho N^3 D^5$
N_{QP}	Impeller flow number, $N_{QP} = Q_P/ND^3$
Nu_d	Nusselt number, $Nu_d = hd_{i.d.}/\lambda$
Pr	Prandtl number, $Pr = C_p\mu/\lambda$
Re	Reynolds number, $Re = \rho ND^2/\mu$

Abbreviations

CFD	Computational fluid dynamics
CV	Control volume
EO	Ethylene oxide
FID	Flame ionisation detector
GC	Gas chromatograph
HCA	Huntsman Corporation Australia
HPCW	High pressure cooling water
HPLC	High-performance liquid chromatography
IBC	Imposed boundary conditions
IO	Inner-outer method
LDV	Laser Doppler velocimetry
LES	Large Eddy Simulation
MFR	Multiple frames of reference method
NIS	Nonionic surfactants
NRE	Narrow-range ethoxylate
PBT	Pitched-blade turbine
QUICK	Quadratic upstream interpolation for convective kinetics
rms	Root mean square
RSM	Reynolds stress model
RXH	Initiator
SG	Sliding grid method
SIMPLE	Semi-implicit method for pressure-linked equations
SIMPLEC	SIMPLE-Consistent
tph	tons per hour

List of Publications

Chiu, Y. N., Easton, A., Ngian, K. F., Pratt, K. C. (2000) Modelling of a stirred alkoxylation reactor (poster). In *IChemE Research 2000*, Bath, UK.

Chiu, Y. N., Easton, A., Ngian, K. F., Pratt, K. C. (2000) Kinetic modelling of a base-catalysed alkoxylation reactor (poster). In *Proceedings of the 2nd Asia Pacific Congress on Catalysis*, Sydney, Australia.

Chiu, Y. N., Easton, A., Naser, J., Ngian, K. F., Pratt, K. C. (2000) Modelling and simulation of a mechanically agitated catalysed ethoxylation reactor. In *Proceedings of the 12th International Congress on Catalysis*, Granada, Spain.

Chiu, Y. N., Easton, A., Ngian, K. F., Pratt, K. C. (2000) Kinetics of a catalysed semi-batch ethoxylation of nonylphenol. In *Proceedings of the 4th Biennial Engineering Mathematics and Applications Conference*, Melbourne, Australia.

Chiu, Y. N., Naser, J., Ngian, K. F. and Pratt, K. C. (2002) Optimisation of an ethoxylation stirred reactor. In *Proceedings of the 9th APCChE Congress and CHEMECA 2002*, Christchurch, New Zealand.

Appendix A

The Polynomial Equation of γ for Alkylphenol Ethoxylation

In this appendix, the derivations of the polynomial expression for solving the quantity γ and the simplified expression for the consumption of ethylene oxide are presented.

A.1 Expression and solution for γ quadratic

The polynomial expression to be derived was given as Equation 2. 33 on page 35 in Chapter 2,

$$\gamma^2 - \gamma\left[Ke_{NP}\left(\frac{R^0}{B^0}-1\right) - \frac{\sum m_i}{B^0}\left(Ke_{NP}-1\right)-1\right] - Ke_{NP}\left(\frac{R^0}{B^0}-1\right) = 0\,.$$

Previously, the quantity γ was defined as the following concentration ratios (Equation 2. 28 on page 35):

$$\gamma = \gamma_i = \frac{[RX(EO)_i H]}{[RX(EO)_i^-]} = Ke_{NP}\frac{[RXH]}{[RX^-]} \qquad \textbf{A. 1}$$

with i=1 to n (Santacesaria *et al*., 1990). Since the total concentration of alkylphenol at any time was defined as

$$m_0 = [RXH]+[RX^-], \qquad \textbf{A. 2}$$

and the total concentration of the i^{th} polyoxyethylene alkylphenol compound was defined as

$$m_i = [RX(EO)_iH] + [RX(EO)_i^-].$$

A. 3

The following expressions for the above dissociated ions $[RX^-]$ and $[RX(EO)_i^-]$ can be derived in terms of the total concentration of the respective hydrophobes:

$$[RX^-] = \left(\frac{Ke_{NP}}{Ke_{NP} + \gamma}\right) m_0 ,$$

A. 4

and

$$[RX(EO)_i^-] = \frac{m_i}{1+\gamma} .$$

A. 5

The summation of the total concentrations of the alkylphenol and the overall polyoxyethylene alkylphenol compounds was equivalent to the initial concentration of the alkylphenol substrate. By denoting R^0 as the initial concentration of the alkylphenol, we obtain

$$R^0 = m_0 + \sum_{i=1} m_i .$$

A. 6

Assuming a complete reaction between the catalyst and the alkylphenol, an expression for the initial concentration of the catalyst, denoted as B^0, can be derived based on electron neutrality as:

$$B^0 = [RX^-] + \sum_{i=1} [RXEO_i^-]$$

A. 7

Substitution of the expressions for $[RX^-]$ and $[RX(EO)_i^-]$ (Equations A. 4 and A. 5) yields

$$B^0 = \left(\frac{Ke_{NP}}{Ke_{NP} + \gamma}\right) m_0 + \frac{\sum m_i}{1+\gamma} .$$

A. 8

Using the relation between R^0 and m_0 in Equation A. 6, the new expression of B^0 can be further manipulated to

$$B^0 = \left(\frac{Ke_{NP}}{Ke_{NP} + \gamma}\right)\left(R^0 - \sum m_i\right) + \frac{\sum m_i}{1+\gamma} .$$

A. 9

Multiplying both sides of Equation A. 9 by (Ke_{NP} + γ) and (1+ γ), we obtain

$$[(Ke_{NP}+\gamma)(1+\gamma)]B^0 = Ke_{NP}(R^0 - \sum m_i)(1+\gamma) + (Ke_{NP}+\gamma)\sum m_i \ .$$

A. 10

Expanding and rearranging of Equation A. 10, a quadratic in γ is obtained

$$B^0\gamma^2 - \gamma(Ke_{NP}\left(R^0 - B^0\right) + \sum m_i\left(1 - Ke_{NP}\right) - B^0\ ) - Ke_{NP}\left(R^0 - B^0\right) = 0$$

A. 11

Finally, division by B^0 gives

$$\gamma^2 - \gamma\left[Ke_{NP}\left(\frac{R^0}{B^0} - 1\right) - \frac{\sum m_i}{B^0}\left(Ke_{NP} - 1\right) - 1\right] - Ke_{NP}\left(\frac{R^0}{B^0} - 1\right) = 0\ ,$$

which is Equation 2. 33. This quadratic expression can be easily solved for γ at each step in the integration of the rate expressions in Equations 2. 29 to 2. 31.

During the initiation stage when $Ke \neq 1$, γ changes with the reaction contents until RXH is present in the reaction mixture. As the propagation stage progresses along, $\sum m_i = R^0$ and consequently, γ becomes constant with a value of $(\frac{R^0}{B^0} - 1)$ (Santacesaria *et al*., 1990).

A.2 Simplification of ethylene oxide consumption

On the basis of the assumption that the concentration of the initiator is negligible into the propagation stage, Equation 2. 25 is simplified to

$$\frac{d[\mathrm{EO}]_b}{dt} = [\mathrm{EO}]_b\,(k_p \sum_{i=1} [\mathrm{RX(EO)}_i^-])$$

A. 12

By substituting Equation A.5 for the expression of [$RX(EO)_i^-$] and provided that $\sum m_i = R^0$ and $\gamma = \frac{R^0}{B^0} - 1$, Equation A. 12 is transformed to

$$\frac{d[\mathrm{EO}]_b}{dt} = k_p \cdot B^0 \cdot [\mathrm{EO}]_b \ .$$

A. 13

Appendix B

Ethoxylation Experimental Overview and Measurements

This appendix presents the details of the experimental overview and the measurements of the ethoxylation runs discussed in Chapter 4.

Appendix B.1 presents the operating conditions for all runs, including type of the initiator used, setting of the agitation speed, reaction temperature and gauge pressure readings, catalyst concentrations, amount of raw materials charged, amount of raw material withdrawn from samples and the final weight of raw materials for ethoxylation.

Appendix B.2 presents the measurements taken from the first ethoxylation run with the operating conditions taken from those of Santacesaria *et al*. (1990).

Appendices B.3 and B.4 present the measurements from the investigation of catalyst concentration and agitation speeds on the ethoxylation rates respectively.

Appendices B.5 and B.6 present the measurements from the ethoxylation kinetic study with the run numbers starting with kin. in Appendix B.1.

B.1 Experimental overview

Experiment No.	Initiator	Agitator speed [RPM]	Temp. [°C]	Press. (gauge) [kPa]	KOH conc. wt %	Raw materials charging [g] Initiator	KOH	Raw materials loss [g] Samples	Catchpot	Water content [% H_2O]
cat.1	Nonylphenol	1500	130	150	0.5	513.2	2.57			
cat.2	Nonylphenol	1500	130	150	0.75	500.0	3.80			
cat.3	Nonylphenol	1500	130	150	0.825	513.5	4.24			
cat.4	Nonylphenol	1500	130	150	0.875	540.0	4.70			
cat.5	Nonylphenol	1500	130	150	0.918	512.0	4.70			
cat.6	Nonylphenol	1500	130	150	0.983	508.6	5.00			
stir.1	Neodol 91	970	100	150	1.0	769.0	7.70	117.2	65.0	0.052
stir.2	Neodol 91	1270	100	150	1.0	858.6	8.55	49.0	45.0	0.027
stir.3	Neodol 91	1700	100	150	1.0	937.9	9.21	43.9	114.4	0.015
kin.1a	Nonylphenol	1700	88	150	1.0	860.0	8.70	133.5	26.0	0.042
kin.1b	Nonylphenol	1700	88	150	1.0	834.0	8.34	144.0	27.0	0.04
kin.2a	Nonylphenol	1700	99.5	150	1.0	1045.8	10.50	210.0	25.0	0.031
kin.2b	Nonylphenol	1700	99.5	150	1.0	999.2	9.98	258.9	26.0	0.03
kin.3a	Nonylphenol	1700	115	200	1.0	874.6	8.74	115.3	30.0	0.067
kin.3b	Nonylphenol	1700	115	150	1.0	830.8	8.30	120.5	26.0	0.05
kin.4a	Nonylphenol	1700	125	150	1.0	864.3	8.63	177.1	40.0	0.035
kin.4b	Nonylphenol	1700	125	150	1.0	761.8	7.60	99.6	25.0	0.04
kin.5a	Nonylphenol	1700	130	150	1.0	803.5	8.03	102.2	25.0	0.05
kin.5b	Nonylphenol	1700	130	150	1.0	380.6	3.81	65.3	15.0	0.05

B.2 Repeat of the run by Santacesaria *et al*. (1990)

	Moles of nonylphenol	Moles of KOH
Santacesaria *et al*. (1990)	0.785	0.0147
Repeated run in this study	1.71	0.032

Time [minute]	P_T(gauge) [kPa]	Temp. [^oC]	Weigh Scale [g]
0	-75	73	0
1	100	71	64.2
2	200	68	129.1
3	300	69	244
7	300	74	-
10	300	74	-
19	300	75	-
21	300	74	-
64	300	74	-
75	297	74	-
126	295	74	-
166	290	74	-
198	285	74	-
219	280	74	-
241	275	74	-
261	270	73.5	-
286	265	73.5	-

B.3 Ethoxylation runs with varying catalyst concentrations

Experiment No. cat.1

Time [minute]	P_T(gauge) [kPa]	Temp. [°C]	Weigh Scale [g]
0	vacuum	126	0
2	60	132	4
4	110	130	11.5
6	160	130	18
10	170	130	24.3
16	150	130	30
21	150	130	36
28	150	131	45

Experiment No. cat.2

Time [minute]	P_T(gauge) [kPa]	Temp. [°C]	Weigh Scale [g]
0	vacuum	127	0
2	50	129	20
3	100	130	30.9
4	150	131	45.2
6	150	130	50.8
8	150	132	58.3
9	150	132	65.6
11	150	130	72.9
12	150	131	78.8
14	150	131	83.7
15	150	130	88.6
17	160	130	95.5
19	160	130	102.3
21	150	130	109

Experiment No. cat.3

Time [minute]	P_T(gauge) [kPa]	Temp. [°C]	Weigh Scale [g]
0	vacuum	128	0
1	50	130	25
2	100	132	35.3
3	160	128	49.6
5	150	131	53.7
6	150	130	57.9
7	150	130	62.5
8	160	130	67
9	150	132	70.4
10	150	130	75.1
11	150	130	77.8
12	150	130	81.9
13	170	130	87.9
15	175	130	94.4
17	160	131	95.1
18	150	131	101.9
19	150	130	106
21	150	130	109
22	150	130	113
24	150	130	118
25	150	130	122.1
26	150	131	126.4
27	150	132	131.6
28	150	132	136.5
29	150	130	142
30	150	130	147.6
31	150	132	153.4

Experiment No. cat.4

Time [minute]	P_T(gauge) [kPa]	Temp. [°C]	Weigh Scale [g]
0	vacuum	127	0
1	50	128	20.8
2	100	129	29.8
3	150	131	39.1
3	150	127	45
4	150	130	48.2
5	150	132	51.7
6	150	132	56.1
7	150	132	60.7
8	220	130	66
8	150	129	70.3
9	150	129	74.9
10	160	130	78.4
11	160	130	83.3
12	150	130	86.6
13	150	130	90.8
14	160	130	95.9
15	150	130	99.9
16	150	129	103.8
17	150	131	107.5
18	150	131	111.8
19	150	129	116.4
20	160	131	121.4
21	150	131	125
23	150	130	130
24	150	130	134.6
24	150	132	137.8
25	150	130	142.9
26	150	130	148
27	150	132	154.4
28	150	130	160.4
29	150	131	164.9
30	150	131	170.3
30	150	132	176
31	150	130	182
32	150	130	186.8
33	150	130	194.8

Experiment No. cat.5

Time [minute]	P_T(gauge) [kPa]	Temp. [°C]	Weigh Scale [g]
0	vacuum	129	0
2	50	130	23.4
3	100	131	30.4
4	150	132	39.2
5	150	132	43.2
6	150	130	47.3
7	150	130	50.9
8	150	132	54.8
9	150	131	58
10	150	132	61.1
11	150	131	64.8
12	150	130	69.6
13	150	130	74.9
14	150	131	77.9
15	150	130	80.6
16	150	131	84.4
18	150	128	89.5
19	150	130	92.8
20	150	129	95.7
21	150	131	99.4
22	150	130	102.8
24	150	131	106.9
25	150	130	109.8
26	150	132	114.8
27	150	132	118.2
28	150	130	123.1
29	150	130	128.1
30	150	130	132.2
31	150	129	137.4
31.5	150	130	142.8
32	150	130	147.8
33	150	130	152.4
34	150	131	157.8
35	150	130	162.6
35.5	150	130	165.1
36	150	130	168.7
37	150	131	173.4
38	150	130	178.4
38.5	150	130	183.2

Experiment No. cat.6

Time [minute]	P_T(gauge) [kPa]	Temp. [°C]	Weigh Scale [g]
0	vacuum	131	0
0.5	70	131	23.3
1	100	131	33
2	150	129	42.5
4	150	134	49.2
5	150	131	53.7
5	150	131	55.5
6	150	133	30.2
7	150	129	63.2
8	150	131	65.4
9	160	132	70.1
10	150	132	74.3
11	150	130	79.2
12	155	128	83.2
13	160	128	88
15	150	131	93.1
16	150	130	97.1
17	150	130	100.9
18	150	129	103.3
19	150	130	107.9
20	150	130	109.8
21	150	131	114.2
22	150	130	119
23	150	130	123.5
23	150	129	128.4
24	150	130	133
33	150	131	139.5

B.4 Ethoxylation runs with varying agitation speeds

Experiment No. stir.1

Time [minute]	P_T(gauge) [kPa]	Temp. [°C]	Weigh Scale [g]
0	vacuum	100.5	5
1	50	100	28.3
2	100	100	43.8
4	150	100	63.7
6	150	100.5	68.8
7	150	100.5	77.7
8	150	100.5	81.9
9.5	150	100.5	90.7
11	150	100.5	96.9
13	220	100	121.7
16.5	150	100	127.3
18	150	101	132.9
19.5	150	100.5	141.3
20.5	150	100.5	146.4
22	150	100	153.2
23.5	150	100	160.1
24.5	150	100.5	167.4
26	150	100	174.6
27.5	150	101	181.7
29	150	101	187.1
30	150	100	195.3
32	150	100	201.7
33.5	150	100	208.5
35	150	101	214.2
37	150	100.5	221.6
38.5	150	100	229.2
40	150	100	236.2
42	150	100.5	243
43.5	150	100	249.3
45	150	100.5	255.1
46.5	150	100.5	262.1
48	150	100	268.3
50	150	100	275.8
52	150	100.5	282.5
53.5	150	100.5	289.7
55	150	100.5	296
57	150	100	304.7
59	150	100	312.2
61	150	101	318.3
63	150	100	327.4
65	150	100	336.3
67	150	100	343.2
69	150	100.5	350.2
71	150	100	357.2
73	150	100	363.7
75	150	100	369.6
77	150	100.5	375.8
79	150	100.5	382.6
81	150	100	389.5
83	150	100	395.6
85	150	100	402
87	150	100	408.6
89	150	100.5	414.4

Experiment No. stir.2

Time [minute]	P_T(gauge) [kPa]	Temp. [°C]	Weigh Scale [g]
0	vac	100	0
1	50	100	27
2	100	100	41.9
3	150	100	62.4
4	150	100.5	67.3
5	150	100	75.1
6	150	100	81.4
7	150	100	89.1
8	150	100.5	94.6
10	150	99.7	101.7
11	150	101	107.5
12	150	100.5	115.1
14	150	100	123.9
15.5	150	100.5	130.8
17	150	100	139.5
18	150	100	147.7
20	150	100.5	155.8
21	150	100	164.4
23	150	100	172.6
25	150	101	181.1
26	150	100.5	188.3
27	150	99.5	194.6
29	150	99.5	202.8
30.5	150	100	210.2
32	150	100.5	217
33	150	100	226.4
35	150	100.5	232.3
37	150	100	240.9
39	150	100	250.1
40.5	150	100.5	256.7
42	150	100.5	263.4
43.5	150	100.5	272.3
45	150	100.5	279
47	150	100	286.2
49	150	100	296.1
51	150	100	304.2
53	150	100.5	311.6
55	150	100	318.6
57	150	100	326.9

Experiment No. stir.3

Time [minute]	P_T(gauge) [kPa]	Temp. [°C]	Weigh Scale [g]
0	vac	100	0
2	50	100	24
3	100	100	43.2
4	150	100	60.9
5	150	100	66.8
6	150	100	71.8
7	150	100	77.4
8	150	100	84.2
9	150	100	91.1
10	150	100	98.1
11	150	100	103.8
12	150	100	109.2
13	150	100	115
14	150	100	122.7
15	150	100	129.4
16	150	100	134.2
17	150	100	139.6
18	150	100	146.3
19	150	100	154.3
20	150	100	160.4
21	150	100	166.4
22	150	100	173.2
23	150	100	179.2
24	150	100	185.4
25	150	100	190.6
26	150	100	196.2
27	150	100	201.7
28	150	100	208.3
29	150	100	214.4
30	150	100	218.8
31	150	100	224.7
32	150	100	232.2
33	150	100	239.3
34	150	100	243.8
35	150	100	248.5
36	150	100	253.6
37	150	100	259
38	150	100	263.8
39.5	150	100	268.2
40.5	150	100	275.7
41.5	150	100	281.1
43	150	100	288.6
44	150	100	292.8

Time [minute]	P_T(gauge) [kPa]	Temp. [°C]	Weigh Scale [g]
45	150	100	297.2
46	150	100	303.1
47	150	100	309
48	150	100	312
49.5	150	100	317.9
51	150	100	324.1
52.5	150	100	330.1
54	150	100	336.9
55	150	100	341.3
56	150	100	347.5
58	150	100	353.6
60	150	100	361.6
62	150	100	369.5
63.5	150	100	373.6
65	150	100	379
67	150	100	385
69	150	100	391.4
70.5	150	100	396.6
72	150	100	401.6
74	150	100	407.7
76	150	100	414.4
78	150	100	419.8
80	150	100	426
82	150	100	430.3
84	150	100	435.8
86	150	100	440.8
88	150	100	446.8
90	150	100	451.3
92	150	100	456.6
94	150	100	460.7
96	150	100	468.7
99	150	100	474.2
102	150	100	478.9
105	150	100	483.8
108	150	100	489.9
112	150	100	495.6
115	150	100	501.3
119	150	100	505.9
122	150	100	509.8
125	150	100	514.2
130	150	100	518.9

B.5 Kinetic runs

Experiment No. kin. 1a

Time [minute]	P_T(gauge) [kPa]	Temp. [°C]	Weigh Scale [g]
0	-101.3	87	0
1	20	87.1	34.8
2	70	86.5	73.4
3	150	86	106.8
16	150	88	109.7
23	150	88	113.2
27	150	88.2	116.8
32	150	88.1	120
36	150	88	123.7
40	150	88.1	127
45	150	88	131.1
49	150	88	135.2
53	150	88	138.9
57	150	88	142.8
62	150	88	145.9
67	150	88	149.4
70	150	88	152.7
74	150	88	156.8
78	150	88	159.5
82	150	88	162
86	150	88.2	165.9
91	150	88	167.9
95	150	88	171
99	150	88	174
104	150	88	177.6
108	150	88	180.3
112	150	88	182.8
117	150	88	185.7
120	150	88	188.6
124	150	88	191.4
127	150	88.3	194.7
129	150	88.1	198
132	150	88.5	201
135	150	88.2	204.8
137	150	88.1	209.9
139	150	88.2	211.2
141.5	150	88.5	217
144	150	88	220.1
146	150	88	223.7
148	150	88	227.5
150.5	150	88	231.7
153	150	88	235.8
155	150	88	239.7
157.5	150	88	244.3
159.5	150	88.5	248.6
162	150	88	251.4
164	150	88	256.3
166	150	88	258.8
168.5	150	88.2	262.5
171	150	88	267.6
173	150	88	270.5

Time [minute]	P_T(gauge) [kPa]	Temp. [°C]	Weigh Scale [g]
175	150	88	275.1
177.5	150	88	280.1
180.5	150	88	285.4
183.5	150	88	291.1
186	150	88	295.7
189	150	88	299.1
192	150	88	303.6
195	150	88	308.4
197.5	150	88	313.6
200	150	88	316.7
202.5	150	88	321.4
205	150	88	325.2
207.5	150	88	328.8
210	150	88.2	333.2
212.5	150	88	336.4
215	150	88	340.9
217.5	150	88	344.9
220	150	88	348.5
222	150	88	351.7
224.5	150	88.1	355.4
227	150	88	359.4
230	150	88.5	363.6
232.5	150	88	368.3
235.5	150	88	372.8
238.5	150	88	376.8
241	150	88	380.8
244	150	88	386.5
248	150	88	391.2
251	150	89	394.9
253	150	88.8	398.4
256	150	88.2	402.3
259	150	88	406.1
262	150	88	410.9
265	150	88	414.5
267	150	88	417.9
270	150	88	423.2
273	150	88.1	426.5
276	150	88	430.6
279	150	88	434.1
282	150	88	438.1
284.5	150	88	441.5
287	150	88	445.2
290	150	88	449.8
293	150	88	452.6
296	150	88	457.3
299	150	88	460.2
302	150	88	463.8
304.5	150	88	465.9
307	150	88	471.1
309	150	88	472.7

Experiment No. kin. 2a

Time [minute]	P_T(gauge) [kPa]	Temp. [°C]	Weigh Scale [g]
0	-101.3	98.5	0
1	20	99	36.1
2	70	98.5	65.5
3	150	98.5	93.9
4	150	99.5	96.5
6	150	98.5	101.2
10	150	98.7	105.7
14	150	99.5	110.1
16.5	150	99.5	112.9
18.5	150	99.3	116.5
21.5	150	99.5	119.6
23	150	99.5	122.8
24.5	150	99.5	124.7
26.5	150	99.5	127.4
28.5	150	99.5	129.8
31	150	99.9	133.1
32.5	150	99.5	136.7
35	150	99.7	139.9
37	150	99.7	143.6
39.5	150	99.3	148.5
42	150	99.5	151.4
44.5	150	99.5	155.2
46.5	150	99.5	157.7
49	150	99	161.8
52.5	150	99.5	165
54.5	150	99.5	168
57	150	99.5	171.3
59.5	150	99.5	174.7
61	150	99.5	176.7
63.5	150	99.5	179.7
66	150	99.5	182.8
68.5	150	99.5	187.2
72	150	99.5	190.6
75	150	99.9	193.8
77.5	150	99.5	197.2
80	150	99.5	200.1
82	150	99.5	203.1
84.5	150	99.5	207.1
86.5	150	99.5	211.7
88.5	150	99.9	216
89.5	150	100	218.4
91	150	99.5	221
92.5	150	99.5	224.1
93.5	150	99.9	227.1
95	150	99.5	232.6
97	150	100	236.5
98.5	150	99.8	240
99.5	150	99.5	244.1
101	150	99.5	247.3
102	150	99.5	250.4
103.5	150	99.5	253.9
104.5	150	99.5	256.2
106	150	99.5	260.9
107.5	150	99.1	266.1
109	150	99.3	269.3
111	150	99.5	273.9
113	150	99.9	278.1
114.5	150	99.8	281.9
115.5	150	99.5	285.4
117	150	99.7	289.2
118.5	150	99.5	293
120	150	99.5	297.5
121.5	150	99.5	300.9
123	150	99.7	304.9
125	150	99.5	310
126.5	150	99.5	313.5
128	150	99.8	317.3
130	150	99.5	321.5
132	150	99.5	326
134	150	99	330.1
136	150	99.7	333.9
138	150	99.5	338.6
140	150	99.5	342
142	150	99.5	346.3
144	150	99.5	350.3
146	150	99.5	351.4
148	150	99.5	359.3
150.5	150	99.5	364.2
152.5	150	99.5	367.8
154.75	150	99.5	371.4
156.75	150	99.5	376.1
159	150	99.5	380.5
161	150	99.5	384.2
163	150	99.5	388.1
165	150	99.5	392
167	150	99.5	395
169	150	99.5	399.1
171	150	99.9	402.6
173	150	99.9	406.5
175	150	99.9	410.6
177.5	150	99.3	414.5
179	150	99.5	417.9
182	150	99	421.5

Experiment No. kin. 3a

Time [minute]	P_T(gauge) [kPa]	Temp. [°C]	Weigh Scale [g]
0	-101.3	114.5	0
1	50	115	17
2	100	115	52.2
3	150	115	71.8
4	200	115	91.7
5	200	115.2	94.5
7	200	116	99
8	200	116.5	103
9.5	200	115	107.9
10.5	200	115	111.8
12	200	115	117.5
13	200	114	121.9
14.5	200	114.5	127.3
16	200	115	131.1
17	200	115	136.4
18.5	200	115	140
19.5	200	115.5	145.1
20.5	200	115	149.2
22	200	115.3	154.1
23	200	114.8	157
24	200	115	160.2
25	200	115	163.7
26.5	200	114.7	167.7
28	200	115	172.3
29	200	115	176.3
30.5	200	115	179.7
32	200	115	183.5
33	200	115	187.8
34.5	200	115	192.5
36	200	114.5	197.3
37	200	115	202.3
38.5	200	116	208.8
39.5	200	115	215.7
40.5	200	115	222.3
41.75	200	115	229.8
43	200	115	236.1
44	200	115	244.1
45	200	115	250.9
46	200	115	257.3

Time [minute]	P_T(gauge) [kPa]	Temp. [°C]	Weigh Scale [g]
47	200	115	264.3
48	200	115	269.7
49	200	115	278
50	200	115	284.3
51	200	115	290.7
52	200	115	298.5
53	200	115	304.7
54	200	115	310.1
55	200	115	317.2
56	200	115	323.7
57	200	115	329.6
58	200	115	337.2
59	200	115	342.6
60	200	115	350.3
61	200	115	356.8
62	200	115	363.6
63.5	200	115	371.1
65	200	114.5	378
66	200	115	385.6
67	200	115	390
68	200	115	398.4
69.5	200	115	404.4
70.5	200	115	410.9
72	200	115	416.2
73	200	115	422.3
74	200	115	432.8
75	200	115	437.9
76	200	115	443.3
77	200	114.5	451.5
78	200	114.5	459
79.5	200	115	463.4
81	200	115	470.5
82	200	115	478.6
83	200	115	483.6
83.5	200	115	490.6
86	200	115	497.9
87.5	200	115	506.3

Experiment No. kin. 4a

Time [minute]	P_T(gauge) [kPa]	Temp. [°C]	Weigh Scale [g]
0	-101.3	124	1.7
2	50	125	28.1
3	100	125	46.2
4	150	126	60
5	150	125	65.5
6.5	150	125	70.6
8	150	124.5	74.9
9	150	125	79.6
10	150	125	82.8
11	150	125.5	86.6
12	150	125	91.5
13	150	125	95.8
14	150	125	99.3
15	150	125	102.8
16	150	124	106.5
17	150	124	111.3
18.5	150	125	115.7
20	150	125	120.7
21	158	125	125.7
22.5	150	125	130.1
23.5	158	125	134.5
25	150	125	138.9
26	150	125	140.5
27	150	125	144.7
28	150	125	148.1
29	150	125	151.7
30.5	150	124.5	155.6
32	150	125	159.7
33	150	125	164
34	150	125	167.2
35	150	125	171.5
36	150	125	176.4
37	150	125.5	183.6
38	150	125	189.9
39	150	125	197.1
40	148	125	202.7
41	150	125	208.5
42	150	124.5	215.2
43	150	125	221.6
44	150	125	228.2
45	150	125	235.3
46	148	125	240.2
47	150	124.5	247

Time [minute]	P_T(gauge) [kPa]	Temp. [°C]	Weigh Scale [g]
48	150	125	253.5
49	148	125	261.1
50	150	125	267
51	151	125	273.6
52	150	124.5	281.5
53	150	124	286.3
54	150	125	291.6
55	150	125	297
56	150	125	304
57	150	125	309.5
58	150	125	316
59	150	124	322
60	150	125	327.1
61	150	125	332.8
62	150	125	338
63	150	125	344.3
64	150	125	350.2
65	150	125	356.1
66	150	124	361
67	150	125	366.5
68	150	125	372.2
69	150	125	377.5
70	150	125	382.8
71	150	125	386.4
72	150	125	392.8
73	150	124	396.8
74	150	124	402.8
75	149	124.5	407.2
76	150	125	411.6
77	150	125	415.4
78	150	125	420.5
79	150	125	425.5
80	150	125	430.2
81	150	124.5	434.6
82.5	150	124.5	440.2
84	150	125	445.7
85	150	125	451.3
95	60	125	-
108	55	124.5	-
128	55	125	-
158	55	125	-
199	60	146.5	-

Experiment No. kin. 5a

Time [minute]	P_T(gauge) [kPa]	Temp. [°C]	Weigh Scale [g]
0	-101.3	129	0
1	50	129	28
2	100	130	44.5
3	150	127	60.5
4.5	150	130	66.1
5.5	150	130	69.4
6.5	150	130	72.5
7.5	150	130	76.1
9	150	130	79.6
10	150	129	83.9
11	150	130	88.1
12	150	130	92.2
13.5	150	128	96.4
14.5	150	130	100.3
15.5	150	129.5	104.2
17	150	130	108.4
18	150	129.5	111.7
19	150	130	115
20	150	130	118.8
21.5	150	130	122.4
22.5	150	130	126.2
24	150	130	130.7
25	150	130	134.9
26	150	130	137.8
27.5	150	130	141.3
28.5	150	130	144.2
29.5	150	130	148.9
31	150	130	151.2
32	150	130	154
33	150	130	157.6
34	150	130	160.4
35.5	150	130	163.9
36.5	150	130	167.3
38	150	130	171.9
39	150	130	174.3
40	150	130	179.3
41	150	130	183.8

Time [minute]	P_T(gauge) [kPa]	Temp. [°C]	Weigh Scale [g]
42	150	130	189
43	150	130	192.6
44	150	130	198.4
45	150	130	203.1
46	150	130	208.3
47	150	130	213.8
48	150	131	217.4
49	150	130	223.7
50	150	130	228.3
51	150	130	233.3
52	150	130	238.4
53	150	130	243.9
54	150	130	249.9
55	150	131	254.9
56	150	130	258.8
57	150	130	262.9
58	150	130	267.8
59	150	130	272
60	150	130	276.9
61	150	130	281.8
62	150	130	286.8
63	150	130	291
67.5	50	130	-
71.5	30	130	-
83	25	131	-
88.5	20-25	130.5	-
89	20-25	130	-

B.6 Kinetic runs (repeated)

Experiment No. kin. 1b

Time [minute]	P_T(gauge) [kPa]	Temp. [°C]	Weigh Scale [g]
0	-101.3	86.5	0
0.5	20	87.2	35
2	70	87.2	71.4
3.5	150	88	103.1
10	150	88	105.4
16	150	88	108.9
21	150	88	111.3
25.5	150	88	113.3
30	150	88	116.1
34.5	150	88	119.1
39	150	88	122
44.5	150	88	125.3
48.5	150	88	127.9
52.5	150	88	130.7
56	150	88	132.4
60	150	88	134.9
64	150	88	138
67.5	150	87.8	140.2
72	150	87.8	143.4
76	150	87.8	146.6
81.5	150	87.8	151
85	150	87.5	152.5
88.5	150	87.5	154.6
92.5	150	87.5	156.9
97.5	150	87.5	160.4
103.5	150	87.5	163.7
107.5	150	87.5	166.7
112.5	150	87.5	169.3
117	150	87.8	170.9
122	150	88	174.2
127	150	88	176.4
132	150	88	179.8
137	150	88	182.5
142	150	88	184.2
144.5	150	88	186.3
147	150	88	187.9
150.5	150	88	190.9

Time [minute]	P_T(gauge) [kPa]	Temp. [°C]	Weigh Scale [g]
154.5	150	88.5	193.5
157	150	88	196.1
159	150	88	198.4
161.5	150	88	201.3
164	150	87.8	204.8
166	150	88.5	207.5
168.5	150	88.2	210.5
170.5	150	88.3	213.3
173	150	88.5	215.7
174.5	150	88	219
176	150	88	221.5
178	150	88	223.7
180	150	88	226.4
182	150	88.2	229.3
184	150	88.5	232.5
185.5	150	88	234.4
187	150	88	237.9
188.5	150	88	241
190.5	150	88	243.3
192.5	150	88	245.1
194	150	88	247.4
195.5	150	88	250.5
197.5	150	88	253
199	150	88	255.7
201	150	88	258
203	150	88	261
205	150	88	263.3
206.5	150	88	266.6
208.5	150	88	269.4
210	150	88	272.2
212	150	88.2	275.4
214	150	88.5	278.5
216	150	88.5	281.3
218	150	88	284.7
220	150	88	287.3

Experiment No. kin. 2b

Time [minute]	P_T(gauge) [kPa]	Temp. [°C]	Weigh Scale [g]
0	-101.3	96.5	0
1	20	97.5	28.9
2	70	98	60.1
4	150	98.9	83
6	150	99.2	89.3
8	150	99.7	93.5
11	150	99.3	95.8
15	150	99.8	100.5
19	150	99	104.6
22	150	99.5	108.6
25	150	99.5	112
28	150	99	114.9
31	150	99.5	118.9
33	150	99.2	121.4
35	150	99	124
37	150	99	126.6
39.5	150	99	129.7
42	150	99	133.5
45	150	99	136.7
48	150	99.5	139
51	150	99.7	142.3
53	150	99.3	145.3
55	150	99.5	146.8
58	150	99.5	150.5
60	150	99.8	153.5
62	150	99.5	155.6
64	150	99	159.2
67	150	99.5	161.4
70	150	99.5	163.8
73	150	99.7	166.8
75	150	99.5	168.8
77	150	99.5	172.3
80	150	99.5	175.2
83	150	99.5	177.1
85	150	99.5	179.3
87	150	99.5	181.9
90	150	99.2	185.7
93	150	99.5	188.9
94.5	150	99.9	191.1
96	150	99.6	194.6
97	150	99.5	197.2
98.5	150	99.5	200.7
100	150	99.4	203.6
102	150	99.5	206.6
103	150	99.5	209.6
104.5	150	99.5	212.1
106	150	99.5	214.8
107	150	99.5	218

Time [minute]	P_T(gauge) [kPa]	Temp. [°C]	Weigh Scale [g]
108	150	99.5	220.9
109	150	99.8	223.4
110	150	99.3	225.9
111	150	99.5	228.8
112	150	99.5	231.2
113.5	150	99.7	234.4
115	150	99.9	239.5
116.5	150	99.5	242.1
118.5	150	99.4	246.1
119.5	150	99	251.8
120.5	150	99.5	252.8
122	150	99.9	255.9
123.5	150	99.5	258.2
125	150	99.9	262.3
126	150	99.8	265.4
127	150	99.8	267.8
128.5	150	99	270.6
130	150	99.7	273.9
131.5	150	99.5	277
133	150	99.6	281
134	150	98.5	283.4
135	150	99.9	286.9
136.5	150	99.8	290.5
138	150	98.5	293.4
139.5	150	99.6	296.6
141	150	99.9	300.4
142.5	150	99.8	303.6
144	150	99.6	307
145.5	150	99.5	310.1
147	150	99.5	313.3
148.5	150	99.8	318.5
150	150	99.8	320.1
152	150	99.5	324.6
153	150	98.9	328
154.5	150	99.5	331.8
156	150	99.9	335.7
158	150	99.5	339.1
160	150	98.9	343.9
162	150	99.8	347.9
164	150	99.5	352.8
166	150	99.9	355.4
167.5	150	99	359
169	150	99	363.3
170.5	150	99.5	366
172	150	99.9	369.6
173.5	150	99.6	373.1
175	150	99.5	376.7
177	150	99.5	380.3

Experiment No. kin. 3b

Time [minute]	P_T(gauge) [kPa]	Temp. [°C]	Weigh Scale [g]
0	-101.3	114	0
1	50	115	24.1
2	100	115	41.1
3	150	115	60.4
4	150	116	64.9
5	150	115	68.3
6	150	115	72.2
7	150	115	74.3
8.5	150	115	77.2
10	150	116	80.4
11.5	150	115	82.9
13	150	115	86.3
14.5	150	115	90.1
16	150	114.5	93.1
17	150	115	95.7
18	150	115	98.5
19.5	150	115	101.5
20.5	150	115	103.7
22	150	115.5	106.4
23	150	115	108.7
24	150	115	110.9
25.5	150	115	114
26.5	150	115	116.6
27.5	150	114.5	119.6
29	150	115	121.5
30	150	115	123.7
31	150	115.5	125.8
32	150	115.5	128.1
33	150	115	130.1
34	150	115	132.4
35	150	115	134.2
36	150	115	137
37.5	150	115	139.3
39	150	115	141.5
40	150	116.5	143.8
41	150	115	145.7
42.5	150	115	148.6
44	150	115	150.7
45	150	115	153
46.5	150	115	155.9
48	150	115	157.6
49.7	150	115	161.2

Time [minute]	P_T(gauge) [kPa]	Temp. [°C]	Weigh Scale [g]
51	150	115	163.2
52.5	150	115	165.2
54	150	115	167.9
55.5	150	115	170.5
56.5	150	115	173.8
58	150	115	177.3
59	150	116	180.6
60	150	116	184
61	150	115.5	186.6
62	150	115	190.7
63	150	115	193.6
64	150	115	196.9
65	150	115	199.8
66	150	115	203.8
67	150	115.5	207.1
68.5	150	115	212.6
69.5	150	115	216.5
70.5	150	115	220.2
71.5	150	115	224.3
72.5	150	115	228
73	150	115.5	230.7
74	150	115	233.6
75	150	115.5	237.7
76	150	115	240.9
77	150	115	244.5
78	150	115	247.9
79	150	115	251.3
80	150	116.5	254.4
81	150	114.5	257.3
82	150	115	261.3
83	150	115	264.9
84	150	115	268.6
85	150	115	271.5
86	150	115	274.8
87	150	117	278.3
88	150	115	282.5
89	150	114	286
90	150	115	290
91	150	116	293.1
92	150	115	296.3
93.2	150	115	300.7

Experiment No. kin. 4b

Time [minute]	P_T(gauge) [kPa]	Temp. [°C]	Weigh Scale [g]
0	-101.3	123.5	0
1	50	124	23.7
2	100	124.5	42.2
3	150	123.5	57.1
4	150	125.5	60.3
5.5	150	125	64.4
6.5	150	125	67.6
7.5	150	124.5	70.7
8.5	150	125	73.6
9.5	150	124	76.2
11	150	125	80.2
12	150	125	83.4
13	150	125	87.3
14	150	125	90.9
15	150	125	93.7
16	150	127	96
17	150	125	99.3
18	150	124	102.5
19	150	124	104.7
20	150	125	106.7
21	150	126	109.9
22	150	125.5	112.6
23	150	124.5	115.4
24	150	124.5	118.7
25.5	150	124.5	121.4
26.5	150	125	124.4
27.5	150	125	127
28.5	150	125	129.9
29.5	150	124.5	133.2
30.5	150	125	135.4
31.5	150	123.5	138
32.5	150	124.5	141.2
34	150	125	143.9
35	150	125	146.8
36.5	150	123.5	149.6
37.5	150	125	152.3
38.5	150	124.5	155.5
39.5	150	125	159.1
40.5	150	124.5	161.8

Time [minute]	P_T(gauge) [kPa]	Temp. [°C]	Weigh Scale [g]
41.5	150	125	165.9
42.5	150	125	169.4
43.5	150	125	173.8
44.5	150	126.5	178.7
45.5	150	124.5	182.7
46.5	150	125	186.9
47.5	150	125.5	191.3
48.2	150	125	194.6
49	150	125	198.4
50	150	125.5	202.6
51	150	125	207
51.8	150	125	211.4
52.5	150	125	214.7
53.1	150	125	218.5
53.9	150	125	222.1
54.8	150	125	226.5
55.5	150	125	230
56.5	150	123.5	234.9
57.5	150	125.5	237.9
58.4	150	125	242.2
59.5	150	125	247.5
60.5	150	125	252.9
61.2	150	125	256.9
62.5	150	125	262.3
63.5	150	125	266.6
64.5	150	125	270.3
65.5	150	125	274.7
66.5	150	125	278.3
67.5	150	123.5	283.2
68.5	150	124	288.1

Experiment No. kin. 5b

Time [minute]	P_T(gauge) [kPa]	Temp. [°C]	Weigh Scale [g]
0	-101.3	127.5	0
1	50	129	23.1
2	100	129.5	34.1
3	150	132	38
5	150	130	43.9
6.5	150	130	45.7
8	150	130	48.8
10	150	130	51.2
11.5	150	130	54.1
13	150	130	56.9
14.5	150	130	59.6
16	150	130	61.8
17.5	150	130	64.5
19	150	130	67.2
20.5	150	130	69.7
22.5	150	130	72.4
24.5	150	130	74.9
26	150	129.5	77.1
28	150	129.5	79.8
30	150	130	83.7
32	150	130	86.6
33	150	129.5	89.7
34	150	129.5	93.3
35.5	150	130	97.9
36.5	150	130.5	100.4
37.5	150	130	104.7
39	150	129	109
40	150	1305	112.3
41	150	130	116.3
42	150	130	119.2
43	150	130	122.3
44	150	130	126.1
45	150	130	129.1
46	150	130	132.8
47	150	130	136.5
48	150	130	139.7

Time [minute]	P_T(gauge) [kPa]	Temp. [°C]	Weigh Scale [g]
49	150	130	143
50	150	130	146.6
43	150	130	192.6
44	150	130	198.4
45	150	130	203.1
46	150	130	208.3
47	150	130	213.8
48	150	130	217.4
49	150	130.5	223.7
50	150	130	228.3

Appendix C

Heat Transfer in Turbulent Pipe Flow

This appendix presents the heat transfer calculation for the case *a* ethylene oxide flow (1) under the conditions specified in Table 7. 3 and (2) using a larger pipe in the same length. The calculations use the Nusselt empirical correlation (Equation 7. 3) for entrance flow not fully developed:

$$Nu_d = 0.036 Re_d^{0.8} Pr^{1/3} \left(\frac{d_{\text{i.d.}}}{L}\right)^{0.055} \text{ for } 10 < \frac{L}{d_{\text{i.d.}}} < 400 .$$

(1) The 40mm pipe used has an inner diameter $d_{\text{i.d.}}$ of 0.0409m, the length L 2.7m and the cross-sectional area A_x $1.314\times10^{-3}m^2$ (Table 7. 2). Ethylene oxide entered the pipe at a mass rate $\dot{m}$ of 11kg/min and the temperature of 17.8°C. The properties of ethylene oxide at 17.8°C are:

ρ=859 kg/m^3;

μ=2.86×10^{-4} kg/ms;

C_p=1.98×10^3J/kg°C;

λ=0.156W/m°C.

Note that both C_p and k were taken as the values at 10.85°C.

$$Re_d = \frac{\rho u_m d_{\text{i.d.}}}{\mu} = \frac{(11/60)/(1.314\times10^{-3})(0.0409)}{2.86\times10^{-4}} = 19953$$

$$Pr = \frac{C_p \mu}{\lambda} = \frac{(1.98\times10^3)(2.86\times10^{-4})}{0.156} = 3.6$$

Calculating Nusselt number by the above correlation, we obtain

$$Nu_d = \frac{hd_{\text{i.d.}}}{\lambda} = 0.036(19953)^{0.8}(3.6)^{1/3}(\frac{0.0409}{2.7})^{0.055} = 120.7$$

$$h = \frac{\lambda}{d_{\text{i.d.}}} Nu_d = \frac{(0.156)(120.7)}{(0.0409)} = 460.37 \text{ W/m}^2\text{°C}.$$

The heat flow per unit length is then

$$\frac{q}{L} = h\pi d(T_w - T_b) = (460.37)\pi(0.0409)(78.9 - 17.8) = 3614.3 \text{ W/m}$$

Note that, $T_w = \frac{(140 + 17.8)}{2} = 78.9\,(°\text{C})$ was taken as the midpoint of the fluid temperatures on either side of the pipe for simplicity (Section 7.3.4.1).

Applying the energy balance to calculate the increase in ethylene oxide bulk temperature in the dip-leg pipe of 2.7m, we have

$$q = \dot{m}C_p(T_{b2} - T_{b1}) = L(\frac{q}{L}) = (2.7)(3614.3) = 9758.5 \text{ W}$$

Therefore,

$$(T_{b2} - 17.8) = \frac{9758.5}{(11/60)(1.98 \times 10^3)} = 26.9\,°\text{C}$$

The ethylene oxide exit temperature is then equal to 44.7°C (=26.9+17.8).

(2) Now, the pipe used in the above calculation is replaced with a 50mm size pipe. The inner diameter $d_{\text{i.d.}}$ and the cross-sectional area A_x become 0.0525m and $2.165 \times 10^{-3}\text{m}^2$ respectively (Table 7. 2); the length L is kept at 2.7m. We now have:

$$Re_d = \frac{\rho u_m d_{\text{i.d.}}}{\mu} = \frac{(11/60)/(2.165 \times 10^{-3})(0.0525)}{2.86 \times 10^{-4}} = 15545$$

$$Pr = \frac{C_p \mu}{\lambda} = \frac{(1.98 \times 10^3)(2.86 \times 10^{-4})}{0.156} = 3.6 \text{ , unchanged}$$

$$Nu_d = \frac{hd_{\text{i.d.}}}{\lambda} = 0.036(15545)^{0.8}(3.6)^{1/3}(\frac{0.0525}{2.7})^{0.055} = 100.2$$

$$h = \frac{\lambda}{d_{\text{i.d.}}} Nu_d = \frac{(0.156)(100.2)}{(0.0525)} = 297.75 \text{ W/m}^2\text{°C}.$$

The total heat is

$$q = h\pi dL(T_w - T_b) = (297.75)\pi(0.0525)(2.7)(78.9 - 17.8) = 8101.6\,\text{W}.$$

But

$$q = \dot{m}C_p(T_{b2} - T_{b1}) = 8101.6\ \text{W}$$

Therefore,

$$(T_{b2} - 17.8) = \frac{8101.6}{(11/60)(1.98 \times 10^3)} = 22.3\,°\text{C}$$

The temperature of ethylene oxide exiting a 50mm pipe is calculated to be 40.1°C (=22.3+17.8).

Appendix D

Experimental Data of Industrial Ethoxylation

This appendix presents the details of pressure variations recorded in the plant batch reports for the simulation runs described in Table 7. 10. The corresponding values for averaged ethylene oxide adduct number, mass and molar fraction of ethylene oxide in the reaction mixture are also derived.

Batch ID N2-71542

Time [minute]	P_T [kPa]	P_{N_2} [kPa]	EO mass rate [kg/min]	$P_{EO}= P_T - P_{N_2}$ kPa	N_{EO}	X_{EO}	Y_{EO}
0	326.5	244.5	15.6	82.1	1.310	0.0689	1.16E-02
0.6	328.6	247.1	15.6	81.6	1.323	0.0685	1.15E-02
1.2	328.6	249.7	15.6	78.9	1.336	0.0665	1.11E-02
1.7	331.4	252.0	15.6	79.4	1.346	0.0670	1.12E-02
2.3	331.4	254.8	15.6	76.6	1.359	0.0648	1.08E-02
2.9	334.0	257.6	15.6	76.4	1.372	0.0648	1.07E-02
3.5	334.0	260.5	15.6	73.5	1.385	0.0625	1.03E-02
4.1	334.0	263.5	15.6	70.6	1.397	0.0603	9.92E-03
4.7	337.7	266.5	15.6	71.2	1.410	0.0609	1.00E-02
5.2	337.7	269.1	15.6	68.6	1.421	0.0588	9.62E-03
5.8	340.7	272.2	15.6	68.5	1.434	0.0588	9.61E-03
6.4	342.8	275.5	15.6	67.3	1.446	0.0579	9.43E-03
7	342.8	278.8	15.6	64.0	1.459	0.0553	8.97E-03
7.6	345.9	282.2	15.6	63.7	1.472	0.0551	8.92E-03
8.2	345.9	285.6	15.6	60.2	1.485	0.0523	8.43E-03
8.7	348.2	288.6	15.6	59.6	1.495	0.0519	8.35E-03
9.3	351.8	287.0	15.6	64.8	1.508	0.0562	9.06E-03
9.9	351.8	289.9	15.6	61.9	1.521	0.0539	8.65E-03

Batch ID N11-74591

Time [minute]	P_T [kPa]	P_{N_2} [kPa]	EO mass rate [kg/min]	P_{EO}= P_T - P_{N_2} kPa	N_{EO}	X_{EO}	Y_{EO}
0	322.6	244	15.73	78.6	7.33	0.1006	8.98E-03
0.7	324.6	245.4	15.73	79.2	7.37	0.1015	9.05E-03
1.3	325.4	246.6	15.73	78.8	7.40	0.1012	8.99E-03
2	326.5	248.1	15.73	78.4	7.44	0.1010	8.95E-03
2.7	328.5	249.5	15.73	79.0	7.47	0.1019	9.01E-03
3.3	329.3	250.8	15.73	78.5	7.50	0.1015	8.95E-03
4	330.1	252.3	15.73	77.7	7.54	0.1007	8.84E-03
4.7	332.4	253.8	15.73	78.5	7.58	0.1019	8.93E-03
5.3	333.2	255.2	15.73	78.0	7.61	0.1015	8.87E-03
6	334.5	256.7	15.73	77.8	7.65	0.1014	8.84E-03
6.7	336.7	258.3	15.73	78.4	7.68	0.1024	8.91E-03
7.3	338.3	259.7	15.73	78.6	7.72	0.1028	8.93E-03
8	339.3	261.3	15.73	78.0	7.75	0.1023	8.85E-03
8.7	341.3	262.9	15.73	78.4	7.79	0.1030	8.88E-03
9.3	342.3	264.3	15.73	78.0	7.82	0.1027	8.84E-03
10	343.2	266.0	15.73	77.2	7.86	0.1019	8.74E-03

Batch ID N40-75579

Time [minute]	P_T [kPa]	P_{N_2} [kPa]	EO mass rate [kg/min]	P_{EO}= P_T - P_{N_2} kPa	N_{EO}	X_{EO}	Y_{EO}
0.0	338.0	212.0	16.26	126.0	25.91	0.2231	9.20E-03
2.0	340.3	214.6	16.26	125.6	26.18	0.2212	9.03E-03
4.0	340.9	217.3	16.26	123.6	26.45	0.2170	8.73E-03
6.0	343.4	220.0	16.26	123.4	26.72	0.2154	8.58E-03
8.0	347.2	222.8	16.26	124.4	26.99	0.2154	8.51E-03
10.0	351.3	225.7	16.26	125.6	27.26	0.2156	8.45E-03